



HAL
open science

On the design of 3D printable architected sheets

Filippo Agnelli

► **To cite this version:**

Filippo Agnelli. On the design of 3D printable architected sheets. Solid mechanics [physics.class-ph]. Institut Polytechnique de Paris, 2021. English. NNT : 2021IPPAX077 . tel-03533041

HAL Id: tel-03533041

<https://theses.hal.science/tel-03533041>

Submitted on 18 Jan 2022

HAL is a multi-disciplinary open access archive for the deposit and dissemination of scientific research documents, whether they are published or not. The documents may come from teaching and research institutions in France or abroad, or from public or private research centers.

L'archive ouverte pluridisciplinaire **HAL**, est destinée au dépôt et à la diffusion de documents scientifiques de niveau recherche, publiés ou non, émanant des établissements d'enseignement et de recherche français ou étrangers, des laboratoires publics ou privés.



INSTITUT
POLYTECHNIQUE
DE PARIS

NNT : 2021IPPAX077

Thèse de doctorat



On the design of 3D printable architected sheets

Thèse de doctorat de l'Institut Polytechnique de Paris
préparée à l'École polytechnique

École doctorale n°626 École doctorale de l'Institut Polytechnique de Paris (EDIPP)
Spécialité de doctorat : Mécanique des fluides et des solides, acoustique

Thèse présentée et soutenue à Palaiseau, le 18 octobre 2021, par

FILIPPO AGNELLI

Composition du Jury :

Grégoire Allaire Professeur, École Polytechnique (CMAP)	Président
Djimédo Kondo Professeur, Université Sorbonne (<i>l'</i> Alembert)	Rapporteur
Arthur Lebée Maître de conférences, École des Ponts ParisTech (Navier)	Rapporteur
Chiara Daraio Professeure, California Institute of Technology	Examinatrice
Dietmar Hömberg Professeur, Technische Universität Berlin	Examineur
Giulia Scalet Professeure adjointe, Università di Pavia	Examinatrice
Andrei Constantinescu Directeur de recherche CNRS, École Polytechnique (LMS)	Directeur de thèse
Grigor Nika Chercheur, Weierstrass Institute	Invité

Ai miei genitori Cristina e Stefano, che hanno sempre sostenuto le mie scelte.

Acknowledgement

Over the past three years, I have learned to what extent the experience of a doctorate exceeds the accomplishments of a long personal work. I have got the chance to meet and collaborate with so many people from various countries and horizons, from whom I learned a lot, both on a professional and personal level. I take the opportunity through these few lines to thank and express my gratitude to the persons who have guided and supported me in this adventure.

First of all, I would like to express my gratitude to my thesis supervisor Andrei Constantinescu. Since the master MAGIS back in 2018, Andrei has always shown me plenty of attention and kindness, devoting extra-time to answer questions on the numerical methods classes, and most importantly to prepare a proposal for the project that have become my master's internship. The highly positive experience during the master's working under his supervision is what made me envisage to undertake a doctorate at LMS. During the PhD, I praise his flawless support (in presence at the lab and from remote during the pandemics), helping me to solve problems, providing scientific knowledge, method, also providing encouragement when needed. All these ingredients have made the thesis an unforgettable experience.

I would like to warmly thank Grigor Nika, with whom I have collaborated during my master and my PhD thesis. Grigor has played a fundamental role to help me understanding the theoretical and numerical aspects of homogenization theory, as well as the topology optimisation algorithms, and I thank him for his patience! I am grateful that we managed to keep the discussions, in spite of the distance, and I hope we will keep have more occasions to collaborate in the future. I am delighted to have him in the jury for my defence.

I would like to thank Djimédo Kondo and Arthur Lebée for kindly accepting to review my manuscript as well as for providing valuable comments and advice.

I am grateful to thank Chiara Daraio, for inviting me to visit her group at Caltech during Spring 2019. I am honoured to have her in the jury for my defence. I take the opportunity to thank Paolo Celli and Connor McMahan for their hospitality at Caltech and for their help and their exchange. They made my visit very pleasant and fruitful.

I would like to thank Grégoire Allaire for his lending expertise on topology optimization, that I could receive during his classes. I am truly honoured to have him as the president of my thesis jury. I take the opportunity to thank Beniamin Bogosel (CMAP) and Charles Dapogny (ex-CMAP) for their availability to help me with technical aspects in the optimisation code with `FreeFem++`.

I would like to thank Dietmar Hömberg and Giulia Scalet for kindly accepting to be part of my thesis jury.

I commend Pierre Margerit for his essential contribution with the identification methods using digital image correlation. It was a pleasure working with him during his stay at LMS, I praise his commitment and knowledge and I wish him the best for the future.

I am indebted to the technical staff of the laboratory: Sylvain Durbecq, Pascal Marie, Simon Hallais, Alexandre Tanguy, Vincent de Greef and Hakim Gharbi for their help in the manufacturing aspects and testing phases. Alexandra Joly, Anna Johnsson, Christiane Periam, Valérie Jamet and Abdelfattah Halim for the administrative and IT aspects.

A warm thank goes also to Gareth Paterson and Aline Becq from the Drahi X-Novation Center, for their help with the printing process.

A special thank to all PhDs/postdocs that I have acquainted at the laboratory, which made this journey so incredible: my office mates Marco, Martin and Kübra, but also Nikolai, Matthias, Yanis, Othmane, Clément, Lucas, Nicole, Camille, Chloé, Alexandre, Jérémy, Jessica, Nikhil, Nicolas, Svetlana, Antoni, Zahra, Vincenzo and many others (pardon me for the persons in forgot to mention in the list).

The dedication required to undertake long studies up to the doctoral degree would not have been possible without the support of friends and my family:

A special thank goes to my friends - PhD students from other laboratories at Polytechnique: Alice, Felipe, Matteo, Tullio, Martina, Simone, Alberto: good luck to you as well for your future defences.
- From ENS Cachan: Roméo, Willy, David, Ronan, Kévin, Thomas, Morgane to cite a few of them
- from the MAGIS master: Mohammad, Pierluigi, Vincenzo and Michele. - My maths buddies Andrea, Carlo, Mattia, as well as Imke, Monica and the rest of the team.

Finally, I express my deepest gratefulness to my parents for their loving support and understanding in both good and bad times. I also have a special thought for my grand parents, who left too early to witness the conclusion of the story but still present in deeds and thoughts. Grazie di tutto.

Contents

Introduction	13
I Background material	19
1 Mechanical characterisation of elastic composite materials	21
1.1 Introduction	21
1.2 Recall on asymptotic homogenisation	23
1.2.1 Problem setting	23
1.2.2 Asymptotic homogenisation method	24
1.2.3 Effective stiffness coefficients	29
1.2.4 Effective equations on the macroscopic scale	29
1.2.5 Comments	30
1.2.6 Periodic homogenisation: summary	30
1.3 Bounds on plane elastic stiffness with orthotropic symmetry	30
1.3.1 Elastic materials with orthotropic symmetry	30
1.3.2 Variational bounds on the effective moduli for orthotropic composites	32
1.4 Elastic panels with a periodic microstructure	34
1.4.1 Problem setting	34
1.4.2 Periodic plate with thickness comparable to the period	36
1.4.3 Effective plate stiffness coefficients	40
1.4.4 Effective equations on the macroscopic scale	43
1.4.5 Comments	44
1.4.6 Elastic panels with a periodic microstructure: summary	44
2 Shape and topology optimisation	47
2.1 An overview of the structural optimisation	47
2.2 Overview of the shape optimisation	48
2.2.1 Ill-posedness of shape optimisation problems and remedies	48
2.2.2 Main categories of shape optimisation techniques	49
2.3 Shape sensitivity analysis using Hadamard's boundary variation method	52
2.3.1 Shape differentiability and computation of shape derivatives	52
2.3.2 Shape derivation using C�ea's Lagrangian method	53
2.3.3 Steepest descent direction	56
2.4 Shape and topology optimisation using a level set method	56
2.4.1 The level set method	56
2.4.2 Coupling shape sensitivity with a level set description	60
2.4.3 Numerical algorithm	61
2.4.4 Formulation in the smooth inter-phase context	62

II	Design of 3D printable architected sheet materials	67
3	Computational design of periodic architected sheets exhibiting a negative Poisson's ratio	69
3.1	Introduction	69
3.2	Computational design	71
3.2.1	Material distribution using a smooth inter-phase approach	71
3.2.2	Optimisation problem	72
3.2.3	Shape derivative in the smooth inter-phase context	72
3.2.4	Approximate formula for the shape derivative	74
3.2.5	Shape derivative of the volume constraint	75
3.2.6	Extension and regularisation of the velocity field and descent direction	76
3.3	Numerical algorithm	76
3.4	Examples of obtained microstructures	77
3.4.1	Example 1	78
3.4.2	Example 2	79
3.4.3	Example 3	80
3.4.4	Example 4	80
3.5	Conclusion and perspectives	81
3.5.1	Conclusion	81
3.5.2	Possible future works	81
4	3D printing and testing of architected polymeric sheets exhibiting a negative Poisson's ratio	83
4.1	Introduction	83
4.2	Materials and methods	84
4.2.1	Manufacturing process: equipment and base material	84
4.2.2	Testing and full-field displacement measurement using Digital Image Correlation (DIC)	85
4.2.3	Experimental estimation of the effective Poisson's ratio	86
4.3	Analysis of fabricated polymer structures	87
4.3.1	Experimental results	87
4.3.2	Comparison to numerical simulations	89
4.4	Conclusion	92
5	Systematic two-scale image analysis of extreme deformations in soft architected sheets	93
5.1	Introduction	93
5.2	Materials and methods	95
5.2.1	Unit cell architecture	95
5.2.2	Fabrication of natural rubber architected sheets	96
5.2.3	Experimental setup and testing	96
5.2.4	Local and global Digital Image Correlation	98
5.2.5	Numerical simulations	99
5.3	Results and discussion	100
5.3.1	Numerical simulations	100
5.3.2	Two-scale kinematic analysis	102
5.3.3	Truss-hinge equivalent kinematic model	106
5.4	Concluding remarks	109

III	Design of 3D printable thin composite panels	111
6	Shape-shifting panel from 3D printed undulated ribbon lattice	113
6.1	Introduction	113
6.2	Design of the unit cell	115
6.3	Extension–bending coupling (EBC) mechanism	116
6.3.1	Deformation mechanisms of undulated ribbons	117
6.3.2	From undulated ribbons to architected unit cells	117
6.3.3	Influence of h^* and t^*	120
6.3.4	Extension–bending effect for smaller Poisson's ratio interval	121
6.3.5	Influence of a varying stiffness along the height	122
6.4	Analysis of fabricated polymer panels	123
6.4.1	Additive manufacturing	123
6.4.2	Mechanical testing	124
6.5	Conclusion and perspectives	126
6.5.1	Projects associated	127
7	Design of thin architected panels with extension–bending coupling effects using topology optimisation	129
7.1	Introduction	129
7.2	Setting of the problem	131
7.3	Optimisation problem	133
7.3.1	Coupling shape sensitivity with a level set description	134
7.3.2	Shape derivative in the smooth inter-phase context	135
7.3.3	Approximate formula for the shape derivative	137
7.3.4	Volume constraint	139
7.3.5	Extension and regularisation of the velocity field and descent direction	139
7.4	Optimisation algorithm	140
7.5	Numerical results	142
7.5.1	Example 1	143
7.5.2	Example 2	146
7.5.3	Example 3	147
7.5.4	Example 4	151
7.6	Conclusion and perspectives	152
	Conclusions and future work	155
	Résumé en français	157
	Bibliography	162
IV	Supplementary materials	179
A	Thin plates theories	181
A.1	Recall on Kirchhoff–Love thin plate theory	181
A.2	Constitutive behaviour of laminate plate as a route for prescribing targets	182
A.3	Two-scale analysis and effective coefficients	184
B	Penalty and augmented Lagrangian methods for constrained optimisation problem	185
B.1	Problem setting	185
B.2	Equality volume constraint: Lagrange multipliers method	185
B.3	Two-sided inequality constraints	186

C	Experimental techniques	189
C.1	Digital Image Correlation	189
C.2	Macroscopic strain computation	191
D	Complementary documents	193
D.1	Homogenisation: numerical implementation with FreeFem++	193
D.2	Compliance plate tensors for shape of chapter 7	194

General notations

Throughout this manuscript, scalars will be denoted by italic small Roman, a , or Greek letters, α ; Vectors by boldface Roman letters, \mathbf{v} , or Greek letters θ ; Second order tensors by boldface italic Roman letters, \mathbf{D} , or Greek letters, ε ; Fourth order tensors by sans-serif Roman capital letters, C . Unless stated explicitly, the space is endowed with an orthonormal reference $(O, \mathbf{e}_1, \mathbf{e}_2, \mathbf{e}_3)$. Cartesian components will be introduced, such that, for example, $v_i, \varepsilon_{ij}, C_{ijkl}$ are the Cartesian components of \mathbf{v}, ε and C respectively. Unless otherwise stated, Latin indices will range from 1 to 3, while Greek indices will range from 1 to 2. Use will be made of Einstein summation convention: repeated indices are summed, unless it is explicitly stated otherwise.

$$a_i b_i = \sum_1^d a_i b_i$$

δ_{ij} denotes the Kronecker symbol: it is a function of two variables (usually just non-negative integers) defined by:

$$\delta_{ij} = \begin{cases} 0 & \text{if } i \neq j \\ 1 & \text{if } i = j \end{cases}$$

If Ω is a bounded domain of \mathbb{R}^3 , its boundary may be denoted by $\partial\Omega$. The average of a quantity over a region Ω is denoted by $\langle \bullet \rangle_\Omega$ is expressed as follows:

$$\langle \bullet \rangle_\Omega = \frac{1}{|\Omega|} \int_\Omega \bullet \, d\mathbf{x}$$

where $|\Omega|$ denotes the volume of the region.

$H^1(\Omega)$ denotes the classical Hilbert space. $H_{\text{per}}^1(\Omega)$ denotes the functional space encompassing all functions of H^1 class, featuring Ω -periodicity, i.e., their trace on opposite sides (or faces) of Ω is equal.

Single dot products between two vectors will be denoted by $\mathbf{u} \cdot \mathbf{v} = u_i v_i$; Double dot products will be denoted by $\boldsymbol{\sigma} : \boldsymbol{\varepsilon} = \sigma_{ij} \varepsilon_{ij}$. Tensor products will make use of the symbol \otimes (e.g., $\mathbf{u} \otimes \mathbf{v}$ with Cartesian components $u_i v_j$, $\boldsymbol{\sigma} \otimes \boldsymbol{\varepsilon}$ with components $\sigma_{ij} \varepsilon_{kl}$). Other types of products will be denoted using matrix notation (e.g., $\boldsymbol{\varepsilon} \mathbf{v}$ with components $\varepsilon_{ij} v_j$, $C \boldsymbol{\varepsilon}$ with components $C_{ijkl} \varepsilon_{kl}$, $C S$ with components $C_{ijkl} S_{ijkl}$).

Partial derivatives will be denoted by $\partial u_i / \partial x_j$. The following notations for differential operators will be used: $\nabla \phi$ with components $\partial \phi / \partial x_j$ will denote the gradient of the scalar field ϕ ; $\nabla \mathbf{u}$ with components $\partial u_i / \partial x_j$ will denote the gradient of the vector field \mathbf{u} . The single dot product $\nabla \cdot \mathbf{u}$ with components $\partial u_i / \partial x_i$ will denote the divergence of the vector field \mathbf{u} ; $\nabla \cdot \boldsymbol{\sigma}$ with components $\partial \sigma_{ij} / \partial x_j$ will denote the divergence of the tensor field $\boldsymbol{\sigma}$.

The duality product will be denoted by $\langle \bullet | \bullet \rangle$.

Introduction

This thesis was prepared at the Laboratoire de Mécanique des Solides at École polytechnique and was supported by École Normale Supérieure Paris-Saclay through a specific doctoral contract¹.

The great advances that have occurred for the last decades in field of additive manufacturing (3D printing) have enabled the processing of three-dimensional objects of complex geometries, including architected materials, i.e., materials with an inner micro-architecture of tailorable geometry. These days, such manufacturing techniques can be performed for several types of materials (including metallic alloys, ceramics and polymers) and at different scales (from microscopic devices to 3D printed houses). Since the effective properties of structured materials derive mostly from their inner geometry, a control on the micro-architecture ensured by the additive manufacturing techniques opens the way to a new range of engineered materials with effective prescribed mechanical properties. Starting from elementary arrangements of material in an designed representative cell, one can build complex structures either by repeating these arrangements periodically or by distributing the cells to obtain a desired macroscopic distribution of properties. The fabrication of macroscopic samples of these hierarchical materials can be used for various applications, including biocompatible scaffolds, medical devices, remote aerospace applications, ultra-light vibration absorbing layers or shock-absorbing layers, high-strength structures with exceptional cooling capabilities, controlled non-linear behaviour, self-folding structures. The high expectations of the printing technologies and their structural applications raised a series of challenges in the design of these structures:

- shape design of the structures and property tuning of architected materials;
- spatial distribution of small-scale structures based on specified loading;
- parameters, influence of the process parameters on the final structure.

Regarding the optimal shape design, systematic algorithms are for example well established for prescribed macroscopic distribution of properties in the case of small strain linear elasticity. Yet, these techniques remain quite limited in use at an industrial scale, partly due to the lack of understanding, missing constitutive models and simulation tools which tackles the possibility to find an optimal configuration. The landscape lacks more coherent global design approach where the structural optimisation would meet manufacturing constraints including geometrical precision, or also material transformation, in the printing process.

The thesis manuscript is divided into three parts, which contain seven chapters, and is completed by four appendices. A brief outline of each part is provided in the following lines.

Part I. Background material

The first part of this manuscript has a bibliographical purpose. The two main domains of the proposed work - namely the asymptotic homogenisation method and the shape optimisation - are presented in two separated chapters.

¹Contrat Doctoral Spécifique Normalien (CDSN):
<https://ens-paris-saclay.fr/recherche/doctorat/contrats-doctoraux-specifiques-normaliens-cdsn>

Chapter 1. Mechanical characterisation of elastic composite materials

This chapter deals with the determination of the overall properties, also called effective properties, of a composite material formed by periodic variations of either material properties or of geometric construction. After an introduction which reviews the state of the art of the mechanical characterisation of elastic structures, the discussion delves into the details of the asymptotic homogenisation theory. The theory consists in trading the representation of an heterogeneous architected material that demands a fine and heavy geometrical description, for an equivalent homogeneous medium that typically exhibits a more complex behaviour (e.g., which includes anisotropies, or more kinematic degrees of freedom). First, the general case of architected materials with a periodic pattern along all directions is reviewed. Assuming that the displacement field inside the medium can be written using an asymptotic expansion, analytical formulas for the effective elastic coefficients that depend on the material distribution inside a rescaled elementary cell are derived. Next, after identifying the general macroscopic behaviour of the architected sheets, the space of admissible tensors with orthotropic material symmetry is obtained. Last, the specific case of plate structures with an in-plane periodic micro-architecture is discussed. Assuming that the thickness of the panel is comparable to the length of the period yields a generalised Kirchhoff–Love thin plate macroscopic behaviour. Once again, the effective plate coefficients are computed analytically from the material distribution inside the unit cell.

Chapter 2. Shape and topology optimisation

The main ingredients required to use shape and topology optimisation are reported in this chapter. After an introduction which defines the philosophy of the shape optimisation problem, we shortly tackle the theoretical problem of non-existence of an optimal domain that minimises a shape-dependent cost functional $\mathcal{J}(S)$ and discuss the techniques to circumvent it. The classification for the main categories of shape optimisation, i.e., parametric, geometric and topology optimisation, are then presented succinctly. The discussion is then centred on topology optimisation, which addresses the problem of shape optimisation in all generality. We rapidly go through the main methods for topology optimisation, including the density methods (e.g., the homogenisation method, the SIMP), topological sensitivity method and the implicit methods (e.g., phase field method, level set method). Next, we recall the concept of a shape derivative, relying on the framework of Hadamard’s method, whereby variations of a given shape S of the form $(\mathbf{I} + \boldsymbol{\theta})(S)$ are considered, for *small velocity fields* $\boldsymbol{\theta}$. Related notions of differentiation with respect to the shape are recalled: in particular, the concept of shape derivative is introduced to extract a notion of shape gradient for the iterative minimisation of the objective. For shape-dependent functions, a formal Lagrangian method for obtaining shape derivatives is presented and formulas for the shape derivative of volume and surface integrals are recalled. The background material on the shape sensitivity method is illustrated through an example about how to find the shape derivative expression of a general type functional:

$$\mathcal{J}(S, \mathbf{u}(S)) = \int_S j(\mathbf{x}, \mathbf{u}(S)) \, d\mathbf{x} + \int_{\partial S} k(\mathbf{s}, \mathbf{u}(S)) \, ds,$$

where \mathbf{u} is the solution of a linear elasticity system. The second ingredient for the selected topology optimisation method, namely the level set method for the description of the shape, is then described. All shapes are assumed to be included in a large computational domain \mathcal{D} and are represented implicitly via the zero level set of a scalar function ϕ . The shape propagation under a velocity field $\boldsymbol{\theta}$ is then described via the *advection* of the level set function through an Hamilton–Jacobi equation. Finally, the combination of shape sensitivity with a level set description is explained. The shape gradient is interpreted as an advection velocity for the level set function and an iterative algorithm is built for the numerical minimisation of the cost function. Two basic steps for this coupling are explained: the “Ersatz material” approach for representing the void part $\mathcal{D} \setminus S$ and the extension and regularisation of the velocity field in order to accelerate the convergence

speed. Finally, the last section of the chapter deals with the diffuse inter-phase approach, which permits to derive a simplified, yet mathematically rigorous, formulation for the shape propagation.

Part II. Design of 3D printable architected sheet materials

This second part proposes the complete design cycle for several auxetic materials where the cycle consists of three steps (i) the design of the micro-architecture (chapter 3), (ii) the manufacturing of the material and (iii) the testing of the material (chapter 4 and chapter 5).

Chapter 3. Computational design of periodic architected sheets exhibiting a negative Poisson's ratio

The term auxetic indicates materials with a negative Poisson's ratio (ν), i.e. materials that tend to expand transversely to an applied uniaxial stretch load and vice versa. In this chapter, a topology optimisation algorithm featuring the level set method and the asymptotic homogenisation permits to obtain periodic architected materials with a prescribed effective elasticity tensor and Poisson's ratio. A target objective was defined in terms of the elastic tensor components:

$$\mathcal{J}(S) = \nu_{ijkl} C_{ijkl}^* + \frac{1}{2} \eta_{ijkl} \left(C_{ijkl}^* - C_{ijkl}^{\text{target}} \right)^2,$$

where C_{ijkl} are the effective elastic coefficients of the structure, while C_{ijkl}^{target} are the prescribed elastic values. The efficiency of the solution method is illustrated through four numerical examples where the designed shape yields an important negative Poisson's ratio. Remarkably, some of the obtained optimal shapes are actually already well known in the literature. As shown in chapter 1, the space of admissible micro-architectural shapes that carries orthotropic material symmetry allows to attain shapes with an effective Poisson's ratio below -1 .

Chapter 4. 3D printing and testing of architected polymeric sheets exhibiting a negative Poisson's ratio

This chapter complements the design cycle for several auxetic materials of chapter 3 with the manufacturing of the material and the testing of the material. The specimens are manufactured using a commercial stereo-lithography Ember printer and are mechanically tested. The observed displacement and strain fields during tensile testing obtained by digital image correlation match the predictions from the finite element simulations and demonstrate the efficiency of the design cycle at small strain.

Chapter 5. Systematic two-scale image analysis of extreme deformations in soft architected sheets

The multi-scale nature of architected materials raises the need for advanced experimental methods suitable for the identification of their effective properties, especially when their size is finite and they undergo extreme deformations. The study in this chapter demonstrates that state-of-the-art image processing methods combined with numerical and analytical models provide a comprehensive quantitative description of these solids and their global behaviour, including the influence of the boundary conditions, of the manufacturing process, and of geometric and constitutive nonlinearities. To this end, an adapted multi-scale digital image correlation analysis is used to track both elongations and rotations of particular features of the unit cell at the local and global (homogenised) scale of the material. This permits to observe with unprecedented clarity the strain fields for various unit cells in the structure and to detect global deformation patterns and heterogeneities of the homogenised strain distribution. This method is here demonstrated on elastic

sheets undergoing extreme longitudinal and shear deformations. These experimental results are compared to non-linear finite element simulations, which are also used to evaluate the effects of manufacturing imperfections on the response. A skeletal representation of the architected solid is then extracted from the experiments and used to create a purely-kinematic truss-hinge model that can accurately capture its behaviour. The analysis proposed in this work can be extended to guide the design of two-dimensional architected solids featuring other regular, quasi-regular or graded patterns, and subjected to other types of loads.

Part III. Design of 3D printable thin composite panels

Chapter 6. Shape-shifting panel from 3D printed undulated ribbon lattice

Materials that change their shape in response to external stimuli opens up new prospects for efficient and versatile design and shaping of three-dimensional objects. In this chapter, we present a novel class of microstructures exhibiting an extension-bending coupling (EBC) effect, that can be harnessed as an elementary building block for shape-shifting panels. They are built with a single material as a network of undulated ribbons. The deformations mechanisms of both single and connected undulated ribbons are analysed using the finite element method to explain the main features of the EBC mechanism. For a particular microstructure of the proposed class, the complete elastic stiffness tensor is computed combining two-scale homogenisation with Kirchhoff–Love plate theory. The range of achievable EBC ratio is then assessed with respect to the geometric parameters of the unit cell. Patterned specimens are manufactured using a commercial FFF Ultimaker 3D printer and are mechanically tested at finite strain up to 20%. The displacement measured by point tracking matches the predictions from the finite element simulations and indicates that the structure maintains its properties at finite strain. Moreover, a tensile test load with point-like boundary is proposed to highlight exceptional out of plane displacement. We envision these structures to be leveraged in combination with responsive materials for the actuation of soft robots, compliant systems and reconfigurable structures, as alternatives to external mechanical motors, control systems and power devices.

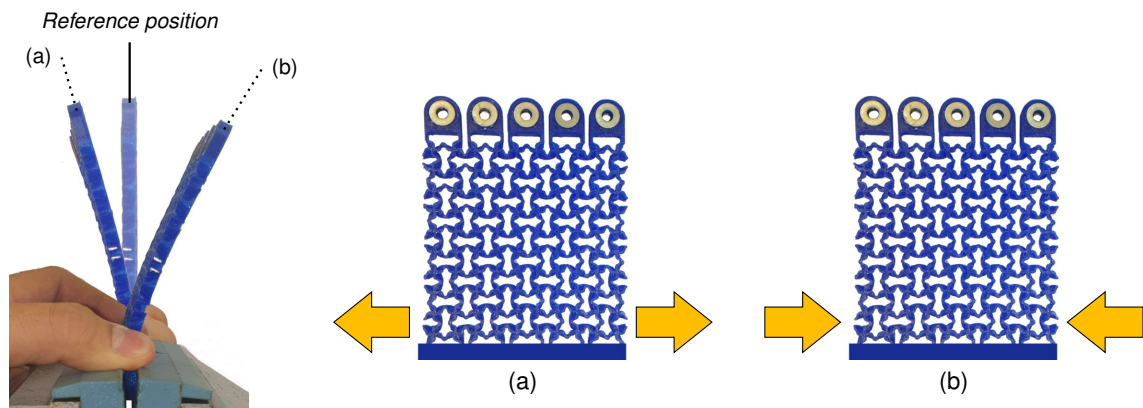


Fig. 1: Manual pinching test. The patterned specimen is clamped at one extremity and left free at the other edge. Applying by hand a tension to the specimen induces a deflection in one direction. Applying a compression, induces a deflection in the opposite direction.

Chapter 7. Design of thin architected panels with extension–bending coupling effects using topology optimisation

In this last chapter, we design the micro-architecture of thin elastic panels to control their macroscopic behaviour, accounting simultaneously for in-plane stiffness, out-of-plane stiffness and the

extension–bending coupling effects. The used topology optimisation method combines inverse homogenisation, the Hadamard shape derivative and a level set method in the diffuse interface context to systematically capture within the unit cell the optimal micro-architecture. The efficiency of the solution method is illustrated through four numerical examples where the designed shape yields an important extension–bending coupling. The deformation responses under tensile loading is assessed numerically both on the complete periodic panel and on its homogenised twin plate. The results demonstrate that the simultaneous control of the in-plane, out-of-plane and their coupled behaviour enables to shift a flat panel into a dome or a saddle shaped structure. Moreover, the obtained unit cells are elementary blocks to create directly 3D printable objects with shape-morphing capabilities.

Part IV. Supplementary materials

This part is provided to complement the discussion with more technical aspects. It is divided in four chapters:

- The first appendix provides a summary on the various thin plates theories, that can be compared to the model derived by asymptotic homogenisation in chapter 1.
- The second appendix is devoted to review the numerical methods which used to enforce volume constraints in optimisation problems in chapter 2, 3 and 7.
- The third appendix delves into the experimental techniques for measuring full-field displacement during mechanical testing. We report the main ingredients used in the digital image correlation employed in chapter 5.
- The last appendix provides additional documents that might interest readers to replicate some of the obtained results.

Part I

Background material

Chapter 1

Mechanical characterisation of elastic composite materials

Contents

1.1	Introduction	21
1.2	Recall on asymptotic homogenisation	23
1.2.1	Problem setting	23
1.2.2	Asymptotic homogenisation method	24
1.2.3	Effective stiffness coefficients	29
1.2.4	Effective equations on the macroscopic scale	29
1.2.5	Comments	30
1.2.6	Periodic homogenisation: summary	30
1.3	Bounds on plane elastic stiffness with orthotropic symmetry	30
1.3.1	Elastic materials with orthotropic symmetry	30
1.3.2	Variational bounds on the effective moduli for orthotropic composites	32
1.4	Elastic panels with a periodic microstructure	34
1.4.1	Problem setting	34
1.4.2	Periodic plate with thickness comparable to the period	36
1.4.3	Effective plate stiffness coefficients	40
1.4.4	Effective equations on the macroscopic scale	43
1.4.5	Comments	44
1.4.6	Elastic panels with a periodic microstructure: summary	44

Asymptotic homogenisation theory has been successfully applied to predict the effective mechanical properties of materials featuring a periodic micro-architecture. The theory is of particular interest for this thesis since it has been widely used for the analysis of composite materials in the framework of structural optimisation of structures (discussed in chapter 2).

1.1 Introduction

This chapter deals with the determination of the overall properties, also called *effective* properties, of composite materials formed by periodic variations of either material properties (laminates or fibre-reinforced composites) or, more interestingly, of geometric construction (honeycombs or other cellular materials characterised by a micro-architecture consisting of an interconnected network of trusses [23, 121]). The effective properties of such materials do not derive much from the intrinsic chemical properties of the base materials, but mostly from their designed architecture. A specific control on the micro-architecture opens the way for the manufacturing of novel composite materials, with unusual or even unprecedented effective material properties. As a result,

cellular materials offer desirable properties that can be harnessed in applications where weight reduction and multifunctional properties are critical. Aerospace sandwich panels, vibration and sound insulators, compact heat exchangers, and biomedical implants are only a few examples of applications.

Since the pioneering works performed in the '80s, the design of elastic composites have been proposed in a variety of theoretical treatments [23, 99, 128, 167]. Lakes introduced a structured material with an auxetic behaviour, i.e., exhibiting a negative value of apparent Poisson's ratio [141]. More recently, rationally designed materials have, for instance, led to stable negative stiffness¹ phases [144], with unprecedented high stiffness, or even to three-dimensional chiral materials that twist under compression [85, 92].

A periodic cellular material is described by a micro-truss arrangement, obtained by tessellating an elementary block, called *unit cell* along independent periodic vectors. In a cellular material, the characteristic length of the unit cell is generally considered several orders of magnitude below the characteristic length of the component. Yet, the study of the unit cell is essential to understand the mechanical response of the material at the macroscopic scale. Several analytical and numerical approaches, as well as experimental investigations, have been proposed in the literature to determine the mechanical properties of cellular materials. Noteworthy contributions in the area of cellular materials are those of Gibson and Ashby [99, 100], Christensen and Klarbring [65], or Pradel and Sab [198] (see also the references therein). Their main goal is to obtain the effective properties of the material in terms of the effective properties of its unit cell, which is a process of homogenisation set to circumvent a detailed – often impractical – analysis of the entire cellular microstructure. The problem is addressed providing closed-form expressions of the effective mechanical properties, relying on certain premises. They generally assume the cell walls behave like Euler–Bernoulli beams, examine the individual cell wall and determine the elastic constants of the cell by solving deformation and equilibrium problems. These studies have demonstrated their efficiency for lattice structures that have a simple arrangements of the cell members, but present limitations when the geometry features a complex geometry.

Other studies have been proposed to model cellular microstructures as an equivalent micropolar medium [54, 140, 198]. In micropolar elasticity, in addition to the translational deformation, an independent microscopic rotational field is usually introduced. For a given cell topology, the micropolar elastic constants of the stiffness matrix are obtained through either an explicit structural analysis of the representative unit cell or an energy approach.

Among numerical approaches, asymptotic homogenisation theory has been successfully applied to predict the effective mechanical properties of materials with a periodic micro-architecture [25, 33, 163, 210]. It has been widely used in the framework of analysis of composite materials, topology optimisation of structures [13, 31, 111] (refer also to chapter 2), but also for the characterisation of porous materials [117], including tissue scaffolds [116] or bone tissue [118, 164]. This theory assumes that any field quantity, such as the displacement, can be described as an asymptotic expansion, which replaced in the governing equations of equilibrium allows to derive the effective properties of the material [106, 210]. Comparisons with experimental investigations have shown that it is a reliable and accurate method to predict the effective mechanical properties of heterogeneous periodic materials. Compared to other homogenisation schemes, a significant advantage of asymptotic homogenisation theory is that the stress distribution in the unit cell can be determined accurately and thus be used for a detailed analysis of the strength and damage of the heterogeneous periodic materials [210]. Furthermore, the theory has neither limitation on the cell topology nor on the range of relative density; essentially, it can handle any lattice regardless of its relative density. It still assumes a finite (bounded) level of contrast among each elementary phase of the microstructure. The results from this theory are generally extrapolated for micro-architected structures with void (or air) phases inside, by replacing the void with an “Ersatz” material: this fictitious material with highly compliant material properties is adjusted to

¹Negative stiffness occurs when applied forces and resulting displacements have opposite directions. The structure is in this case unstable, as the body can release energy without any outside forcing.

have negligible mechanical contribution and offer a good approximation of the effective behaviour for structures with voids.

In this chapter, a few topics are selected to demonstrate the use of asymptotic homogenisation theory for deriving equations associated to the macroscopic behaviour, and to discuss how variational bounds based on the cell boundary value problems can estimate the magnitudes of the effective coefficients. In section 1.2, the effective properties of elastic composite materials with a periodic microstructure are formally derived and studied. In section 1.3, variational bounds such as the ones of Milton and Kohn [169] are exploited to delimit the admissible elastic behaviour that can be obtained from the anisotropic mixture of two well-ordered isotropic materials. In section 1.4, a particular case where the overall characteristic length in one direction is much smaller than those in the other two (as in honeycomb panels) is examined. This assumption is for instance verified in composite panels: these panels have typically a two-dimensional periodic cellular core structure formed by thin-walled cells, sandwiched between two parallel plates. The thickness of these periodic plates is often of the same order of magnitude as the cellular period. Homogenisation theory indicate that the effective equation governing the macroscale behaviour is similar to that for a thin Kirchhoff–Love type of plate [46, 67, 133]. The derivation of a two-dimensional effective equation is performed while accounting for the three-dimensional micro-architecture. The chapter is complemented by an appendix that review some of the existing kinematics models for plates (see appendix A).

1.2 Recall on asymptotic homogenisation

1.2.1 Problem setting

Domain definition. Let us consider a composite solid occupying a open bounded domain Ω of \mathbb{R}^d (depending on the dimension of the problem, $d = 2, 3$). The domain is delimited by a regular boundary Γ , which may be decomposed into two parts, namely Γ^u and its complement Γ^t . A point M of Ω is represented by a set of Cartesian coordinates in this reference, i.e., the components of the position vector denoted by \mathbf{x} . The domain Ω may be divided into N parts, corresponding to the number of phases in the solid. The part of Ω occupied by the phase $\alpha \in \llbracket 0, N \rrbracket$ of the solid is denoted by S^α . The boundary of the phase S^α is denoted by Γ^α . The interface between two phases S^α and S^β is denoted by $\Gamma^{\alpha\beta}$ and defined by: $\Gamma^{\alpha\beta} = \Gamma^\alpha \cap \Gamma^\beta$.

Linear elasticity problem. The composite solid is assumed to behave as a linearly elastic anisotropic body. The elastic properties in Ω are represented by a periodic fourth-order stiffness tensor \mathbb{C} , of components C_{ijkl} . Since the solid is heterogeneous, the coefficients C_{ijkl} are piecewise smooth functions of \mathbf{x} (in particular, C_{ijkl} can be discontinuous at the interface $\Gamma^{\alpha\beta}$). They verify symmetry and positive definiteness, i.e.

$$C_{ijkl} = C_{jikl} = C_{ijlk} = C_{klij}, \quad (1.2.1)$$

$$\exists m \in \mathbb{R}^{+*} \mid C_{ijkl} \xi_{ij} \xi_{kl} \geq m \xi_{ij} \xi_{ij} \quad \forall \{\xi_{ij} \mid \xi_{ij} = \xi_{ji}\}. \quad (1.2.2)$$

The solid is clamped at the boundary Γ^u and is submitted to body forces \mathbf{f} , as well as surface forces \mathbf{t} at the boundary Γ^t . In the framework of linear elasticity, the displacement field \mathbf{u} , the strain field $\varepsilon(\mathbf{u})$ expressed by the compatibility equation

$$\varepsilon_{kl}(\mathbf{u}) = \frac{1}{2} \left(\frac{\partial u_k}{\partial x_l} + \frac{\partial u_l}{\partial x_k} \right) \quad (1.2.3)$$

and the stress field σ satisfy the following set of equations:

$$\begin{cases} \frac{\partial \sigma_{ij}}{\partial x_j} + f_i = 0 & \text{in } \Omega, \\ \sigma_{ij} = C_{ijkl}(\mathbf{x}) \varepsilon_{kl}(\mathbf{u}) & \text{in } \Omega, \\ u_i = 0 & \text{on } \Gamma^u, \\ \sigma_{ij} n_j = t_i & \text{on } \Gamma^t \quad (n_j \text{ denotes the external normal of } \Gamma^t). \end{cases} \quad (1.2.4)$$

Note that the problem (1.2.4) should be understood in the sense of distributions. Naturally, this implies:

$$\begin{cases} u_i |_{S^\alpha} = u_i |_{S^\beta} & \text{on } \Gamma^{\alpha\beta}, \\ \sigma_{ij} n_j |_{S^\alpha} = \sigma_{ij} n_j |_{S^\beta} & \text{on } \Gamma^{\alpha\beta}. \end{cases}$$

Variational formulation. Let $\mathcal{V}(\Omega) := \{\mathbf{v} \in H^1(\Omega) \mid [v_i]_{\Gamma^u} = 0\}$ be the kinematic admissible space associated to Ω . The variational formulation of the problem (1.2.4) reads:

$$\begin{aligned} &\text{Find } \mathbf{u} \in \mathcal{V}(\Omega) \text{ such that:} \\ &\int_{\Omega} C_{ijkl} \varepsilon_{kl}(\mathbf{u}) \varepsilon_{ij}(\mathbf{v}) \, d\mathbf{x} = \int_{\Omega} f_i v_i \, d\mathbf{x} + \int_{\Gamma^t} t_i v_i \, ds, \quad \forall \mathbf{v} \in \mathcal{V}(\Omega). \end{aligned} \quad (1.2.5)$$

Replacing $\varepsilon(\mathbf{u})$ by its expression (1.2.3) and by virtue of (1.2.1), the variational formulation can also be written as:

$$\begin{aligned} &\text{Find } \mathbf{u} \in \mathcal{V}(\Omega) \text{ such that:} \\ &\int_{\Omega} C_{ijkl} \frac{\partial u_k}{\partial x_\ell} \frac{\partial v_i}{\partial x_j} \, d\mathbf{x} = \int_{\Omega} f_i v_i \, d\mathbf{x} + \int_{\Gamma^t} t_i v_i \, ds, \quad \forall \mathbf{v} \in \mathcal{V}(\Omega). \end{aligned}$$

The equivalence between the strong problem (1.2.4) and the variational formulation (1.2.5) is straightforward with classical methods. The variational formulation is used to study the existence and uniqueness of the \mathbf{u} . The proof for existence and uniqueness, which is for instance carried out in the book of Sanchez-Palencia, section 6.1, pages 86–87 [210], makes use of the Lax–Milgram theorem and Korn’s inequality.

1.2.2 Asymptotic homogenisation method

The heterogeneous solid is assumed to be *spatially periodic*, i.e., with a microstructure described by a regular arrangement of identical elementary blocks, referred to as unit cells² (see Fig. 1.1). The period, i.e., the characteristic length of the unit cell l , is assumed to be small in comparison to the characteristic size of the domain L . The small parameter ϵ referred to as the scale factor, expresses this difference of scales.

$$\epsilon = \frac{l}{L} \ll 1.$$

In the sequel, we study the limiting case where ϵ approaches 0. Let $Y = [0, 1]^d$ be the rescaled periodic unit cell, described by the set of coordinates $\mathbf{y} = \mathbf{x}/\epsilon$.

Elastic moduli. Let $C_{ijkl}(\mathbf{y})$ be piecewise smooth, Y -periodic functions that verify the conditions (1.2.1)–(1.2.2). Let us study the specific problem where the spatial variation of the elastic stiffness

²The same periodic solid can be represented by many, if not an infinity, of unit cells. For instance, if Y is a unit cell, then any cell homothetic of Y by an integer factor is also a unit cell. But there are non-trivial situations where non-homothetic unit cells can represent the same microstructure (refer to the book of Sab and Lebée, section 8.1, page 148 [208] for further details).

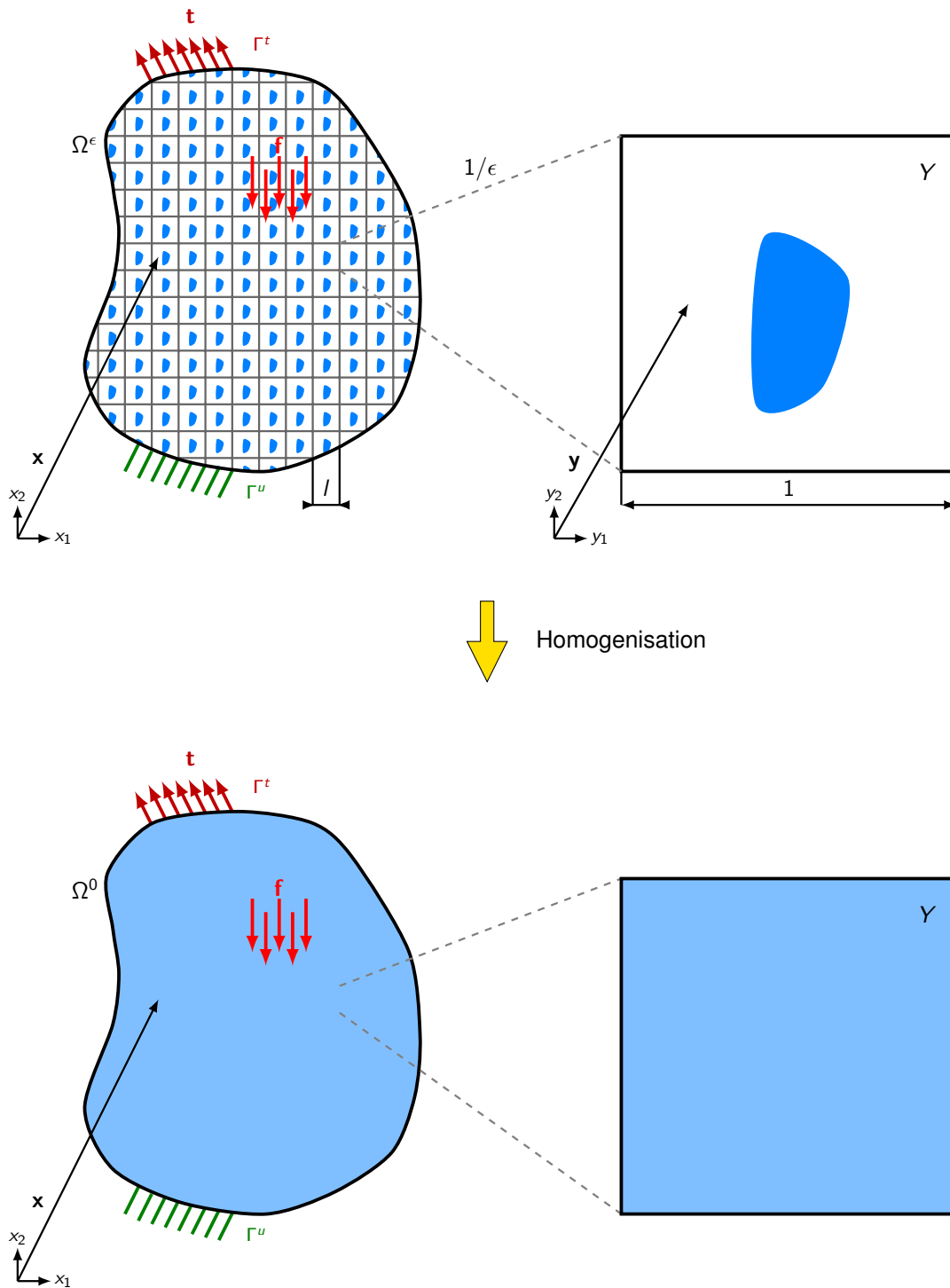


Fig. 1.1: homogenisation concept of a periodic composite material. Case for $d = 2$.

$C^\epsilon(\mathbf{x})$ is expressed as follows.

$$C_{ijkl}^\epsilon(\mathbf{x}) = C_{ijkl}\left(\frac{\mathbf{x}}{\epsilon}\right).$$

The superscript ϵ is introduced to highlight the dependence on the scale factor ϵ . Assuming the domain Ω given in section 1.2.1, the problem under consideration reads:

$$\begin{cases} \frac{\partial \sigma_{ij}^\epsilon}{\partial x_j} + f_i = 0 & \text{in } \Omega, \\ \sigma_{ij}^\epsilon = C_{ijkl}(\mathbf{x}/\epsilon) \varepsilon_{kl}(\mathbf{u}^\epsilon) & \text{in } \Omega, \\ u_i^\epsilon = 0 & \text{on } \Gamma^u, \\ \sigma_{ij}^\epsilon n_j = t_i & \text{on } \Gamma^t. \end{cases} \quad (1.2.6)$$

Note that the given forces \mathbf{t} and \mathbf{f} are independent of ϵ .

Asymptotic expansion. An asymptotic analysis of the problem (1.2.6) is performed, i.e., the displacement field \mathbf{u}^ϵ in Ω is searched as the sum of displacement terms expressed as follows:

$$u_k^\epsilon(\mathbf{x}) = \sum_{n=0}^{+\infty} \epsilon^n u_k^{(n)}(\mathbf{x}, \mathbf{y}) = u_k^{(0)}(\mathbf{x}, \mathbf{y}) + \epsilon u_k^{(1)}(\mathbf{x}, \mathbf{y}) + \epsilon^2 u_k^{(2)}(\mathbf{x}, \mathbf{y}) + \dots \quad (1.2.7)$$

where each term $\mathbf{u}^{(i)}$ ($i \neq 0$) satisfies periodic boundary conditions on the unit cell Y . The asymptotic expansion (1.2.7) can be seen as a first macroscopic displacement $\mathbf{u}^{(0)}$, which is then corrected by higher order terms $\mathbf{u}^{(i)}$ (in practice, only the first two terms of the expansion will be considered here). These functions $\mathbf{u}^{(i)}$ depend on two coordinates systems, namely the global (slow) variable $\mathbf{x} \in \Omega$ and local (fast) variable $\mathbf{y} \in Y$ and are Y -periodic in \mathbf{y} . For the sake of simplicity, \mathbf{x} denotes both the spatial position vector and the global (slow) variable³. Considering a one-dimensional case, the typical structure of \mathbf{u}^ϵ is depicted in Fig. 1.2: the displacement results from a juxtaposition of a smooth function with respect to \mathbf{x} and of a small (factor ϵ) but highly oscillating term (varying with respect to \mathbf{x}/ϵ).

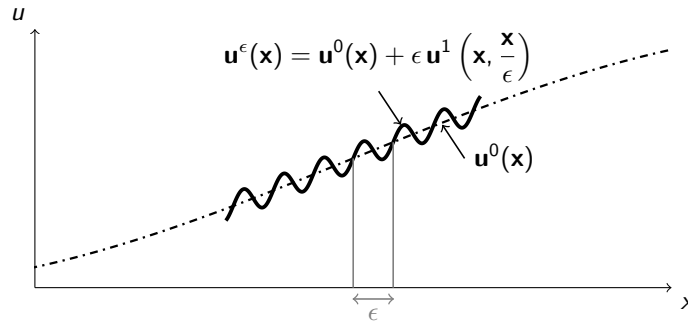


Fig. 1.2: schematic structure of the displacement field \mathbf{u}^ϵ . Note that the dependence of $\mathbf{u}^{(0)}$ on \mathbf{x} only is obtained in eq. (1.2.18).

Derivatives for these type of quantities can therefore be computed as follows:

$$\frac{d\bullet}{dx_i} = \frac{\partial\bullet}{\partial x_i} + \frac{1}{\epsilon} \frac{\partial\bullet}{\partial y_i}, \quad (1.2.8)$$

where the d/dx_i corresponds to the derivative with respect to the real spatial variable \mathbf{x} , while $\partial/\partial x_i$ corresponds to the derivative with respect to the fictitious global variable \mathbf{x} . Equation (1.2.8)

³A more extensive explanation is provided in the book of Sanchez Hubert and Sanchez-Palencia, pages 126–127 [209].

yields in particular a new expression for the strain:

$$\varepsilon_{k\ell}(\mathbf{v}) = \varepsilon_{\mathbf{x}k\ell}(\mathbf{v}) + \varepsilon^{-1} \varepsilon_{\mathbf{y}k\ell}(\mathbf{v}), \quad (1.2.9)$$

where:

$$\varepsilon_{\mathbf{x}k\ell}(\mathbf{v}) = \frac{1}{2} \left(\frac{\partial u_k}{\partial x_\ell} + \frac{\partial u_\ell}{\partial x_k} \right), \quad \varepsilon_{\mathbf{y}k\ell}(\mathbf{v}) = \frac{1}{2} \left(\frac{\partial v_k}{\partial y_\ell} + \frac{\partial v_\ell}{\partial y_k} \right).$$

Problem (1.2.6) and eq. (1.2.9) yield an expansion for the stress tensor in Ω of the form:

$$\sigma_{ij}^\varepsilon(\mathbf{x}) = \sum_{n=0}^{+\infty} \varepsilon^{n-1} \sigma_{ij}^{(n-1)}(\mathbf{x}, \mathbf{y}) = \varepsilon^{-1} \sigma_{ij}^{(-1)}(\mathbf{x}, \mathbf{y}) + \sigma_{ij}^{(0)}(\mathbf{x}, \mathbf{y}) + \varepsilon \sigma_{ij}^{(1)}(\mathbf{x}, \mathbf{y}) + \dots \quad (1.2.10)$$

where:

$$\sigma_{ij}^{(-1)}(\mathbf{x}, \mathbf{y}) = C_{ijkl} \varepsilon_{\mathbf{y}k\ell}(\mathbf{u}^{(0)}), \quad (1.2.11)$$

$$\sigma_{ij}^{(0)}(\mathbf{x}, \mathbf{y}) = C_{ijkl} \left(\varepsilon_{\mathbf{x}k\ell}(\mathbf{u}^{(0)}) + \varepsilon_{\mathbf{y}k\ell}(\mathbf{u}^{(1)}) \right), \quad (1.2.12)$$

$$\sigma_{ij}^{(1)}(\mathbf{x}, \mathbf{y}) = C_{ijkl} \left(\varepsilon_{\mathbf{x}k\ell}(\mathbf{u}^{(1)}) + \varepsilon_{\mathbf{y}k\ell}(\mathbf{u}^{(2)}) \right). \quad (1.2.13)$$

Introducing the expansion (1.2.10) in the equilibrium (1.2.6) leads to a series of problems at each order:

$$\frac{\partial \sigma_{ij}^{(-1)}}{\partial y_j} = 0 \quad \text{order } \mathcal{O}(\varepsilon^{-2}) \quad (1.2.14)$$

$$\frac{\partial \sigma_{ij}^{(-1)}}{\partial x_j} + \frac{\partial \sigma_{ij}^{(0)}}{\partial y_j} = 0 \quad \text{order } \mathcal{O}(\varepsilon^{-1}) \quad (1.2.15)$$

$$\frac{\partial \sigma_{ij}^{(0)}}{\partial x_j} + \frac{\partial \sigma_{ij}^{(1)}}{\partial y_j} + f_i = 0 \quad \text{order } \mathcal{O}(\varepsilon^0) \quad (1.2.16)$$

Last, introducing the expansion (1.2.10) in the boundary conditions of (1.2.6) yields:

$$\begin{cases} u_i^{(0)} = 0 & \text{on } \Gamma^u, & u_i^{(n)} \text{ are } Y\text{-periodic.} & (n \neq 0) \\ \sigma_{ij}^{(0)} n_j = t_i, & & \sigma_{ij}^{(m)} n_j = 0 & \text{on } \Gamma^t. & (m \neq 0) \end{cases} \quad (1.2.17)$$

The next paragraphs are devoted to the formal analysis of the series of problems at each order.

Problem in ε^{-2} . By virtue of the Lax–Milgram theorem, this problem has a unique solution. As stated in the beginning of the section, C_{ijkl} depend on \mathbf{y} (they may be varying throughout the unit cell). In order to satisfy eq. (1.2.11) and (1.2.14), we must verify that $\varepsilon_{\mathbf{y}k\ell}(\mathbf{u}^{(0)}) = 0$. All displacements $\mathbf{u}^{(0)}$ depending only on the global coordinate satisfy this condition. Therefore, the solution of the problem composed of (1.2.11) and (1.2.14) must verify

$$u_i^{(0)}(\mathbf{x}, \mathbf{y}) = u_i^{(0)}(\mathbf{x}) \quad \text{in } \Omega, \quad (1.2.18)$$

$$\sigma_{ij}^{(-1)}(\mathbf{x}, \mathbf{y}) = 0. \quad (1.2.19)$$

Problem in ϵ^{-1} . Using the previous result, the $\partial/\partial x_j$ member in eq. (1.2.15) becomes zero. This problem thus yields the first order correction $\mathbf{u}^{(1)}$ of the displacement field:

$$\begin{cases} \frac{\partial}{\partial y_j} [C_{ijkl} (\varepsilon_{xk\ell}(\mathbf{u}^{(0)}) + \varepsilon_{y k\ell}(\mathbf{u}^{(1)}))] = 0, \\ \mathbf{u}^{(1)} \text{ is } Y\text{-periodic.} \end{cases} \quad (1.2.20)$$

The existence and uniqueness (up to a constant) of a solution for this equation is established in the book by Sanchez-Palencia [210], section 6.2, pages 89–90.

Note that the variable \mathbf{x} only appears in the factor $\varepsilon_{xk\ell}(\mathbf{u}^{(0)})$. By linearity of the problem (1.2.20), $\mathbf{u}^{(1)}(\mathbf{x}, \mathbf{y})$ may then be written under the form:

$$u_i^{(1)}(\mathbf{x}, \mathbf{y}) = \varepsilon_{xk\ell}(\mathbf{u}^{(0)}) w_i^{k\ell}(\mathbf{y}) + \bar{u}_i(\mathbf{x}), \quad (1.2.21)$$

where $\bar{\mathbf{u}}(\mathbf{x})$ is a constant field and $\mathbf{w}^{k\ell}(\mathbf{y})$ the displacement fields, which verify the following set of equations referred to as the *cell problem*.

$$\begin{cases} \frac{\partial}{\partial y_j} [C_{ijpq} (\delta_{pk}\delta_{q\ell} + \varepsilon_{y p q}(\mathbf{w}^{k\ell}))] = 0, \\ \mathbf{w}^{k\ell} \text{ is } Y\text{-periodic.} \end{cases} \quad (1.2.22)$$

Note that the above equation is established using the symmetry property of $C(\mathbf{y})$ defined in eq. (1.2.1). From this equation, it is clear that $\mathbf{w}^{k\ell}$ must have an ‘‘average’’ value of 0 over Y , i.e.

$$\langle w_i^{k\ell} \rangle_Y = \frac{1}{|Y|} \int_Y w_i^{k\ell} d\mathbf{y} = 0.$$

In order to study this problem, let us define the space of Y -periodic functions with zero average:

$$\tilde{\mathcal{V}}(Y) := \{ \mathbf{v} \in H_{per}^1(Y) \mid \langle v_i \rangle_Y = 0 \}.$$

In its weak form, the cell problem (1.2.22) reads:

Find $\mathbf{w}^{k\ell} \in \tilde{\mathcal{V}}(Y)$ such that:

$$\int_Y C_{ijpq} (\delta_{pk}\delta_{q\ell} + \varepsilon_{y p q}(\mathbf{w}^{k\ell})) \varepsilon_{y ij}(\mathbf{v}) d\mathbf{y} = 0, \quad \forall \mathbf{v} \in \tilde{\mathcal{V}}(Y). \quad (1.2.23)$$

The loading is given by the distributed body force $\frac{\partial}{\partial y_j} C_{ijpq} \delta_{pk} \delta_{q\ell}$, which stems directly from the fundamental macroscopic strains modes (an illustration for the two-dimensional case is provided in Fig. 1.3) and the distribution of elastic moduli $C(\mathbf{y})$ in the unit cell.

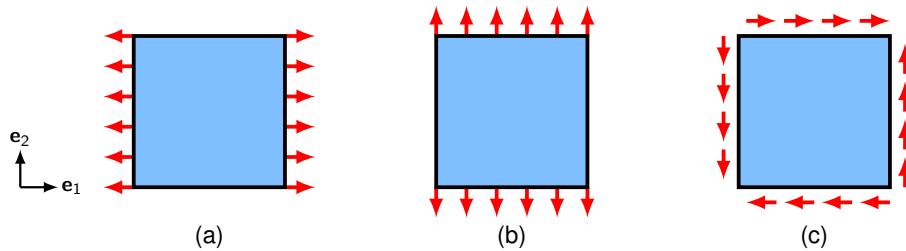


Fig. 1.3: schematic view of the three mean deformation modes applied on a homogeneous two-dimensional unit cell Y : tensile deformations along the coordinate axes \mathbf{e}_1 (a), \mathbf{e}_2 (b), and simple shear deformation (c). They act as a body force in the cell problem (1.2.23).

1.2.3 Effective stiffness coefficients

Once the functions $\mathbf{w}^{k\ell}$ are known (which only depend on the medium and not on the external loading), the homogenised coefficients of the effective medium can easily be obtained.

The macroscopic constitutive law equally follows from the average of equation (1.2.12), replacing the displacement $\mathbf{u}^{(1)}$ by its expression given in equation (1.2.21):

$$\left\langle \sigma_{ij}^{(0)} \right\rangle_Y = C_{ijk\ell}^* \varepsilon_{xk\ell}(\mathbf{u}^{(0)}), \quad (1.2.24)$$

where $C_{ijk\ell}^*$ are the effective stiffness coefficients expressed by:

$$C_{ijk\ell}^* = \frac{1}{|Y|} \int_Y C_{ijpq} (\delta_{pk} \delta_{q\ell} + \varepsilon_{ypq}(\mathbf{w}^{k\ell})) dy. \quad (1.2.25)$$

In order for these coefficients to represent the coefficients of a linear elastic material, they shall satisfy symmetry (1.2.1) and positive definiteness (1.2.2). In order to verify these conditions, the effective coefficients should be expressed in a more convenient way. Choosing $\mathbf{v} = \mathbf{w}^{ij}$ in the cell problem in its weak form (1.2.23) and renaming the indices yields:

$$\int_Y C_{mnpq} (\delta_{pk} \delta_{q\ell} + \varepsilon_{ypq}(\mathbf{w}^{k\ell})) \varepsilon_{ymn}(\mathbf{w}^{ij}) dy = 0.$$

Adding the above expression to the expression of the effective coefficients (1.2.25) yields a more convenient expression for the effective coefficients:

$$C_{ijk\ell}^* = \frac{1}{|Y|} \int_Y C_{mnpq} (\delta_{pk} \delta_{q\ell} + \varepsilon_{ypq}(\mathbf{w}^{k\ell})) (\delta_{mi} \delta_{nj} + \varepsilon_{ymn}(\mathbf{w}^{ij})) dy. \quad (1.2.26)$$

From here the symmetry $C_{ijk\ell}^* = C_{k\ell ij}^*$ is immediate by using the symmetry of C_{ijkl} . Equation (1.2.26) also implies the positivity of $C_{ijk\ell}^*$. Indeed if ξ is a symmetric matrix, the positivity of C_{ijkl} yields:

$$C_{ijk\ell}^* \xi_{ij} \xi_{k\ell} = \frac{1}{|Y|} \int_Y C_{mnpq} (\xi_{mn} + \varepsilon_{ymn}(\mathbf{w}^{ij} \xi_{ij})) (\xi_{pq} + \varepsilon_{ypq}(\mathbf{w}^{k\ell} \xi_{k\ell})) dy \geq 0.$$

In particular, when the above equation is zero, then the positive definiteness of C_{mnpq} ⁴ yields $\xi_{mn} + \varepsilon_{mn}(\mathbf{w}^{ij} \xi_{ij}) = 0$. Averaging this equation over a cell Y gives $\xi_{mn} = 0$.

1.2.4 Effective equations on the macroscopic scale

Problem in ϵ^0 . Let us denote the macroscopic stress tensor by $\Sigma^{(0)}$ such that:

$$\Sigma_{ij}^{(0)} = \left\langle \sigma_{ij}^{(0)} \right\rangle_Y.$$

Averaging the problem (1.2.16) over Y , and taking into account the Y -periodicity leads to the macroscopic equilibrium equation.

$$\begin{cases} \frac{\partial \Sigma_{ij}^{(0)}}{\partial x_j} + f_i = 0 & \text{in } \Omega, \\ \Sigma_{ij}^{(0)} = C_{ijk\ell}^* \varepsilon_{xij}(\mathbf{u}^{(0)}) & \text{in } \Omega, \\ u_i^{(0)} = 0 & \text{on } \Gamma^u, \\ \Sigma_{ij}^{(0)} n_j = t_i & \text{on } \Gamma^t. \end{cases} \quad (1.2.27)$$

⁴This property is verified under the assumption of a finite contrast between the phase, i.e., in the absence of voids inside the unit cell. In practice, when we deal with porous composites, a highly compliant "Ersatz" material is introduced to mimic the void phase.

Consequently, the effective behaviour expressed in eq. (1.2.27) is associated to a linear classical elasticity boundary value problem. For the sake of simplicity, the superscript (0) in eq. (1.2.27) will be dropped in the sequel.

1.2.5 Comments

The approach presented here only considered the first order. Including higher order terms implies considering variations of a different characteristic length (different exponents of ϵ). From the point of view of the macroscopic problem, this would imply to consider a continuum model different from the Cauchy continuum, for example strain gradient elasticity (higher order continuum). Interested readers could refer to the works in [2, 47, 54, 124, 239] for examples with higher orders developments.

1.2.6 Periodic homogenisation: summary

The estimation of the effective elastic properties of a periodic heterogeneous material are obtained following this procedure:

1. Solve the local problems over the unit cell Y expressed hereafter in its weak formulation:

$$\text{Find } \mathbf{w}^{k\ell} \in \tilde{\mathcal{V}}(Y) := \{ \mathbf{v} \in H_{per}^1(Y) \mid \langle v_i \rangle_Y = 0 \} \text{ such that:} \quad (1.2.28)$$

$$\int_Y C_{ijpq} (\delta_{pk} \delta_{q\ell} + \varepsilon_{ypq}(\mathbf{w}^{k\ell})) \varepsilon_{yij}(\mathbf{v}) \, d\mathbf{y} = 0, \quad \forall \mathbf{v} \in \tilde{\mathcal{V}}(Y).$$

There are three local problems in two dimensions, and six in three dimensions.

2. Compute the effective elastic coefficients using the relation:

$$C_{ijk\ell}^* = \frac{1}{|Y|} \int_Y C_{mnpq} (\delta_{pk} \delta_{q\ell} + \varepsilon_{ypq}(\mathbf{w}^{k\ell})) (\delta_{mi} \delta_{nj} + \varepsilon_{ymn}(\mathbf{w}^{ij})) \, d\mathbf{y}. \quad (1.2.29)$$

1.3 Bounds on plane elastic stiffness with orthotropic symmetry

In this section, we focus more specifically on two-dimensional composite sheets, i.e., when the problem is set assuming $d = 2$. The sheets are assumed to be very thin along the third direction, therefore the plane stress state is assumed.

1.3.1 Elastic materials with orthotropic symmetry

Assuming that the local stiffness tensor $C(\mathbf{y})$ is isotropic, the effective stiffness coefficients $C_{ijk\ell}^*$ in (1.2.29) can carry a general biclinic symmetry (fully anisotropic plane tensor). However, due to several mechanical and material science reasons, such as a particular symmetries, these tensor often carry orthotropic symmetry, or even the quadratic symmetry [88, 89]. The case of plane orthotropic tensor is the most general case considered in the present study.

The linear elastic constitutive equation averaged over the unit cell relating the macroscopic stress and strain tensors, denoted as Σ and ε_x respectively, has therefore the following expression for

the two-dimensional problems in the case of an orthotropic tensor:

$$\begin{pmatrix} \Sigma_{11} \\ \Sigma_{22} \\ \Sigma_{12} \end{pmatrix} = \begin{pmatrix} C_{1111}^* & C_{1122}^* & 0 \\ C_{1122}^* & C_{2222}^* & 0 \\ 0 & 0 & C_{1212}^* \end{pmatrix} \begin{pmatrix} \varepsilon_{x11} \\ \varepsilon_{x22} \\ 2\varepsilon_{x12} \end{pmatrix} \quad (1.3.1)$$

Alternatively, the effective strain could be expressed as a function of the effective stress with the following effective material tensor:

$$\begin{pmatrix} \varepsilon_{x11} \\ \varepsilon_{x22} \\ 2\varepsilon_{x12} \end{pmatrix} = \begin{pmatrix} 1/E_1^* & -\nu_{12}^*/E_1^* & 0 \\ -\nu_{21}^*/E_2^* & 1/E_2^* & 0 \\ 0 & 0 & 1/G_{12}^* \end{pmatrix} \begin{pmatrix} \Sigma_{11} \\ \Sigma_{22} \\ \Sigma_{12} \end{pmatrix}$$

where E_i^* denote the homogenised Young moduli, ν_{ij}^* denote the apparent Poisson's ratios and G_{ij}^* denotes the homogenised shear modulus. Note that these coefficients can equally be denoted by *effective*, to highlight their reference to the homogenised unit cell. Let us further remark, that by symmetry of the elastic compliance matrix, the following ratios have to be equal:

$$\frac{\nu_{12}^*}{E_1^*} = \frac{\nu_{21}^*}{E_2^*}.$$

The elastic moduli C_{ijkl}^* in eq. (1.3.1) can be expressed in terms of the compliance moduli, i.e., Young moduli and Poisson's ratios from the inversion of the corresponding compliance tensor:

$$C_{1111}^* = \frac{E_1^*}{1 - \nu_{12}^*\nu_{21}^*}, \quad C_{2222}^* = \frac{E_2^*}{1 - \nu_{12}^*\nu_{21}^*}, \quad C_{1122}^* = \frac{\nu_{21}^* E_1^*}{1 - \nu_{12}^*\nu_{21}^*}.$$

Finally, a simple calculation immediately yields a relation between the stiffness coefficients and the the apparent Poisson's ratios:

$$\nu_{12}^* = \frac{C_{1122}^*}{C_{2222}^*}, \quad \nu_{21}^* = \frac{C_{1122}^*}{C_{1111}^*}. \quad (1.3.2)$$

For material behaviour carrying orthotropic symmetry, it is recalled that ν_{12}^* characterises the contraction of the structure in the direction of Oy axis when the cell stretched in the direction of Ox axis and in general $\nu_{12}^* \neq \nu_{21}^*$. However, in the special case of materials obeying "quadratic" symmetry (i.e., transverse isotropy by looking at the three-dimensional problem), we have $C_{1111}^* = C_{2222}^*$ and we trivially obtain that $E_1^* = E_2^* = E^*$ and $\nu_{12}^* = \nu_{21}^* = \nu^*$.

Since the material tensor characterising the microstructure is positive definite, then C^* is also positive definite by construction. In terms of the physical parameters E_1^* , E_2^* , ν_{12}^* and ν_{21}^* , the positive definiteness of the effective material tensor requires that the stiffness tensor is positioned with the *stability* bounds (see the works of Ting and Chen [237] for a detailed discussion). As these bounds hold for any elastic stiffness tensor C which carries an orthotropic symmetry, we drop the superscript "*" in the following equation⁵:

$$|\nu_{12}| \leq \sqrt{\frac{E_1}{E_2}}, \quad |\nu_{21}| \leq \sqrt{\frac{E_2}{E_1}}, \quad 1 - \nu_{12}\nu_{21} > 0. \quad (1.3.3)$$

In Fig. 1.4 we plot the Poisson's ratios against the *stability* bounds of certain optimal shapes from some recent articles published and see how they compare with our own optimised microstructures from chapter 3. A material that would have $E_1 = E_2$ and $\nu_{21} = \nu_{12} = \nu = -1$ would fall on the lower *stability* bound. From the graph of Fig. 1.4, we understand that the structure has to loose its "quadratic" symmetry and accept an important stiffness unbalance between the directions 1 and 2, expressed by the ratio E_2/E_1 to reach one extreme negative Poisson's ratio.

⁵Theses relations are obtained by computing the eigenvalues of C^* , and ensuring that they remain strictly positive.

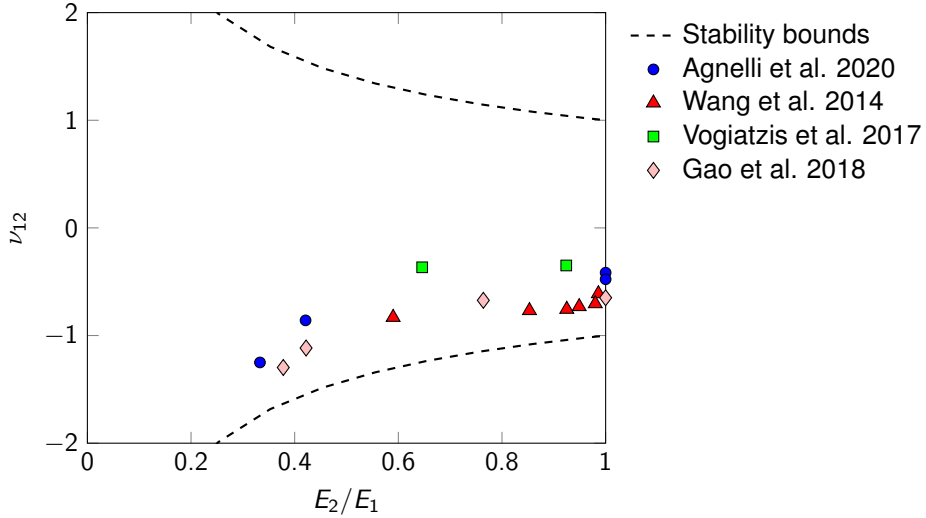


Fig. 1.4: optimal shapes obtained from chapter 3 (refer also to the related article [3]) as well as from the literature [95, 244, 250] plotted against the stability bounds (1.3.3). Remark that extreme Poisson's ratio (i.e., below -1) are reachable for anisotropic structures.

The shapes from the literature, that have been designed by using an optimisation algorithm based upon the level set function, share generic features: lattice architectures with re-entrant corners (like re-entrant honeycomb) or rotating semi-rigid units connected by flexible hinges. Moreover, the orthotropic microstructures with $E_2^*/E_1^* < 0.8$ are only lattice architectures featuring re-entrant corners. Let us further mention the recent contributions of [264] who designed a chiral bi-material micro-architecture with $E_2^*/E_1^* \approx 0.65$ and an effective Poisson's ratio $\nu_{12} = -0.8$ using the SIMP optimisation method, which would also fill in the data cloud of Fig. 1.4. Lastly, the examples from literature, aimed to reach a maximal negative Poisson's ratio, fall at a certain distance from the inferior stability bound. We therefore understand the need for tighter bounds to be used as a guide to effectively explore the ability of the algorithm to ascertain which elastic moduli are attainable in future designs.

1.3.2 Variational bounds on the effective moduli for orthotropic composites

A lot of work has been done in the literature in order to obtain bounds on the elastic stiffness tensor C^* in terms of the volume fractions and elastic moduli of the various phases that make up the composite. The research have been culminating with the pioneering work of Hashin and Shtrikman [110], which included the characterisation of all possible *isotropic* effective elasticity tensors by mixing two isotropic materials in specified proportions. When the effective elasticity tensor C^* becomes anisotropic, more elastic bounds has been proposed by Beran [34], Dederichs and Zeller [74], Willis [257], Milton and Kohn [169], Torquato [238] among others. In this work, we have in particular explored the Milton and Kohn bounds [169], as they only involve the volume fractions of the components. In their paper, Milton and Kohn obtained bounds on the effective material tensor C^* of an *anisotropic* composite formed from two well-ordered *isotropic* components in the context of linear elasticity involving only the volume fractions of the components. The upper "bulk and shear modulus type" bound read:

$$\rho_2 \text{Tr}[\Lambda_h(C^1 - C^*)^{-1}] \leq \frac{1}{d(K^1 - K^2)} - \frac{\rho_1}{dK^1 + 2(d-1)G^1}, \quad (1.3.4)$$

$$\rho_2 \text{Tr}[\Lambda_s(C^1 - C^*)^{-1}] \leq \frac{(d-1)(d+2)}{4(G^1 - G^2)} - \frac{\rho_1 d(d-1)(K^1 + 2G^1)}{2G^1[dK^1 + 2(d-1)G^1]}. \quad (1.3.5)$$

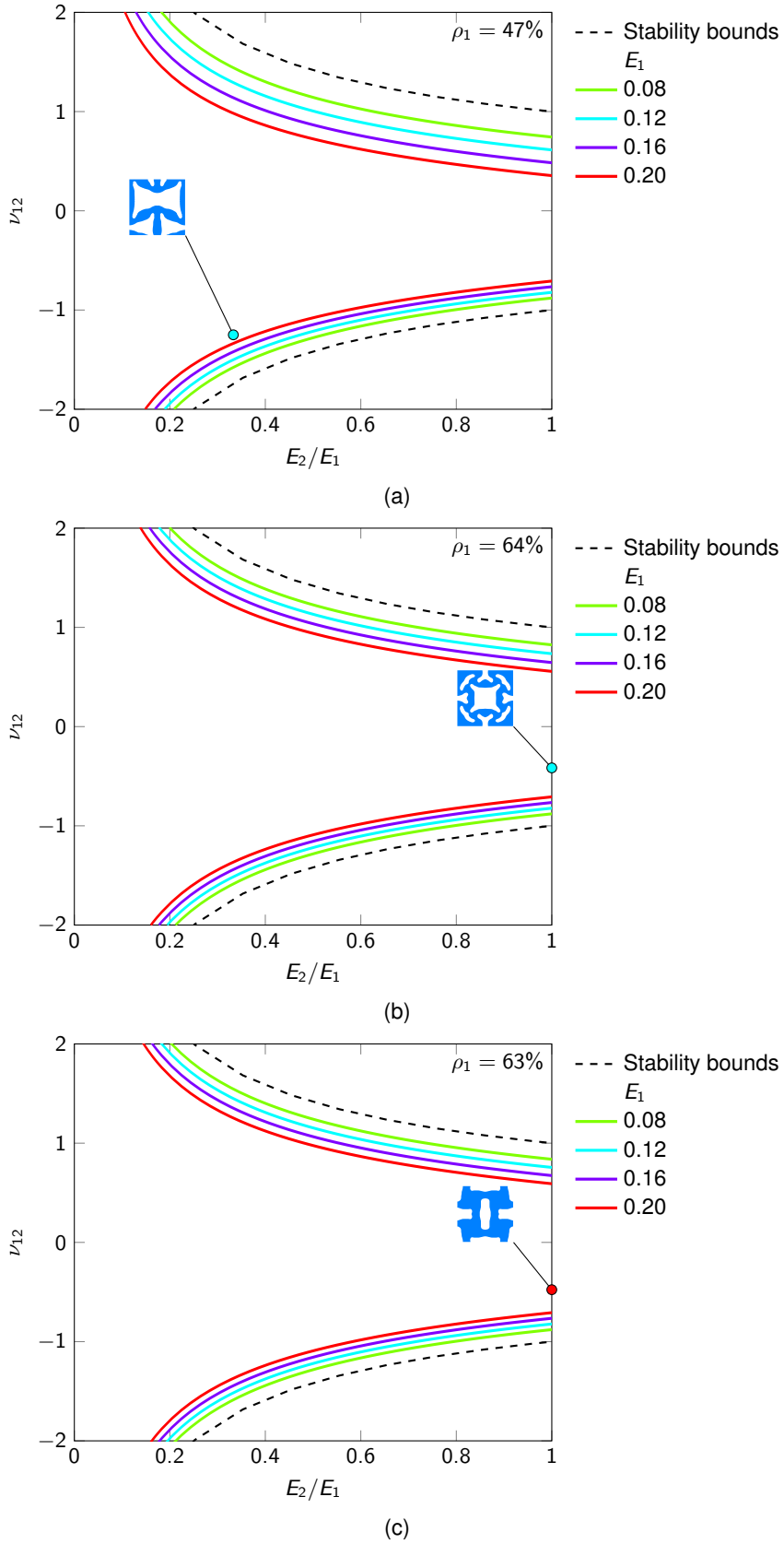


Fig. 1.5: Milton–Kohn bounds [169] for different values of E_1 represented by coloured solid lines, plotted for the three microstructures of chapter 3. The dashed black line are the thermodynamic bounds derived from eq. (1.3.3). In (a) note that the re-entrant honeycomb structure which carries orthotropic symmetry is close to attain the lower bound, while in (b), (c) we can see where the microstructures with quadratic symmetry fall with respect to the bounds.

The lower “bulk and shear modulus type” bound read:

$$\rho_1 \text{Tr}[\Lambda_h(C^* - C^2)^{-1}] \leq \frac{1}{d(K^1 - K^2)} - \frac{\rho_2}{dK^2 + 2(d-1)G^2}, \quad (1.3.6)$$

$$\rho_1 \text{Tr}[\Lambda_s(C^* - C^2)^{-1}] \leq \frac{(d-1)(d+2)}{4(G^1 - G^2)} - \frac{\rho_2 d(d-1)(K^2 + 2G^2)}{2G^2[dK^2 + 2(d-1)G^2]}. \quad (1.3.7)$$

In the above equations, ρ_α , K^α , G^α and C^α denote the volume fraction, bulk modulus, shear modulus, and elastic material tensor characterising phase S^α of the composite, where, $\alpha = 1, 2$. Note that the results in eq. (1.3.4)–(1.3.7) are obtained assuming that:

$$K^1 \geq K^2, \quad G^1 \geq G^2.$$

Λ_h and Λ_s represent the orthogonal projections on hydrostatic and shear fields respectively. These projections have components:

$$(\Lambda_h)_{ijkl} = \frac{1}{d}\delta_{ij}\delta_{kl}, \quad (\Lambda_s)_{ijkl} = \frac{1}{2}(\delta_{ik}\delta_{jl} + \delta_{il}\delta_{jk}) - \frac{1}{d}\delta_{ij}\delta_{kl}.$$

The bounds for the Poisson’s ratios are easily derived by replacing C^* by its expression in terms of Young’s moduli E_i , shear moduli G_{ij} and Poisson’s ratios ν_{ij} . Let us remark that comparing optimal unit cells with different volume fractions and different Young’s moduli makes it impossible overlay the data in a single plot. In other words, the bounds that account for the mixture of materials will be specific for each material density and effective elastic stiffness. This aspect is illustrated by plotting the Milton–Kohn bounds for the Poisson’s ratio in Fig. 1.5 for three optimal shapes obtained using topology optimisation [3] (refer to chapter 3).

It is pointed out in the paper of Milton and Kohn [169] that these bounds are sharp in the sense that equality is attained for composites with specific sequentially layered microstructures. Computing the lower “bulk modulus type” bounds, we notice that the *re-entrant honeycomb* structure obtained in example 1 is close to attain the lower Milton–Kohn bound.

In a nutshell, these bounds present a natural way to explore numerically which elastic tensor moduli are attainable. It is clear from Fig. 1.5 that the more extreme the Poisson’s ratio is, the closer to zero asymptotically the ratio of Young moduli must be.

1.4 Elastic panels with a periodic microstructure

The purpose of this section is to derive and study the effective properties of heterogeneous elastic panels formed by periodic variations of geometric constructions (like cellular or honeycomb microstructures). This section is based upon the following references [46, 163, 208, 209].

The examined case assumes the overall characteristic length in one direction is much smaller than those in the other two, as in cellular panels. Typically these panels have a two-dimensional periodic cellular core structure formed by thin-walled cells, sandwiched between two parallel plates. They are widely used due to their high strength-to-weight ratio. The thickness of these periodic plates is often of the same order of magnitude as the cellular period. The homogenisation theory leads to effective equation governing the macroscale behaviour that is similar to that for a Kirchhoff–Love plate [46, 133, 156, 163, 208].

1.4.1 Problem setting

Domain definition. Let us consider a plane panel of thickness h normal to the axis (O, \mathbf{e}_3) . Its mid-plane, referred to as ω , is a bounded domain of \mathbb{R}^2 , with regular boundary $\partial\omega$. For convenience, the mid-plane ω of the undeformed plate is assumed to lie in the $(O, \mathbf{e}_1, \mathbf{e}_2)$ plane. As a

result, let Ω_h be the bounded domain of \mathbb{R}^3 occupied by the heterogeneous panel, defined as:

$$\Omega_h = \omega \times] - h/2, h/2[\quad (\omega \subset \mathbb{R}^2, h \in \mathbb{R}^{+*})$$

The plate is delimited by a regular boundary Γ_h , which may be decomposed as follows:

$$\Gamma_h = \Gamma_h^\pm \cup \Gamma_h^{lat} \quad \begin{cases} \Gamma_h^\pm = \omega \times \{\pm h/2\} & \text{(top and bottom)} \\ \Gamma_h^{lat} = \partial\omega \times] - h/2, h/2[& \text{(lateral)} \end{cases}$$

In this reference, a point M of Ω_h is represented by a set of Cartesian coordinates \mathbf{x} , which may be decomposed into in-plane coordinates $(x_\alpha) = (x_1, x_2)$ and transverse coordinate x_3 .

The heterogeneous panel is assumed to be *spatially periodic*, i.e., with a microstructure described by a regular tessellation of unit cells along its mid-plane. Exactly as described in section 1.2, a small parameter ϵ referred to as the scale factor, is introduced to express the ratio between the size of the unit cell and the size of the domain Ω_h .

In the sequel, we study the limiting case where h and ϵ approach 0 (the relation between ϵ and h will be detailed in the next paragraphs). Let Y denote the rescaled periodic unit cell. This yields: $Y = [0, 1]^2 \times [-1/2, 1/2]$. It is described by the set of coordinates \mathbf{y} defined as follows.

$$y_\alpha = x_\alpha/\epsilon, \quad y_3 = x_3/h.$$

Elastic moduli. The panel is assumed to behave as a linearly elastic anisotropic body. Let $C_{ijkl}(\mathbf{y})$ be piecewise smooth, (y_1, y_2) -periodic functions, that verify symmetry and positive definiteness. In the framework of linear elasticity, we study the specific problem where the spatial distribution of the elastic stiffness $C^{h\epsilon}$ is expressed as follows:

$$C_{ijkh}^{h\epsilon}(\mathbf{x}) = \frac{1}{h^3} C_{ijkh} \left(\frac{x_1}{\epsilon}, \frac{x_2}{\epsilon}, \frac{x_3}{h} \right)$$

The superscript h and ϵ are introduced to highlight the dependence on the panel thickness and the scale factor. Remark that the elastic moduli are assumed to depend on h mainly according to $1/h^3$. This assumption was first proposed by Caillerie in [46]. As a matter of fact, h is a parameter which is tending to zero: the plate is then thinner and thinner and it must be more and more rigid to be able to stand the stresses which are applied to it.

The plate is clamped at the boundary Γ_h^{lat} and is submitted to body forces \mathbf{f} , as well as surface forces \mathbf{t}^h at the boundary Γ_h^\pm . Assuming the domain Ω_h defined above, the problem under consideration reads:

$$\begin{cases} \frac{\partial \sigma_{ij}^{h\epsilon}}{\partial x_j} + f_i = 0 & \text{in } \Omega_h, \\ \sigma_{ij}^{h\epsilon} = C_{ijkh}^{h\epsilon} \varepsilon_{k\ell}(\mathbf{u}^{h\epsilon}) & \text{in } \Omega_h, \\ u_i^{h\epsilon} = 0 & \text{on } \Gamma_h^{lat}, \\ \sigma_{ij}^{h\epsilon} n_j = t_i^h & \text{on } \Gamma_h^\pm. \quad (n_j \text{ denotes the external normal of } \Gamma_h^\pm) \end{cases} \quad (1.4.1)$$

As discussed in the works of Caillerie [46], the longitudinal components of the surface forces t_α^h are considered to be $1/h$ times bigger than their normal components (t_3 does not depend on h). Indeed it is easier to bend a plate by acting a normal force on it than by acting a moment on it with the help of longitudinal forces. If all the stresses had been taken in the same order, only the normal forces t_3 would have occurred in the final result.

Formulation of the problem on the open set Ω . In order to get rid of the difficulty arising from the dependence on h of Ω_h , the domain is expanded in $\Omega = \omega \times] - 1/2, 1/2[$ via the following

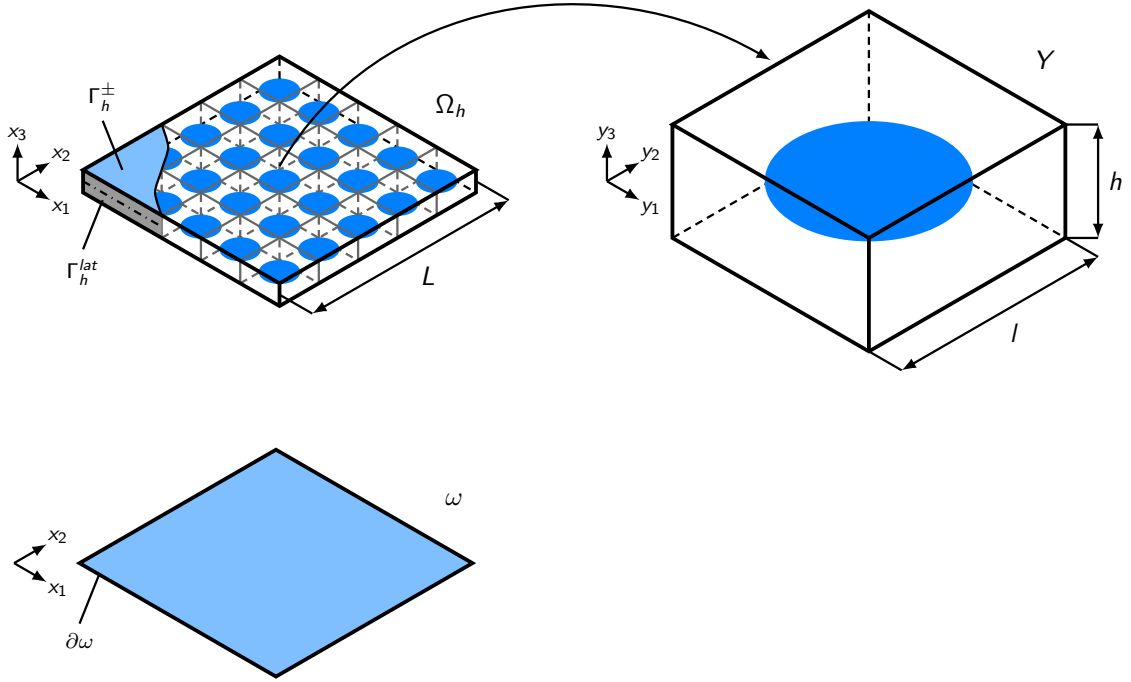


Fig. 1.6: architected panel Ω_h with a in-plane periodic arrangement of unit cells Y . The cell's aspect ratio r is defined as $r = h/l$. Concept of homogenisation yields an equivalent anisotropic homogeneous plate.

change of variables:

$$z_1 = x_1, \quad z_2 = x_2, \quad z_3 = x_3/h.$$

Under this change of variable, Γ_h^{lat} and Γ_h^\pm become Γ^{lat} and Γ^\pm respectively. Let $\varphi^{h\epsilon}$ be any function defined on Ω_h . We set: $\varphi^\epsilon(z_1, z_2, z_3) = \varphi^{h\epsilon}(z_1, z_2, hz_3)$. This means in particular:

$$C_{ijkh}^\epsilon(\mathbf{z}) = \frac{1}{h^3} C_{ijkl} \left(\frac{z_1}{\epsilon}, \frac{z_2}{\epsilon}, z_3 \right).$$

Problem (1.4.1) may then be written as follows:

$$\begin{cases} \frac{\partial \sigma_{i\beta}^\epsilon}{\partial z_\beta} + \frac{1}{h} \frac{\partial \sigma_{i3}^\epsilon}{\partial z_3} + f_i = 0 & \text{in } \Omega, \\ \sigma_{ij}^\epsilon = C_{ijk\delta}^\epsilon \varepsilon_{k\delta}(\mathbf{u}^\epsilon) + \frac{1}{h} C_{ijk3}^\epsilon \varepsilon_{k3}(\mathbf{u}^\epsilon) & \text{in } \Omega, \\ u_i^\epsilon = 0 & \text{on } \Gamma^{lat}, \\ \sigma_{\alpha j}^\epsilon n_j = \frac{t_\alpha}{h} \quad \sigma_{3j}^\epsilon n_j = t_3 & \text{on } \Gamma^\pm. \end{cases} \quad (1.4.2)$$

In order to study the different limit processes (h or ϵ tends to zero) some a priori estimates related to the field $\mathbf{u}^{h\epsilon}$ and to the tensor $\sigma^{h\epsilon}$ are discussed in [46].

1.4.2 Periodic plate with thickness comparable to the period

Let us first study the specific but important case where $h = l = \epsilon L$. The generalisation to $h = r l = r \epsilon L$, where r denotes the cell's aspect ratio, will be easy to deduce from the first case.

Asymptotic expansion. An asymptotic analysis of equation (1.4.2) is performed, i.e., the displacement field \mathbf{u}^ϵ is searched as the sum of displacement terms as follows:

$$\begin{aligned} u_k^\epsilon(\mathbf{z}) &= \sum_{i=0}^{+\infty} \epsilon^i u_k^{(i)}(\mathbf{x}, \mathbf{y}) \\ &= u_k^{(0)}(\mathbf{x}, \mathbf{y}) + \epsilon u_k^{(1)}(\mathbf{x}, \mathbf{y}) + \epsilon^2 u_k^{(2)}(\mathbf{x}, \mathbf{y}) + \epsilon^3 u_k^{(3)}(\mathbf{x}, \mathbf{y}) + \epsilon^4 u_k^{(4)}(\mathbf{x}, \mathbf{y}) + \dots \end{aligned} \quad (1.4.3)$$

where each term $v_i^{(k)}$ satisfies (y_1, y_2) -periodic boundary conditions. These functions $v_i^{(k)}$ depend on two coordinate systems, namely the global (slow) variable \mathbf{x} and local (fast) variable \mathbf{y} . For the sake of simplicity, note that \mathbf{x} is introduced both as the fictitious global variable and as the spatial position vector in Ω^h in eq. (1.4.1).

Derivatives for these type of quantities can be computed as follows:

$$\frac{d\bullet}{dz_i} = \delta_{i\alpha} \frac{\partial \bullet}{\partial x_\alpha} + \frac{1}{\epsilon} \frac{\partial \bullet}{\partial y_i}. \quad (1.4.4)$$

Equation (1.4.4) directly yields a new expression for the strain field:

$$\varepsilon_{k\ell}(\mathbf{v}) = \delta_{k\gamma} \delta_{\ell\delta} \varepsilon_{x\gamma\delta}(\mathbf{v}) + \frac{\delta_{k\gamma} \delta_{\ell 3}}{2} \frac{\partial v_3}{\partial x_\gamma} + \frac{\delta_{k3} \delta_{\ell\delta}}{2} \frac{\partial v_3}{\partial x_\delta} + \epsilon^{-1} \varepsilon_{y k \ell}(\mathbf{v}), \quad (1.4.5)$$

where:

$$\varepsilon_{x\gamma\delta}(\mathbf{v}) = \frac{1}{2} \left(\frac{\partial v_\gamma}{\partial x_\delta} + \frac{\partial v_\delta}{\partial x_\gamma} \right), \quad \varepsilon_{y k \ell}(\mathbf{v}) = \frac{1}{2} \left(\frac{\partial v_k}{\partial y_\ell} + \frac{\partial v_\ell}{\partial y_k} \right).$$

Considering that the elastic coefficients are in $1/\epsilon^3$, this yields an expansion for the stress tensor of the form:

$$\sigma_{ij}^{h\epsilon}(\mathbf{z}) = \sum_{n=0}^{+\infty} \epsilon^{n-4} \sigma_{ij}^{(n-4)}(\mathbf{x}, \mathbf{y}), \quad (1.4.6)$$

where:

$$\sigma_{ij}^{(-4)}(\mathbf{x}, \mathbf{y}) = C_{ijkl} \varepsilon_{y k \ell}(\mathbf{u}^{(0)}), \quad (1.4.7)$$

$$\sigma_{ij}^{(-3)}(\mathbf{x}, \mathbf{y}) = C_{ij\gamma\delta} \varepsilon_{x\gamma\delta}(\mathbf{u}^{(0)}) + C_{ij3\delta} \frac{\partial u_3^{(0)}}{\partial x_\delta} + C_{ijkl} \varepsilon_{y k \ell}(\mathbf{u}^{(1)}), \quad (1.4.8)$$

$$\sigma_{ij}^{(-2)}(\mathbf{x}, \mathbf{y}) = C_{ij\gamma\delta} \varepsilon_{x\gamma\delta}(\mathbf{u}^{(1)}) + C_{ij3\delta} \frac{\partial u_3^{(1)}}{\partial x_\delta} + C_{ijkl} \varepsilon_{y k \ell}(\mathbf{u}^{(2)}), \quad (1.4.9)$$

$$\sigma_{ij}^{(-1)}(\mathbf{x}, \mathbf{y}) = C_{ij\gamma\delta} \varepsilon_{x\gamma\delta}(\mathbf{u}^{(2)}) + C_{ij3\delta} \frac{\partial u_3^{(2)}}{\partial x_\delta} + C_{ijkl} \varepsilon_{y k \ell}(\mathbf{u}^{(3)}), \quad (1.4.10)$$

$$\sigma_{ij}^{(0)}(\mathbf{x}, \mathbf{y}) = C_{ij\gamma\delta} \varepsilon_{x\gamma\delta}(\mathbf{u}^{(3)}) + C_{ij3\delta} \frac{\partial u_3^{(3)}}{\partial x_\delta} + C_{ijkl} \varepsilon_{y k \ell}(\mathbf{u}^{(4)}). \quad (1.4.11)$$

Introducing the expansion (1.4.6) in the equilibrium equation (1.4.2) leads to a series of problems

at each order:

$$\frac{\partial \sigma_{ij}^{(-4)}}{\partial y_j} = 0 \quad \text{order } \mathcal{O}(\epsilon^{-5}) \quad (1.4.12)$$

$$\frac{\partial \sigma_{i\beta}^{(-4)}}{\partial x_\beta} + \frac{\partial \sigma_{ij}^{(-3)}}{\partial y_j} = 0 \quad \text{order } \mathcal{O}(\epsilon^{-4}) \quad (1.4.13)$$

$$\frac{\partial \sigma_{i\beta}^{(-3)}}{\partial x_\beta} + \frac{\partial \sigma_{ij}^{(-2)}}{\partial y_j} = 0 \quad \text{order } \mathcal{O}(\epsilon^{-3}) \quad (1.4.14)$$

$$\frac{\partial \sigma_{i\beta}^{(-2)}}{\partial x_\beta} + \frac{\partial \sigma_{ij}^{(-1)}}{\partial y_j} = 0 \quad \text{order } \mathcal{O}(\epsilon^{-2}) \quad (1.4.15)$$

$$\frac{\partial \sigma_{i\beta}^{(-1)}}{\partial x_\beta} + \frac{\partial \sigma_{ij}^{(0)}}{\partial y_j} = 0 \quad \text{order } \mathcal{O}(\epsilon^{-1}) \quad (1.4.16)$$

$$\frac{\partial \sigma_{i\beta}^{(0)}}{\partial x_\beta} + \frac{\partial \sigma_{ij}^{(1)}}{\partial y_j} + f_i = 0 \quad \text{order } \mathcal{O}(\epsilon^0) \quad (1.4.17)$$

The above series of problem is associated with boundary conditions, obtained by introducing the expansion (1.4.6) in eq. (1.4.2) and reported here:

$$\begin{cases} u_i^{(0)} = 0 \quad \text{on } \Gamma^{lat}, & u_i^{(n)} \text{ are } (y_1, y_2)\text{-periodic, } (n \neq 0) \\ \sigma_{\alpha 3}^{(-1)} n_3 = t_\alpha^\pm, & \sigma_{\alpha 3}^{(m)} n_3 = 0 \quad \text{on } \Gamma^\pm, (m \neq -1) \\ \sigma_{33}^{(0)} n_3 = t_3^\pm, & \sigma_{33}^{(m)} n_3 = 0 \quad \text{on } \Gamma^\pm, (m \neq 0) \end{cases} \quad (1.4.18)$$

In the sequel, we will try to solve the series of problems at each order. The existence of a solution for each order is discussed in [46].

Problem in ϵ^{-5} . As stated in the beginning of the section, C depends on \mathbf{y} (since it is different in different points of the unit cell). In order to satisfy equation (1.4.12), we must verify that $\varepsilon_{y_{k\ell}}(\mathbf{u}^{(0)}) = 0$. All displacements $\mathbf{u}^{(0)}$ depending only on the global coordinate satisfy this condition, and they are solution of equation (1.4.12). Hence:

$$u_i^{(0)}(\mathbf{x}, \mathbf{y}) = u_i^{(0)}(\mathbf{x}) \quad \text{in } \Omega, \quad (1.4.19)$$

$$\sigma_{ij}^{(-4)}(\mathbf{x}, \mathbf{y}) = 0. \quad (1.4.20)$$

Problem in ϵ^{-4} . Using the result above, the $\partial/\partial z_\beta$ member in eq. (1.4.13) becomes zero. The problem in ϵ^{-4} yields the first order correction $\mathbf{u}^{(1)}$ of the displacement field:

$$\begin{cases} \frac{\partial}{\partial y_j} \left[C_{ij\gamma\delta} \varepsilon_{x\gamma\delta}(\mathbf{u}^{(0)}) + C_{ij3\delta} \frac{\partial u_3^{(0)}}{\partial x_\delta} + C_{ijk\ell} \varepsilon_{y_{k\ell}}(\mathbf{u}^{(1)}) \right] = 0, \\ \mathbf{u}^{(1)} \text{ is } (y_1, y_2)\text{-periodic.} \end{cases} \quad (1.4.21)$$

The existence and unicity (up to a constant) of solution for this equation is established in the work by Caillerie [46], pages 176–177. By linearity of the problem (1.4.21), it is shown that $\mathbf{u}^{(1)}(\mathbf{x}, \mathbf{y})$ has an expression of the form:

$$u_i^{(1)}(\mathbf{x}, \mathbf{y}) = \varepsilon_{x\gamma\delta}(\mathbf{u}^{(0)}) w_i^{\gamma\delta}(\mathbf{y}) + \frac{\partial u_3^{(0)}}{\partial x_\delta} w_i^{3\delta}(\mathbf{y}) + \bar{u}_i(\mathbf{x}), \quad (1.4.22)$$

where the vector $\bar{\mathbf{u}}(\mathbf{x})$ is an unknown and represents the depth-averaged displacement, and $\mathbf{w}^{k\delta}$ are the displacements created by the mean deformation, solution of the following local problem,

referred to as a *cell problem*.

$$\begin{cases} \frac{\partial}{\partial y_j} [C_{ijpq} (\delta_{pk} \delta_{q\delta} + \varepsilon_{ypq}(\mathbf{w}^{k\delta}))] = 0, \\ \mathbf{w}^{k\delta} \text{ is } (y_1, y_2)\text{-periodic.} \end{cases} \quad (1.4.23)$$

Again, it is clear that $\mathbf{w}^{k\ell}$ must have an “average” value of zero over Y , i.e.:

$$\langle w_i^{k\ell} \rangle_Y = \frac{1}{|Y|} \int_Y w_i^{k\ell} d\mathbf{y} = 0.$$

This time, let $\tilde{\mathcal{V}}(Y)$ be the space of (y_1, y_2) -periodic functions with zero average defined as follows:

$$\tilde{\mathcal{V}}(Y) := \{ \mathbf{v} \in H_{loc}^1(Y) \mid (y_1, y_2)\text{-periodic, } \langle v_i \rangle_Y = 0 \}.$$

The local problem (1.4.23) reads in its weak form:

$$\begin{aligned} &\text{Find } \mathbf{w}^{k\delta} \in \tilde{\mathcal{V}}(Y) \text{ such that:} \\ &\int_Y C_{ijpq} (\delta_{pk} \delta_{q\delta} + \varepsilon_{ypq}(\mathbf{w}^{k\delta})) \varepsilon_{yij}(\mathbf{v}) d\mathbf{y} = 0, \quad \forall \mathbf{v} \in \tilde{\mathcal{V}}(Y). \end{aligned} \quad (1.4.24)$$

From the above equation, it follows that:

$$\mathbf{w}^{31} = (-y_3, 0, 0), \quad \mathbf{w}^{32} = (0, -y_3, 0).$$

Moreover, note that:

$$C_{ijpq} (\delta_{p3} \delta_{q\delta} + \varepsilon_{ypq}(\mathbf{w}^{3\delta})) = C_{ij3\delta} - C_{ij3\delta} = 0.$$

A new expression of the constitutive law (1.4.8) may then be obtained from eq. (1.4.22):

$$\sigma_{ij}^{(-3)} = [C_{ijpq} (\delta_{p\gamma} \delta_{q\delta} + \varepsilon_{ypq}(\mathbf{w}^{\gamma\delta}))] \varepsilon_{x\gamma\delta}(\mathbf{u}^{(0)}). \quad (1.4.25)$$

Problem in ϵ^{-3} . Let us apply the operator “mean” to the problem (1.4.14) and let us take into account the Y -periodicity. The problem then reads:

$$\frac{\partial}{\partial X_\beta} \left[\left(\frac{1}{|Y|} \int_Y C_{ijpq} (\delta_{pk} \delta_{q\delta} + \varepsilon_{ypq}(\mathbf{w}^{k\delta})) d\mathbf{y} \right) \varepsilon_{x\gamma\delta}(\mathbf{u}^{(0)}) \right] = 0.$$

The above equation yields: $\varepsilon_{x\gamma\delta}(\mathbf{u}^{(0)}) = 0$. Thus, the leading order displacement $\mathbf{u}^{(0)}$ and the displacement at the next order $\mathbf{u}^{(1)}$ read as follows:

$$u_i^{(0)}(\mathbf{x}) = \delta_{i3} U_3(\mathbf{x}), \quad u_i^{(1)}(\mathbf{x}, \mathbf{y}) = -y_3 \delta_{i\delta} \frac{\partial U_3}{\partial X_\delta} + \bar{u}_i(\mathbf{x}), \quad (1.4.26)$$

$$\sigma_{ij}^{(-3)}(\mathbf{x}, \mathbf{y}) = 0. \quad (1.4.27)$$

Note that the in-plane displacement is linear in y_3 as assumed in the approximation of Kirchhoff–Love for simple plates (see appendix A.1), and that the depth-averaged in-plane displacements \bar{u}_i are of higher order than the leading-order transverse displacement U_3 , to which \bar{u}_3 is the next order correction. Using equation (1.4.26) and (1.4.27), the problem (1.4.14) reduces to:

$$\begin{cases} \frac{\partial}{\partial y_j} \left[y_3 C_{ij\gamma\delta} \chi_{x\gamma\delta}(U_3) + C_{ij\gamma\delta} \varepsilon_{x\gamma\delta}(\bar{\mathbf{u}}) + C_{ij3\delta} \frac{\partial \bar{u}_3}{\partial X_\delta} + C_{ijkl} \varepsilon_{ykel}(\mathbf{u}^{(2)}) \right] = 0, \\ \mathbf{u}^{(2)} \text{ is } (y_1, y_2)\text{-periodic.} \end{cases} \quad (1.4.28)$$

where $\chi(U_3)$ denotes the flexural curvature:

$$\chi_{x\gamma\delta}(U_3) = -\frac{\partial^2 U_3}{\partial x_\gamma \partial x_\delta}. \quad (1.4.29)$$

Thus $\mathbf{u}^{(2)}$ can be written in the form:

$$u_i^{(2)} = \varepsilon_{x\gamma\delta}(\bar{\mathbf{u}}) w_i^{\gamma\delta} - y_3 \delta_{i3} \frac{\partial \bar{u}_3}{\partial x_\delta} + \chi_{x\gamma\delta}(U_3) p_i^{\gamma\delta}, \quad (1.4.30)$$

where $\mathbf{w}^{\gamma\delta}$ are the solutions to the cell problem (1.4.23) and $\mathbf{p}^{\gamma\delta}$ is the solution to another cell problem governed by:

$$\begin{cases} \frac{\partial}{\partial y_j} [C_{ijpq} (y_3 \delta_{p\gamma} \delta_{q\delta} + \varepsilon_{ypq}(\mathbf{p}^{\gamma\delta}))] = 0, \\ \mathbf{p}^{\gamma\delta}(\mathbf{y}) \text{ is } (y_1, y_2)\text{-periodic.} \end{cases} \quad (1.4.31)$$

In its weak form, eq. (1.4.31) reads:

$$\begin{aligned} &\text{Find } \mathbf{p}^{\gamma\delta} \in \tilde{\mathcal{V}}(Y) \text{ such that:} \\ &\int_Y C_{ijpq} (y_3 \delta_{p\gamma} \delta_{q\delta} + \varepsilon_{ypq}(\mathbf{p}^{\gamma\delta})) \varepsilon_{yij}(\mathbf{v}) d\mathbf{y} = 0, \quad \forall \mathbf{v} \in \tilde{\mathcal{V}}(Y). \end{aligned} \quad (1.4.32)$$

Note that the first local problem (1.4.24) is concerned with the in-plane deformation modes, while the local problem (1.4.32) corresponds to the out-of-plane curvature modes. An illustration of the deformation modes is provided in Fig. 1.7.

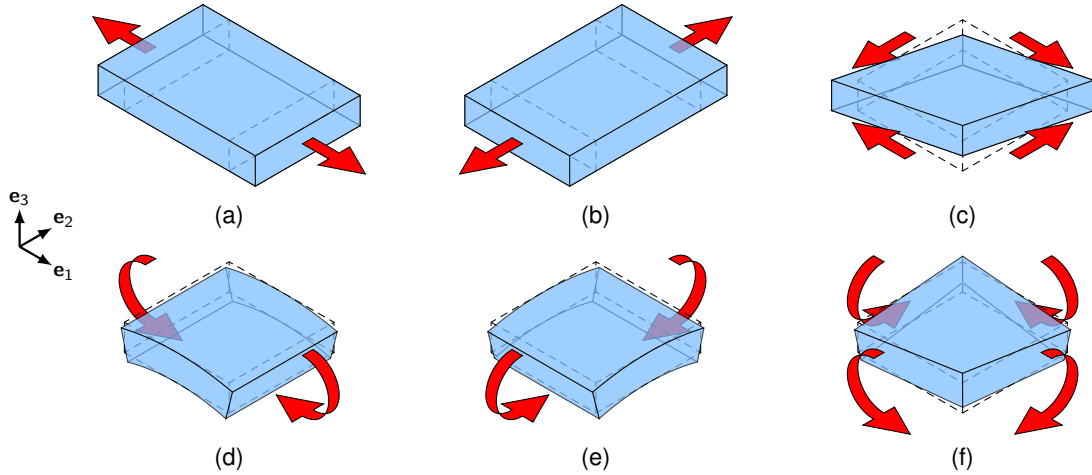


Fig. 1.7: strain modes imposed to solve the local problems (1.4.24) and (1.4.32). The undeformed unit cell is represented by dotted lines, whereas the deformed configuration is indicated by solid lines. The first row displays the three in-plane modes: tensile deformations along the coordinate axes e_1 (a), e_2 (b) and simple in-plane shear deformation (c), whereas the second row corresponds to the out of the plane modes, namely bending deformations along the coordinate axes e_1 (d), e_2 (e) and a shear bending (f).

1.4.3 Effective plate stiffness coefficients

Once the functions $\mathbf{w}^{k\delta}$ and $\mathbf{p}^{\gamma\delta}$ are known (which only depend on the medium and not on the external loading), the homogenised coefficients of the effective medium can easily be obtained.

The stress in eq. (1.4.9) takes the form:

$$\begin{aligned} \sigma_{ij}^{(-2)}(\mathbf{x}, \mathbf{y}) &= C_{ijkl} (\delta_{k\gamma} \delta_{\ell\delta} + \varepsilon_{\mathbf{y}kl}(\mathbf{w}^{\gamma\delta})) \delta_{k\gamma} \delta_{\ell\delta} \varepsilon_{\mathbf{x}\gamma\delta}(\bar{\mathbf{u}}) \\ &+ C_{ijkl} (y_3 \delta_{k\gamma} \delta_{\ell\delta} + \varepsilon_{\mathbf{y}kl}(\mathbf{p}^{\gamma\delta})) \delta_{k\gamma} \delta_{\ell\delta} \chi_{\mathbf{x}\gamma\delta}(U_3). \end{aligned} \quad (1.4.33)$$

Using the local problems defined in equations (1.4.23) and (1.4.31), we obtain by averaging over Y that:

$$\begin{cases} \frac{1}{|Y|} \int_Y C_{3\beta pq} (\delta_{p\gamma} \delta_{q\delta} + \varepsilon_{\mathbf{y}pq}(\mathbf{w}^{\gamma\delta})) d\mathbf{y} = 0, \\ \frac{1}{|Y|} \int_Y C_{3\beta pq} (y_3 \delta_{p\gamma} \delta_{q\delta} + \varepsilon_{\mathbf{y}pq}(\mathbf{p}^{\gamma\delta})) d\mathbf{y} = 0, \end{cases}$$

which also yields:

$$\left\langle \sigma_{i3}^{(-2)} \right\rangle_Y = 0.$$

Let us further define the generalized stresses, which are decomposed into the resultant \mathbf{N} and couple stresses \mathbf{M} for unit width:

$$N_{ij}^{(m)}(\mathbf{x}) = \frac{h}{|Y|} \int_Y \sigma_{ij}^{(m)}(\mathbf{x}, \mathbf{y}) d\mathbf{y} = h \left\langle \sigma_{ij}^{(m)} \right\rangle_Y \quad \forall m \in \llbracket -5, +\infty \llbracket \quad (1.4.34)$$

$$M_{ij}^{(m)}(\mathbf{x}) = \frac{h}{|Y|} \int_Y y_3 \sigma_{ij}^{(m)}(\mathbf{x}, \mathbf{y}) d\mathbf{y} = h \left\langle y_3 \sigma_{ij}^{(m)} \right\rangle_Y \quad \forall m \in \llbracket -5, +\infty \llbracket \quad (1.4.35)$$

The first macroscopic constitutive law follows from the average of eq. (1.4.33):

$$N_{\alpha\beta}^{(-2)} = A_{\alpha\beta\gamma\delta}^* \varepsilon_{\mathbf{x}\gamma\delta}(\bar{\mathbf{u}}) + B_{\alpha\beta\gamma\delta}^* \chi_{\mathbf{x}\gamma\delta}(U_3),$$

where $A_{\alpha\beta\gamma\delta}^*$ and $B_{\alpha\beta\gamma\delta}^*$ are the effective elastic stiffness coefficients expressed by:

$$\begin{cases} A_{\alpha\beta\gamma\delta}^* = \frac{h}{|Y|} \int_Y C_{\alpha\beta k\ell} (\delta_{k\gamma} \delta_{\ell\delta} + \varepsilon_{\mathbf{y}k\ell}(\mathbf{w}^{\gamma\delta})) d\mathbf{y}, \\ B_{\alpha\beta\gamma\delta}^* = \frac{h}{|Y|} \int_Y C_{\alpha\beta k\ell} (y_3 \delta_{k\gamma} \delta_{\ell\delta} + \varepsilon_{\mathbf{y}k\ell}(\mathbf{p}^{\gamma\delta})) d\mathbf{y}. \end{cases} \quad (1.4.36)$$

In addition, by averaging the problem (1.4.33) after multiplying by y_3 , we have:

$$\begin{aligned} M_{i3\beta}^{(-2)} &= \left(\frac{h}{|Y|} \int_Y y_3 C_{i\beta pq} (\delta_{p\gamma} \delta_{q\delta} + \varepsilon_{\mathbf{y}pq}(\mathbf{w}^{\gamma\delta})) d\mathbf{y} \right) \varepsilon_{\mathbf{x}\gamma\delta}(\bar{\mathbf{u}}) \\ &+ \left(\frac{h}{|Y|} \int_Y y_3 C_{i\beta pq} (y_3 \delta_{p\gamma} \delta_{q\delta} + \varepsilon_{\mathbf{y}pq}(\mathbf{p}^{\gamma\delta})) d\mathbf{y} \right) \chi_{\mathbf{x}\gamma\delta}(U_3). \end{aligned}$$

As before, using the local problems defined in equations (1.4.23) and (1.4.31), we obtain by averaging over Y that:

$$\begin{cases} \frac{h}{|Y|} \int_Y C_{3\beta pq} y_3 (\delta_{p\gamma} \delta_{q\delta} + \varepsilon_{\mathbf{y}pq}(\mathbf{w}^{\gamma\delta})) d\mathbf{y} = 0, \\ \frac{h}{|Y|} \int_Y C_{3\beta pq} y_3 (y_3 \delta_{p\gamma} \delta_{q\delta} + \varepsilon_{\mathbf{y}pq}(\mathbf{p}^{\gamma\delta})) d\mathbf{y} = 0. \end{cases}$$

The second constitutive law may then be rewritten as follows:

$$M_{\alpha\beta}^{(-2)} = C_{\alpha\beta\gamma\delta}^* \varepsilon_{\mathbf{x}\gamma\delta}(\bar{\mathbf{u}}) + D_{\alpha\beta\gamma\delta}^* \chi_{\mathbf{x}\gamma\delta}(U_3),$$

where $C_{\alpha\beta\gamma\delta}^*$ and $D_{\alpha\beta\gamma\delta}^*$ are the effective elastic stiffness coefficients expressed by:

$$\begin{cases} C_{\alpha\beta\gamma\delta}^* = \frac{h}{|Y|} \int_Y y_3 C_{\alpha\beta k\ell} (\delta_{k\gamma} \delta_{\ell\delta} + \varepsilon_{\mathbf{y}k\ell}(\mathbf{w}^{\gamma\delta})) \, d\mathbf{y}, \\ D_{\alpha\beta\gamma\delta}^* = \frac{h}{|Y|} \int_Y y_3 C_{\alpha\beta k\ell} (y_3 \delta_{k\gamma} \delta_{\ell\delta} + \varepsilon_{\mathbf{y}k\ell}(\mathbf{p}^{\gamma\delta})) \, d\mathbf{y}. \end{cases} \quad (1.4.37)$$

In order for the effective coefficients given in (1.4.36) and (1.4.37) to represent the coefficients of a linear elastic material, they shall satisfy a number of conditions reported for instance by Caillerie in [46]:

$$A_{\alpha\beta\gamma\delta} = A_{\beta\alpha\gamma\delta} = A_{\alpha\beta\delta\gamma} = A_{\gamma\delta\alpha\beta}, \quad (1.4.38)$$

$$B_{\alpha\beta\gamma\delta} = B_{\beta\alpha\gamma\delta} = B_{\alpha\beta\delta\gamma} = C_{\gamma\delta\alpha\beta} = C_{\delta\gamma\alpha\beta} = C_{\gamma\delta\beta\alpha}, \quad (1.4.39)$$

$$D_{\alpha\beta\gamma\delta} = D_{\beta\alpha\gamma\delta} = D_{\alpha\beta\delta\gamma} = D_{\gamma\delta\alpha\beta}, \quad (1.4.40)$$

$$\exists m \in \mathbb{R}^{+*} \mid A_{\alpha\beta\gamma\delta} \xi_{\alpha\beta} \xi_{\gamma\delta} \geq m \xi_{\alpha\beta} \xi_{\alpha\beta}, \quad \forall \{\xi_{\alpha\beta} \mid \xi_{\alpha\beta} = \xi_{\beta\alpha}\}, \quad (1.4.41)$$

$$\exists m \in \mathbb{R}^{+*} \mid D_{\alpha\beta\gamma\delta} \xi_{\alpha\beta} \xi_{\gamma\delta} \geq m \xi_{\alpha\beta} \xi_{\alpha\beta}, \quad \forall \{\xi_{\alpha\beta} \mid \xi_{\alpha\beta} = \xi_{\beta\alpha}\}. \quad (1.4.42)$$

The above equation indicates that A and D shall satisfy the symmetry and positivity properties, while B only verifies the short symmetry. From (1.4.36) and (1.4.37), the short symmetry is clearly verified. However there are no evidence regarding the long symmetry and the positive definiteness. Therefore, in order to verify these conditions, the effective coefficients should be expressed in a more convenient way. Choosing $\mathbf{v} = \mathbf{w}^{\gamma\delta}$ or $\mathbf{v} = \mathbf{p}^{\gamma\delta}$ in the first cell problem in its weak form (1.4.24) and renaming the indices gives:

$$\int_Y C_{ijpq} (\delta_{p\gamma} \delta_{q\delta} + \varepsilon_{\mathbf{y}pq}(\mathbf{w}^{\gamma\delta})) \varepsilon_{\mathbf{y}ij}(\mathbf{w}^{\gamma\delta}) \, d\mathbf{y} = 0, \quad (1.4.43)$$

$$\int_Y C_{ijpq} (\delta_{p\gamma} \delta_{q\delta} + \varepsilon_{\mathbf{y}pq}(\mathbf{w}^{\gamma\delta})) \varepsilon_{\mathbf{y}ij}(\mathbf{p}^{\gamma\delta}) \, d\mathbf{y} = 0. \quad (1.4.44)$$

Similarly, choosing $\mathbf{v} = \mathbf{w}^{\gamma\delta}$ or $\mathbf{v} = \mathbf{p}^{\gamma\delta}$ in the second cell problem in its weak form (1.4.32) and renaming the indices gives:

$$\int_Y C_{ijpq} (y_3 \delta_{p\gamma} \delta_{q\delta} + \varepsilon_{\mathbf{y}pq}(\mathbf{p}^{\gamma\delta})) \varepsilon_{\mathbf{y}ij}(\mathbf{w}^{\gamma\delta}) \, d\mathbf{y} = 0, \quad (1.4.45)$$

$$\int_Y C_{ijpq} (y_3 \delta_{p\gamma} \delta_{q\delta} + \varepsilon_{\mathbf{y}pq}(\mathbf{p}^{\gamma\delta})) \varepsilon_{\mathbf{y}ij}(\mathbf{p}^{\gamma\delta}) \, d\mathbf{y} = 0. \quad (1.4.46)$$

By respectively adding eq. (1.4.43) and (1.4.45) to the definition of the effective coefficients $A_{\alpha\beta\gamma\delta}^*$ and $B_{\alpha\beta\gamma\delta}^*$ (eq. (1.4.36)) we get a new expression for the effective coefficients:

$$A_{\alpha\beta\gamma\delta}^* = \frac{h}{|Y|} \int_Y C_{ijkl} (\delta_{k\gamma} \delta_{\ell\delta} + \varepsilon_{\mathbf{y}k\ell}(\mathbf{w}^{\gamma\delta})) (\delta_{i\alpha} \delta_{j\beta} + \varepsilon_{\mathbf{y}ij}(\mathbf{w}^{\alpha\beta})) \, d\mathbf{y}, \quad (1.4.47)$$

$$B_{\alpha\beta\gamma\delta}^* = \frac{h}{|Y|} \int_Y C_{ijkl} (y_3 \delta_{k\gamma} \delta_{\ell\delta} + \varepsilon_{\mathbf{y}k\ell}(\mathbf{p}^{\gamma\delta})) (\delta_{i\alpha} \delta_{j\beta} + \varepsilon_{\mathbf{y}ij}(\mathbf{w}^{\alpha\beta})) \, d\mathbf{y}. \quad (1.4.48)$$

By respectively adding eq. (1.4.44) and (1.4.46) to the definition of the effective coefficients $C_{\alpha\beta\gamma\delta}^*$ and $D_{\alpha\beta\gamma\delta}^*$ (eq. (1.4.37)) we get a new expression for the effective coefficients:

$$C_{\alpha\beta\gamma\delta}^* = \frac{h}{|Y|} \int_Y C_{ijkl} (\delta_{k\gamma} \delta_{\ell\delta} + \varepsilon_{\mathbf{y}k\ell}(\mathbf{w}^{\gamma\delta})) (y_3 \delta_{i\alpha} \delta_{j\beta} + \varepsilon_{\mathbf{y}ij}(\mathbf{p}^{\alpha\beta})) \, d\mathbf{y}, \quad (1.4.49)$$

$$D_{\alpha\beta\gamma\delta}^* = \frac{h}{|Y|} \int_Y C_{ijkl} (y_3 \delta_{k\gamma} \delta_{\ell\delta} + \varepsilon_{\mathbf{y}k\ell}(\mathbf{p}^{\gamma\delta})) (y_3 \delta_{i\alpha} \delta_{j\beta} + \varepsilon_{\mathbf{y}ij}(\mathbf{p}^{\alpha\beta})) \, d\mathbf{y}. \quad (1.4.50)$$

From eq. (1.4.47) and (1.4.50), the symmetry $A_{\alpha\beta\gamma\delta}^* = A_{\gamma\delta\alpha\beta}^*$ and $D_{\alpha\beta\gamma\delta}^* = D_{\gamma\delta\alpha\beta}^*$ is immediate

by using the symmetry of C_{ijkl} . Equation (1.4.47) and (1.4.50) also imply the positivity of $A_{\alpha\beta\gamma\delta}^*$ and $D_{\gamma\delta\alpha\beta}^*$. Let us demonstrate it on $A_{\alpha\beta\gamma\delta}^*$ (the approach for $D_{\gamma\delta\alpha\beta}^*$ will be analogous). If ξ is a symmetric matrix, the positivity of C_{ijkl} yields:

$$A_{\alpha\beta\gamma\delta}^* \xi_{\gamma\delta} \xi_{\alpha\beta} = \frac{h}{|Y|} \int_Y C_{ijkl} \left(\delta_{k\gamma} \delta_{l\delta} \xi_{\gamma\delta} + \varepsilon_{ykl} (\mathbf{w}^{\gamma\delta} \xi_{\gamma\delta}) \right) \left(\delta_{i\alpha} \delta_{j\beta} \xi_{\alpha\beta} + \varepsilon_{yij} (\mathbf{w}^{\alpha\beta} \xi_{\alpha\beta}) \right) d\mathbf{y} \geq 0.$$

In particular, when the above equation is zero, then the positive definiteness of C_{ijkl} yields $\delta_{i\alpha} \delta_{j\beta} \xi_{\alpha\beta} + \varepsilon_{yij} (\mathbf{w}^{\alpha\beta} \xi_{\alpha\beta}) = 0$. Averaging this expression over a cell Y yields $\xi_{\alpha\beta} = 0$.

From eq. (1.4.48) and (1.4.49), it is also clear that: $B_{\alpha\beta\gamma\delta}^* = C_{\gamma\delta\alpha\beta}^*$. For this reason, we will drop the notation of C^* in the sequel, and replace it by the notation \mathbb{B}^* .

Let us now discuss the most general case where $h = r \epsilon L$. The unit cell Y is redefined as: $Y = [0, 1]^2 \times [-r/2, r/2]$ where r is the cell's aspect ratio (by construction, we have that $r = \mathcal{O}(1)$). Then the results for the effective coefficients read the same as in eq. (1.4.47)–(1.4.50), but are slightly modified in the sense that the volume $|Y|$ is no longer elementary, i.e., equal to 1. Using this approach, note that the scaling is made with respect to ϵ for both in-plane and out of the plane components. Through this choice, the rescaled unit cell's Y thus preserves its aspect ratio, unlike in the monograph of Caillerie [46].

1.4.4 Effective equations on the macroscopic scale

Problem in ϵ^{-2} . Integrating eq. (1.4.15) on Y and adding the boundary conditions (1.4.18) leads to:

$$\frac{\partial N_{\alpha\beta}^{(-2)}}{\partial x_\beta} + \frac{1}{|Y|} \int_{\Gamma^\pm} t_\alpha^\pm ds = 0.$$

By setting $T_\alpha = \frac{h}{|Y|} \int_{\Gamma^\pm} t_\alpha^\pm ds$, we recover one of the thin plate balance equations:

$$\frac{\partial N_{\alpha\beta}^{(-2)}}{\partial x_\beta} + T_\alpha = 0.$$

In the above equation, T_α represents the area-averaged tangential traction applied on the surfaces.

Similarly, integrating eq. (1.4.15) on Y after multiplying by y_3 and adding the boundary conditions (1.4.18) leads to:

$$\frac{\partial M_{\alpha\beta}^{(-2)}}{\partial x_\beta} + \left[\frac{h}{|Y|} \int_{\Gamma^\pm} y_3 t_\alpha^\pm ds \right] - N_{\alpha 3}^{(-1)} = 0.$$

Differentiating the above equation with respect to the variable x yields:

$$\frac{\partial^2 M_{\alpha\beta}^{(-2)}}{\partial x_\alpha \partial x_\beta} + \frac{\partial}{\partial x_\alpha} \left[\frac{h}{|Y|} \int_{\Gamma^\pm} y_3 t_\alpha^\pm ds \right] - \frac{\partial N_{\alpha 3}^{(-1)}}{\partial x_\alpha} = 0.$$

Problem in ϵ^{-1} . The derivative of $N_{\alpha 3}^{(-1)}$ in the above may be obtained integrating the next orders' equilibrium (1.4.16) on Y and adding the boundary conditions (1.4.18). We report the specific component obtained after a change of indices.

$$\frac{\partial N_{\alpha 3}^{(-1)}}{\partial x_\alpha} = \frac{h}{|Y|} \int_{\Gamma^\pm} t_3^\pm ds.$$

By setting $Q_\alpha = \frac{h}{|Y|} \int_{\Gamma^\pm} y_3 t_\alpha^\pm ds$ and $T_3 = \frac{h}{|Y|} \int_{\Gamma^\pm} t_3^\pm ds$, we recover the second thin plate balance equations:

$$\frac{\partial^2 M_{\alpha\beta}^{(-2)}}{\partial x_\alpha \partial x_\beta} + \frac{\partial Q_\alpha}{\partial x_\alpha} - T_3 = 0.$$

To sum up, we obtain the following set of equations:

$$\begin{cases} \frac{\partial N_{\alpha\beta}^{(-2)}}{\partial x_\beta} + T_\alpha = 0 & \text{in } \omega, \\ \frac{\partial^2 M_{\alpha\beta}^{(-2)}}{\partial x_\alpha \partial x_\beta} + \frac{\partial Q_\alpha}{\partial x_\alpha} - T_3 = 0 & \text{in } \omega, \\ N_{\alpha\beta}^{(-2)} = A_{\alpha\beta\gamma\delta}^* \varepsilon_{\mathbf{x}\gamma\delta}(\bar{\mathbf{u}}) + B_{\alpha\beta\gamma\delta}^* \chi_{\mathbf{x}\gamma\delta}(U_3) & \text{in } \omega, \\ M_{\alpha\beta}^{(-2)} = B_{\gamma\delta\alpha\beta}^* \varepsilon_{\mathbf{x}\gamma\delta}(\bar{\mathbf{u}}) + D_{\alpha\beta\gamma\delta}^* \chi_{\mathbf{x}\gamma\delta}(U_3) & \text{in } \omega, \\ U_3 = 0, \quad \bar{u}_\alpha = 0 & \text{in } \partial\omega. \end{cases} \quad (1.4.51)$$

Consequently, the effective behaviour of a periodic composite panel is associated to a thin plate elasticity boundary value problem expressed in eq. (1.4.51).

1.4.5 Comments

In the limiting case when the panel is just a plate formed by an isotropic elastic material, the macroscopic problem (1.4.51) reduces to the well known Kirchhoff–Love plate equations [156] (a quick review on the kinematic assumptions for the Kirchhoff–Love plate is provided in appendix A.1). The proof is carried out for instance in the book of Mei and Vernescu, section 5.4, pages 196–199 [163]).

The obtained macroscopic model is also quite similar to the classical laminate plate theory (CLPT) (interested reader can refer to appendix A.2 for additional information about this model). In fact, the latter can be retrieved assuming that $C(\mathbf{y})$ is only depending on y_3 . In this case, the constitutive behaviour enforces that $B^* = \mathbb{T}B^*$.

Here again, the approach presented only considers the first order (in the plane). The extension to the next order of the asymptotic would lead to a bending gradient model for thick plates as illustrated in the book of Sab and Lebée, chapter 9, page 172 [208]. We also note that equivalent homogenisation and dimension reduction that leads to the theory of Reissner–Mindlin for thick plates does not yet exist, to our knowledge.

1.4.6 Elastic panels with a periodic microstructure: summary

The estimation of the effective elastic properties of a periodic heterogeneous panel are obtained following this procedure:

1. Solve the local problems over the unit cell Y expressed hereafter in their weak formulation:

Find $\mathbf{w}^{\gamma\delta} \in \tilde{\mathcal{V}}(Y) := \{\mathbf{v} \in H_{loc}^1(Y) \mid (y_1, y_2)\text{-periodic}, \langle v_i \rangle_Y = 0\}$ such that:

$$\int_Y C_{ijpq} (\delta_{p\gamma} \delta_{q\delta} + \varepsilon_{ypq}(\mathbf{w}^{\gamma\delta})) \varepsilon_{yij}(\mathbf{v}) \, d\mathbf{y} = 0, \quad \forall \mathbf{v} \in \tilde{\mathcal{V}}(Y). \quad (1.4.52)$$

Find $\mathbf{p}^{\gamma\delta} \in \tilde{\mathcal{V}}(Y)$ such that:

$$\int_Y C_{ijpq} (y_3 \delta_{p\gamma} \delta_{q\delta} + \varepsilon_{ypq}(\mathbf{p}^{\gamma\delta})) \varepsilon_{yij}(\mathbf{v}) \, d\mathbf{y} = 0, \quad \forall \mathbf{v} \in \tilde{\mathcal{V}}(Y). \quad (1.4.53)$$

2. Compute the effective elastic coefficients using the following relations:

$$A_{\alpha\beta\gamma\delta}^* = \frac{h}{|Y|} \int_Y C_{ijkl} (\delta_{k\gamma} \delta_{l\delta} + \varepsilon_{ykl}(\mathbf{w}^{\gamma\delta})) (\delta_{i\alpha} \delta_{j\beta} + \varepsilon_{yij}(\mathbf{w}^{\alpha\beta})) \, d\mathbf{y}, \quad (1.4.54)$$

$$B_{\alpha\beta\gamma\delta}^* = \frac{h}{|Y|} \int_Y C_{ijkl} (y_3 \delta_{k\gamma} \delta_{l\delta} + \varepsilon_{ykl}(\mathbf{p}^{\gamma\delta})) (\delta_{i\alpha} \delta_{j\beta} + \varepsilon_{yij}(\mathbf{w}^{\alpha\beta})) \, d\mathbf{y}, \quad (1.4.55)$$

$$D_{\alpha\beta\gamma\delta}^* = \frac{h}{|Y|} \int_Y C_{ijkl} (y_3 \delta_{k\gamma} \delta_{l\delta} + \varepsilon_{ykl}(\mathbf{p}^{\gamma\delta})) (y_3 \delta_{i\alpha} \delta_{j\beta} + \varepsilon_{yij}(\mathbf{p}^{\alpha\beta})) \, d\mathbf{y}. \quad (1.4.56)$$

Chapter 2

Shape and topology optimisation

Contents

2.1	An overview of the structural optimisation	47
2.2	Overview of the shape optimisation	48
2.2.1	Ill-posedness of shape optimisation problems and remedies	48
2.2.2	Main categories of shape optimisation techniques	49
2.3	Shape sensitivity analysis using Hadamard's boundary variation method	52
2.3.1	Shape differentiability and computation of shape derivatives	52
2.3.2	Shape derivation using C�ea's Lagrangian method	53
2.3.3	Steepest descent direction	56
2.4	Shape and topology optimisation using a level set method	56
2.4.1	The level set method	56
2.4.2	Coupling shape sensitivity with a level set description	60
2.4.3	Numerical algorithm	61
2.4.4	Formulation in the smooth inter-phase context	62

Shape and topology optimisation are mathematical methods used to optimise material layout within a given design space, for a given set of loads, boundary conditions and constraints with the goal of maximising the performance of the system. These methods are expected to bring a potential paradigm shift in the design cycle of structures, replacing the classical trial and error efforts by more natural and automatic procedures.

2.1 An overview of the structural optimisation

Additive manufacturing processes is enabling to tailor the shape design and tune the properties of architected materials, giving an opportunity to rethink the strategies in mechanical design for parts and structures, in order to improve as much as possible some characteristics related to their mechanical behaviour. This is what "Structural Optimisation" is about.

The design cycle of a structure has evolved tremendously over the last decades. During the design of a new object, an initial concept is proposed and evaluated with respect to various criteria (performances, aesthetic, economical. . .). Then, the design is either accepted, or changed to be improved. In the past, this improvement task was almost exclusively relying on the expertise of engineers. Even today when dealing with complicated problems, where mechanical knowledge is very limited (friction contacts at hinges of assemblies, bolted assemblies...), it is still common practice to use guidelines of design, which are obtained from empirical methods after a long period of trial and error efforts. This design loop could end after a significant number of iterations, resulting in a high design cost and, in all probability, in a structure that may not be optimal, i.e., with room for further improvements. Breakthroughs of the last decades in the computational field

have enabled the implementation of systematic algorithms and methods based on a mathematical formulation into the design process of structures. These methods of course have naturally aroused across many scientific fields, but for the sake of brevity, the studies in the framework of solid mechanics will be the only ones discussed here. For this reason, the words “structure” and “shape” may be interchanged in this text.

A wide variety of structural optimisation problems have appeared in the literature, including the optimisation of the material properties [205, 223], the minimisation of the stress concentration [10, 79] or the maximisation of the energy absorption [260]. Present day techniques permit to incorporate geometric [42, 178, 250] and material non-linearities [57, 162], as well as manufacturability constraints [165, 174, 243] in the design optimisation.

The chapter is organised as follows. In section 2.2, we provide a short review on the existing shape optimisation techniques. Section 2.3 reviews the main elements of the Hadamard’s boundary variation method, which is a standard method for evaluating the sensitivity of a function with respect to its domain - which implies a notion of differentiation with respect to the shape. The particular case of functions depending on the domain, through solutions to the linearised elasticity problem is considered. Finally, section 2.4 discusses a particular numerical framework based upon the level set method for the implementation of shape optimisation algorithms. This framework shall be utilised throughout the next chapters in this manuscript (in particular chapter 3 and 7, which are concerned with the computational design of 3D printable sheets structures).

2.2 Overview of the shape optimisation

In a general manner, shape optimisation consists in tailoring the shape of an object to meet (or maximise) a desired set of properties. Since the seminal works of Bendsøe and Kikuchi on a methodology for optimal shape design [31], there has been an increasing number of publications on the topic, see [32, 80] and the references therein for a historical review. Existing algorithms and methods based on a mathematical formulation for optimal shape design have now reached a level of maturity which makes them viable to implement the methods in computer aided engineering systems for production use.

The mathematical formulation of a shape optimisation problem can be generally defined as the minimisation of a cost functional \mathcal{J} over the domain of interest S :

$$\inf_{S \in \mathcal{U}_{ad}} \mathcal{J}(S), \quad (2.2.1)$$

where \mathcal{U}_{ad} is a set of admissible shapes to which S shall belong.

2.2.1 Ill-posedness of shape optimisation problems and remedies

Non existence of optimal solutions. As this problem lacks an optimal solution for a great variety of problems (see examples in the book of Allaire [9], section 6.2.1, pages 129–132, with an illustration reported in Fig. 2.1), there is a need to enforce further constraints, leading to different approaches for shape optimisation.

Techniques to avoid non-existence. There are two main techniques which may help to bypass this difficulty.

- Relaxation of the original problem: since the main obstruction to the existence of optimal shapes seems to be that they tend to be porous, a quite natural idea consists in enlarging the set of admissible shapes by including “homogenised” structures in \mathcal{U}_{ad} . In this way the characteristic function S is replaced by a density field ρ which varies continuously in the interval $[0, 1]$. This viewpoint is mathematically justified owing to the homogenisation theory¹, and urges to think

¹Following the pioneering work of Murat and Tartar [176]. Interested readers may refer to [8, 236] for further details.

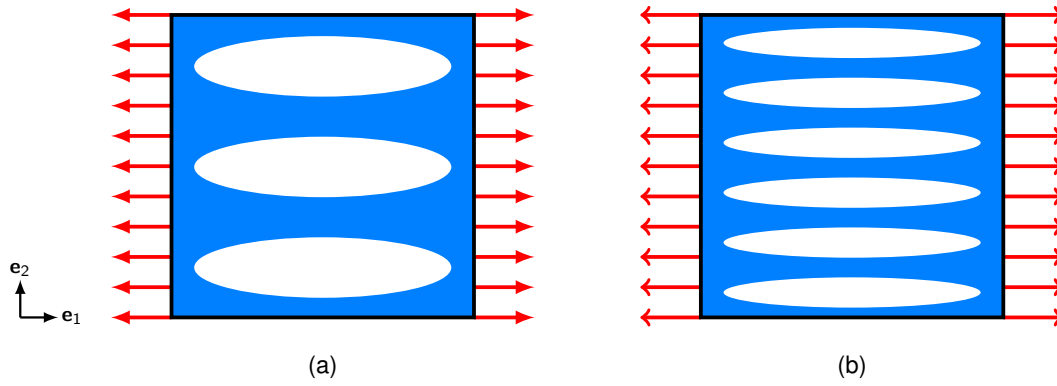


Fig. 2.1: example extracted from the book of Allaire [9], where the goal is to maximise the stiffness of a membrane along its horizontal direction. Note that the shape must also verify an equality volume constraint. Let us compare two membranes with the same volume, but different number of holes. The shape in (b) is more rigid than that in (a). In fact, the rigidity of such structure could be always further improved by creating smaller and smaller inclusions of weak phase aligned with the direction of the force. Without constraints on the size or smoothness of the holes, we understand this process could be continued without any limit. Therefore, there is no minimum point or optimal solution for such problem.

over the problem of finding the optimal shape as that of finding the optimal distribution (and organisation at the infinitesimal scale) of a mixture of material and void within a computational domain. This idea is at the core of density-based methods in structural optimisation.

- Restriction of the original problem: the converse idea consists in imposing additional constraints on the set of admissible shapes, to avoid extreme oscillations of its boundary or to impose limitations on its topology. The contributions of Ambrosio and Buttazzo [18] among others proved that trading an objective function $\mathcal{J}(S)$ for the very close function $\mathcal{J}(S) + \tau\mathcal{P}(S)$, where $\tau > 0$ is a fixed penalisation parameter and $\mathcal{P}(S)$ is the perimeter of the shape S , leads to existence of optimal shapes in the considered class. The monograph of Murat and Simon [175] proved the existence of local optima for problem (2.2.1), for a large variety of objective functions, assuming that the admissible shapes are uniformly Lipschitz, i.e., provided with a "sufficiently regular" boundary. Other techniques permit to enforce topological constraints on shapes, which in turn can prevent the homogenisation effect. In the linear elasticity setting, Chambolle [56] proved that for two-dimensional problems, imposing an upper bound on the number of connected components of the complementary \bar{S} of any shape S in a large computational box \mathcal{D} can lead to a well-posed optimisation problem.

2.2.2 Main categories of shape optimisation techniques

When shape optimisation techniques were introduced in computational mechanics, many ways of handling the *structural* optimisation problems have been established, depending on the sought application. These methods mainly differ in the involved ways to represent *shapes*, and to compute the sensitivity of the objective criterion with respect to the design. The description of a shape is essential in the procedure, as it should conciliate two antagonistic requirements. On one hand, shape optimisation techniques require to be able to perform mechanical computations on the considered shapes, e.g. by means of finite differences, finite element, and not all kind of representations lend themselves to such computations. On the other hand, the representation adopted must be versatile enough to allow for a robust account of shapes' deformations. Traditionally, three main categories are recognised: size optimisation, geometric optimisation, and topology optimisation. Let us provide a brief explanation on their main features.

- **Size optimisation.** The goal here is to optimise a given structural criterion through changes in the main size, e.g. width, height and thickness distribution, of a component with a pre-defined shape [30, 32, 64]. It is well established and widely used in industrial applications; yet the incapacity of generating any changes in shape represents one of its main limitations.

- **Geometric optimisation.** The optimisation parameter is the boundary of the structure itself. The shape of a domain can be represented numerically through a finite element mesh [32, 11], or other means such as a piecewise polynomial function, e.g. NURBS [195], Catmull-Clark [50] or T-Splines [217] in the context of isogeometric analysis [120]. Optimisation of the materials properties using an isogeometric analysis with a NURBS parametrisation was for instance carried out for auxetic structures [96, 254, 255]. In the context of thin-walled structures, shape optimisation has been used to generate approximately bending free structural forms in spatial structures [184]. In comparison to the size optimisation, the domain here has much more freedom to vary, yet no change in the topology is allowed.
- **Topology optimisation.** It provides a remedy to shape optimisation's limitation regarding the preservation of the initial topology. Design changes are typically expressed by the creation of holes, their evolution and relative connectivity. A problem of topology optimisation calls for the search of the optimal distribution of material in a given domain under a minimum set of restrictions. The problem is thus defined a priori with minimum restrictions, as a problem of finding the best possible shape that solves problem (2.2.1). Indicated for exploring a larger set of shapes, and thus increasing the possibility to obtain better optimal solutions, this category was of particular interest for this work and will be developed in the sequel.

Note that these tools are often being used sequentially in the development of an industrial product. Topology optimisation is rather utilised during the conceptual design stage, to find an appropriate shape among a wide space of admissible shapes; Geometric optimisation is interesting during the basic design stage; Size optimisation is mostly used during the detailed design stage, when the main configuration of the parts is already set.

Through a bibliographic investigation, it was possible to identify the main methods of topology optimisation in the literature, which differ in the way topological changes occur.

Density methods. These are the most commonly used methods in commercial topology optimisation software. A density field $\rho(\mathbf{x}) \in [0, 1]$ is defined in the design domain and the original topology optimisation problem is traded for a problem of optimal distribution of the material density. One of the pioneering approach to perform topology optimisation is known as the homogenisation method, mainly developed in [12, 31]. A typical solution of an homogenised problem results in an optimal shape like the one on the left of Fig. 2.2. It is clear from there that the notion of a "shape" is lost, i.e., there is no clear boundary of the domain. This is a significant drawback of the homogenisation method for the subsequent object fabrication. Of course, it may always be possible to interpret the final density distribution, assuming that low densities correspond to holes and densities close to high densities correspond to the real structure and design a shape that serves as an initialisation for a problem of Geometric Optimisation. However, this is not always a trivial task.

In order to get back into a classical shape, a penalisation of intermediate densities is viable (see right part of Fig. 2.2). The strategy is as follows. Upon convergence to an optimal density, a few more iterations of the algorithm are run, enforcing the density to take values close to 0 or 1. This changes the optimal density and produces a quasi-optimal shape. Of course, the procedure is purely numerical and mesh dependent.

Another idea to get back into a classical shape, consists in penalising intermediate densities by using a fictitious interpolation scheme for the material properties at each iteration, which has the tendency to produce a binarised result. The Solid Isotropic Material with Penalisation (SIMP) method uses the scheme $C_{ijkl}(\rho) = \rho^p C_{ijkl}$, where C_{ijkl} is the elasticity tensor of the full material ($\rho = 1$) and p is the penalisation power, used to create classical shapes (usually $p = 3$ is used). To know more about the SIMP method and more generally about penalisation methods, interested readers are invited to look at the works of Bendsøe and Sigmund [30, 32, 193] for such methods.

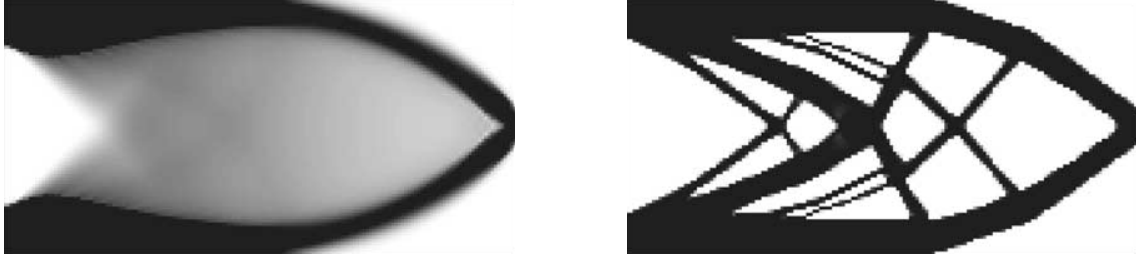


Fig. 2.2: two-dimensional cantilever computed with the homogenisation method. Density distribution of a composite (left), penalised solution (right). Results extracted from the works of Allaire, Jouve and Toader [14].



Fig. 2.3: Two-dimensional cantilever computed with the level set method. Initial shape is presented in the left figure. The shape of the cantilever remains clear through all the iterations. Results extracted from the works of Allaire, Jouve and Toader [13].

Implicit methods. These methods have emerged thank to the development of efficient methods for interface-tracking in various fields such as computational fluids dynamics. They are becoming quite popular in topology optimisation – the most famous of them being the *Phase Field Method* and the *Level Set Method*. In the former method, discussed in [24, 49, 232], the “shape” S is described by a phase field $\phi \in [0, 1]$ defined all over the design domain \mathcal{D} . $\phi = 0$ indicate areas with void phase, conversely $\phi = 1$ represents areas containing material. In a physically accurate setting each point in space either does or does not contain material, i.e., $\phi \in \{0, 1\}$, leading to a sharp transition. However, in the realm of optimisation a smooth transition between material and void is desired in order to calculate derivatives. This is achieved by explicitly allowing impure phases, i.e., states with $0 < \phi < 1$. The transition is seen as the interphase between material and void. A time-dependent evolutionary equation of the phase field function ϕ is introduced. As discussed in [232], the change of the phase field function with respect to time is assumed to be linearly dependent upon the direction in which the free energy function is minimised:

$$\frac{\partial \phi}{\partial t} = \kappa \nabla^2 \phi - f'(\phi),$$

where $\kappa > 0$ is a positive coefficient of the diffusion term, while f is usually taken as double well potential. The above formula is known as the Allen–Cahn equation.

With respect to the level set method, it was devised by [187, 188] for numerically tracking fronts and free boundaries. Its great advantages compared to the homogenisation method and its variant, like the SIMP method, is the “clear” and smooth description of the shape’s boundary and its independence of the mechanical framework at play. It is versatile and computationally very efficient. The pioneering contributions of Allaire et al. [13], Wang et al.[248] were among the first to describe a new implementation of the level set method for structural optimisation. An example of optimal cantilever obtained via the level set method is shown in Fig. 2.3. This last technique was retained for this work and will therefore be presented in detail in the forthcoming section 2.4.1.

Lastly, a completely different alternative consists in performing *topological sensitivity analyses*, according to which the sensitivity of \mathcal{J} with respect to the nucleation of infinitesimally small holes inside shapes is evaluated (see for instance [19, 44, 81]).

2.3 Shape sensitivity analysis using Hadamard's boundary variation method

The principle of shape optimisation consists in changing iteratively the shape of a structure in order to minimise as much as possible the value of the objective function. As discussed in the paper of Sigmund [224], the size, i.e., number of variable, of a typical shape optimisation problem is usually prohibitive for discrete or zero-order methods; gradient-based continuous optimisation algorithms are generally preferable. However, in order to calculate a notion of gradient, a method for describing variations of a shape shall be introduced. The first step towards this direction is the mathematical representation of the shape. In the sequel, we introduce a particular method for describing variations of a shape, namely Hadamard's boundary variation method, as well as the inferred notions of differentiation with respect to the domain.

Hadamard's boundary variation method. The approach here is due to the analysis of Murat and Simon [175] which is based on Hadamard's variation method. (more explanation can also be found in [9, 75, 225], while an historical background can be found in [196]). Starting from a smooth reference domain S_0 (also referred to as reference shape), subset of the design domain $\mathcal{D} \subset \mathbb{R}^d$, suppose that all admissible shapes are obtained by applying a smooth vector field θ :

$$S = \{\mathbf{x} + \theta(\mathbf{x}) \mid \mathbf{x} \in S_0\},$$

with $\theta \in W^{1,\infty}(\mathcal{D}, \mathbb{R}^d)$ such that θ is tangential on $\partial\mathcal{D}$ (this last condition ensures that $\mathcal{D} = (\mathbf{I}_d + \theta)\mathcal{D}$). It is well known that, for sufficiently small θ , $(\mathbf{I}_d + \theta)$ is a diffeomorphism in Y . In other words, every admissible shape S will now be represented by a vector field $\theta : \mathcal{D} \rightarrow \mathbb{R}^d$ and will be expressed by $S = (\mathbf{I}_d + \theta)(S_0)$ (an illustration of the concept is provided in Fig. 2.4). Variations of a given shape end up being parametrised by means of an open subset of a Banach space [70]. Since θ belongs to some functional space (e.g., $W^{1,\infty}(\mathcal{D}, \mathbb{R}^d)$ or $C^{1,\infty}(\mathcal{D}, \mathbb{R}^d)$), it is henceforth possible to define a notion of derivation with respect to θ .

Note that the shape representation described above implies that for θ small enough, all admissible shapes will have the same topology with the reference domain S_0 , since a change of topology is not possible via continuous transformations of the domain S_0 . We are now ready to define a notion of differentiability with respect to the domain.

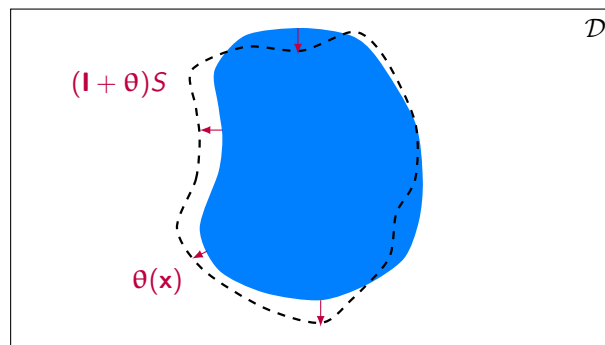


Fig. 2.4: Variation $(\mathbf{I}_d + \theta)(S)$ of a reference shape S .

2.3.1 Shape differentiability and computation of shape derivatives

Definition of the shape derivative. The shape derivative of a function $\mathcal{J}(S_0)$ is defined as the Fréchet derivative in the Banach space $W^{1,\infty}(\mathcal{D}, \mathbb{R}^d)$ at 0 of the application $\theta \rightarrow \mathcal{J}((\mathbf{I}_d + \theta)(S_0))$.

Then, the following asymptotic expansion holds in the vicinity of 0:

$$\mathcal{J}((\mathbf{I}_d + \theta) S_0) = \mathcal{J}(S_0) + \mathcal{J}'(S_0)(\theta) + o(\theta), \quad \text{with} \quad \lim_{\theta \rightarrow 0} \frac{|o(\theta)|}{\|\theta\|_{W^{1,\infty}}}, \quad (2.3.1)$$

where $\mathcal{J}'(S_0)$ is a continuous linear form on $W^{1,\infty}(\mathcal{D}, \mathbb{R}^d)$. A weaker notion of differentiability, which is also convenient for the purpose, is that of the *directional derivative* of a objective function $\mathcal{J} : S \rightarrow \mathbb{R}^d$ at S in the direction $\theta \in W^{1,\infty}(\mathcal{D}, \mathbb{R}^d)$, which is defined as the limit in \mathbb{R} (if it exists):

$$\mathcal{J}'(S)(\theta) = \lim_{\delta \rightarrow 0} \frac{\mathcal{J}((\mathbf{I}_d + \delta\theta)(S)) - \mathcal{J}(S)}{\delta}. \quad (2.3.2)$$

A classical result is derived from Hadamard's structure theorem and states that the shape derivative depends only on the normal component of θ on the boundary ∂S (the tangential component can be omitted). This implies² that for two given $(\theta_1, \theta_2) \in W^{1,\infty}(\mathcal{D}, \mathbb{R}^d)$ such that $\theta_2 - \theta_1 \in C^1(\mathcal{D}, \mathbb{R}^d)$ and $\theta_1 \cdot \mathbf{n} = \theta_2 \cdot \mathbf{n}$ on ∂S , the derivative $\mathcal{J}'(S)$ verifies: $\mathcal{J}'(S)(\theta_1) = \mathcal{J}'(S)(\theta_2)$.

Shape derivative of functions independent on the domain. We recall two results for the shape derivatives of integrals, whose integrands do not depend on the domain. Their proof are carried out in the book of Allaire [9].

- Let $f \in W^{1,1}(\mathbb{R}^d)$ and $\mathcal{J} : C(S) \rightarrow \mathbb{R}$ be defined by $\mathcal{J}(S) = \int_S f(\mathbf{x}) \, d\mathbf{x}$.

Then \mathcal{J} is differentiable at S and $\forall \theta \in W^{1,\infty}(\mathcal{D}, \mathbb{R}^d)$ we have:

$$\begin{aligned} \mathcal{J}'(S)(\theta) &= \int_S \frac{\partial(\theta_r(\mathbf{x}) f(\mathbf{x}))}{\partial x_r} \, d\mathbf{x} \\ &= \int_{\Gamma^S} \theta_r(\mathbf{s}) n_r(\mathbf{s}) f(\mathbf{s}) \, ds, \end{aligned} \quad (2.3.3)$$

where \mathbf{n} denotes the external normal of the mean curvature of Γ^S .

- Let $f \in W^{2,1}(\mathbb{R}^d)$ and $\mathcal{J} : C(S) \rightarrow \mathbb{R}$ be defined by $\mathcal{J}(S) = \int_{\Gamma^S} f(\mathbf{s}) \, ds$.

Then \mathcal{J} is differentiable at S and $\forall \theta \in W^{1,\infty}(\mathcal{D}, \mathbb{R}^d)$ we have:

$$\begin{aligned} \mathcal{J}'(S)(\theta) &= \int_{\Gamma^S} \left(\theta_r(\mathbf{s}) \frac{\partial f(\mathbf{s})}{\partial s_r} + f(\mathbf{s}) \left(\frac{\partial \theta_r}{\partial s_r} - \frac{\partial(\theta_\ell n_\ell)}{\partial s_r} n_r \right) \right) ds \\ &= \int_{\Gamma^S} \theta_r(\mathbf{s}) n_r(\mathbf{s}) \left(\frac{\partial f(\mathbf{s})}{\partial \mathbf{n}} + H(\mathbf{s}) f(\mathbf{s}) \right) ds, \end{aligned} \quad (2.3.4)$$

where $H = \nabla \cdot \mathbf{n}(\mathbf{s})$ is the mean curvature of Γ^S .

It is recalled that the above results of shape derivatives of integrals are valid when the integrands are independent of the shape S . The case of shape derivation for functions that depend on the domain S is discussed in the next section. The aim is to extend the results about shape derivation of integrals to the general case of shape dependent integrands.

2.3.2 Shape derivation using C ea's Lagrangian method

The definition provided in eq. (2.3.2) is not a constructive computation for $\mathcal{J}'(S)$. In fact, there are more than one way to compute the shape derivative of $\mathcal{J}'(S_0)$ (see [9] for a detailed presentation). In this study, we have made use of the method of C ea [45], which is a very useful tool for finding the expression of the shape derivative of a functional $\mathcal{J}(S, \mathbf{u}(S))$ that depends on the shape, but also

²The proof of this result is carried out in the book of Allaire, proposition 6.17, pages 131–133 [9].

on the solution $\mathbf{u}(S)$ of a partial differential equation, since it avoids the direct calculation of the shape derivative of $\mathbf{u}(S)$. This method is formal, in the sense that we assume enough smoothness of the shape for all necessary operations and also we assume the shape differentiability of all the functions at play. It amounts to regard the partial differential equation as a constraint of the optimisation problem that the variable \mathbf{u} needs to satisfy. In the sequel, the method is presented in detail using a general example.

Consider the following objective function:

$$\mathcal{J}(S, \mathbf{u}(S)) = \int_S j(\mathbf{x}, \mathbf{u}) d\mathbf{y} + \int_{\Gamma^s} k(\mathbf{x}, \mathbf{u}) ds, \quad (2.3.5)$$

where $\mathbf{u} \in H^1(S)$ is the displacement of the structure, the unique solution of the linearised elasticity system:

$$\begin{cases} \frac{\partial \sigma_{ij}}{\partial x_j} + f_i = 0 & \text{in } S, \\ \sigma_{ij} = C_{ijkl}^S \varepsilon_{kl}(\mathbf{u}) & \text{in } S, \\ u_i = 0 & \text{on } \Gamma^u, \\ \sigma_{ij} n_j = t_i & \text{on } \Gamma^t \quad (n_j \text{ denotes the external normal of } \Gamma^t). \end{cases} \quad (2.3.6)$$

In the above equation, the elastic properties in S are represented by a periodic fourth-order stiffness tensor C^S of components C_{ijkl}^S . C_{ijkl}^S are constant functions in S . The solid is clamped at the boundary Γ^u and is submitted to body forces \mathbf{f} , as well as surface forces \mathbf{t} at the boundary Γ^t . Note that in most applications, the boundary Γ^u and Γ^t are fixed, i.e., they do not change during the shape optimisation process. Furthermore, in many applications, $\Gamma^u \subset \partial\mathcal{D}$ and $\Gamma^t \subset \partial\mathcal{D}$ (recall that \mathcal{D} is the design domain). In other words, the boundary conditions are enforced at the boundary of the design domain. This choice is motivated by the fact that prescribed boundary regions often represent contact areas or loading zones, which must remain unchanged to avoid lack of material or conversely material interpenetration.

Let $\mathcal{V}(S) := \{\mathbf{v} \in H^1(S) \mid [v_i]_{\Gamma^u} = 0\}$ be the kinematic admissible space associated to S . The weak formulation of the problem (2.3.6) reads.

Find $\mathbf{u} \in \mathcal{V}(S)$ such that:

$$\int_S C_{ijkl} \varepsilon_{kl}(\mathbf{u}) \varepsilon_{ij}(\mathbf{q}) d\mathbf{x} - \int_S f_i q_i d\mathbf{x} - \int_{\Gamma^t} t_i q_i ds = 0, \quad \forall \mathbf{q} \in \mathcal{V}(S). \quad (2.3.7)$$

Instead of deriving directly the functional $\mathcal{J}(S, \mathbf{u}(S))$ and trying to calculate the Eulerian or Lagrangian derivative of $\mathbf{u}(S)$, we formulate the Lagrangian function:

$$\begin{aligned} \mathcal{L}(S, \mathbf{v}, \mathbf{q}) &= \int_S j(\mathbf{y}, \mathbf{v}) d\mathbf{x} + \int_{\Gamma^s} k(\mathbf{y}, \mathbf{v}) ds \\ &+ \int_S C_{ijkl} \varepsilon_{kl}(\mathbf{v}) \varepsilon_{ij}(\mathbf{q}) d\mathbf{x} - \int_S f_i q_i d\mathbf{x} - \int_{\Gamma^t} t_i q_i ds, \end{aligned} \quad (2.3.8)$$

where $\mathbf{v}, \mathbf{q} \in H^1(\mathbb{R}^d)$ do not depend on the domain S . As we will see in the sequel, the shape derivative of the objective functional \mathcal{J} at S will be derived by fixing the domain S and taking the optimality conditions for the Lagrangian function \mathcal{L} .

- Setting the partial derivative of \mathcal{L} with respect to \mathbf{q} in the direction of a test function $\boldsymbol{\varphi} \in$

$H^1(\mathcal{D}, \mathbb{R}^d)$ at the optimal point $(S, \mathbf{u}, \mathbf{p})$ equal to zero yields:

$$\begin{aligned} \left\langle \frac{\partial \mathcal{L}}{\partial \mathbf{q}}(S, \mathbf{u}, \mathbf{q}) \mid \boldsymbol{\varphi} \right\rangle &= 0 \\ \Leftrightarrow \int_S C_{ijkl} \varepsilon_{kl}(\mathbf{u}) \varepsilon_{ij}(\boldsymbol{\varphi}) d\mathbf{x} - \int_S f_i \varphi_i d\mathbf{x} - \int_{\Gamma^t} t_i \varphi_i ds &= 0. \end{aligned} \quad (2.3.9)$$

Equation (2.3.9) shows that the function \mathbf{u} is in fact the unique solution of the state equation (2.3.7).

- The partial derivative of \mathcal{L} with respect to \mathbf{v} , at the optimal point, in the direction $\boldsymbol{\varphi} \in H^1(\mathcal{D}, \mathbb{R}^d)$ gives:

$$\begin{aligned} \left\langle \frac{\partial \mathcal{L}}{\partial \mathbf{v}}(S, \mathbf{u}, \mathbf{p}) \mid \boldsymbol{\varphi} \right\rangle &= 0 \\ \Leftrightarrow \int_S \frac{\partial j(\mathbf{x}, \mathbf{u})}{\partial v_i} \varphi_i d\mathbf{x} + \int_{\Gamma^s} \frac{\partial k(\mathbf{x}, \mathbf{u})}{\partial v_i} \varphi_i ds + \int_S C_{ijkl} \varepsilon_{kl}(\boldsymbol{\varphi}) \varepsilon_{ij}(\mathbf{p}) d\mathbf{x} &= 0. \end{aligned} \quad (2.3.10)$$

Therefore, \mathbf{p} is the unique solution in of the adjoint state equation (2.3.10).

- Finally, the shape derivative of the functional \mathcal{J} will be equal to the shape derivative of the Lagrangian function \mathcal{L} at the optimal point $(S, \mathbf{u}, \mathbf{p})$, i.e.:

$$\left\langle \frac{\partial \mathcal{L}}{\partial S}(S, \mathbf{u}, \mathbf{p}) \mid \boldsymbol{\theta} \right\rangle = \mathcal{J}'(S)(\boldsymbol{\theta}). \quad (2.3.11)$$

To prove this result, take first any $\mathbf{p} \in H^1(\mathbb{R}^d)$ and see that:

$$\mathcal{L}(S, \mathbf{u}(S), \mathbf{p}) = \mathcal{J}(S),$$

where \mathbf{u} is the solution of the state equation. Then, taking the shape derivative of both members and using the rule of composite derivatives yields:

$$\mathcal{J}'(S)(\boldsymbol{\theta}) = \left\langle \frac{\partial \mathcal{L}}{\partial S}(S, \mathbf{u}(S), \mathbf{p}) \mid \boldsymbol{\theta} \right\rangle + \left\langle \frac{\partial \mathcal{L}}{\partial \mathbf{v}}(S, \mathbf{u}(S), \mathbf{p}) \mid \mathbf{u}'(S)(\boldsymbol{\theta}) \right\rangle.$$

If $\mathbf{q} = \mathbf{p}(S)$, i.e., the solution of the adjoint state (2.3.10), the last term disappears and relation (2.3.11) is revealed.

The shape derivative of \mathcal{L} is much easier to calculate, since it has been constructed such that the functions \mathbf{v} and \mathbf{q} are independent of S . Thus, only the results of Equation (2.3.3) and (2.3.4) need to be applied. A simple calculation yields:

$$\begin{aligned} \mathcal{J}'(S)(\boldsymbol{\theta}) &= \int_{\Gamma^s} \theta_r n_r (j(\mathbf{u}) + C_{ijkl} \varepsilon_{kl}(\mathbf{u}) \varepsilon_{ij}(\mathbf{p}) - f_i p_i) ds \\ &\quad + \int_{\Gamma^s} \theta_r n_r \left(\frac{\partial k(\mathbf{u})}{\partial n} + H k(\mathbf{u}) \right) ds \\ &\quad - \int_{\Gamma^t} \theta_r n_r \left(\frac{\partial t_i p_i}{\partial n} + H(t_i p_i) \right) ds. \end{aligned}$$

If we further assume that $\boldsymbol{\theta} = \mathbf{0}$ on Γ^t (typically the material distribution in the clamped or loaded

region is fixed a priori), then the shape derivative of \mathcal{J} reads:

$$\begin{aligned} \mathcal{J}'(S)(\boldsymbol{\theta}) &= \int_{\Gamma^S} \theta_r n_r (j(\mathbf{u}) + C_{ijkl} \varepsilon_{kl}(\mathbf{u}) \varepsilon_{ij}(\mathbf{p}) - f_i p_i) ds \\ &+ \int_{\Gamma^S} \theta_r n_r \left(\frac{\partial k(\mathbf{u})}{\partial n} + H k(\mathbf{u}) \right) ds. \end{aligned} \quad (2.3.12)$$

2.3.3 Steepest descent direction

Once the shape derivative of the functional $\mathcal{J}(S)$ has been found in the general form³:

$$\mathcal{J}'(S)(\boldsymbol{\theta}) = \int_{\Gamma^S} \theta_r n_r f(\mathbf{s}) ds,$$

where in the case of the considered problem (2.3.5)–(2.3.12), f reads:

$$f(\mathbf{s}) = j(\mathbf{u}) + C_{ijkl} \varepsilon_{kl}(\mathbf{u}) \varepsilon_{ij}(\mathbf{p}) + \frac{\partial k(\mathbf{u})}{\partial n} + H k(\mathbf{u}) - f_i p_i,$$

a descent direction, corresponding to a notion of gradient descent, is revealed under the choice:

$$\boldsymbol{\theta}(\mathbf{s}) = -t f(\mathbf{s}) \mathbf{n}(\mathbf{s}) \quad (2.3.13)$$

for a small positive step $t > 0$. Substituting $\boldsymbol{\theta}(\mathbf{s})$ in the shape derivative expression and back to the asymptotic expansion formula (2.3.1), we can formally write for $\mathcal{J}(S_t) = \mathcal{J}((\mathbf{I}_d + t\boldsymbol{\theta})(S))$.

$$\mathcal{J}((\mathbf{I}_d + \boldsymbol{\theta}) S_k) = \mathcal{J}(S_k) - t \int_{\Gamma^S} f^2(\mathbf{s}) ds + o(t^2) \leq \mathcal{J}(S_k), \quad (2.3.14)$$

which guarantees a descent direction.

At this stage, the missing ingredient to solve the state equation (2.3.9), the adjoint state (2.3.10) and eventually compute the shape derivative (2.3.12) is a geometrical representation of domain S . We decide to address this matter using a level set representation, presented in the next section.

2.4 Shape and topology optimisation using a level set method

As mentioned in the introduction of the chapter, since the pioneering publications on shape and topology optimisation using a level set method (see works of Sethian et al. [219], Allaire et al. [13, 14] and Wang et al. [248]), there has been a burst of publications on the topic. The method has proved its effectiveness and robustness in structural optimisation for a great variety of problems, and it has reached a level of maturity which was desirable to exploit in this study. In this section, the basic notions of the level set method are recalled, and its combined use with the shape sensitivity (described in section 2.3) in order to build a shape and topology optimisation method are described.

2.4.1 The level set method

The level set method, developed by Osher and Sethian [188], is a technique for tracking interfaces which are implicitly defined via the zero level set of an auxiliary scalar function ϕ . Beyond the simplicity of the geometric description of a boundary interface, this method offers a very convenient framework for studying the motion of evolving domains over a period of time. Indeed, such a problem can be translated in terms of a partial differential equation for an associated time-dependent level set function $\phi(t)$. In addition, it also allows topological changes to occur in the domain. These aspects are very convenient when it comes to theoretical and numerical studies.

³results expressed in eq. (2.3.3), (2.3.4) and (2.3.12)

Since its appearance, it has been applied in a wide variety of fields, ranging from the computational fluid dynamics, mechanics, structural optimisations [187], to image processing, computer graphics and meshing (interested readers may look at the book of Osher and Fedkiw [186] for an extensive discussion on the topic).

For the sake of simplicity, let us first consider the simple yet fundamental case of a bi-phase composite (the number of phases $N = 2$). Insights to extend the study to multi-phase composites will be provided at the end of the section.

The key idea consists in replacing the usual representation of a domain $S \in \mathbb{R}^d$ by an implicit representation, as the negative sub-domain of an auxiliary scalar function ϕ defined on the whole space \mathbb{R}^d (for practical numerical cases, ϕ will be defined on a large but bounded domain, referred to as working or design domain \mathcal{D}). The function ϕ is sometimes referred to as a level set function for S . More precisely, S is known via a function $\phi : \mathcal{D} \rightarrow \mathbb{R}$ defined in eq. (2.4.1) (see also Fig. 2.5). Let us remark that the choice of a level set function for a given shape S is not unique.

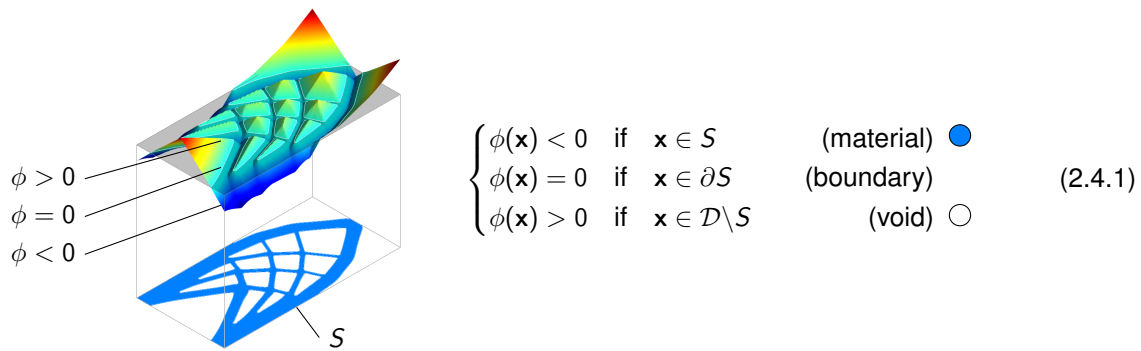


Fig. 2.5: Representation of the shape S in a two-dimensional domain \mathcal{D} : a 3D representation of the level set sliced by the plane $\phi = 0$ projection of the level set on the Cartesian plane (center), characteristic sets defined by the level set, i.e., void and material phases and their reciprocal boundary.

Implicitly-defined domains and geometry. Note that such a function always exists and can be constructed using techniques of partition of unity. Although very different in appearance, the usual and implicit descriptions of a domain are equivalent, and local geometric quantities of the shape S can be expressed in terms of an associated level set function⁴.

For any point $\mathbf{x} \in \partial S$ at which $\nabla \phi(\mathbf{x}) \neq 0$, the unit normal vector $\mathbf{n}(\mathbf{x})$ to ∂S , pointing outward, can be expressed as follows:

$$\mathbf{n}(\mathbf{x}) = \frac{\nabla \phi(\mathbf{x})}{|\nabla \phi(\mathbf{x})|}. \quad (2.4.2)$$

Note that other formulae exist in the same spirit for different geometric quantities (including mean curvature, Gaussian curvature of ∂S , etc.), however these quantities are not required in the sequel and will not be presented here (interested readers may refer to [70] for further details).

Implicit description of the evolution. For a domain $S(t)$ that evolves in the time interval $t = [0, T]$ under a velocity field $\theta(t, \mathbf{x})$, let $\phi(t, \mathbf{x}(t))$ be a time-dependent level set function, such that the boundary of the domain, $\partial S(t)$, is given by the set of points $\mathbf{x}(t)$ satisfying:

$$\phi(t, \mathbf{x}(t)) = 0, \quad \forall t \in [0, T].$$

⁴A detailed explanation is provided in the book of Younes [262], pages 28–29

A simple derivation in time yields:

$$\frac{\partial \phi}{\partial t}(t, \mathbf{x}) + \dot{\mathbf{x}}(t) \cdot \nabla \phi(t, \mathbf{x}) = 0, \quad \forall t, \forall \mathbf{x} \in \partial S(t). \quad (2.4.3)$$

Equation (2.4.3) is a partial differential equation which describes the level set advection of the boundary under a velocity field $\dot{\mathbf{x}}(t)$. Each point $\dot{\mathbf{x}}(t) \in \partial S(t)$ satisfies a Lagrangian type differential equation: $\dot{\mathbf{x}}(t) = \theta(t, \mathbf{x}(t))$. Including this expression in eq. (2.4.3) hence yields:

$$\frac{\partial \phi}{\partial t}(t, \mathbf{x}) + \theta(t, \mathbf{x}(t)) \cdot \nabla \phi(t, \mathbf{x}) = 0, \quad \forall t, \forall \mathbf{x} \in \partial S(t), \quad (2.4.4)$$

which can be extended in the whole computational domain \mathcal{D} , since the same reasoning is valid for any value c of the level set $\phi(t, \mathbf{x}(t)) = c$. If only the normal component of the velocity field is of interest, like in shape optimisation, the advection velocity can be written as:

$$\theta(t, \mathbf{x}) = V(t, \mathbf{x}) \mathbf{n}(t, \mathbf{x}), \quad (2.4.5)$$

where $V(t, \mathbf{x})$ is a velocity scalar field, whereas $\mathbf{n}(t, \mathbf{x})$ is the unit normal vector, defined in eq. (2.4.2). Then, eq. (2.4.4) takes the form of a *Hamilton-Jacobi equation*:

$$\frac{\partial \phi}{\partial t}(t, \mathbf{x}) + V(t, \mathbf{x}) |\nabla \phi(t, \mathbf{x})| = 0, \quad \forall t, \forall \mathbf{x} \in \mathcal{D}. \quad (2.4.6)$$

The method used to solve equation (2.4.6) depends on the discretisation of the level set function.

- A rather common choice is to mesh the domain \mathcal{D} once and for all using a structured grid and utilize finite difference schemes to approximate the differential operators. This is for instance the method that was selected in the study of chapter 3. A robust, explicit, second-order scheme developed by Osher and Sethian [188] has been used to solve (2.4.6) under a CFL⁵ condition for the time step.
- Another choice is to use an unstructured mesh and possibly also adjust it so that the zero level set is explicitly discretised [43]. This method is much more complex from a point of view of numerical implementation, however it presents at the same time many benefits compared to the classical one, especially in problems where the knowledge of the exact position of the boundary plays an important role. For such a method, other schemes have been developed, based mainly on the method of characteristics. We address the interested reader to [43, 71] and to the references therein for more information about the level set method using unstructured meshes. In chapter 7, we solve (2.4.6), relying on the `advect` package, developed by Bui, Dapogny and Frey (refer also to their associated article [43]), which is based upon the method of characteristics.

Initialising level set functions: signed-distance function. Up to this point, the level set function was introduced as a generic function, without giving any specific information about it: in fact, many level set functions can be associated to a domain $\mathcal{D} \subset \mathbb{R}^d$. Yet, it is well-known since the early hours of the level set method [63, 188] that during evolution, the level set function may become too steep or flat, even if it starts from a smooth initialisation. This in turn may cause instabilities in locating accurately ∂S , or difficulties in the computation of the normal vector or curvatures of ∂S by means of formulae such as (2.4.2) (also see [186]). A way to guarantee the level sets' smoothness is to reinitialize it periodically as the signed distance function to the domain S .

⁵Courant–Friedrichs–Lewy

The signed distance function to S is the function $\mathbb{R}^d \ni \mathbf{x} \mapsto d_S(\mathbf{x})$ defined by :

$$\forall \mathbf{x} \in \mathbb{R}^d, d_S(\mathbf{x}) = \begin{cases} -d(\mathbf{x}, \partial S) & \text{if } \mathbf{x} \in \mathcal{D} \setminus S, \\ 0 & \text{if } \mathbf{x} \in \partial S, \\ d(\mathbf{x}, \partial S) & \text{if } \mathbf{x} \in S. \end{cases} \quad (2.4.7)$$

This signed distance function has furthermore the interesting property of being smooth near ∂S , provided ∂S is a smooth boundary.

When it comes to constructing the signed distance function from a pre-defined boundary domain or level set function, there exist mainly two types of approaches⁶, both of them being based on an approximation of the solution of the Eikonal equation (see Equation (2.4.8)). The first one consists in treating this equation as a stationary boundary value problem, starting from the knowledge of the distance in the elements of the computational grid or mesh which are close to the interface ∂S , and propagating the information throughout the whole domain. The most popular of them are the Fast-Marching method [218] and the Fast-Sweeping method [265]. Another way of addressing the problem is to consider it as an unsteady problem and then to devise a propagation method for extending the signed distance field from the boundary of S [229].

In the next chapter, the second method was preferred to redistance the level set. In chapter 3, we redistanced the level set function ϕ using an in-house programming in `FreeFem++` by solving a partial differential equation, as proposed in [186]. Since d_S satisfies the Eikonal equation:

$$|\nabla d_S| = 1 \quad \text{almost everywhere in } \mathcal{D}. \quad (2.4.8)$$

starting from an initial level set function $\phi^0(\mathbf{x})$, d_S can be obtained as the stationary solution of the following partial differential equation:

$$\begin{cases} \frac{\partial \phi}{\partial t} + \text{sign}(\phi^0) |\nabla \phi| = \text{sign}(\phi^0), & \forall t, \forall \mathbf{x} \in \mathcal{D}, \\ \phi(0, \mathbf{x}) = \phi^0. \end{cases} \quad (2.4.9)$$

using the same numerical scheme as for the advection equation (2.4.6). In chapter 7, we utilise the package `mshdist` developed by Pascal Frey and Charles Dapogny [71].

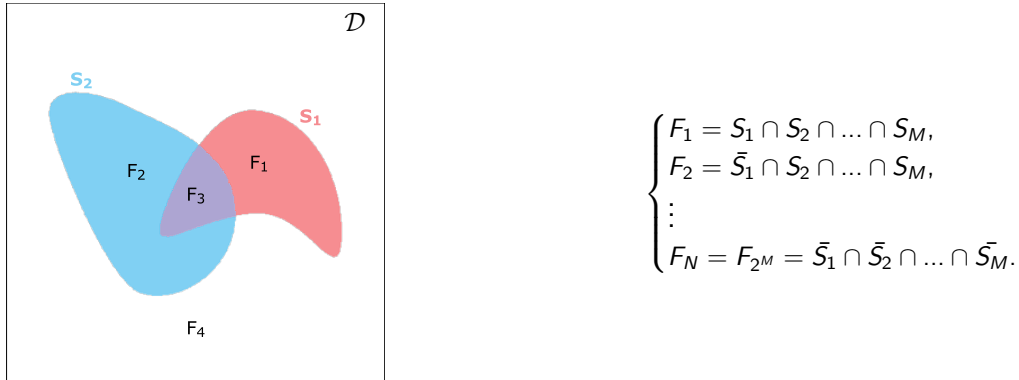


Fig. 2.6: Representation of different material in the unit cell for $d = 2$.

Extension to a multi-phase composite with N sub-domains. In this work, we have only explored the simple yet fundamental case of a bi-phase composite (the number of phases $N = 2$). In this case, a single level set ϕ is required to characterise \mathcal{D} as shown in Fig. 2.5. The present work

⁶Interested reader may refer to the monograph of Osher and Fedkiw [186] for a detailed presentation on structured grids; To Dapogny and Frey [71] and to the references therein for unstructured meshes.

however may be simply extended to investigate multi-phase composites with $N > 2$ sub-domains. In a general framework, the design domain \mathcal{D} is then divided into several sub-domains. The part of \mathcal{D} occupied by the phase α is denoted F_α . We can then introduce a series of level set functions $\phi_\gamma, \gamma \in \llbracket 1, M \rrbracket$ and define corresponding shapes S_γ associated to the part where the ϕ_γ is negative. Combining the various level set functions enables to treat up to $N = 2^M$ distinct phases $F_\alpha, \alpha \in \llbracket 1, 2^M \rrbracket$ as illustrated in Fig. 2.6.

The problem of the shape evolution looks exactly like the one of eq. (2.4.6), however it expressed as a system of N level set functions. More information dealing with multi-phase composites (where $N > 2$) can be found in the works of Wang et al. [249], and more recently in Allaire et al. [15, 165], Nika and Constantinescu [181].

2.4.2 Coupling shape sensitivity with a level set description

In section 2.3 we have calculated a shape derivative and extracted a vector field that indicates how to change the shape in a way that reduces some cost functional and in section 2.4.1 we have presented the basic elements of the level set method for the description of an interface that evolves in time under a velocity field: $\theta(t, \mathbf{x}) = V(t, \mathbf{x}) \mathbf{n}(t, \mathbf{x})$. What remains is to combine these two notions by taking an advection field proportional to the shape gradient and construct a method that is able to optimize at the same time the shape and the topology of the structure. It simply comes down to interpret the shape gradient calculated via shape sensitivity analysis as an advection velocity for a level set function that describes the shape.

Ersatz material. Using the so-called ‘‘ersatz material’’ approach, the state equation (2.3.6) is extended to the whole domain \mathcal{D} . To do this, the holes $\bar{S} = \mathcal{D} \setminus S$ are filled by a weak phase that mimics the void, but at the same time avoids the singularity of the rigidity matrix. One possible method consists in defining an elasticity tensor $C(\mathbf{x})$ which is a mixture of C^S in S and of the weak material mimicking holes in $\mathcal{D} \setminus S$.

$$C(\mathbf{x}) = C^S (1 + \text{sign}^+(\phi)(\mathbf{x}) (\epsilon - 1)) \quad (2.4.10)$$

where ϵ is a small parameter, set to 10^{-4} in this work. The displacement \mathbf{u} of eq. (2.3.6) is finally computed as the solution of the problem:

$$\begin{cases} \frac{\partial \sigma_{ij}}{\partial x_j} + f_i = 0 & \text{in } \mathcal{D}, \\ \sigma_{ij} = C_{ijkl}(\mathbf{x}) \varepsilon_{kl}(\mathbf{u}) & \text{in } \mathcal{D}, \\ u_i = 0 & \text{on } \Gamma^u, \\ \sigma_{ij} n_j = t_i & \text{on } \Gamma^t. \end{cases} \quad (2.4.11)$$

(n_j denotes the external normal of Γ^t)

Extension and regularisation of the velocity field and descent direction. The shape sensitivity analysis provides a shape gradient defined only on the boundary of the domain Γ^S . For a level set function defined on a fixed grid, the boundary is not explicitly discretised. We could assume that the normal velocity V is defined for the nodes of the elements that are crossed by the zero level set. Then, one possibility is to consider $V = 0, \forall \mathbf{x} \in \mathcal{D} \setminus \Gamma^S$. Unfortunately, this choice would limit the movement of the boundary to small distance, which would result in an increased number of iterations until convergence, and thus a slower algorithm. A remedy to this inconvenience is to extend the velocity field in all the domain. At the same time, it would be numerically beneficial to smooth a bit the shape gradient, but in a way that guarantees the descent nature of the new advection velocity. The sequel describes one way to combine these two requirements. Initially, the shape derivative has the form:

$$\mathcal{J}'(S)(\theta) = \int_{\Gamma^S} \theta_r n_r f(\mathbf{s}) ds$$

or, for an advection velocity of the type $\theta(\mathbf{s}) = V(\mathbf{s}) \mathbf{n}(\mathbf{s})$, we have:

$$\mathcal{J}'(S)(V\mathbf{n}) = \int_{\Gamma^S} V(\mathbf{s}) f(\mathbf{s}) ds.$$

Instead of choosing $V(\mathbf{s}) = -f(\mathbf{s})$, the extended velocity $V(\mathbf{x})$ in the Hamilton–Jacobi equation (2.4.6) is chosen as the unique solution to the following problem expressed in its variational formulation:

$$\int_{\mathcal{D}} (\alpha^2 \nabla V(\mathbf{x}) \cdot \nabla W(\mathbf{x}) + V(\mathbf{x}) W(\mathbf{x})) d\mathbf{x} = \int_{\Gamma^S} W(\mathbf{s}) f(\mathbf{s}) ds \quad \forall W \in H^1(\mathcal{D}), \quad (2.4.12)$$

where $\alpha \in \mathbb{R}^{+*}$ is a small positive scalar (of the order of the mesh size) to control the regularisation width and take $W = -V$. This operation reveals that:

$$\mathcal{J}'(S)(V\mathbf{n}) = - \int_{\mathcal{D}} (\alpha^2 |\nabla V|^2 + V^2) d\mathbf{x} \quad (2.4.13)$$

which guarantees again a descent direction for \mathcal{J} . Interested readers may refer to the works of de Gournay [73] for a discussion over the importance of this procedure in the context of shape optimisation.

2.4.3 Numerical algorithm

We recall that the information given from the shape gradient is local, i.e., it refers to a neighbourhood around the current shape. Therefore, an iterative algorithm needs to be constructed so as to minimise progressively the cost functional. Using a simple steepest descent algorithm, which guarantees the decrease of the cost functional at each time step, the optimisation algorithm has the following structure:

Data: Initialise a level set function ϕ_0 corresponding to an initial shape S^0 ;

for $k \geq 0$ *iterate until convergence do*

 Redistance ϕ_k into the signed distance function d_{S^k} using eq. (2.4.9);

 Compute \mathbf{u}_k and \mathbf{p}_k , solutions of the state (2.3.9) and adjoint (2.3.10) equations for the domain S^k ;

 Compute the shape gradient $\mathcal{J}(S^k)(\theta^k)$ for the domain S^k using eq. (2.4.13);

 Deform the domain S^k by solving the Hamilton-Jacobi equation (2.4.6);

 // Shape S^{k+1} is characterised by the level set ϕ_{k+1} after a time step Δt_k

 // The time step Δt_k is chosen so that $\mathcal{J}(S^{k+1}) \leq \mathcal{J}(S^k)$

end

Algorithm 1: Major steps of a topology optimisation algorithm, adapted from the work of Allaire, Jouve and Toader [14].

Stopping criteria. Several convergence criteria can be adopted, which usually test the decrease in the objective function and the total advection time, i.e., the algorithm terminates when $|\mathcal{J}(S_{k+1}) - \mathcal{J}(S_k)| < \epsilon_k$ and $\Delta t_k < t_{\text{im}}$, where ϵ_k and t_{im} are user defined scalar parameters. Since their choice is not a priori obvious, it is also common practise to set a computational cost criterion in terms of total number of iterations.

Sensitivity to initial guesses. As we already mentioned in the previous section, it is well known that problems of designing optimal microstructures do not possess a global minimum [9]. As a result initial starting shapes/guesses ϕ_0 have a considerable effect on the final design of the micro-structure. Furthermore, they may lead the algorithm towards non-physical shapes (e.g., disconnected materials island in a void matrix), or to shapes representing local minima, yet very

far from the target. In this case, we can always restart the algorithm, either using different initial guesses or using a different set of algorithmic parameters (like a different time step Δt_k , different penalisation parameter etc.). Additionally, we can start the algorithm with an initial shape that is a known local minimum from the literature, in which case the algorithm converges very fast (this is a test typically undertaken to assess the relevance of the code).

In order to discuss the influence of the initial design of the material cell on the optimised solution, several kinds of initial designs may be tested. Initial designs are generally a combination patterns with various micro-perforations.

Discussion on topological changes. Let us further note, that even though the notion of shape derivative (or more precisely the Hadamard's method for shape variations) does not permit nucleations, the level set method can naturally combine two adjacent "holes" into one by breaking the "barrier" between them, thus effectively changing the topology of the structure. This is why in practice, it is desirable to start with an initial guess that contains a large number of nucleations [14, 248]. However, as explained in [165], the topological change may induce an increase of the objective function \mathcal{J} , which we allow (up to a small tolerance) in the hope that afterwards the algorithm will locate a better shape. In practice, since most changes of topology occur in the first few iterations, the tolerance for accepting increases of the objective function \mathcal{J} is defined at the k^{th} iteration as:

$$\mathcal{J}(S^{k+1}) < \mathcal{J}(S^k)(1 + \eta_{\text{tol}} \exp(-0.1k)), \quad (2.4.14)$$

where η_{tol} is a parameter set to a small value ($\eta_{\text{tol}} = 0.05$ in our scripts). The decreasing exponential reduces the tolerance over the iterations: until iteration 16, an increase by $1.e-2$ is accepted, while after 40 iterations, an increase by $1.e-3$ is no longer accepted.

Difficulty of a sharp interface formulation in a fixed mesh framework. The essential ingredients that must be considered in the calculation of the shape derivative of a problem such as eq. (2.4.11) are the transmission conditions and the differentiability of the displacement \mathbf{u} with respect to the interface Γ_S . Furthermore, when a numerical implementation is sought, an additional element must be taken into account: the way in which the transmission conditions (continuity of the displacement and continuity of the normal stress across the interface) are interpreted by finite element methods in a fixed mesh framework.

In general these methods either partially preserve the transmission conditions (e.g., classical Lagrange finite elements method) or exactly preserve the transmission conditions (e.g., extended finite elements X-FEM [227], adapted interface meshing [43], etc.).

2.4.4 Formulation in the smooth inter-phase context

To tackle the preceding problem, let us now present a specific approach, which can be coined as smooth or diffuse inter-phase approach. This approach is a mathematically convenient approximation of the sharp-interface problem, which permits to bypass with the complications induced at the interface. More precisely, the interface Γ_S between S and \bar{S} is modelled as a thin layer of (small) width $2e > 0$ rather than as a sharp interface. In this context, we rely on the notion of signed distance function (2.4.7) for the level set method.

The results in this section are just reported from the works of Michailidis et al. [15, 165], where the signed distance function was used for the formulation of multi-phase problems. Following their idea, the level set function serves as a base to define the local stiffness tensor $C(\mathbf{x})$ in \mathcal{D} as a interpolation between the strong phase and the weak phase with a smooth Heaviside type of

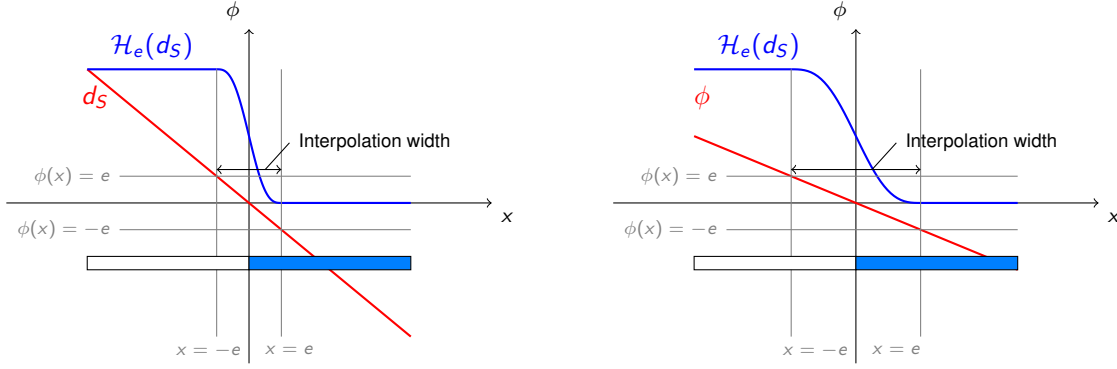


Fig. 2.7: intermediate zone for regularisation with the signed distance function (left). In the case where the level set function becomes flat (right), the inter-phase can become too large.

function, defined as follows (see also Fig. 2.7):

$$\mathcal{H}_e(t) = \begin{cases} 0 & \text{if } t < -e, \\ \frac{1}{2} \left(1 + \frac{t}{e} + \frac{1}{\pi} \sin\left(\frac{\pi t}{e}\right) \right) & \text{if } |t| \leq e, \\ 1 & \text{if } t > e. \end{cases} \quad (2.4.15)$$

This choice of the regularising function above is not unique: it is possible to use other type of regularising functions (see [249] for instance). Hence, the properties of the material occupying the domain \mathcal{D} are then defined as a smooth interpolation between the tensors C^S and $C^{\bar{S}} = \epsilon C^S$.

$$C^e(\mathbf{x}) = \mathcal{H}_e(\phi(\mathbf{x}))(C^{\bar{S}} - C^S) + C^S = C^S (1 + \mathcal{H}_e(\phi(\mathbf{x}))(\epsilon - 1)) \quad (2.4.16)$$

The description provided in the above equation replaces the the one in eq. (2.4.10). A serious problem arising directly from this choice, is that the interpolation zone, where $C^e(\mathbf{x})$ takes intermediate values between C^S and $C^{\bar{S}}$, can thicken or slim down during the optimisation process, depending on the slope of level set function (an illustration of this effect is provided in Fig. 2.7). In order to control this interval over time, it is therefore essential to re-initialise the level set function into the signed distance function d_S introduced in eq. (2.4.7) at each iteration.

The elasticity problem (2.4.11) now reads:

$$\begin{cases} \frac{\partial \sigma_{ij}}{\partial x_j} + f_i = 0 & \text{in } \mathcal{D}, \\ \sigma_{ij} = C_{ijkl}^e(\mathbf{x}) \varepsilon_{kl}(\mathbf{u}) & \text{in } \mathcal{D}, \\ u_i = 0 & \text{on } \Gamma^u, \\ \sigma_{ij} n_j = t_i & \text{on } \Gamma^t. \quad (n_j \text{ denotes the external normal of } \Gamma^t) \end{cases} \quad (2.4.17)$$

We now differentiate the cost functional $\mathcal{J}(S)$ expressed in eq. (2.3.5) with respect to the domain, using once again the formal Lagrangian method discussed above. To this end, we introduce a Lagrangian $\mathcal{L}(S, \mathbf{v}, \mathbf{q})$, whose stationarity provides the optimality conditions for the minimisation problem. At $\theta = \mathbf{0}$, cancelling the partial derivative of \mathcal{L} with respect to \mathbf{q} yields the variational formulation of the state \mathbf{u} . In the same way, by setting the partial derivative of \mathcal{L} with respect to \mathbf{v} equal to 0 leads to the variational formulation of the adjoint \mathbf{p} . Eventually, the shape derivative of the objective function is the partial derivative of \mathcal{L} with respect to θ , evaluated at \mathbf{u} and \mathbf{p} . This

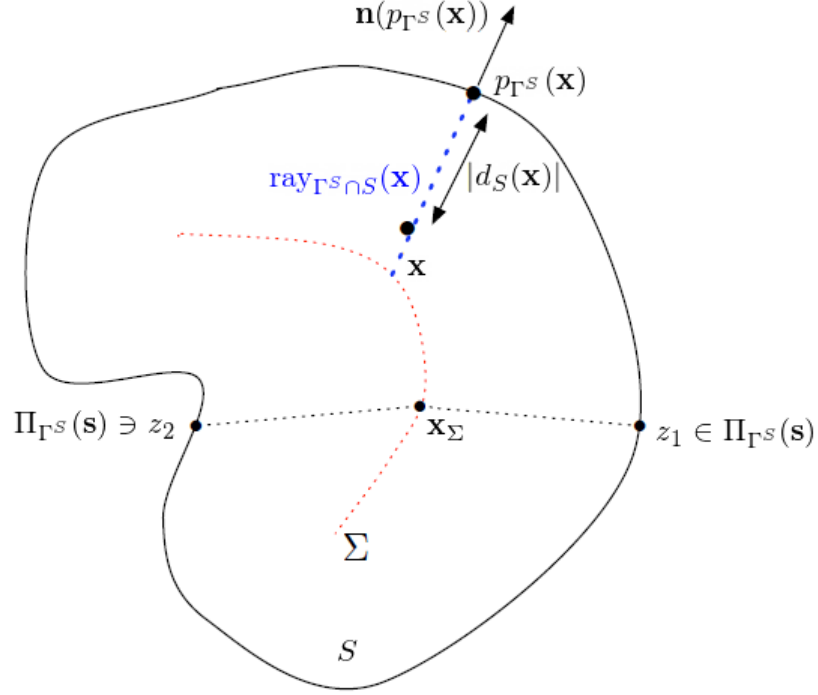


Fig. 2.8: for a point \mathbf{x} lying outside the skeleton Σ of Ω , unique projection point $p_{\Gamma^S}(\mathbf{x})$ and line segment $\text{ray}_{\Gamma^S \cap S}(\mathbf{x})$. For a point $\mathbf{x}_\Sigma \in \Sigma$, at least two points z_1, z_2 belong to the set of projections $\Pi_{\Gamma^S}(\mathbf{x}_\Sigma)$. Figure adapted from [15].

reads:

$$\begin{aligned} \mathcal{J}'(S)(\theta) &= \int_{\mathcal{D}} (C_{ijkl})'(\theta) \varepsilon_{kl}(\mathbf{u}) \varepsilon_{ij}(\mathbf{p}) \, d\mathbf{x} \\ \mathcal{J}'(S)(\theta) &= \int_{\mathcal{D}} \mathcal{H}'_e(d_S) d'_S(\theta) \left(C_{ijkl}^{\bar{S}} - C_{ijkl}^S \right) \varepsilon_{kl}(\mathbf{u}) \varepsilon_{ij}(\mathbf{p}) \, d\mathbf{x}, \end{aligned} \quad (2.4.18)$$

where $(C_{ijkl})'(\theta)$ is the directional shape derivative of $C_{ijkl}(S)$, $d'_S(\theta)$ is the directional shape derivative of the signed distance function, while $\mathcal{H}'_e(d_S)$ is the standard derivative of the real smooth Heaviside \mathcal{H}_e defined in eq. (2.4.15). To compute this terms properly, we recall a few basic information on the signed distance function and explore its shape differentiability, which holds in a non-classical and subtle sense. Starting from a regular domain $S \subset \mathcal{D}$, let us consider shape variations in the sense of Hadamard exactly as described in section 2.3.

Shape differentiability of the signed distance function. Unfortunately, the signed distance function is not, strictly speaking, shape differentiable in the sense of Equation (2.3.1). One reason is the lack of smoothness of the gradient of d_S at the skeleton Σ . However, its point-wise values $d_S(\mathbf{x})$ are shape differentiable for $\mathbf{x} \in \mathcal{D} \setminus \Sigma$. This is the purpose of the next results which can be found in [70] for detailed and complete proofs.

Assume $S \subset \mathcal{D}$ is an open set of class \mathcal{C}^1 , and fix a point $\mathbf{x} \notin \Sigma$. Then $d_S(\theta(\mathbf{x}))$ is Gateaux-differentiable (i.e. admits a directional derivative) at $\theta = \mathbf{0}$, as an application from $W^{1,\infty}(\mathcal{D}, \mathbb{R}^d)$ into \mathbb{R} , and its derivative is:

$$d'_S(\theta)(\mathbf{x}) = -\theta(p_{\Gamma^S}(\mathbf{x})) \cdot \mathbf{n}(p_{\Gamma^S}(\mathbf{x})), \quad (2.4.19)$$

where $p_{\Gamma^S}(\mathbf{y})$ is the projection of \mathbf{x} onto Γ^S .

Another main result is required to handle integral functions of the signed distance function and is provided in [15], section 2.3. It makes use of the coarea formula (recalled for instance in the book

of Delfour and Zolésio, Chapter 5, page 251 [75]). If φ is an integrable function over \mathcal{D} , then:

$$\int_{\mathcal{D}} \varphi(\mathbf{x}) d\mathbf{x} = \int_{\Gamma_S} \left(\int_{\text{ray}_{\partial S(\mathbf{s})} \cap \mathcal{D}} \varphi(\mathbf{z}) \prod_{h=1}^{d-1} (1 + d_S(\mathbf{z}) \kappa_h(\mathbf{s})) d\mathbf{z} \right) d\mathbf{s}, \quad (2.4.20)$$

where κ_i denotes the principal curvatures of Γ_S (refer to Fig. 2.8 for a geometric illustration).

Application to the shape derivation of the cost functional eq. (2.3.5). Starting from the expression in eq. (2.4.18) and replacing $d_S(\boldsymbol{\theta}(\mathbf{x}))$ by its expression (2.4.19) yields:

$$\mathcal{J}'(S)(\boldsymbol{\theta}) = - \int_{\mathcal{D}} \mathcal{H}'_e(d_S) \theta_r(p_{\Gamma^S}(\mathbf{x})) n_r(p_{\Gamma^S}(\mathbf{x})) \left(C_{ijkl}^{\bar{S}} - C_{ijkl}^S \right) \varepsilon_{kl}(\mathbf{u}) \varepsilon_{ij}(\mathbf{p}) d\mathbf{x}.$$

It remains to transform this expression by the coarea formula in order to deduce a boundary integral. Using formula (2.4.20) gives:

$$\begin{aligned} \mathcal{J}'(S)(\boldsymbol{\theta}) = & - \int_{\Gamma^S} \theta_r(\mathbf{s}) n_r(\mathbf{s}) \left(\int_{\text{ray}_{\Gamma^S(\mathbf{s})} \cap \mathcal{D}} \mathcal{H}'_e(d_S) \right. \\ & \left. \left(C_{ijkl}^{\bar{S}} - C_{ijkl}^S \right) \varepsilon_{kl}(\mathbf{u}) \varepsilon_{ij}(\mathbf{p}) \prod_{h=1}^{d-1} (1 + d_S(\mathbf{z}) \kappa_h(\mathbf{s})) d\mathbf{z} \right) d\mathbf{s}. \end{aligned}$$

The above integral may be decomposed over S and \bar{S} . We can rewrite the expression as follows.

$$\mathcal{J}'(S)(\boldsymbol{\theta}) = - \int_{\Gamma^S} \boldsymbol{\theta}(\mathbf{s}) \mathbf{n}(\mathbf{s}) (f_S(\mathbf{s}) + f_{\bar{S}}(\mathbf{s})) d\mathbf{s} \quad (2.4.21)$$

where $f_S(\mathbf{s})$ and $f_{\bar{S}}(\mathbf{s})$ are defined by:

$$\begin{cases} f_S(\mathbf{s}) = \int_{\text{ray}_{\Gamma^S(\mathbf{s})} \cap S} \mathcal{H}'_e(d_S) \left(C_{ijkl}^{\bar{S}} - C_{ijkl}^S \right) \varepsilon_{kl}(\mathbf{u}) \varepsilon_{ij}(\mathbf{p}) \prod_{h=1}^{d-1} (1 + d_S(\mathbf{z}) \kappa_h(\mathbf{s})) d\mathbf{z}, \\ f_{\bar{S}}(\mathbf{s}) = \int_{\text{ray}_{\Gamma^S(\mathbf{s})} \cap \bar{S}} \mathcal{H}'_e(d_S) \left(C_{ijkl}^{\bar{S}} - C_{ijkl}^S \right) \varepsilon_{kl}(\mathbf{u}) \varepsilon_{ij}(\mathbf{p}) \prod_{h=1}^{d-1} (1 + d_S(\mathbf{z}) \kappa_h(\mathbf{s})) d\mathbf{z}. \end{cases}$$

This last equation provides a simple way of choosing a descent direction for a shape gradient based algorithm. Indeed it is enough to perturb the interface Γ^S by choosing the vector field:

$$\boldsymbol{\theta}(\mathbf{x}) = (f_S(\mathbf{x}) + f_{\bar{S}}(\mathbf{x})) \mathbf{n}(\mathbf{x}), \quad (2.4.22)$$

which ensures that the directional derivative in eq. (2.4.21) is negative and thus yields a decrease of the objective function (see eq. (2.3.5)). Then, we obtain:

$$\mathcal{J}'(S)(\boldsymbol{\theta}) = - \int_{\Gamma^S} (f_S(\mathbf{s}) + f_{\bar{S}}(\mathbf{s}))^2 d\mathbf{s} < 0. \quad (2.4.23)$$

Part II

Design of 3D printable architected sheet materials

Chapter 3

Computational design of periodic architected sheets exhibiting a negative Poisson's ratio

Contents

3.1	Introduction	69
3.2	Computational design	71
3.2.1	Material distribution using a smooth inter-phase approach	71
3.2.2	Optimisation problem	72
3.2.3	Shape derivative in the smooth inter-phase context	72
3.2.4	Approximate formula for the shape derivative	74
3.2.5	Shape derivative of the volume constraint	75
3.2.6	Extension and regularisation of the velocity field and descent direction	76
3.3	Numerical algorithm	76
3.4	Examples of obtained microstructures	77
3.4.1	Example 1	78
3.4.2	Example 2	79
3.4.3	Example 3	80
3.4.4	Example 4	80
3.5	Conclusion and perspectives	81
3.5.1	Conclusion	81
3.5.2	Possible future works	81

Topology optimisation via a level set method (section 2.4) and asymptotic homogenisation (section 1.2) permit to design periodic micro-architected materials with a prescribed effective elasticity tensor and Poisson's ratio. The space of admissible micro-architectural shapes that carries orthotropic material symmetry allows to attain shapes with an effective Poisson's ratio below -1 (section 1.3).

3.1 Introduction

The Poisson's ratio (ν) is a measure of the relative amount a given material contracts transversally under a uniaxial stretch loading [102]. Unlike most conventional materials, *auxetic materials* tend to expand transversely to an applied uniaxial stretch load and vice versa, leading to a so-called negative Poisson's ratio. This effect is obtained from microstructural deformation mechanisms that typically involve rotations [83, 142]. Auxetic materials with tailored micro-architecture can display

superior mechanical properties [212], including enhanced stiffness and energy absorption capabilities [122, 150], indentation resistance [145], greater fracture toughness [61], crashworthiness [119], phononic performance [226] as well as many other interesting properties. As such, these materials have attracted increasing interest for technological applications in a wide range of fields, from stretchable electronics, medical and biomedical engineering [7, 127, 129, 148, 251], to the sport equipment and textile industries [78, 90, 134, 192, 253].

Since the seminal works performed in the '80s, the design of periodic auxetic structures has attracted research interests and several types of auxetic materials have been introduced. In 1985, Almgren introduced a re-entrant honeycomb structure with Poisson's ratio of -1 using rods, hinges, and springs [17]. The re-entrant honeycomb structure was also introduced as a "bi-mode" extremal material which supports a stress with a negative determinant in the monograph of Milton and Cherkaev [168]. Conceptual designs of composite materials with Poisson's ratio approaching -1 were presented in the works of Milton [166]. Some important features of auxetic materials, such as the re-entrant corners, were discussed in the key works of Lakes [141, 143], Friis et al. [93] and Evans [82]. A new class of auxetic materials, that obtain their auxetic behaviour from the *rotating squares* mechanism were introduced in the works of Grima et al. [103, 104]. Moreover, a separate class of auxetics with a 2D-extruded design that exploits the buckling mechanism in structures was proposed in the works of Bertoldi et al. [35].

Design techniques using modern numerical methods such as shape and topology optimisation [13, 32] arose as a natural way to tailor mechanical properties through a design of complex geometries. For materials with a periodic micro-architecture, the effective elastic properties can be derived by means of asymptotic homogenisation, with periodic boundary conditions applied on a unit cell and the associated boundary value problem resolved [210] (see Chapter 1). The works of Sigmund presented a topology optimisation framework for designing 2D and stacked 2D auxetic truss-based structures [222] and for a designing 2D continuum-based micro-mechanism with negative Poisson's ratio [146]. Since these works, different techniques have been adopted for auxetic structure design optimisation, including the SIMP¹, phase-field, level set methods, etc. (refer to the discussion in Section 2.2). In the works of Wang et al. [68, 247], the SIMP method was used to include geometrical non-linearities and to tackle manufacturing constraints. The resulting architectures attain the desired response through uniform features, like the thickness of connecting rods. In more recent developments, the method is extended to thermodynamic topology optimisation or graded materials [49, 126]. Furthermore, alternative optimisation methods as found in the works of Wang, Mei and Wang [249], Vogiatzis et al. [244], Nika and Constantinescu [181], Wang et al. [250], among others, use asymptotic homogenisation, the level set method and the Hadamard's shape derivative to identify material regions and track boundary changes to systematically design auxetic shapes. Wang, Mei and Wang [249], design linear elastic and thermoelastic materials with negative Poisson's ratio, while Nika and Constantinescu [181] design linear elastic multi-materials with negative Poisson's ratio.

The classical theory of elasticity states that isotropic three-dimensional materials may exhibit Poisson's ratios bounded in $[-1, 0.5]$; Two-dimensional isotropic systems can exhibit Poisson's ratios bounded in $[-1, 1]$. The effective elastic tensor that characterises the auxetic material however has a priori orthotropic symmetry. In two-dimensional systems, the effective elastic stiffness is characterised by two Poisson's ratios ν_{12} , ν_{21} , which are a priori not bounded, hence they can assume any positive or negative values in certain directions [237]. For instance, Poisson's ratios smaller than -1 have been reported according to Lakes [143]. In the topology optimisation literature, most of the 2D-extruded auxetic shapes obtained tend to exhibit a quadratic symmetry, i.e., $\nu_{12} = \nu_{21}$. However, as was already mentioned, this need not be the case.

The aim of this chapter is to complete a design cycle for several auxetic materials. We combine topology optimisation with the level set method and the asymptotic homogenisation to systematically obtain the micro-architecture. The discussion is organised as follows. Section 3.2 presents the computational design of the micro-architected material. It sets up the optimisation problem

¹Solid Isotropic Material with Penalisation

to systematically identify optimal auxetic shapes. Section 3.3 draws up the numerical algorithm and addresses certain algorithmic issues that arise. Section 3.4 introduces the optimal auxetic micro-architectures obtained and describes some of their properties. A short summary and additional remarks in Section 3.5 conclude the chapter.

3.2 Computational design

The considered micro-architected materials are two-dimensional periodic assemblies of square unit cells. The unit cells are a bi-phase composite with a strong and weak phase, e.g., polymer material and void respectively.

The notation used in the previous chapters are maintained. Let $Y = [0, 1]^2$ denote the rescaled two-dimensional unit cell. For the optimisation, Y represents the working (or design) domain. Consider two sub-domains labelled $(S, \bar{S}) \subset Y$ that are smooth, open, bounded subsets, corresponding to the strong and the weak phase. In the sequel, the word *shape* will denote the strong phase S of the micro-architected unit cell, e.g., polymer phase of the composite. Last, the interface between two phases S and \bar{S} is denoted by Γ^S . The material properties in Y are represented by a periodic fourth order tensor $C(\mathbf{y})$, which carries the usual symmetries and positive definiteness defined in chapter 1, see eq. (1.2.1)–(1.2.2).

The strong phase of the micro-architected unit cell, i.e., the shape S is represented by a real-valued auxiliary level set function ϕ . As discussed in section 2.4, the principle of the level set method is to implicitly define the interface of a shape via the zero level set of the function ϕ (see eq. (3.2.1) and Fig. 3.1).

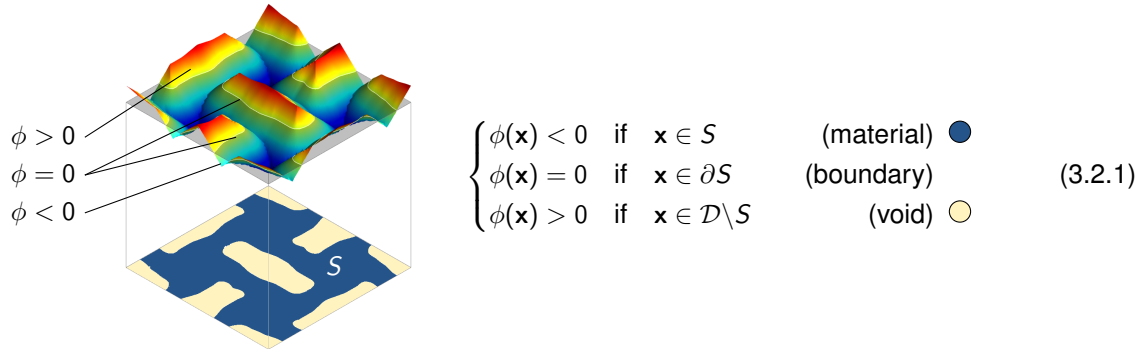


Fig. 3.1: Representation of the shape in a two-dimensional unit cell: a 3D representation of the level set sliced by the plane $\phi = 0$ projection of the level set on the Cartesian plane (center), characteristic sets defined by the level set, i.e., void and material phases and their reciprocal boundary.

3.2.1 Material distribution using a smooth inter-phase approach

The distribution of $C(\mathbf{y})$ inside the unit cell Y is based upon an specific approach, which can be coined as smoothed or diffuse interphase approach. This approach offers some advantages: either for a mathematical approximation or for physical reasons, it may be desirable to model the interface Γ^S between S and \bar{S} as a thin layer of (small) width $2e > 0$ rather than as a sharp interface. In this context, we rely on the notion of signed distance function expressed in eq. (2.4.7). Following the idea of Allaire et al. [15] (see also [165]), the properties of the material occupying the unit cell Y are then defined as a smooth interpolation between the tensors C^S and $C^{\bar{S}}$.

$$C^e(\mathbf{y}) = \mathcal{H}_e(\phi(\mathbf{y}))(C^{\bar{S}} - C^S) + C^S, \quad (3.2.2)$$

where $\mathcal{H}_e(\phi)$ is a smooth Heaviside type of function defined in eq. (2.4.15). To maintain a precise

control on the smoothness of \mathcal{H}_e , it is desirable to select the signed distance function d_S as a level set function. A number of practical aspects arising from this choice are examined in section 2.4.4.

3.2.2 Optimisation problem

Define the objective function $\mathcal{J}(S)$:

$$\mathcal{J}(S) = v_{ijkl} C_{ijkl}^* + \frac{1}{2} \eta_{ijkl} \left(C_{ijkl}^* - C_{ijkl}^{\text{target}} \right)^2, \quad (3.2.3)$$

where C_{ijkl}^* are the effective elastic coefficients of the structure (1.2.29) defined in Section 1.2, C_{ijkl}^{target} are the prescribed elastic values, while v_{ijkl} and η_{ijkl} are the weight coefficients, which exhibit the same symmetries as the elastic coefficients. Replacing the effective elastic coefficients by their expression yields the following expression for the objective function:

$$\begin{aligned} \mathcal{J}(S) = & \frac{v_{ijkl}}{|Y|} \int_Y C_{mnpq} \left(\delta_{pk} \delta_{ql} + \varepsilon_{ypq}(\mathbf{w}^{k\ell}) \right) \left(\delta_{mi} \delta_{nj} + \varepsilon_{ymn}(\mathbf{w}^{ij}) \right) dy \\ & + \frac{\eta_{ijkl}}{2} \left(\left[\frac{1}{|Y|} \int_Y C_{mnpq} \left(\delta_{pk} \delta_{ql} + \varepsilon_{ypq}(\mathbf{w}^{k\ell}) \right) \left(\delta_{mi} \delta_{nj} + \varepsilon_{ymn}(\mathbf{w}^{ij}) \right) dy \right] - C_{ijkl}^{\text{target}} \right)^2, \end{aligned}$$

where $\mathbf{w}^{k\ell} \in \tilde{\mathcal{V}}(Y) := \{\mathbf{v} \in H_{\text{per}}^1(Y) \mid \langle v_i \rangle_Y = 0\}$ is the solution of the cell problem introduced in (1.2.28). In addition, let \mathcal{U}_{ad} define the set of admissible shapes contained in the working domain Y with a prescribed volume expressed by:

$$\mathcal{U}_{ad} := \{S \subset Y \text{ is open, bounded, and smooth} \mid \rho_m \leq |S| \leq \rho_M\}, \quad (3.2.4)$$

where $|S|$ corresponds to the shape's volume fraction, while ρ_m and ρ_M are two real numbers ranging between 0 and 1. Let us briefly discuss the benefits of choosing an interval for the volume fraction rather than setting a specific single value target. In fact, adjusting a specific target volume fraction, compatible with a given elastic stiffness target is a tedious task. On one hand, if the prescribed material volume fraction is set relatively low, the target could fall outside the range of achievable tensors [168, 169] (see also the discussion in Section 1.3), resulting in a final shape with undesired effects (see for example the gap between the target and the obtained results in the two first final shapes of [3]). On the other hand, if the prescribed material volume fraction is set relatively high, the algorithm may converge to shapes that are excessively bulky (e.g., large blocs connected with thin hinges) or in the worst case scenario, it would leave some unconnected material phases (islands) in the final microstructure.

Therefore, the topology optimisation problem is written as follows:

$$\begin{aligned} \inf_{S \subset \mathcal{U}_{ad}} \mathcal{J}(S, \mathbf{w}^{k\ell}(S)) = & v_{ijkl} C_{ijkl}^*(S, \mathbf{w}^{k\ell}(S)) + \frac{1}{2} \eta_{ijkl} \left(C_{ijkl}^*(S, \mathbf{w}^{k\ell}(S)) - C_{ijkl}^{\text{target}} \right)^2. \\ \mathbf{w}^{k\ell} \in \tilde{\mathcal{V}}(Y) \text{ satisfy: } & \int_Y C_{ijpq} \left(\delta_{pk} \delta_{ql} + \varepsilon_{ypq}(\mathbf{w}^{k\ell}) \right) \varepsilon_{yij}(\mathbf{v}) dy = 0, \quad \forall \mathbf{v} \in \tilde{\mathcal{V}}(Y). \end{aligned} \quad (3.2.5)$$

Recall that the functional $\tilde{\mathcal{V}}(Y)$ is defined as: $\tilde{\mathcal{V}}(Y) := \{\mathbf{v} \in H_{\text{per}}^1(Y) \mid \langle v_i \rangle_Y = 0\}$.

3.2.3 Shape derivative in the smooth inter-phase context

Using the method of C ea, discussed in [45], for the calculation of the shape derivative of the objective function, we formulate the Lagrangian function $\mathcal{L} : W^{1,\infty}(Y, \mathbb{R}^2) \times \tilde{\mathcal{V}} \times \tilde{\mathcal{V}} \rightarrow \mathbb{R}$ as follows:

$$\begin{aligned} \mathcal{L}(S, \mathbf{v}^{k\ell}, \mathbf{q}) &= v_{ijk\ell} C_{ijk\ell}^* + \frac{1}{2} \eta_{ijk\ell} \left(C_{ijk\ell}^* - C_{ijk\ell}^{\text{target}} \right)^2 \\ &+ \int_Y C_{ijpq}^e(\mathbf{y}) \left(\delta_{pk} \delta_{q\ell} + \varepsilon_{ypq}(\mathbf{v}^{k\ell}) \right) \varepsilon_{yij}(\mathbf{q}) \, d\mathbf{y}. \end{aligned} \quad (3.2.6)$$

Here, \mathbf{q} is intended as the Lagrange multiplier associated to the enforcement of the state equation. $\mathbf{v}^{k\ell}$ and \mathbf{q} are vector-valued functions defined in Y which do not depend on S . As usual, stationarity of the Lagrangian provides the optimality conditions for the minimisation problem.

Direct problem. Differentiating \mathcal{L} in (3.2.6) with respect to \mathbf{q} in the direction of a test function $\boldsymbol{\varphi} \in \tilde{\mathcal{V}}(Y)$ gives:

$$\left\langle \frac{\partial \mathcal{L}}{\partial \mathbf{q}} \mid \boldsymbol{\varphi} \right\rangle = \int_Y C_{ijpq}^e \left(\delta_{pk} \delta_{q\ell} + \varepsilon_{ypq}(\mathbf{v}^{k\ell}) \right) \varepsilon_{yij}(\boldsymbol{\varphi}) \, d\mathbf{y}. \quad (3.2.7)$$

Upon setting the above equation equal to zero, we recover (by construction) the variational formulation of first state equation (1.2.28). The solution of this problem is denoted by $\mathbf{w}^{k\ell}$.

Adjoint problem. Differentiating \mathcal{L} in (3.2.6) with respect to $\mathbf{v}^{k\ell}$ in the direction of a test function $\boldsymbol{\varphi} \in \tilde{\mathcal{V}}(Y)$ results in:

$$\begin{aligned} \left\langle \frac{\partial \mathcal{L}}{\partial \mathbf{v}^{k\ell}} \mid \boldsymbol{\varphi} \right\rangle &= \left[\frac{v_{ijk\ell}}{|Y|} + \frac{\eta_{ijk\ell}}{|Y|} \left(C_{ijk\ell}^* - C_{ijk\ell}^{\text{target}} \right) \right] \int_Y C_{mnpq}^e \left(\delta_{pk} \delta_{q\ell} + \varepsilon_{ypq}(\mathbf{v}^{k\ell}) \right) \varepsilon_{ymn}(\boldsymbol{\varphi}) \, d\mathbf{y} \\ &+ \int_Y C_{ijpq}^e \varepsilon_{ypq}(\boldsymbol{\varphi}) \varepsilon_{yij}(\mathbf{q}) \, d\mathbf{y} = 0. \end{aligned}$$

The integral over Y on the first line is equal to 0 from the state equation (3.2.7). Therefore, the above equation yields:

$$\int_Y C_{ijpq}^e \varepsilon_{yij}(\boldsymbol{\varphi}) \varepsilon_{yij}(\mathbf{q}) \, d\mathbf{y} = 0.$$

Choosing $\boldsymbol{\varphi} = \mathbf{q}$ and using the positive definiteness of C as well as the Y -periodicity of \mathbf{q} , we obtain that the solution of the adjoint state is identically zero.

$$\hat{\mathbf{q}} = \mathbf{0}. \quad (3.2.8)$$

Shape derivative. Deforming the interface Γ^S in the direction of a smooth vector field $\boldsymbol{\theta}$ (see section 2.3.2 for details), the shape derivative of the objective function is found to be the shape derivative of the Lagrangian at the optimal point:

$$\mathcal{J}'(S)(\boldsymbol{\theta}) = \left\langle \frac{\partial \mathcal{L}}{\partial S}(S, \mathbf{w}^{k\ell}, \mathbf{0}) \mid \boldsymbol{\theta} \right\rangle. \quad (3.2.9)$$

Thus:

$$\begin{aligned} \mathcal{J}'(S)(\boldsymbol{\theta}) &= \left[\frac{v_{ijk\ell}}{|Y|} + \frac{\eta_{ijk\ell}}{|Y|} \left(C_{ijk\ell}^* - C_{ijk\ell}^{\text{target}} \right) \right] \int_Y d_S'(\boldsymbol{\theta}) \\ &\quad \left(C_{mnpq}^e(d_S) \right)' \left(\delta_{pk} \delta_{q\ell} + \varepsilon_{ypq}(\mathbf{w}^{k\ell}) \right) \left(\delta_{mi} \delta_{nj} + \varepsilon_{ymn}(\mathbf{w}^{ij}) \right) \, d\mathbf{y}, \end{aligned}$$

where $(C_{mnpq}^e(d_S))'$ denotes the derivation with respect to the signed distance function d_S . Some

elementary algebra, using the shape differentiability of $d_S(\mathbf{y})$ for almost every $\mathbf{y} \in Y$, yields:

$$\begin{aligned} \mathcal{J}'(S)(\theta) &= \left[\frac{v_{ijkl}}{|Y|} + \frac{\eta_{ijkl}}{|Y|} \left(C_{ijkl}^* - C_{ijkl}^{\text{target}} \right) \right] \int_Y -\theta_r(p_{\partial S}(\mathbf{y})) n_r(p_{\partial S}(\mathbf{y})) \\ &\quad \left(C_{mnpq}^e(d_S) \right)' \left(\delta_{pk} \delta_{ql} + \varepsilon_{ypq}(\mathbf{w}^{kl}) \right) \left(\delta_{mi} \delta_{nj} + \varepsilon_{ymn}(\mathbf{w}^{ij}) \right) d\mathbf{y} \\ &= \left[\frac{v_{ijkl}}{|Y|} + \frac{\eta_{ijkl}}{|Y|} \left(C_{ijkl}^* - C_{ijkl}^{\text{target}} \right) \right] \int_Y -\theta_r(p_{\partial S}(\mathbf{y})) n_r(p_{\partial S}(\mathbf{y})) \\ &\quad \mathcal{H}'_e(d_S) \left(C_{mnpq}^{\bar{S}} - C_{mnpq}^S \right) \left(\delta_{pk} \delta_{ql} + \varepsilon_{ypq}(\mathbf{w}^{kl}) \right) \left(\delta_{mi} \delta_{nj} + \varepsilon_{ymn}(\mathbf{w}^{ij}) \right) d\mathbf{y}, \end{aligned}$$

where \mathbf{n} is the outer unit normal to S . It remains to transform this expression by the co-area formula in order to deduce a boundary integral. Using the formula (2.4.20) of Chapter 2 yields:

$$\begin{aligned} \mathcal{J}'(S)(\theta) &= \left[\frac{v_{ijkl}}{|Y|} + \frac{\eta_{ijkl}}{|Y|} \left(C_{ijkl}^* - C_{ijkl}^{\text{target}} \right) \right] \int_{\Gamma^S} -\theta_r(\mathbf{s}) n_r(\mathbf{s}) \left(\int_{\text{ray}_{\Gamma^S \cap Y}} \mathcal{H}'_e(d_S) \left(C_{mnpq}^{\bar{S}} - C_{mnpq}^S \right) \right. \\ &\quad \left. \left(\delta_{pk} \delta_{ql} + \varepsilon_{zpq}(\mathbf{w}^{kl}) \right) \left(\delta_{mi} \delta_{nj} + \varepsilon_{zmn}(\mathbf{w}^{ij}) \right) (1 + d_S(\mathbf{z}) \kappa(\mathbf{s})) d\mathbf{z} \right) d\mathbf{s}, \end{aligned}$$

where κ denotes the principal curvature of Γ^S . The above integral may be decomposed over S and \bar{S} . We can rewrite the expression as follows.

$$\mathcal{J}'(S)(\theta) = - \left[\frac{v_{ijkl}}{|Y|} + \frac{\eta_{ijkl}}{|Y|} \left(C_{ijkl}^* - C_{ijkl}^{\text{target}} \right) \right] \int_{\Gamma^S} \theta_r(\mathbf{s}) n_r(\mathbf{s}) (f_S(\mathbf{s}) + f_{\bar{S}}(\mathbf{s})) d\mathbf{s}, \quad (3.2.10)$$

where:

$$\begin{cases} f_S(\mathbf{s}) = \int_{\text{ray}_{\Gamma^S \cap S}} \mathcal{H}'_e(d_S) \left(C_{mnpq}^{\bar{S}} - C_{mnpq}^S \right) \left(\delta_{pk} \delta_{ql} + \varepsilon_{zpq}(\mathbf{w}^{kl}) \right) \left(\delta_{mi} \delta_{nj} + \varepsilon_{zmn}(\mathbf{w}^{ij}) \right) \\ \quad (1 + d_S(\mathbf{z}) \kappa(\mathbf{y})) d\mathbf{z}, \\ f_{\bar{S}}(\mathbf{s}) = \int_{\text{ray}_{\Gamma^S \cap \bar{S}}} \mathcal{H}'_e(d_S) \left(C_{mnpq}^{\bar{S}} - C_{mnpq}^S \right) \left(\delta_{pk} \delta_{ql} + \varepsilon_{zpq}(\mathbf{w}^{kl}) \right) \left(\delta_{mi} \delta_{nj} + \varepsilon_{zmn}(\mathbf{w}^{ij}) \right) \\ \quad (1 + d_S(\mathbf{z}) \kappa(\mathbf{y})) d\mathbf{z}. \end{cases}$$

3.2.4 Approximate formula for the shape derivative

Although formula (3.2.10) is satisfying from a mathematical point of view, its numerical evaluation is not completely straightforward. There are two delicate issues. First, one has to compute the principal curvature $\kappa(\mathbf{y})$ for any point $\mathbf{y} \in \Gamma^S$ on the interface. Second, one has to perform a one-dimensional integration along the rays of the energy-like quantity. This is a classical task in the level set framework but, still, it is of interest to devise a simpler approximate formula for the shape derivative.

A first approximate formula is to assume that the interface is roughly plane, namely to assume that the principal curvature $\kappa(\mathbf{y})$ vanish. In such a case we obtain a ‘‘Jacobian-free’’ approximate shape derivative. This gives a new expression for $\{f_S$ and $f_{\bar{S}}$:

$$\begin{cases} f_S(\mathbf{s}) = \int_{\text{ray}_{\Gamma^S \cap S}} \mathcal{H}'_e(d_S) \left(C_{mnpq}^{\bar{S}} - C_{mnpq}^S \right) \left(\delta_{pk} \delta_{ql} + \varepsilon_{zpq}(\mathbf{w}^{kl}) \right) \left(\delta_{mi} \delta_{nj} + \varepsilon_{zmn}(\mathbf{w}^{ij}) \right) d\mathbf{z} \\ f_{\bar{S}}(\mathbf{s}) = \int_{\text{ray}_{\Gamma^S \cap \bar{S}}} \mathcal{H}'_e(d_S) \left(C_{mnpq}^{\bar{S}} - C_{mnpq}^S \right) \left(\delta_{pk} \delta_{ql} + \varepsilon_{zpq}(\mathbf{w}^{kl}) \right) \left(\delta_{mi} \delta_{nj} + \varepsilon_{zmn}(\mathbf{w}^{ij}) \right) d\mathbf{z} \end{cases}$$

A second approximate formula is obtained when the smoothing parameter e is small. Note that, since the support of the function \mathcal{H}_e is of size $2e$, the integral in formula (3.2.10) is confined to a tubular neighbourhood of Γ^S of width $2e$. Therefore, if e is small, one may assume that the

functions depending on \mathbf{z} are constant along each ray, equal to their value at $\mathbf{s} \in \Gamma^S$. In other words, for small e we assume:

$$\varepsilon_{zmn} \approx \varepsilon_{smn} \quad d_S(\mathbf{z}) \approx d_S(\mathbf{s}) = 0, \quad (3.2.11)$$

which yields the approximate formulas, for $\mathbf{y} \in \Gamma$,

$$\begin{cases} f_S(\mathbf{s}) = \left(C_{mnpq}^{\bar{S}} - C_{mnpq}^S \right) \left(\delta_{pk} \delta_{q\ell} + \varepsilon_{spq}(\mathbf{w}^{k\ell}) \right) \left(\delta_{mi} \delta_{nj} + \varepsilon_{smn}(\mathbf{w}^{ij}) \right) \int_{\text{ray}_{\Gamma^S} \cap S} \mathcal{H}'_e(d_S) d\mathbf{z}, \\ f_{\bar{S}}(\mathbf{s}) = \left(C_{mnpq}^{\bar{S}} - C_{mnpq}^S \right) \left(\delta_{pk} \delta_{q\ell} + \varepsilon_{spq}(\mathbf{w}^{k\ell}) \right) \left(\delta_{mi} \delta_{nj} + \varepsilon_{smn}(\mathbf{w}^{ij}) \right) \int_{\text{ray}_{\Gamma^S} \cap \bar{S}} \mathcal{H}'_e(d_S) d\mathbf{z}. \end{cases}$$

Furthermore, most rays have a length larger than $2e$ so that

$$\int_{\text{ray}_{\Gamma^S} \cap S} \mathcal{H}'_e(d_S) d\mathbf{z} + \int_{\text{ray}_{\Gamma^S} \cap \bar{S}} \mathcal{H}'_e(d_S) d\mathbf{z} = \mathcal{H}_e(e) - \mathcal{H}_e(-e) = 1. \quad (3.2.12)$$

In turn, we obtain the following approximate formula for:

$$\begin{aligned} \mathcal{J}'(S)(\boldsymbol{\theta}) = & - \left[\frac{v_{ijkl}}{|Y|} + \frac{\eta_{ijkl}}{|Y|} \left(C_{ijkl}^*(S) - C_{ijkl}^{\text{target}} \right) \right] \int_{\Gamma^S} \theta_r(\mathbf{s}) n_r(\mathbf{s}) \\ & \left(C_{mnpq}^{\bar{S}} - C_{mnpq}^S \right) \left(\delta_{pk} \delta_{q\ell} + \varepsilon_{spq}(\mathbf{w}^{k\ell}) \right) \left(\delta_{mi} \delta_{nj} + \varepsilon_{smn}(\mathbf{w}^{ij}) \right) d\mathbf{s}. \end{aligned} \quad (3.2.13)$$

Note that, since the support of the function \mathcal{H}_e is of size $2e$, the integral in formula (3.2.13) is confined to a tubular neighbourhood of Γ^S of width $2e$. Numerical results performed in [15] reveal that the latter simplification (3.2.13), which we shall refer to as the approximate shape derivative, works very well in practice for problems of compliance minimisation. Formula (3.2.13) is also used by Wang, Mei and Wang in their numerical simulations (see section 4.3. in [249]).

3.2.5 Shape derivative of the volume constraint

The result in eq. (3.2.13) corresponds to the unconstrained optimisation problem. To ensure that $S \subset \mathcal{U}_{\text{ad}}$, we rely on an augmented Lagrangian approach to enforce the volume constraint [36, 183]. Hence, the optimisation problem (3.2.5) is a constraint-free minimisation of a (Lagrangian-like) weighted sum of the cost functional $\mathcal{J}(S)$ and the constraint $\mathcal{P}(S)$ that reads:

$$\inf \left(\mathcal{J}(S) + \mathcal{P}(S, \lambda, \mu) \right), \quad (3.2.14)$$

where the constraint can be expressed as:

$$\begin{cases} \mathcal{P}(S, \lambda, \mu) = \left(\lambda (|S| - \rho^{\text{target}}) + \frac{\mu}{2} (|S| - \rho^{\text{target}})^2 \right) & \text{for an equality volume constraint;} \\ \mathcal{P}(S, \lambda, \mu) = \min_{\rho_m \leq |S| - v \leq \rho_M} \left(\lambda v + \frac{\mu}{2} |v|^2 \right) & \text{for a two-sided inequality volume constraint.} \end{cases} \quad (3.2.15)$$

where $|S|$ is the material volume, defined as:

$$|S| = \int_Y (1 - \mathcal{H}_e(d_S)) d\mathbf{y}, \quad (3.2.16)$$

while λ and μ are the Lagrange multipliers for the volume constraint. A brief presentation on used schemes to update these parameters through the optimisation process is provided in appendix B.3. From the constraint gives rise to an additional term in the shape derivative of $\mathcal{J}(S)$. We denote by $\mathcal{P}'(S)$ the shape derivative of the volume constraint $\mathcal{P}(S)$ in the direction $\boldsymbol{\theta}$. Under

the approximations of the previous section, we also obtain a “Jacobian-free” approximate expression which reads (see appendix B.3):

$$\mathcal{P}'(S)(\theta) = \begin{cases} [\lambda + \mu(|S| - \rho_M)] \int_{\Gamma^S} \theta_r n_r d\mathbf{y} & \text{if } \lambda + \mu(|S| - \rho_M) > 0 \\ [\lambda + \mu(|S| - \rho_m)] \int_{\Gamma^S} \theta_r n_r d\mathbf{y} & \text{if } \lambda + \mu(|S| - \rho_m) < 0 \\ 0 & \text{otherwise} \end{cases} \quad (3.2.17)$$

It is worth noticing that the above expression has the same structure of the unconstrained shape derivative in eq. (3.2.13).

3.2.6 Extension and regularisation of the velocity field and descent direction

Although eq. (3.2.13) for the advection of the level set function is solved in the whole domain Y , shape sensitivity analysis provides us with a shape gradient defined only on the boundary of the domain Γ^S . Since the boundary is not explicitly discretised in our case, we can assume that the normal velocity V is defined for the nodes of the elements that are crossed by the zero level set. Then, one possibility is to consider $V = 0, \forall \mathbf{y} \in Y \setminus \Gamma^S$. Unfortunately, this choice would limit the movement of the boundary to small distance, which would result in an increased number of iterations until convergence, and thus a slower algorithm. A remedy to this inconvenience is to extend the velocity field in all the domain. At the same time, it would be numerically beneficial to smooth a bit the shape gradient, but in a way that guarantees the descent nature of the new advection velocity. The sequel describes one way to combine these two requirements. Initially, the shape derivative has the form:

$$\mathcal{J}'(S)(\theta) = - \int_{\Gamma^S} \theta_r(\mathbf{s}) n_r(\mathbf{s}) f(\mathbf{s}) ds, \quad (3.2.18)$$

or, for an advection velocity of the type $\theta(\mathbf{s}) = V(\mathbf{s}) \mathbf{n}(\mathbf{s})$,

$$\mathcal{J}'(S)(V\mathbf{n}) = \int_{\Gamma^S} -V(\mathbf{s}) f(\mathbf{s}) ds. \quad (3.2.19)$$

Like in section 2.4.2, instead of choosing $V(\mathbf{s}) = -f(\mathbf{s})$, the extended velocity $V(\mathbf{y})$ is chosen as the unique solution to the following problem expressed in its variational formulation:

$$\int_Y (\alpha^2 \nabla V(\mathbf{y}) \cdot \nabla W(\mathbf{y}) + V(\mathbf{y}) W(\mathbf{y})) d\mathbf{y} = \int_{\Gamma^S} W(\mathbf{s}) f(\mathbf{s}) ds \quad \forall W \in H^1(Y), \quad (3.2.20)$$

where $\alpha \in \mathbb{R}^{+*}$ is a small positive scalar (of the order of the mesh size) to control the regularisation width and take $W = -V$. This operation reveals that:

$$\mathcal{J}'(S)(V\mathbf{n}) = - \int_Y (\alpha^2 |\nabla V|^2 + V^2) d\mathbf{y}, \quad (3.2.21)$$

which guarantees again a descent direction for \mathcal{J} .

3.3 Numerical algorithm

The optimisation of $\mathcal{J}(S)$ is carried out by advecting an initial shape S_0 with velocity V obtained from the shape derivative $\mathcal{J}'(S)(\theta)$ in the direction θ (see Allaire, Jouve and Toader [14] or Wang,

Mei and Wang [249]). The advection is realised by solving the Hamilton–Jacobi equation:

$$\frac{\partial \phi}{\partial t}(t, \mathbf{y}) + V(t, \mathbf{y}) |\nabla \phi(t, \mathbf{y})| = 0 \quad \forall t, \forall \mathbf{y} \in Y, \quad (3.3.1)$$

where $V(\mathbf{s}) = \theta(\mathbf{s}) \cdot \mathbf{n}(\mathbf{s})$ is the velocity of the interface computed from the constrained shape derivative $\mathcal{J}(S)(\theta)$ in eq. (3.2.21).

The numerical algorithm presented in Algorithm 2, makes use of the gradient method and reports the list of steps to achieve at each iteration of the loop. Additional mathematical results and algorithmic issues can be found in the works of Allaire, Jouve and Toader [14], Allaire et al. [15], Wang, Mei and Wang [249] for more details about the mathematical results and algorithmic issues for the solution method. An extension of this algorithm to cases with more than two phases is presented in Nika and Constantinescu [181].

Data: Initialise a level set function ϕ_0 corresponding to an initial shape S^0 ;

for $k \geq 0$ *iterate until* $k > 100$ **do**

Redistance ϕ_k into the signed distance function d_{S^k} using eq. (2.4.9);

Compute the local solutions $\mathbf{w}^{m\ell}$, for $m, \ell = 1, 2$ by solving the state equation(1.2.28) for the domain S^k ;

Update the Lagrange multiplier λ^k ;

Compute the shape gradient $\mathcal{J}(S^k)(\theta^k)$ for the domain S^k using eq. (3.2.21);

Deform the domain S^k by solving the Hamilton-Jacobi equation (3.3.1);

// Shape S^{k+1} is characterised by the level set ϕ_{k+1} after a time step Δt_k

// The time step Δt_k is chosen so that $\mathcal{J}(S^{k+1}) \leq \mathcal{J}(S^k)$

end

Algorithm 2: major steps of a topology optimisation algorithm, adapted from the work of Allaire, Jouve and Toader [14].

Stopping criterion. In this study, the choice of a relevant and effective stopping criterion was not obvious. Early stage simulations revealed that most of the changes in shape and topology generally occur in the first 25 iterations, and that the later iteration only contribute to small improvements. The optimisation is assumed to be terminated when 100 iterative steps are reached. In the case of an example where more iterations are needed, it is always possible to restart the algorithm with the current shape S^{100} as the initial guess.

Additional remarks. Let us remark that the algorithm does not allow for nucleations of voids. However the level set method is well known to handle easily topology changes, i.e., merging or cancellation of holes. Therefore, algorithm is able to perform topology optimisation if the number of holes of the initial design is sufficiently large and converges smoothly to a (local) minimum which strongly depends on the initial topology. As explained in section 2.4.3, a change in topology may result in an increase of the objective function \mathcal{J} , therefore the shape S^{k+1} is accepted only if eq. (2.4.14) is verified.

3.4 Examples of obtained microstructures

In all the examples that follow, the unit cell Y was meshed with a structured symmetric grid of 100×100 quadrangular each formed of four equal linear triangular elements ($P1$). We recall that the distribution of elastic properties are defined by eq. (7.3.7). The material properties in each phases, S and \bar{S} are characterised by an isotropic fourth order tensor:

$$C_{ijkl}^\alpha = \frac{E^\alpha}{1 + \nu^\alpha} (\delta_{ik} \delta_{jl} + \delta_{il} \delta_{jk}) + \frac{E^\alpha \nu^\alpha}{(1 + \nu^\alpha)(1 - \nu^\alpha)} \delta_{ij} \delta_{kl} \quad \alpha \in \{S, \bar{S}\}$$

Example	C^{target}	$C^*(S)$	Shape S
1	$\begin{pmatrix} 0.1 & -0.1 & * \\ -0.1 & 0.1 & * \\ * & * & * \end{pmatrix}$	$\begin{pmatrix} 0.12 & -0.05 & 0 \\ -0.05 & 0.04 & 0 \\ 0 & 0 & 0.006 \end{pmatrix}$	
2	$\begin{pmatrix} 0.1 & -0.1 & * \\ -0.1 & 0.1 & * \\ * & * & * \end{pmatrix}$	$\begin{pmatrix} 0.12 & -0.05 & 0 \\ -0.05 & 0.12 & 0 \\ 0 & 0 & 0.003 \end{pmatrix}$	
3	$\begin{pmatrix} 0.2 & -0.1 & * \\ -0.1 & 0.2 & * \\ * & * & * \end{pmatrix}$	$\begin{pmatrix} 0.19 & -0.09 & 0 \\ -0.09 & 0.19 & 0 \\ 0 & 0 & 0.06 \end{pmatrix}$	
4	$\begin{pmatrix} 0.2 & -0.1 & * \\ -0.1 & 0.1 & * \\ * & * & * \end{pmatrix}$	$\begin{pmatrix} 0.19 & -0.07 & 0 \\ -0.09 & 0.08 & 0 \\ 0 & 0 & 0.003 \end{pmatrix}$	

Table 3.1: from left column to right column: target elastic stiffness tensor C^{target} , final elastic tensor $C^*(S)$, and unit cell shape S for the discussed examples. Let us remark that the microstructures from example 2 and 3 carry a quadratic symmetry, while the microstructure from example 1 and 4 carry a general orthotropic symmetry.

The material properties are normalised as follows: the Young's modulus was set to $E^S = 0.91$ MPa for the strong phase (material) and $E^{\bar{S}} = 0.91 \times 10^{-3}$ MPa for the weak phase (void). The Poisson's ratio was set to $\nu = 0.3$ for both phases. Under the plane stress assumption, the components of the elastic tensor of the base material are $C_{1111}^S = C_{2222}^S = 1.0$ MPa; $C_{1122}^S = 0.3$ MPa; $C_{1212}^S = 0.35$ MPa. All computations were carried out using an in house programming of the preceding Algorithm 2 operating on the software FreeFEM++ [114].

The main intention of the present work was to design micro-architected materials exhibiting an effective negative Poisson's ratio. However, in all examples the target objective was defined only in terms of the coefficients C_{1111}^* , C_{1122}^* , C_{2222}^* (using the relation in eq. (1.3.2)). The shear coefficient C_{1212}^* as well as the C_{1211}^* and C_{1222}^* coefficients were left free. Therefore, only the elastic moduli of the unit cell corresponding to the direction 11 and 22 directions of strain and stresses were controlled.

For each numerical example, we provide the initials guesses for the shapes, which are typically a plate filled with holes, as illustrated in Fig. 3.2(a), 3.4(a), 3.5(a) and 3.6(a).

3.4.1 Example 1

The first microstructure to be optimised is a structure whose target effective Poisson's ratio is equal $\nu^{\text{target}} = -1$. The volume constraint was set to $\rho^{\text{target}} = 50\%$. We further note that for this structure we enforced a symmetry of the shape along the Oy axis, by symmetrising the level set function ϕ after each iteration in the algorithm. The initial and final shape of the microstructure on the unit cell and as a periodic material are represented in Fig. 3.2.

The final shape can be characterised as an re-entrant honeycomb structure and looks similar to the designs imagined by Almgren [17]. Its homogenised coefficients, displayed in table 3.1, show that the structure exhibits an effective orthotropic behaviour and a simple calculation yields $\nu_{12}^* = -1.25$ and $\nu_{21}^* = -0.42$. Hence, the expansion of the structure along the e_2 direction when stretched in the e_1 axis is larger than the expansion along the e_1 axis when stretched in the e_2 axis. This non-symmetric effect has been enabled as the symmetry relation was only imposed along the vertical axis in the algorithm.

The convergence history of the cost functional and of the volume constraint displayed in Fig. 3.3 shows that the target coefficient got stabilised in slightly more than 20 iteration and that the later

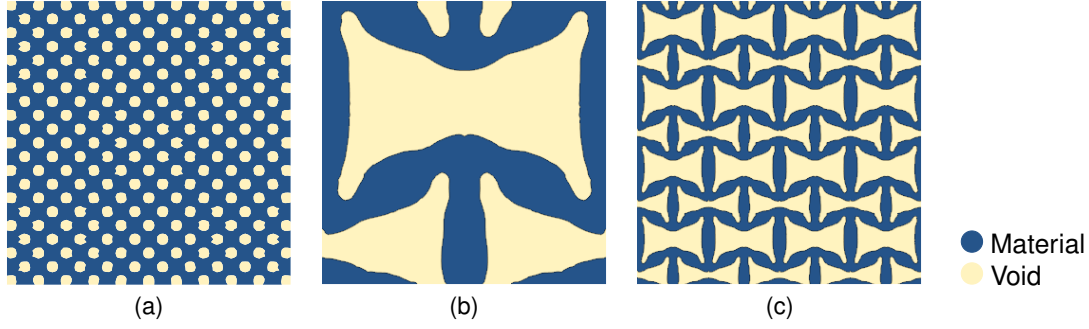


Fig. 3.2: initial and final shape of the microstructure: (a) initial shape consisting of a series of circular micro-perforations (b) final, optimal, shape of the unit cell after 100 iterations (c) final, optimal, shape of the periodic material.

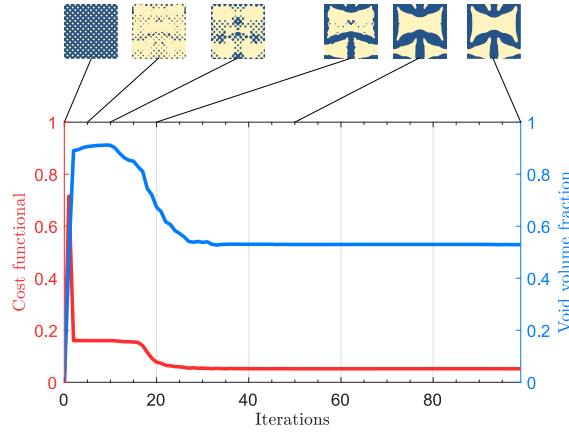


Fig. 3.3: evolution of the cost functional (in red) and volume constraint V (in blue) during 100 iterations.

iteration contributed only to small improvements without bringing the cost functional to less than 0.06 which corresponds to 92% decrease of the initial value. The gap with respect to the target moduli can be read from Table 3.1. It is interesting to remark, that the final optimised microstructure has a shear moduli close to 0. However, the final effective Poisson's ratio is close to the set target as will be discussed in the comparison with the printed samples. The volume constraint has a different evolution than the cost functional with an initial increase given by the initial evolution of the holes and then a fast and a slow evolution which lies within the proposed range of the constraint. The final volume ratio is at approximately $f(S) = 47\%$ and lies in the vicinity of the imposed value.

3.4.2 Example 2

For the second microstructure to be optimised, the target effective Poisson's ratio was also $\nu^{\text{target}} = -1$. The target tensor possesses a quadratic symmetry, meaning the desired mechanical properties along the O_x and O_y axis should be equal. This time, the void volume fraction constraint was of an inequality type, and was set to $16\% \leq |S| \leq 60\%$. To counter the loss of symmetry observed in the previous example, a symmetry of the shape was enforced along both the O_x axis and O_y axis, by symmetrising the level set function during the algorithmic iterations. The initial and final shape of the microstructure on the unit cell and as a periodic material are represented in Fig. 3.4, while the target and final elastic moduli are shown in table 3.1.

As prescribed, the resulting structure exhibits a quadratic symmetry. The computed effective Poisson's ratio is $\nu^* = \nu_{12}^* = \nu_{21}^* = -0.42$. By comparing at the target and the obtained elastic tensor, one can remark that the diagonal elastic moduli C_{1111}^* and C_{2222}^* are fairly close to the target but the shear C_{1122}^* fails at attaining the desired properties of $\nu^{\text{target}} = -1$. This suggests that there

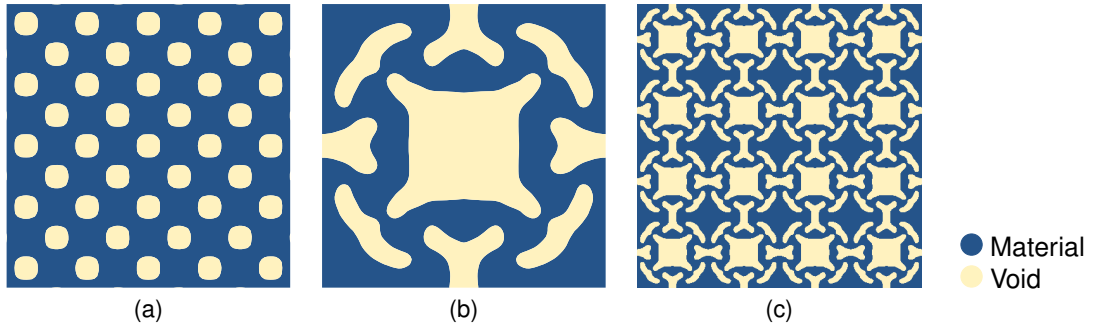


Fig. 3.4: design process of the material. Image (a) depicts the initial guess of the microstructure, (b) depicts the optimal microstructure after 100 iterations, (c) depicts the macroscopic material assembled periodically from the optimal unit cell of image (b).

is a trade-off between symmetrical tensor and extreme negative Poisson's ratio in the optimisation algorithm. This will further be discussed in the following section. Finally, let us remark that the final volume ratio is at approximately $f(S) = 36\%$ and lies in the middle of the imposed interval. As before, the final optimised microstructure has a shear modulus C_{1212}^* close to 0.

3.4.3 Example 3

For the third microstructure to be optimised, the target effective Poisson's ratio was $\nu^{\text{target}} = -0.5$. The target tensor possesses a quadratic symmetry, meaning the desired mechanical properties along the O_x and O_y axis should be equal. The void volume fraction constraint is set to $\rho^{\text{target}} = 60\%$ and is updated the same way as in the first example. As in example 2, a symmetry of the shape was enforced along the O_x and O_y axis. The initial and final shape of the microstructure on the unit cell and as a periodic material are represented in Fig. 3.5, while the target and final elastic moduli are shown in table 3.1.

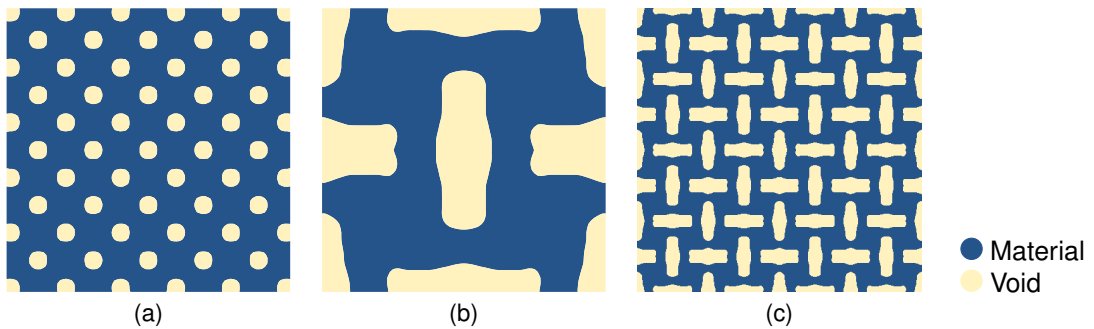


Fig. 3.5: design process of the material. Image (a) depicts the initial guess of the microstructure, (b) depicts the optimal microstructure after 100 iterations, (c) depicts the macroscopic material assembled periodically from the optimal unit cell of image (b).

The final shape is of the rotating units type, discussed in Grima et al. [104]. As prescribed, the resulting structure exhibits a quadratic symmetry. The computed effective Poisson's ratio is $\nu^* = \nu_{12}^* = \nu_{21}^* = -0.47$. By comparing the target and the obtained elastic tensor, one can remark that the final elastic moduli are fairly close to the target and that this structure has a shear modulus C_{1212}^* which is of the same order of magnitude as the other moduli. Finally, let us remark that the final volume ratio is at approximately $f(S) = 63\%$ and lies in the vicinity of the imposed value.

3.4.4 Example 4

The last microstructure to be optimised is the first one to have a target effective Poisson's ratio with orthotropic symmetry. More precisely, the target Poisson's ratios are equal $\nu_{12}^{\text{target}} = -0.5$ and

$\nu_{21}^{\text{target}} = -1$. The volume constraint was of an inequality type, and was set to $20\% < |S| < 65\%$. As in example 2 and 3, a symmetry of the shape was enforced along the O_x and O_y axis. The initial and final shape of the microstructure on the unit cell and as a periodic material are represented in Fig. 3.6, while the target and final elastic moduli are shown in table 3.1.

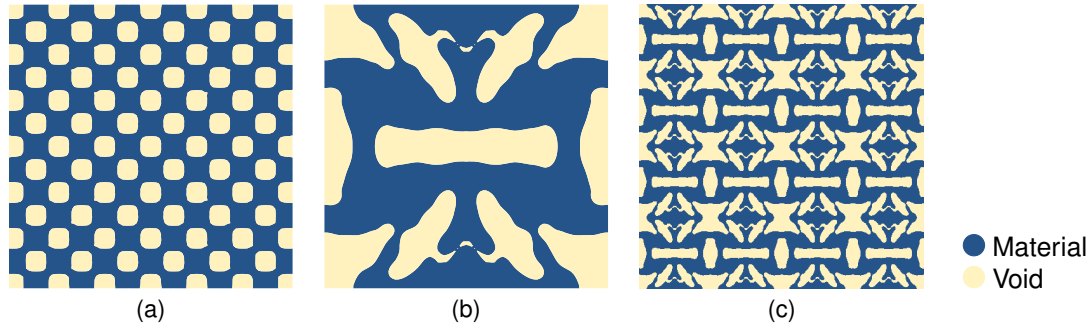


Fig. 3.6: design process of the material. Image (a) depicts the initial guess of the microstructure, (b) depicts the optimal microstructure after 100 iterations, (c) depicts the macroscopic material assembled periodically from the optimal unit cell of image (b).

As prescribed, the resulting structure exhibits an orthotropic symmetry. The computed effective Poisson's ratios are $\nu_{12}^* = 0.37$ and $\nu_{21}^* = -0.88$. By comparing the target and the obtained elastic tensor, one can remark that the final elastic moduli are relatively close to the target. In addition, let us remark that this structure has a shear modulus C_{1212}^* close to 0. Finally, the final volume ratio is at approximately $|S| = 40\%$ and lies in the vicinity of the imposed value.

The final shape features a peculiar cut in the central top and bottom connections. However, it does not affect much the elastic behaviour of the cell, due to the smooth inter-phase approach. In addition, these small details are thorny to handle during the printing, because their size can be below the printer resolution. We can therefore wonder whether to what extent very small features (in the order of one or two elements in size) remaining in the final shape are important in reaching the target tensor.

3.5 Conclusion and perspectives

3.5.1 Conclusion

In this work, we used a topology optimisation method to design optimal shapes that achieve a negative Poisson's ratio. By removing certain material constraints, e.g., isotropy, from the algorithm we expanded the space of admissible shapes and as a result the algorithm was able to attain shapes with a Poisson's ratio below -1 . The effective elasticity tensor characterising the material with Poisson's ratio below -1 is orthotropic and although the theoretical problem of reachable elasticity tensors has been solved in the seminal work of Milton and Cherkaev [168] the algorithm suggests that the more we expand the space of admissible shapes by allowing shapes to deviate from isotropic symmetry the closer to the *stability* bounds the effective material approaches (see Fig. 1.4).

3.5.2 Possible future works

- Extend this work to three-dimensional micro-architectures. Besides the computational cost, the extension from 2D to 3D does not bring additional difficulty.
- Extend this work to 2D plate, to optimise the bending stiffness.
- Study the sensitivity to imperfections.

Chapter 4

3D printing and testing of architected polymeric sheets exhibiting a negative Poisson's ratio

Contents

4.1	Introduction	83
4.2	Materials and methods	84
4.2.1	Manufacturing process: equipment and base material	84
4.2.2	Testing and full-field displacement measurement using Digital Image Correlation (DIC)	85
4.2.3	Experimental estimation of the effective Poisson's ratio	86
4.3	Analysis of fabricated polymer structures	87
4.3.1	Experimental results	87
4.3.2	Comparison to numerical simulations	89
4.4	Conclusion	92

Architected sheet specimens are manufactured using a commercial stereolithography Ember 3D printer and are mechanically tested. The observed displacement and strain fields during tensile testing obtained by digital image correlation (Appendix C.1) match the predictions from the finite element simulations and demonstrate the efficiency of the design cycle.

4.1 Introduction

The great advances that have occurred for the last decades in techniques of additive manufacturing (also referred to as 3D printing) have enabled the processing of three-dimensional objects with complex geometries, including structured materials, i.e., materials with architected microstructures of tailorable geometry [180, 241]. These days, such techniques can be performed for several types of materials (including metallic alloys [26], ceramics [125] and polymers) and at different scales (from microscopic devices [29, 138, 172, 213] to 3D printed houses).

The purpose of this chapter is merely to exploit the 3D printing possibilities to digitally fabricate specimens from the optimal designs obtained in Chapter 3 and validate their design against the numerically predicted behaviour.

This chapter is organised as follows. Section 4.2 provides details on fabrication, experimental setups, as well as the methodology to experimentally measure the Poisson's ratio. The experimental testing of the structures and the interpretation of results using Digital Image Correlation (DIC) are reported in section 4.3. A short summary in section 4.4 concludes the chapter.

4.2 Materials and methods

4.2.1 Manufacturing process: equipment and base material

The optimal shapes have been additively manufactured with digital light processing stereolithography technology (DLP) using a commercial Ember 3D printer. A digital projector screen flashes a single image of each layer across the entire surface of the vat filled of photo-sensitive liquid resin at once, causing chains of molecules to link and thus forming solid polymer. The process is repeated until the 3D model is complete. Then the vat is drained of liquid, revealing the solidified model and the solid model is washed with a solvent.

The printer has a resolution of $50\ \mu\text{m}$, corresponding to 1 pixel in the digital projector screen, and a range of the processing layer thickness of $10 - 100\ \mu\text{m}$. The largest processing build volume is $64\ \text{mm} \times 40\ \text{mm} \times 134\ \text{mm}$ (note that $64\ \text{mm} \times 40\ \text{mm}$ correspond to a 1280×800 pixels picture). For a thickness of $25\ \mu\text{m}$ per layer, the speed range is of $18\ \text{mm}\cdot\text{h}^{-1}$. The printable minimal feature size of the specimens is announced at $0.4\ \text{mm}$ corresponding roughly to 8 pixels.

We selected a rubber-like material, commercially denoted as GM08b¹, as the base material because of its compliant nature. Fig. 4.1 displays a representative tensile stress–strain curve of this material. As expected for a rubber-like material it does not display an ideal linear elastic behaviour, but rather exhibits a gradual variation of the stiffness with increasing strain.

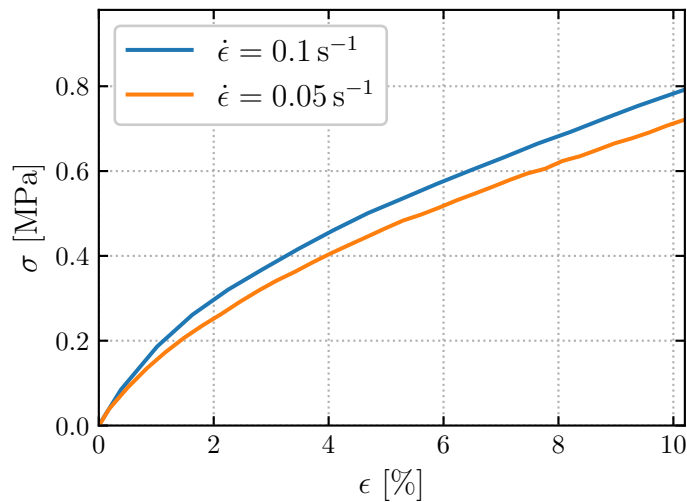


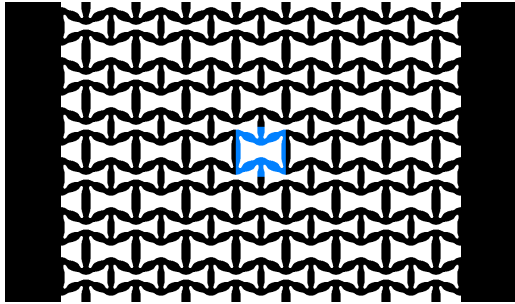
Fig. 4.1: Base material response to uniaxial tensile loading up to 10% strain. Rational stress-strain curves.

The optimal shapes obtained in examples 1–3 of Chapter 3 (see Fig. 3.2, 3.4 and 3.5) are represented by the final level set function. The later presents a smooth variation between values corresponding to the two materials in a neighbourhood of their interface and therefore the level set representation has been binarised and extruded in the Oz direction in order to create a three-dimensional object. More precisely, the 3D printed samples have been produced by the following procedure:

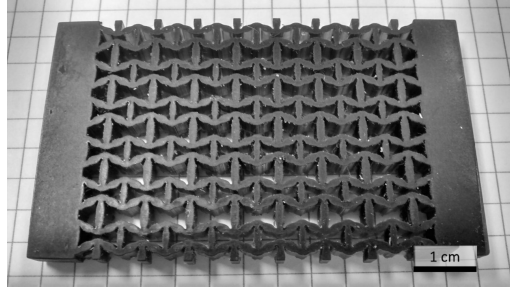
- (i) Binarise the level set function obtained by shape optimisation.
- (ii) Create a periodic array for each sample: 8×6 unit cells for Example 1, 5×4 unit cells for Example 2 and Example 3. The final result was a binarised 1280×800 pixels image (see Fig. 4.2 for details).
- (iii) Extrude the preceding image to obtain the 3D sheet of the desired height. The dimensions of the printed samples are $64 \times 38 \times 6\ \text{mm}$ for Example 1 and $64 \times 40 \times 6\ \text{mm}$ for Example 2 and 3.

¹Characteristics of this material can be found in the manufacturers data sheet (visit the DWS website)

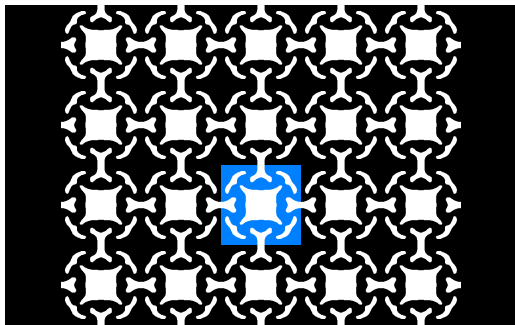
- (iv) Print the files with the following processing parameters: laser power was 5 W, the exposure time 1 s per layer and the layer thickness was 50 μm .
- (v) Wash the samples in an isopropanol bath for 5 min.
- (vi) Post-cure the samples for 30 min in an UV oven at 2000 W (this step helps to finish the polymerisation of possible residual resin).



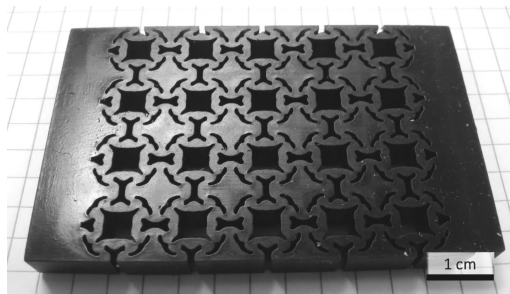
Example 1: Input design



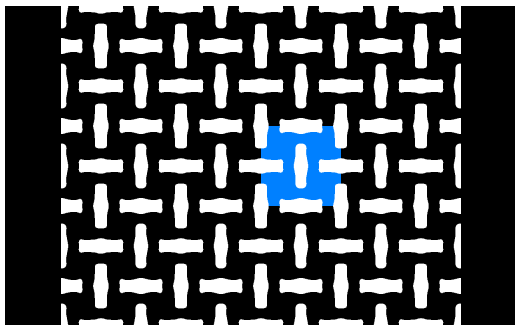
Example 1: Fabricated result



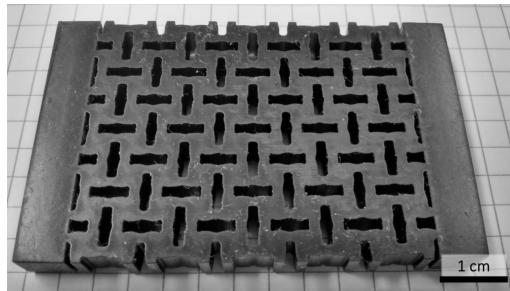
Example 2: Input design



Example 2: Fabricated result



Example 3: Input design



Example 3: Fabricated result

Fig. 4.2: Fabricated specimen from the examples of Chapter 3. Digital image fed into the 3D printer (left) and final printed specimen (right). The red coloured unit cells were the cells observed during the digital image correlation measurements.

4.2.2 Testing and full-field displacement measurement using Digital Image Correlation (DIC)

A series of uniaxial static tensile tests were undertaken to assess the tensile properties of the auxetic lattice structures by using a home-made testing machine with a symmetric displacement of the two cross-heads and equipped with a 100 N load cell. The tensile tests were performed at a rate of 0.05 mm.s⁻¹ up to 3 mm, which corresponds to a strain rate of $\dot{\epsilon} = 10^{-3} \text{ s}^{-1}$ up to a maximal strain of $\epsilon = 5\%$. The specimens are clamped at both ends with metallic bars, to constrain their displacement.

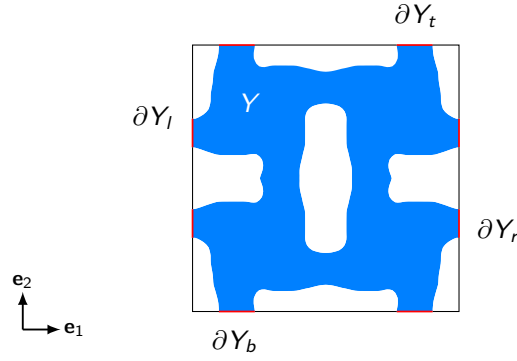


Fig. 4.3: representation of a unit cell.

The tensile tests were recorded and used for full-field measurements by digital image correlation (DIC). The recordings were obtained using a high-resolution digital camera (Schneider Optics 8-bit camera with a Makro-UNIFOC 100/77 lens) mounted on the tensile testing machine and grey scale pictures resolution of 4904×3280 pixels were recorded every second during the loading. The camera was mounted on a perpendicular axes with respect to the plane of the specimen, which enables the direct use of a 2D DIC. To improve the precision of the measurement, a white speckle pattern was placed on the sample by airbrushing.

The DIC was performed using the CorrelManuV 2D (CMV) software, developed by M. Bornert [16]. The processed displacement field corresponds to a single unit cell in the middle of the structure at five different loading time steps, using a 100×100 grid, i.e., having 10000 measurement points. For each node, the subset size was set to 20×20 pixels, while the searching area was set to 100×100 pixels. The measurement included a computation without transformation, i.e., rotation of the subset window and a re-optimisation allowing transformations with a reduced searching area of 30×30 pixels.

4.2.3 Experimental estimation of the effective Poisson's ratio

We discuss here the applied procedure to measure/compute the effective Poisson's ratio of a unit cell in both measurement by Digital Image Correlation and numerical estimation using a finite element method. The following developments are conducted in the case of small strain assumption.

Like in the previous chapter, let Y denote the bounded domain of two-dimensional unit cell and let ∂Y denote its boundary. The boundary can be decomposed into its four edges, namely ∂Y_b (bottom), ∂Y_t (top), ∂Y_r (right), ∂Y_l (left). An illustration in Fig. 4.3 depicts the configuration. The effective material is supposed to carry a natural orthotropic material behaviour (see 1.3). The effective Poisson's ratio ν_{12}^* , characterising the transverse strain of the structure in the direction (O, e_2) axis when stretched in the direction (O, e_1) , is defined as:

$$\nu_{12}^* = \frac{C_{1122}^*}{C_{2222}^*} \quad (4.2.1)$$

We remind that C_{1122}^* and C_{2222}^* are coefficients of the effective elastic stiffness tensor. In general $\nu_{12} \neq \nu_{21}$. During a uniaxial tensile test in the direction (O, e_1) , eq. (4.2.1) yields to the negative of the ratio of macroscopic transverse strain to macroscopic axial strain:

$$\nu_{12}^* = -\frac{\varepsilon_{x22}^*}{\varepsilon_{x11}^*} \quad (4.2.2)$$

In the small strain assumption, the strain field can be linearised as:

$$\varepsilon_x^* = \langle \varepsilon \rangle_Y = \frac{1}{2} (\langle \mathbf{F}^T \rangle_Y + \langle \mathbf{F} \rangle_Y) - \mathbf{I} \quad (4.2.3)$$

where \mathbf{F} is the average transformation gradient, defined as:

$$\langle \mathbf{F} \rangle_Y = \frac{1}{|Y|} \int_Y (\mathbf{I} + \nabla \mathbf{u}) dy \quad (4.2.4)$$

Ostrogradsky's theorem enables to express the transformation gradient at the boundary ∂Y :

$$\begin{aligned} \langle \mathbf{F} \rangle_Y &= \frac{1}{|Y|} \left(\int_Y \mathbf{I} dy + \oint_{\partial Y} \mathbf{u} \otimes \mathbf{n} ds \right) \\ &= \mathbf{I} + \frac{1}{|Y|} \left(- \int_{\partial Y_b} u_i \delta_{2j} ds + \int_{\partial Y_r} u_i \delta_{1j} ds + \int_{\partial Y_t} u_i \delta_{2j} ds - \int_{\partial Y_l} u_i \delta_{1j} ds \right) \\ &= \mathbf{I} + \frac{1}{|Y|} \begin{bmatrix} \int_{\partial Y_r} u_1 ds - \int_{\partial Y_l} u_1 ds & \int_{\partial Y_t} u_1 ds - \int_{\partial Y_b} u_1 ds \\ \int_{\partial Y_r} u_2 ds - \int_{\partial Y_l} u_2 ds & \int_{\partial Y_t} u_2 ds - \int_{\partial Y_b} u_2 ds \end{bmatrix} \end{aligned}$$

Thus, the longitudinal components of eq. (4.2.3) can be expressed as follows :

$$\begin{cases} \varepsilon_{x11}^* = \frac{1}{|Y|} \left(\int_{\partial Y_r} u_1 ds - \int_{\partial Y_l} u_1 ds \right) \\ \varepsilon_{x22}^* = \frac{1}{|Y|} \left(\int_{\partial Y_t} u_2 ds - \int_{\partial Y_b} u_2 ds \right) \end{cases} \quad (4.2.5)$$

The above expression, permits to define a new expression for the effective Poisson's ratio:

$$\nu_{12}^* = - \frac{\int_{\partial Y_t} u_2 ds - \int_{\partial Y_b} u_2 ds}{\int_{\partial Y_r} u_1 ds - \int_{\partial Y_l} u_1 ds} \quad (4.2.6)$$

In the experiment, it is naturally impossible to define a displacement in the void phase. The integral of the contour is then computed by integrating exclusively the displacement of the material in contact with the edge measured by DIC. Note that this restriction of the boundary is only acceptable for unit cells with a horizontally and vertically symmetric shape. Using a finite element method, equation (4.2.6) becomes:

$$\nu_{12}^* = - \frac{\frac{1}{N_t} \sum_{i=1}^{N_t} u_2^i - \frac{1}{N_b} \sum_{i=1}^{N_b} u_2^i}{\frac{1}{N_r} \sum_{i=1}^{N_r} u_1^i - \frac{1}{N_l} \sum_{i=1}^{N_l} u_1^i} \quad (4.2.7)$$

where $N_i, i \in \{t, b, r, l\}$ are respectively the number of nodes on top, bottom, right and left edges.

4.3 Analysis of fabricated polymer structures

4.3.1 Experimental results

The stress strain response under a uniaxial tensile test along Ox for the three materials are displayed in Fig. 4.4(a). One can observe a linear behaviour of the samples that up to a maximal strain of 5% strain despite the non-linearity of the rubber-like base material in the same strain range. This indicates the samples have an expected structural deformation where different parts of the "lattice" behave as rigid struts and deformable hinges. This effect will be highlighted by the DIC measurements discussed later.

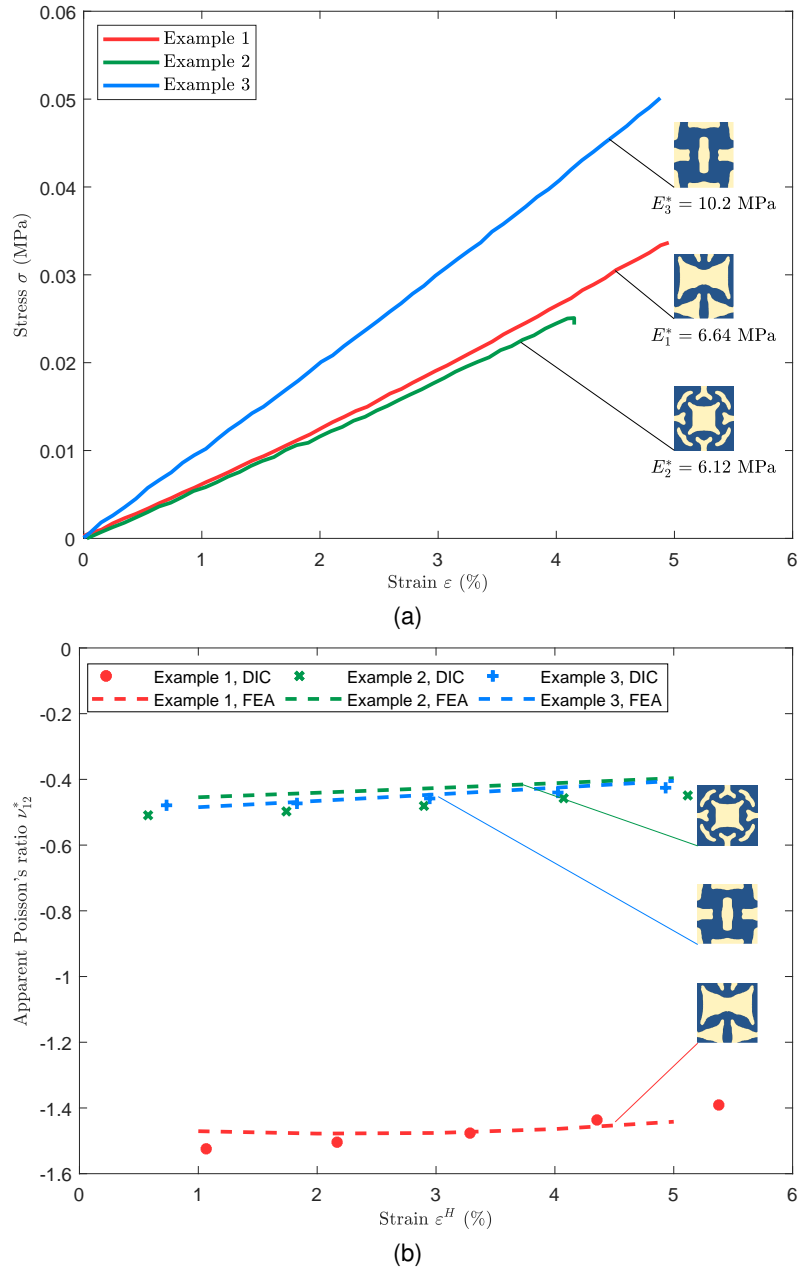


Fig. 4.4: (a) Effective stress–strain curves for all three examples overlaid in the same plot obtained experimentally by performing a uniaxial tensile test. One can clearly observe all three structures exhibit linear behaviour for strains up to 5%. (b) Comparison of the evolution of the Poisson's ratio plotted as a function of the effective strain from measurements taken by digital image correlation versus computations made by finite element analysis. We can clearly observe a trend on all three materials of the loss of their auxeticity as the uniaxial strain increases beyond the 5% mark.

ε_x^*	DIC ¹ [%]	FEM ¹ [%]	DIC ² [%]	FEM ² [%]	DIC ³ [%]	FEM ³ [%]
$\langle \varepsilon_{11} \rangle_Y$	1.250	0.543	0.526	0.404	0.937	0.828
$\langle \varepsilon_{11} \rangle_Y$	-1.010	-0.284	-0.450	-0.204	-0.643	-0.407
$\langle \varepsilon_{12} \rangle_Y$	0.039	0.004	0.053	0.002	0.010	0.001

Table 4.1: Mean strain components of the base material measured by DIC and computed by FEA on the unit cells from Fig. 4.5 for the structures in Examples 1-3, denoted by the superscript. The measurement corresponds to the maximal loading with an effective strain of 5%.

One can directly observe a lateral expansion during the tensile extension indicating a negative Poisson's ratio for all the samples. The precise measurements of the Poisson's ratio corresponding to a single central unit cell are presented in Fig. 4.4(b). The precise method for the computation of the Poisson's ratio of a single unit cell from DIC measurements was based on periodic homogenisation assumptions. The results show that the initial effective Poisson's ratio was for all samples close to the announced values in the optimisation process and was not degraded during the manufacturing process. During tensile loading, the effective Poisson's ratio tends to increase, indicating a decrease of the "auxeticity" of the samples of up to increases by 10% for a 5% strain.

4.3.2 Comparison to numerical simulations

Finite element computation were undertaken under the assumption of small strains, large displacements and plane stress using the finite element solver *Cast3M* [51]. The mesh was obtained using image processing from the binarised images of the optimal level set function and completed to the sample geometry. The elastic material behaviour was defined as the tangent behaviour at the origin of the tensile curve of the material. The sample was loaded with a given resultant force at the clamps of the tensile machine.

Let us first remark, that the evolution is close to predictions of the deformation of the samples obtained by the finite element method under the assumption of large displacements. Second, one can remark that the evolution of the Poisson's ratio with applied strain has already been observed and discussed in [68] on polymeric filament structure. Moreover, they arrived to correct the phenomenon up to 20% strain using a nonlinear material behaviour in the optimisation process, see [68, 250] for more details on the subject. In the case of the optimisation procedure presented here, the extension to non-linear material behaviour is currently under investigation and will appear in subsequent work of the authors.

The displacements fields obtained using DIC permit a further comparison with predictions and give an insight of the deformation mechanism of the samples, i.e., how the structure moves and deforms. Fig. 4.5 displays the measured and the computed vertical displacement, i.e., the u_y displacement component of the central unit cell. A comparison of the values and the shapes of the colour maps exhibits a good match between the measurements and finite element prediction. Moreover the displacement fields permit to better understand the local movements of the micro-structure which conducts to the global auxeticity effect by combining almost rigid regions submitted to translations and rotations with local concentrated deformation exhibiting local hinges. A further comparison in terms on mean displacements over a unit cell between DIC measurements and FEM computations at the maximal loading of 5% strain is given in Table 4.1. The mean was computed only over the base material of a unit cell and does represent the mean deformation of the later. Nevertheless, this mean value represents the mean loading of the base material and one can notice that the micro-structure does not leave the region of 1% strain of the uniaxial tensile response of the base material displayed in Fig. 4.1. In Fig. 4.5 one can equally notice the excellent quality of the printing process as the edges of the printed shapes observed on left column of Fig. 4.5 are close to the edges of the shape represented by the level set and displayed here as the border of the finite element meshes on the right column of Fig. 4.5.

By looking at the strain field of a unit cell (see Fig. 4.6), computed by finite elements from the

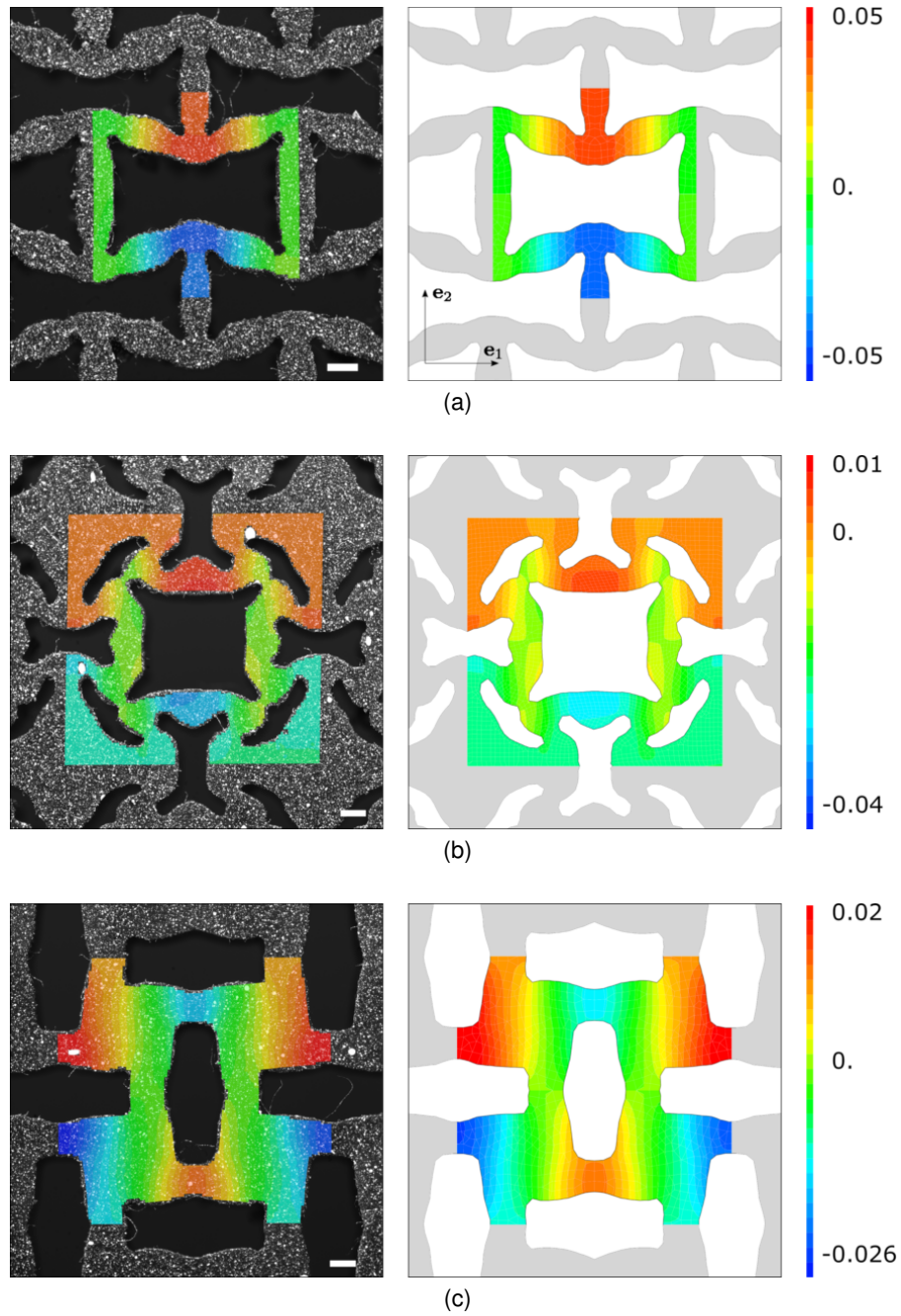


Fig. 4.5: Plots of the dimensionless values of the transverse displacement field along e_2 for each unit cell of the optimised structure. The samples are loaded along e_1 at 5% effective strain. The displacement field for the images on the left were measured using Digital Image Correlation, while for the images on the right using finite element analysis. Image (a) is the optimised structure of Example 1, image (b) the optimised structure of Example 2, image (c) is the optimised structure of Example 3. Scale bar in all images is 1 mm.

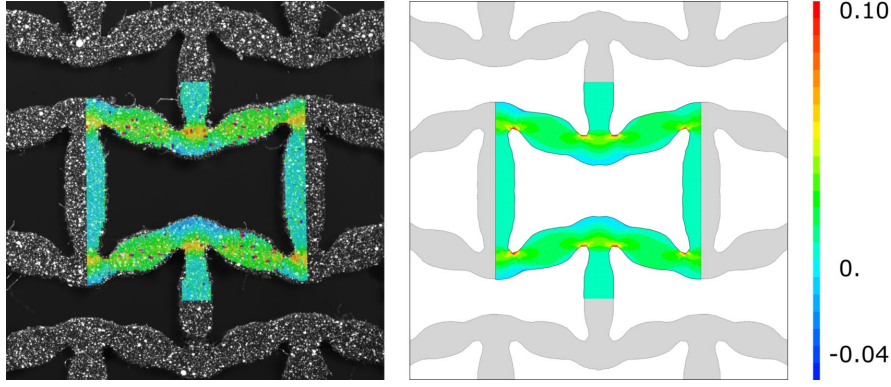


Fig. 4.6: Plot of the dimensionless values of the horizontal tensile strain field in a single unit cell of the optimised structure. The strain field for the image on the left was computed from the raw displacement field obtained by Digital Image Correlation, while for the image on the right using finite element analysis. We remark that our DIC approach generated some outliers that shall not be taken into account.

Example	$C^*(S)$	$C^{*,exp}(S)$	Shape S
2	$\begin{pmatrix} 0.12 & -0.05 & 0 \\ -0.05 & 0.12 & 0 \\ 0 & 0 & G \end{pmatrix}$	$\begin{pmatrix} 0.10 & -0.044 & 0 \\ -0.044 & 0.10 & 0 \\ 0 & 0 & G \end{pmatrix}$	
3	$\begin{pmatrix} 0.19 & -0.09 & 0 \\ -0.09 & 0.19 & 0 \\ 0 & 0 & G \end{pmatrix}$	$\begin{pmatrix} 0.204 & -0.09 & 0 \\ -0.09 & 0.204 & 0 \\ 0 & 0 & G \end{pmatrix}$	

Table 4.2: Comparison between the effective $C^*(S)$ (see also Table 3.1) and measured elasticity tensor $C^{*,exp}(S)$ displayed in the left and center column respectively. The right column displays the optimal shape in each case. We recall that the measured elasticity tensor $C^{*,exp}(S)$ was determined by combining DIC measurements and FEM computations.

displacement field in both full-field measurement and simulation, we can notice that the strain field is mostly concentrated on the hinges of the structure. This further emphasises the predominance of structural deformation as a lattice structure with rods and hinges at small strain. A subtle effect of this prevalence is the small effect of the out of plane strain, which should otherwise be perceived as a difference between the 2D modelling during the optimisation process and the complete 3D character of the polymer sheets. Let us also recall that the polymer is practically incompressible and exhibit therefore an important variation of thickness under tensile loading.

The next steps in the analysis of the micro-architected material is the complete experimental measurement of its elastic tensor. Let us recall that the effective constitutive law (1.3.1) is a linear relation between the components of the effective stress and strain, from which the elastic moduli could be identified by a least square fitting. The main difficulty is that only the effective strain, ε_x^* , can be directly measured from the experiment, see values in Table 4.2. However, as suggested in [207], the effective stress, Σ , can be numerically computed from the experimental applied forces if the geometry and the constitutive behaviour of the base material. As a consequence, C^* , the effective elastic tensor of the design phase is obtained as a linear fit from ε_x^* and Σ . The computation can be performed on several unit cells of the specimen. In order to compare the values of the elasticity tensor C^* computed in the design phase, the resultant forces were normalised.

Specimens in examples 2 and 3 feature a behaviour with a quadratic symmetry, which leads to a system of three equations with three unknowns for each unit cell. One has to identify three moduli $C_{1111}^* = C_{2222}^*$, C_{1122}^* , C_{1212}^* using the 11, 22, 12 strain and stress components. The estimated elastic moduli on the central unit cell, i.e., with position (3,3) and coloured red in Fig. 4.2, are displayed in Table 4.2. The C_{1212}^* modulus is missing as the signal to noise ratio of the effective shear strains

and stresses was too small to provide meaningful value.

4.4 Conclusion

The results showed that optimal shapes could be directly printed without additional enhancement of the surface, which is a direct consequence of the smoothed interface technique used in the optimisation. Moreover the manufactured materials had the designed mechanical behaviour. The targeted elastic moduli and the underlying Poisson's ratios have been experimentally attained and the local material behaviour was close to predictions.

The local displacement field computed and measured on the micro-structure showed that measurements match numerical predictions. Moreover one can observe from the strain field that the global deformation is composed of rigid regions and localised hinges, indicating that the structures behave as rotating rigid units.

A possible sequel for this study consists in looking at the response of these specimens under extreme loading, i.e., when the strains are so important that the behaviour goes beyond linear elasticity. This is the purpose of the next chapter (see also [4]).

Chapter 5

Systematic two-scale image analysis of extreme deformations in soft architected sheets

Contents

5.1	Introduction	93
5.2	Materials and methods	95
5.2.1	Unit cell architecture	95
5.2.2	Fabrication of natural rubber architected sheets	96
5.2.3	Experimental setup and testing	96
5.2.4	Local and global Digital Image Correlation	98
5.2.5	Numerical simulations	99
5.3	Results and discussion	100
5.3.1	Numerical simulations	100
5.3.2	Two-scale kinematic analysis	102
5.3.3	Truss-hinge equivalent kinematic model	106
5.4	Concluding remarks	109

State-of-the art image processing methods combined with numerical and analytical models provide a comprehensive quantitative description of architected sheets and their global behaviour, including the influence of the boundary conditions, of the manufacturing process, and of geometric and constitutive non-linearities. To this end, an adapted multi-scale digital image correlation analysis is used to track both elongations and rotations of particular features of the unit cell at the local and global (homogenised) scale of the material. This permits to observe with unprecedented clarity the strains for various unit cells in the structure and to detect global deformation patterns and heterogeneities of the homogenised strain distribution. This method is here demonstrated on elastic sheets undergoing extreme longitudinal and shear deformations, but it can be extended to guide the design of two-dimensional architected solids featuring other regular, quasi-regular or graded patterns, and subjected to other types of loads.

5.1 Introduction

Architected sheets are a particular class of two-dimensional solids whose patterned designs are tailored to achieve a variety of exceptional mechanical behaviours, including extreme stretchability, auxeticity and morphing capabilities [40, 52, 60, 153, 108, 159, 201, 235]. They are increasingly seen as applicable to fields ranging from stretchable electronics, medical and biomedical engineering [7, 127, 129, 148, 251], to the sport equipment and textile industries

[78, 90, 134, 192, 253], and they have witnessed significant advances in their design and fabrication. When it comes to designing techniques, modern numerical methods such as shape and topology optimisation [8, 32] have become prevalent in this realm, leading to more sophisticated and often unimaginable geometries [95, 181, 244, 250, 254]. Present day techniques even permit to incorporate geometric non-linearity and manufacturability constraints in the design optimisation [68, 247, 263]. At the same time, digitally controlled manufacturing techniques such as photolithography [234], 3D printing [180, 241], water jetting [69] and laser cutting [170, 235] now permit to fabricate architected solids with unprecedented complexity and at a continuously decreasing cost.

Despite these breakthroughs, unleashing the potential of these systems demands advanced methods suitable for the experimental investigations on the deformation patterns and mechanical behaviour, which are to date in their early stages. In practice, specimens designed for mechanical characterisation usually exhibit highly heterogeneous strain fields associated with: (i) their intrinsic multi-scale behaviour, that can be separated between the microscopic scale (material continuum) and the macroscopic scale (the global scale of the specimen); (ii) boundary layers that emerge from the boundary conditions and the finite size of the specimens; (iii) inherent anisotropic effective properties; (iv) sensitivity to shape imperfections. This high heterogeneity of the strain fields limits the level of identification that can be achieved from experimental measurements. For example, qualitative experimental insights on the behaviour of regions where macroscopic strains can be considered homogeneous have been reported in [161, 170]. As a consequence, only the central region of a specimen is typically used to validate numerical predictions [3, 68, 220], especially when one wants to compute the homogenised properties of the medium. It should be noted that the interaction of scales is a key point for quantitatively understanding the behaviour of architected solids. Experimentally, a precise separation between micro-scale and macro-scale kinematic fields based on a first-order expansion of the fields can be performed, as illustrated in [206]. However, to the best of our knowledge, this technique has hardly ever been adopted in the context of architected solids, being limited to the case of perforated sheets [161]. The complexity of this interaction of scales has additionally motivated the development of reduced-order models [103, 94, 109, 151], to provide a better understanding of the underlying mechanisms and guidelines for design strategies. These reduced models often represent an idealised version of the unit cell, and are inaccurate if not accompanied by robust experimental methods for the calibration of their parameters. On the opposite side of the spectrum of available numerical tools, lie models based on the complete description of the specimen, which are typically used to provide a direct term of comparison with experimental results [190, 199, 113]. The (often small) discrepancies between simulated and measured response have origins at multiple scales. They are either found at the microscopic scale, where the manufacturing process is a source of shape imperfections, or at the macroscopic scale, where applied boundary conditions may distort the unit cell pattern.

The purpose of this chapter is to demonstrate that various state-of-the-art methods in image processing can be combined to provide comprehensive data on the multi-scale response of architected sheets. The developed procedure, applicable to any two-dimensional architected solids, is here applied to investigate the deformation mechanisms of a soft auxetic sheet under extreme longitudinal and shear loading. The acquired images of the structure are first used to identify its exact geometry, which may differ from the designed one due to imperfections in the fabrication process. Meshes are built directly from the identified shape and used both for the measurement of the full kinematic field (via Digital Image Correlation) as for the numerical computations (via the Finite Element Method). It is shown that doing so significantly improves the match between measurements and numerical predictions with respect to models that rely on the as-designed specimen geometry. This highlights the high sensitivity of the mechanical response of the specimen to geometrical imperfections. Then, we provide a two-scale analysis of the measured kinematic field: (i) at the continuum material level (microscopic scale) and (ii) at the unit cell level (macroscopic scale). This leads to the quantification of the macroscopic strain heterogeneities and the characteristic deformation patterns, which are influenced by the boundary conditions as well as the inherent Poisson's ratio of the microstructure. The kinematic analysis

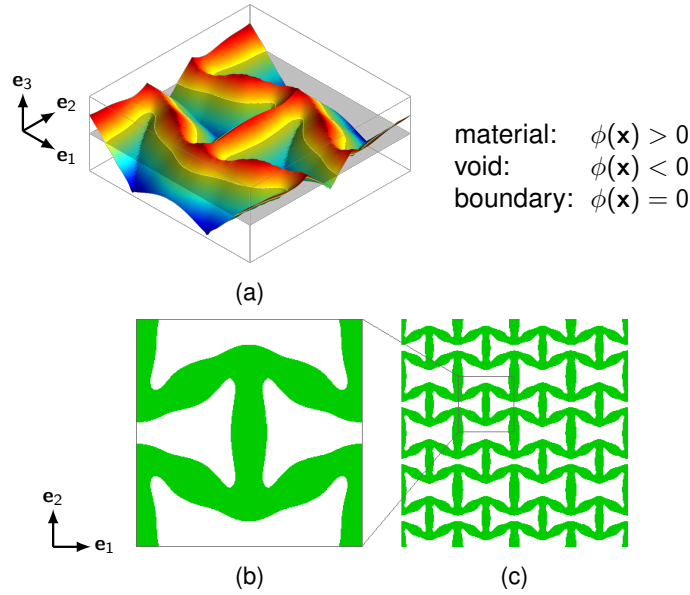


Fig. 5.1: Geometry of the re-entrant honeycomb. (a) Three-dimensional representation of the level set function (signed distance function) ϕ , sliced by the plane $z = 0$. The function results from the topology optimisation procedure of [3]. (b) Unit cell, the boundary is described with the zero level set. The material volume fraction is $|S| = 0.48$. (c) 4×4 repetitive array of unit cells.

is complemented by a procedure aiming at extracting the skeletal representation of the specimen from the experimentally-recorded images. This experimentally-extracted skeleton, whose shape changes during the deformation process, is then used to identify the parameters for an accurate reduced-order model of the architected solid.

The study is organised as follows: section 5.2 provides details on fabrication, experimental setups, testing methods, material models and modelling strategy. The results are reported in section 5.3, and include the material constitutive law calibration, the multi-scale experimental analysis and the numerical simulations. The skeletal representation of the architected sheet geometry is discussed in the same Section. A short summary in section 5.4 concludes the chapter.

5.2 Materials and methods

5.2.1 Unit cell architecture

To demonstrate our approach, we choose to analyse the periodic auxetic microstructure recently proposed in [3] (also discussed in section 3.4.1). The design results from a topology optimisation procedure combining the level set method and the asymptotic homogenisation theory [14, 181] aiming to maximize the auxetic behaviour. The level set function ϕ serves as a base to define the material distribution in the unit cell (see Fig. 5.1(a)), and is defined as the *signed distance function*, for smoothness and regularity purposes. The optimisation problem is formulated as a constrained minimisation problem, where the objective functional to be minimised is a squared distance between the effective elastic moduli over the unit cell and a prescribed elastic moduli C^{target} (refer to chapter 3 for further details). This type of objective functional was first proposed in [249].

Starting from the architecture provided in [3], we merely operate a vertical shift to obtain a symmetric design. The resulting unit cell is depicted in Fig. 5.1(b,c). The designed geometry is a re-entrant honeycomb with a couple of peculiar features. First, the structure is characterised by a repetitive alternation of two types of concave hexagons. Second, the trusses do not have constant width, i.e., the linkages appear slightly thinner than the cores of the bars. This feature is shared with other shapes available in the literature, that also stem from topology optimisation algorithms

based on the level set method aiming to minimize the Poisson's ratio [250, 244]. It is also similar to the bi-mode extremal material presented in [168].

Mechanically, this architected material carries an effective orthotropic behaviour (provided that the base material is isotropic [211]). Assuming an a-priori linear elastic behaviour implies that four independent coefficients need to be identified, namely one (respectively two) effective Young's modulus, two (respectively one) effective Poisson's ratios and the effective shear modulus. The theoretical values of the Poisson's ratios in [3] are $\nu_{12}^* = -1.25$ and $\nu_{21}^* = -0.4$. The complete effective tensor C^* is provided in the results of chapter 3 alongside a discussion on both the elastic behaviour of the unit cell at small strain and the identification of effective elastic coefficients.

The choice to demonstrate our procedure on this specific microstructure is motivated by several reasons. First, this shape is an auxetic material with microstructural deformation mechanisms, which makes it a candidate to be studied using multi-scale approach. Second, its orthotropic behaviour is the most generic state that can be achieved when designing composites with single base material. Third, this architected material is amenable to large strain analyses.

5.2.2 Fabrication of natural rubber architected sheets

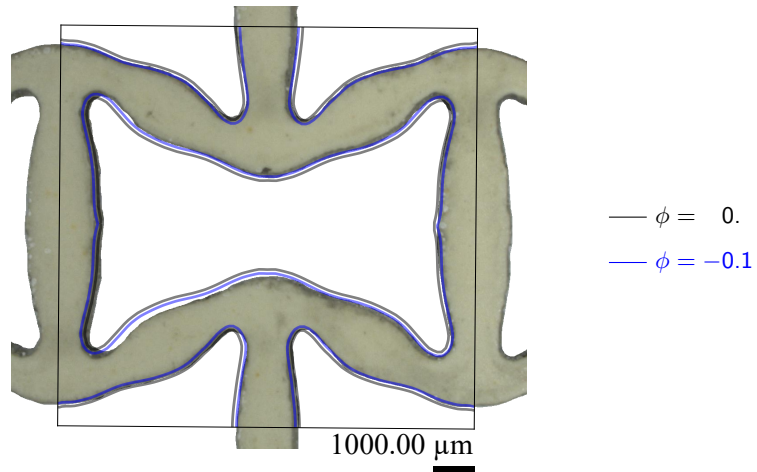
We fabricated three sorts of specimens consisting of periodic assemblages of the unit cell: two specimens designed for uniaxial tension along directions e_1 and e_2 , hereafter referred to as specimens T_1 and T_2 respectively, and one specimen designed for a simple shear test, hereafter referred to as specimen S . The periodic array for each sample is set at:

- 5×8 unit cells for the tensile specimen T_1 (see Fig. 5.2(b)),
- 8×5 unit cells for the tensile specimen T_2 ,
- a sequence of two lattices of 8×5 unit cells for the shear specimen S (see Fig. 5.2(c)). The arrangement is made to balance the torques.

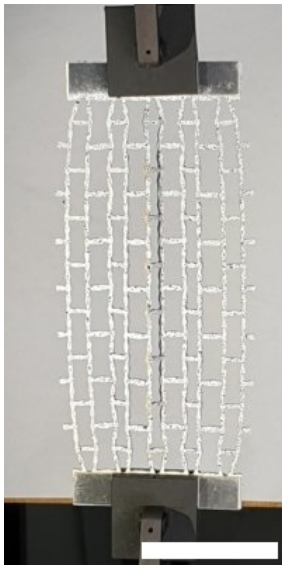
For all specimens, the size of the square unit cell was set at $10 \text{ mm} \times 10 \text{ mm}$, yielding a $50 \text{ mm} \times 80 \text{ mm}$ lattice. The generated pattern is then completed by $50 \text{ mm} \times 10 \text{ mm}$ rectangular solid tabs that permit the clamping to the uniaxial testing machine. The specimens are laser cut from a 1.5 mm-thick natural rubber sheet with a Universal ILS9 120 W laser cutter (single cut at 35% power and 5% speed). To avoid burning the rubber, the machine blows compressed air onto the part being cut. Prior to applying the speckle pattern on the specimens, these are thoroughly washed with standard dish-washing soap.

5.2.3 Experimental setup and testing

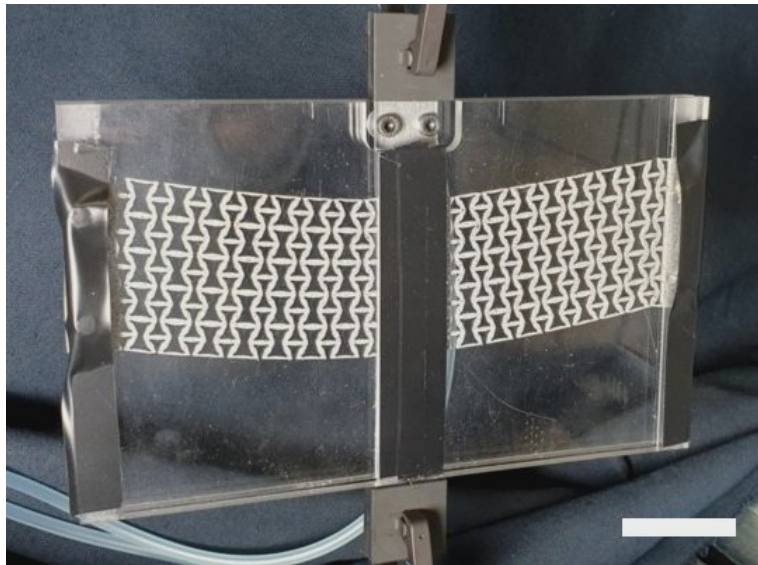
To provide a complete characterisation of the selected geometry, the evolving pattern transformations are investigated through uniaxial tensile and simple shear tests, as shown in Fig. 5.2(b,c). The experiments are conducted under displacement control at a quasi-static strain rate $\dot{\epsilon} = 0.125 \text{ min}^{-1}$ up to 0.5 effective engineering strain for the tensile test and up to 0.45 effective engineering strain for the shear case. The tests are performed on an Instron 10 kN universal testing machine, with a mounted 50 N load cell ensuring accurate measurements down to $\pm 0.1 \text{ N}$. The specimens are clamped at both ends with metallic bars, to constrain their displacement (see Fig. 5.2(b)). The choice of hard clamp, which yield a strain heterogeneity in the specimens, was merely intended to facilitate the description of the boundary conditions in the numerical simulations. Recent works in the literature [255] attempted to apply less constraining boundary conditions using rings and networks ensuring a homogeneous state of strain, at the cost of higher uncertainties on boundary conditions and stress state. For the shear test, a specific setup shown in Fig. 5.2(c) is designed to arrange the specimen in the tensile machine. PMMA confining plates, preventing out-of-plane displacement, are held together at their edges and are attached to the (sliding) upper grip. Conversely, the central rectangular rod is attached to the (fixed) lower grip.



(a)



(b)



(c)

Fig. 5.2: (a) View of a unit cell of the fabricated specimen under a Keyence VHX-1000 optical microscope. (b-c) Setup for the tensile test (specimen T_1 here) and shear test (specimen S). In the shear test, PMMA confining plates are held together at their edges and are attached to the (sliding) upper grip. Conversely, the central rectangular rod is attached to the (fixed) lower grip. Scale bar is 40 mm.

The experiments were piloted using the Instron BlueHill software. Each mechanical test was recorded and used for full-field measurements by Digital Image Correlation (DIC). The recordings were obtained using a high-resolution digital camera (JAI Spark SP-20000-USB camera with a resolution of 5120×3840 pixels equipped with a Tokina AT-X Pro 100 mm F2.8 macro lens), mounted on a perpendicular axis with respect to the plane of the specimen. To improve the precision of the measurements, a gray scale speckle pattern was placed on the sample by aerosol spray. Using an in-built computer program, 8-bit gray scale sub-images were stored every second during the loading, with a resolution of 5064×2438 pixels for the tensile tests and resolution of 2292×2488 pixels for the shear test (the resolution for the shear is approximately two times smaller than in the tensile test because the camera was installed to record the whole specimen, yet only half of the specimen is useful for the observations).

5.2.4 Local and global Digital Image Correlation

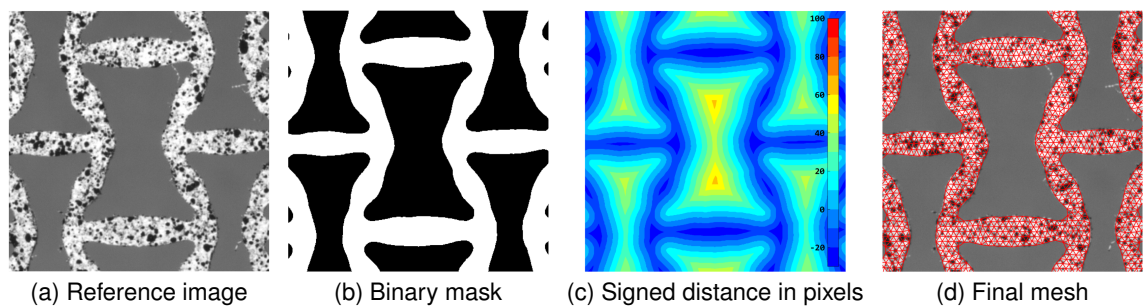


Fig. 5.3: Procedure implemented to build the *experimental* meshes \mathcal{M}^{DIC} . From the reference acquired image of the specimen (a), a binary mask (b) is obtained by thresholding and median filtering. Then the distance transform of the mask is computed, and the obtained signed distance function (c) is used to build the triangulation with a uniform edge length [194].

All the experimental results shown in this work make use of the the Digital Image Correlation technique (DIC) to extract the structure motion from acquired images during the test. DIC procedures are based on the comparison of subsequent pictures of the structure [215]: given a *reference* image G and a *current* image g , the problem consists in finding the displacement field $\mathbf{u}(\mathbf{X})$ which minimizes the differences between the two images over the *Region Of Interest* \mathcal{D} (ROI). The choices of the parametrisation of the trial displacement field $\mathbf{u}(\mathbf{X})$ and the domain \mathcal{D} are the main elements that distinguish: (i) the *local* approach [230], where \mathcal{D} is divided into small sub-domains over which the displacement is assumed to be homogeneous, i.e., $\mathbf{u}(\mathbf{X}) = \mathbf{U}$ and (ii) the *global* approach [228, 37] where the displacement is defined over a finite-elements mesh covering the full ROI \mathcal{D} (i.e., $\mathbf{u}(\mathbf{X}) = \mathbf{N}(\mathbf{X}) \cdot \{\mathbf{u}\}$ with $\mathbf{N}(\mathbf{X})$ containing the finite element shape functions and $\{\mathbf{u}\}$ the nodal displacements to be determined). More details about the theoretical background and implementation are given in appendix C.1.

While the comparison between both approaches in terms of efficiency and accuracy is still a hot topic in the community [115, 207], they are both used for different purposes in the present study. Indeed, the global approach assumes the displacement field continuity over the domain \mathcal{D} , which is well suited for the study of the structure at the *microscopic* scale (corresponding to the material continuum). Conversely, the local approach is employed to follow the motion of features associated to the *macroscopic* scale (corresponding to the pattern periodicity), for example to study the motion of the corner nodes of each unit cell.

All DIC results presented in this paper are obtained from an in-house academic code written by means of MATLAB scripts. For the global approach, linear triangular elements are used for meshing. The meshes are generated following the steps illustrated in Fig. 5.3. Starting from the reference image (i.e., where the specimen is unstrained), a binary mask is obtained employing median filtering and gray level thresholding. The distance transform of the mask is then computed to obtain the *experimental* signed distance function from the specimen boundaries (see

Fig. 5.3(c)). Finally, the mesh of the specimen is generated using the `DistMesh` procedure proposed by Persson [194] from the obtained signed distance function. A uniform edge length of 12 pixels is chosen to correctly capture the localisation of strains in the structure, while keeping a good DIC resolution (sub-pixel accuracy). Hereafter, the resulting mesh is referred as to \mathcal{M}_i^{DIC} (i denotes the specimen name).

Theoretical background and implementation details associated to the DIC procedure are reported in appendix C.1. For both local or global formulations, the DIC is performed iteratively following a Newton–Raphson procedure. The resulting displacement update (eq. (C.1.7)) is used as the convergence criterion (eq. (C.1.12)): the minimisation is stopped when the maximum displacement step is below $\delta = 10^{-3}$ pixels (corresponding to a strain step of approximately 10^{-4} given the chosen edge length).

5.2.5 Numerical simulations

Finite element method implementation. Finite element computations are undertaken under the assumption of large strains plane stress using the finite element solver `Cast3M` [51]. In the simulations, the conditions of the mechanical tests are exactly reproduced, e.g., the sample is loaded in with a prescribed displacement at the two ends. In both cases, the specimen is meshed with $P2$ triangle elements. The geometry of the specimen used for the computations is obtained following two strategies:

- from the *theoretical* level set function ϕ , using image processing to detect and extract the 0-level contour image of the level set function. Hereafter this mesh is referred as to $\mathcal{M}_i^{\phi=0}$ (i denotes the specimen name). For all specimens, the total numbers of elements and nodes are 80,000 and 171,534, respectively. $\mathcal{M}^{\phi=0}$ is perfectly periodic, i.e., it does not embed any geometrical defects;
- from the *experimental* mesh \mathcal{M}_i^{DIC} (used for the global DIC presented in section 5.2.4). The total numbers of elements and nodes for the FE model are 78,380 and 166,982, respectively. By comparison to the theoretical mesh $\mathcal{M}_i^{\phi=0}$, \mathcal{M}_i^{DIC} captures several geometrical imperfections induced by the fabrication process and by the positioning of the specimen in the tensile machine.

Rubber material models. The constitutive behaviour of natural rubber is modelled as an incompressible hyperelastic material. Let $\mathbf{F} = \frac{\partial \mathbf{x}}{\partial \mathbf{X}}$ denote the deformation gradient mapping a material point from the reference position \mathbf{X} to its current location \mathbf{x} . We adopt the Mooney–Rivlin model [173, 204], which is normally acceptable for intermediate elongations, i.e., between 50 -100%. The strain energy function of Mooney–Rivlin hyperelastic constitutive law is expressed as a function of strain invariants $I_1, I_2, I_3 = J^2$ of the left Cauchy-Green tensor $\mathbf{B} = \mathbf{F}\mathbf{F}^T$. The strain energy density function takes the form:

$$W = C_{10}(I_1 - 3) + C_{01}(I_2 - 3) + \frac{1}{d}(J - 1)^2 \quad (5.2.1)$$

where C_{10} , C_{01} and d are material parameters. For the case of an incompressible Mooney–Rivlin material under uniaxial elongation, $\lambda_1 = \lambda$ and $\lambda_2 = \lambda_3 = 1/\sqrt{\lambda}$. Then the true stress (Cauchy stress) differences can be calculated as:

$$\begin{aligned} \sigma_{11} - \sigma_{33} &= 2C_{10} \left(\lambda^2 - \frac{1}{\lambda} \right) - 2C_{01} \left(\frac{1}{\lambda^2} - \lambda^2 \right) \\ \sigma_{22} - \sigma_{33} &= 0 \end{aligned} \quad (5.2.2)$$

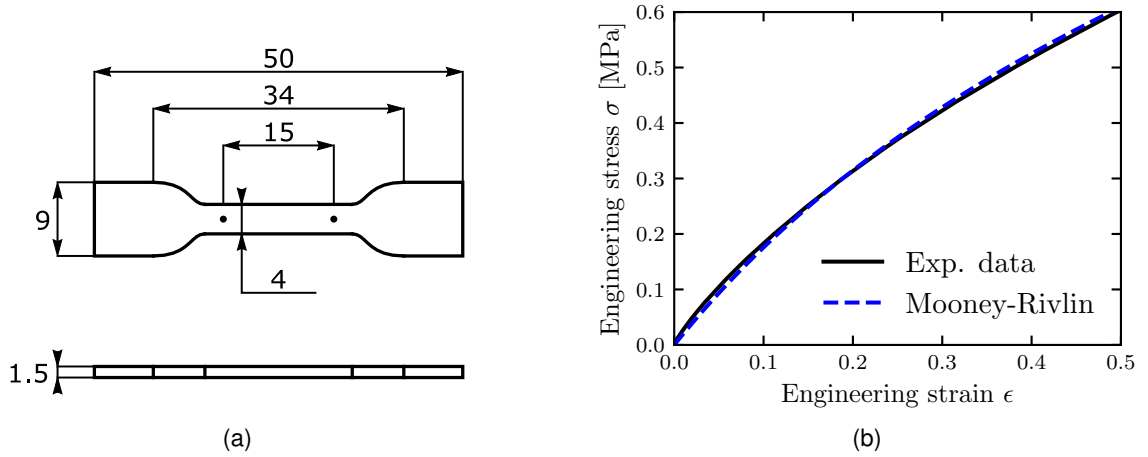


Fig. 5.4: (a) The dogbone geometry with its dimensions in mm. (b) Measured engineering stress-strain response under uniaxial tension. The Mooney–Rivlin hyperelastic model is employed to fit the stress–strain response and calibrate material parameters.

In the case of simple tension, $\sigma_{22} = \sigma_{33} = 0$. Then we can write:

$$\sigma_{11} = \left(2C_{10} + \frac{2C_{01}}{\lambda} \right) \left(\lambda^2 - \frac{1}{\lambda} \right) \quad (5.2.3)$$

and the engineering stress (force per unit reference area) for an incompressible Mooney–Rivlin material under simple tension can be calculated using $\sigma_{11}^{\text{eng}} = \sigma_{11} \lambda_2 \lambda_3 = \sigma_{11} / \lambda = \sigma_{11} / (1 + e_{11}^{\text{eng}})$. Hence:

$$\begin{aligned} \sigma_{11}^{\text{eng}} &= \left(2C_{10} + \frac{2C_{01}}{\lambda} \right) (\lambda - \lambda^{-2}) \\ \sigma_{11}^{\text{eng}} &= \left(2C_{10} + \frac{2C_{01}}{1 + e_{11}^{\text{eng}}} \right) \left(1 + e_{11}^{\text{eng}} - \frac{1}{(1 + e_{11}^{\text{eng}})^2} \right) \end{aligned} \quad (5.2.4)$$

5.3 Results and discussion

5.3.1 Numerical simulations

Calibration of material parameters. The mechanical behaviour of natural rubber is identified from uniaxial tensile tests. Dogbone specimens are fabricated using a cutting die to make specimens for uniaxial tension (the dimensions of test specimens are depicted on Fig. 5.4(a)) and are subjected to the uniaxial tensile tests with a speed of 10 mm/min. The measured engineering stress-strain response is shown in Fig. 5.4(b). It is shown that the Mooney–Rivlin model is suitable to capture the tensile behaviour well up to 0.5 engineering strain for this natural rubber. The material coefficients $C_{10} = 0.199$ MPa and $C_{01} = 0.134$ MPa in the Mooney–Rivlin model for this natural rubber are identified by a non-linear fit from the experimental data.

Shape sensitivity analysis. We first report the measured engineering stress-strain curves for all tests (see Fig. 5.5). For tensile tests (specimens T_1 and T_2), the experiments are juxtaposed to the numerical results (for the shear, the frictions in the setup hinder an experimental estimate of the load.) Fig. 5.5(b) and even more Fig. 5.5(c-d) reveal a significant gap in stiffness between the numerical predictions on the theoretical mesh $\mathcal{M}^{\phi=0}$ (stiffest dashed gray curve) and on the experimental mesh \mathcal{M}^{DIC} . The latter model is in better agreement with the experiments (black curves). The strong differences between the two approaches in the numerical analyses suggest that the material effective stiffness is highly sensitive to the shape uncertainties induced during the laser

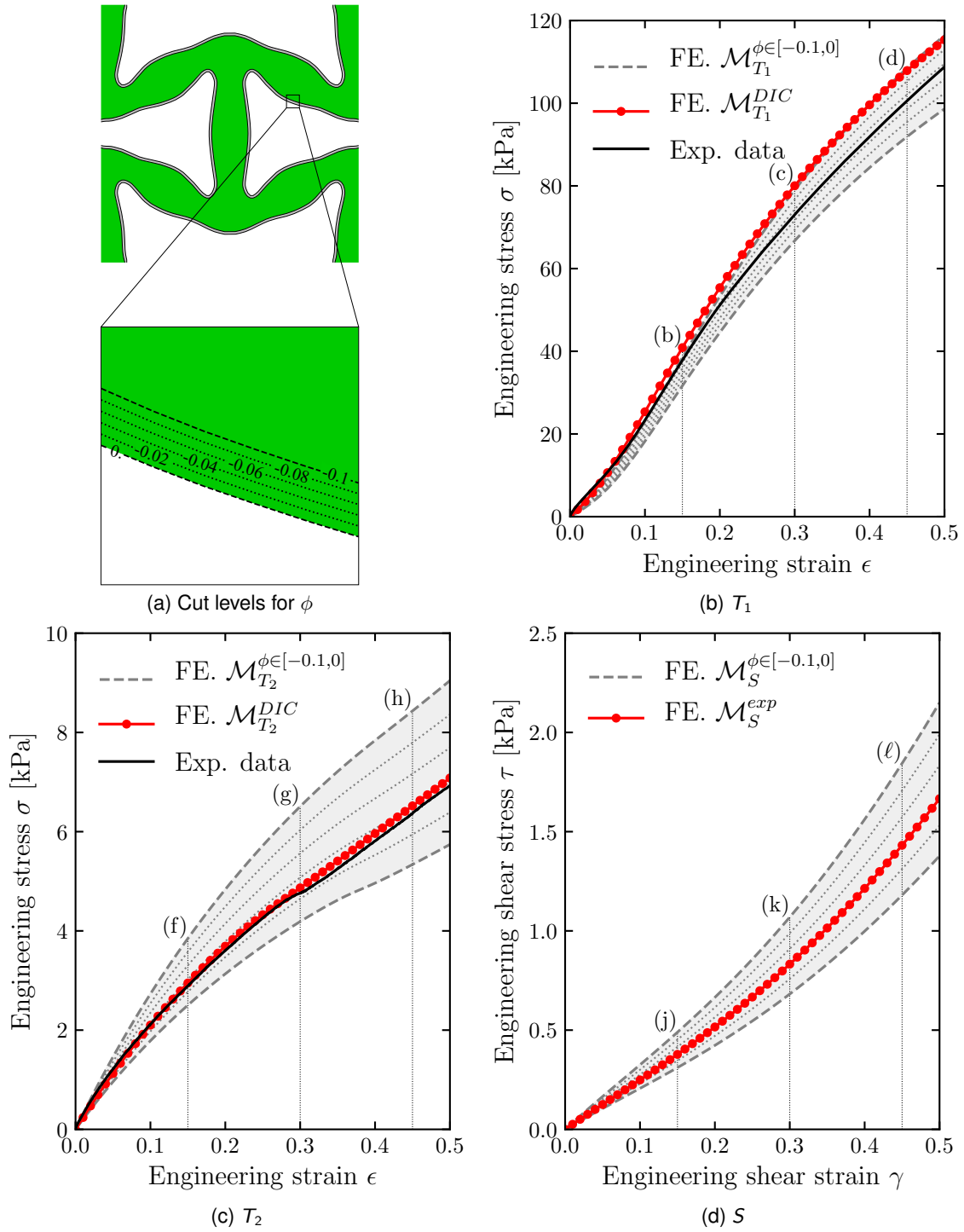


Fig. 5.5: (a) Unit cell contour defined by the level set function ϕ with varying cutting heights. (b-d) Effective stress-strain curves for the structure. Comparison between experiments and numerical simulations with the Mooney–Rivlin hyperelastic model. The shaded gray areas encompass the stress-strain curves for $\phi \in [-0.1, 0]$. The letters appearing at 0.15, 0.3 and 0.45 effective strains refer to the deformed shapes in Fig. 5.6.

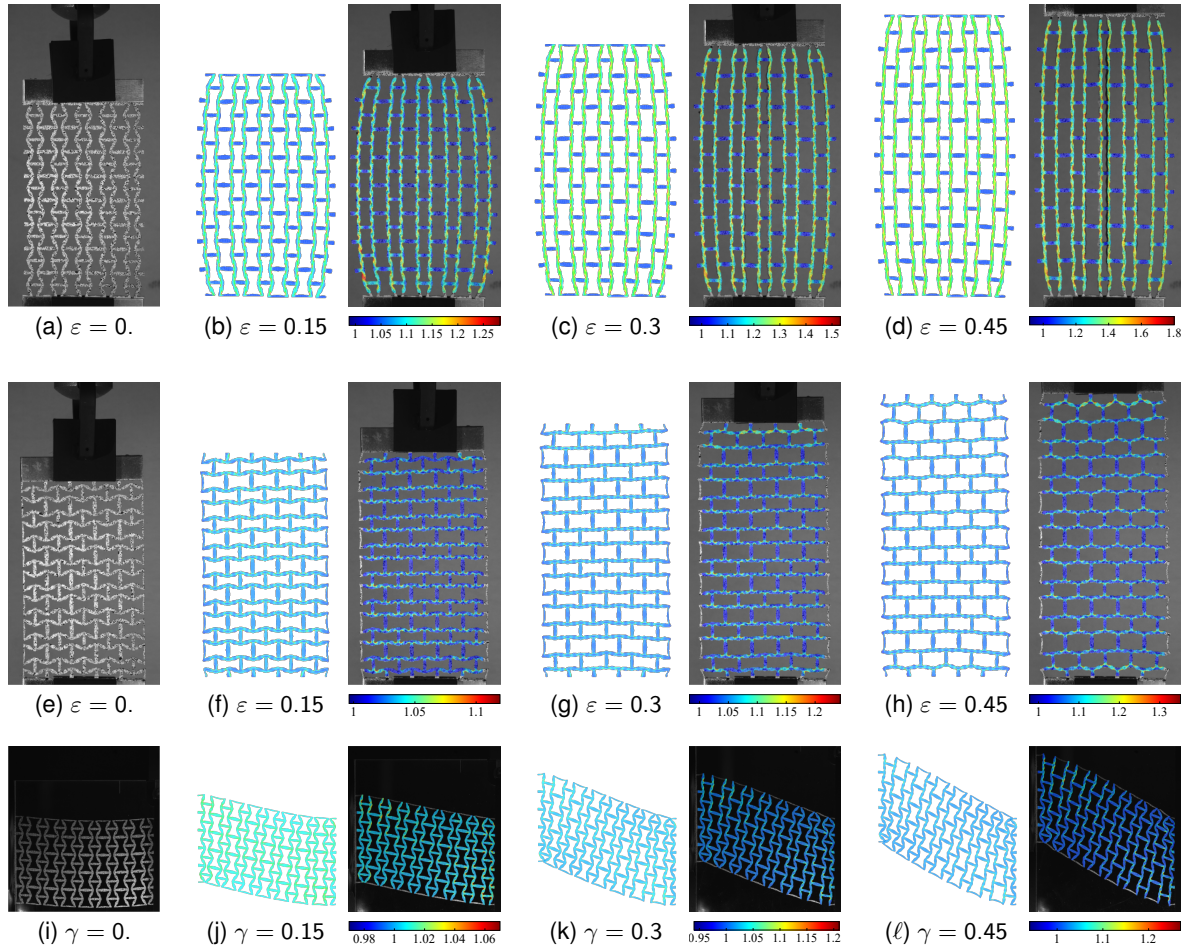


Fig. 5.6: Numerical and experimental deformed configurations of specimens T_1 (a-d), T_2 (e-h) and S (i-ℓ) at different levels of imposed engineering effective strain: 0, 0.15, 0.30 and 0.45. The principal stretch λ_1 is plotted as a colour map in each figure. The colour bar is the same for both the numerical and experimental results.

cutting. To analyse the sensitivity of the mechanical behaviour to shape uncertainty, additional numerical simulations are carried out using *eroded* theoretical meshes, i.e., by progressively reducing the size of the trusses. In practice, we operate an erosion of the contour by introducing a negative offset to the signed distance function ϕ of Fig. 5.1(a). The shapes for offsets varying between -0.1 and 0 , with a step of 0.02 is shown in Fig. 5.5(a). The experimental stress-strain curves of specimen T_2 (Fig. 5.5(c)) are most similar to the eroded model with the level set shifted by -0.06 . Using the properties of the signed distance function ϕ , the experimental specimen is expected to be fabricated with trusses that are roughly $120 \mu\text{m}$ thinner than expected. This gap to the laser cutting process. In hindsight, observing the specimens under an optical microscope (see Fig. 5.2(a)) confirms that these are thinner than expected and also reveals that the error on the thickness is not constant along the trusses. In the following, the simulations performed on the experimental mesh \mathcal{M}^{DIC} are used for the comparison with experiments and general validation.

5.3.2 Two-scale kinematic analysis

Scale of the sheet material continuum. For all the tests, the acquired images of the structure are reported in Fig. 5.6 for stages corresponding to 0, 0.15, 0.3 and 0.45 engineering strain. The principal stretch field λ_1 resulting from the global-DIC procedure performed on a full set of acquired pictures is superimposed to the images. Following the procedure described in section 5.2.4,

the *experimental* mesh \mathcal{M}^{DIC} used to perform the DIC is defined at the reference stage. The obtained displacements fields permit a further comparison with predictions and give an insight on the deformation mechanism of the samples, i.e., how the structure moves and deforms.

In all the tests, the distribution of the elongation (Fig. 5.6) obtained from the displacement field in both full-field measurement indicates that the strain field is mostly concentrated on the hinges of the structure. This emphasizes the predominance of structural deformation at small strain, where different parts of the *lattice* behave as rigid struts and deformable hinges, in spite of the soft natural rubber. For the tensile tests, a lateral expansion indicating a negative Poisson's ratio is visible in both T_1 and T_2 specimens. Despite these general observations, some discrepancies can be noticed between the two tensile specimens. First, the amount of transverse strain is obviously different between specimen T_1 and T_2 , expressing the orthotropic nature of the design. Second, while the most of strain is localised at the hinge regions in the specimens T_2 and S , a clear elongation of the members is identified on specimen T_1 .

Fig. 5.6(b-d) shows that specimen T_1 undergoes a positive strain in the trusses under tension (at 0.15 effective strain, $\lambda_1 \approx 1.15$ in green), whereas the perpendicular members exhibit negative strain (with $\lambda_1 < 1$). This transverse compressive state is responsible for an out-of-plane buckling at ~ 0.15 effective engineering strain. Beyond this stage, a wrinkling deformation is observed i.e., each transverse branch becomes corrugated (see the central unit cells in Fig. 5.2(b), 5.6(c-d)). This particular instability is typical of the clamped boundary conditions imposed on the specimen, responsible for compressive stresses that develop in the transverse direction [55]. The buckling and post-buckling modelling, beyond the scope of the paper, is neither accounted nor permitted in the two-dimensional finite element model. Since DIC measurement is also based on a two-dimensional model, the out of plane deformation appears as compression state in the stretch field in Fig. 5.6(c,d). Looking at Fig. 5.5(b), this illustrates why the numerical simulation (curve in red) perfectly matches the experiment (curve in black) until 0.15 effective engineering strain, while it tends to overestimate the effective stress at larger strains. The maximal relative error between the experiment and the simulation is of 9.5%.

Specimen T_2 remains mostly unstrained at the core of the trusses throughout the test ($\lambda_1 \approx 1$ in blue). The specimen remained in the plane during the whole test. However, unit cells located at its edges experienced snap-through instabilities just before 0.3 effective engineering strain. Indeed, the buckled cells that were almost unstrained in Fig. 5.6(f) become the most strained in Fig. 5.6(g,h). The full movie of the tensile test provided in the supplementary material permits to better appreciate the effect (see Movie 2). This effect is observed in both the experiments and the numerical simulations. This feature is also detected in Fig. 5.5(b) where a local change in the slope of the stress-strain curve corresponding to the relaxation of the center cells accompanying the edge cells snap-through is identified. Note that the samples are *monostable* unlike the examples of [201], i.e., once unloaded, the specimens return to their initial configurations. In Fig. 5.5(c), the numerical simulation (curve in red) correctly matches the experiment (curve in black) until 0.5 effective engineering strain. The small gap that appears around 0.3 effective engineering strain is attributed to the snapping effect which is not captured by the numerical stress-strain curve. The maximal relative error between the experiment and the simulation is of 3%.

Regarding the shear test, specimen S is mounted horizontally (refer to Fig. 5.2(b)). Therefore, its own weight induces an initial bending visible in Fig. 5.6(i). Nonetheless, the role of the weight rapidly becomes negligible as the applied shear load increases ($\gamma > 0.1$). As we establish a relative good agreement between simulation and experiments under uniaxial tension (besides structural instabilities that were not accounted), the finite element method permits to estimate the stress distribution during shear test (see Fig. 5.5(d)). The maximal effective shear stress τ computed numerically is around 1.75 kPa, yielding a resultant load of 0.14N. Note that experimentally, a nearly constant force of 3.5N was measured, mostly indebted to frictional forces in the setup holding the specimen. Since the contributions of the specimen response and the frictional forces could not be separated in the measured load, no experimental load values could be provided for the shear specimen. Moving on to the deformed of the specimen S , we remark, more than in any

$C^*(S)$	$C^{*,exp}(S)$
$\begin{pmatrix} 0.12 & -0.05 & 0 \\ -0.05 & 0.04 & 0 \\ 0 & 0 & 0.006 \end{pmatrix}$	$\begin{pmatrix} 0.1207 & -0.0487 & 0 \\ -0.0487 & 0.0318 & 0 \\ 0 & 0 & 0.0044 \end{pmatrix}$

Table 5.1: Comparison between the effective $C^*(S)$ (see also Table 1 of [3]) and measured elasticity tensor $C^{*,exp}(S)$ displayed in the left and right column respectively. The measured elasticity tensor $C^{*,exp}$ was determined by combining DIC measurements and FEM computations.

other tests of the present work, a strong heterogeneity in the strain field. Rather than experiencing a homogeneous shear, the specimen S undergoes rotations, leaving zones with predominant tension (top left and bottom right of S , see Fig. 5.6(k-ℓ)), predominant compression (top right and bottom left of S), and predominant shear (at the center of S). These observations will be developed in the next paragraphs.

Scale of the unit cell. Next, we intend to analyse the global kinematics of the material, i.e., the averaged kinematic values over the unit cells. To this end, we perform a local-DIC measurement for all the tests. We measure the macroscopic displacement at each node of the lattice, and derive the strain field, depicted in Fig. 5.7. In particular, Fig. 5.7(a,e) illustrate the evolution of the averaged transverse strain with respect to the averaged longitudinal strain for all unit cells of the specimens. The ratio of the averaged strain components (i.e., the slope of the curves) yields the effective Poisson's ratios, ν_{12} and ν_{21} respectively.

At small strain, we can provide the complete experimental measurement of the effective elastic stiffness tensor. Let us recall that the effective constitutive law (1.3.1) is a linear relation between the components of the effective stress and strain, from which the elastic moduli could be identified by a least square fitting. The main difficulty is that only the effective strain, ε^* , can be directly measured from the experiment, see for instance Fig. 5.7. However, as suggested in [207], the effective stress Σ can be numerically computed from the experimental applied forces if the geometry and the constitutive behaviour of the base material are validated. As a consequence, C^* , the effective elastic tensor of the design phase is obtained as a linear fit from ε^* and Σ . The computation could be performed on several unit cells of the specimen, yet here we will merely report the behaviour of the central unit cell. In order to compare the values of the elasticity tensor C^* computed in the design phase we have non-dimensionalised the resultant forces.

For the computations, the elastic moduli of the base material were fixed according to [3] for comparison purposes. Hence, the base material was defined with a Young's modulus $E_m = 0.91$ MPa and with a Poisson's ratio $\nu = 0.3$. Under the plane stress assumption, the components of the elastic tensor of the base material become $C_{1111}^m = C_{2222}^m = 1.0$ MPa; $C_{1122}^m = 0.3$ MPa ; $C_{1212}^m = 0.35$ MPa.

Experimentally, we remark that T_1 is around four times stiffer than T_2 for an effective strain ranging from 0. to 0.1.

At finite strains, the mechanical behaviour shifts rapidly, indicating in particular a decrease of the "auxeticity" of the specimen. Beyond 10% effective strain, both effective Poisson's ratios no longer satisfy the small strain prediction of [3] (reported also in chapter 3). This effect is known in re-entrant honeycombs: the evolution of the Poisson's ratio with applied strain has already been observed and discussed in [245]. Note also that improvements in the design of re-entrant honeycombs using a non-linear material behaviour in the optimisation process would permit to stabilize the Poisson's ratio in a range up to 0.2 engineering strain, as shown in [263].

Strain heterogeneity in the specimen. We further explore the strain heterogeneity in the specimen. The question has an importance in itself, as mathematical optimisation methods are generally defined on unit cells with periodic boundary conditions. Indeed, the interest is often on

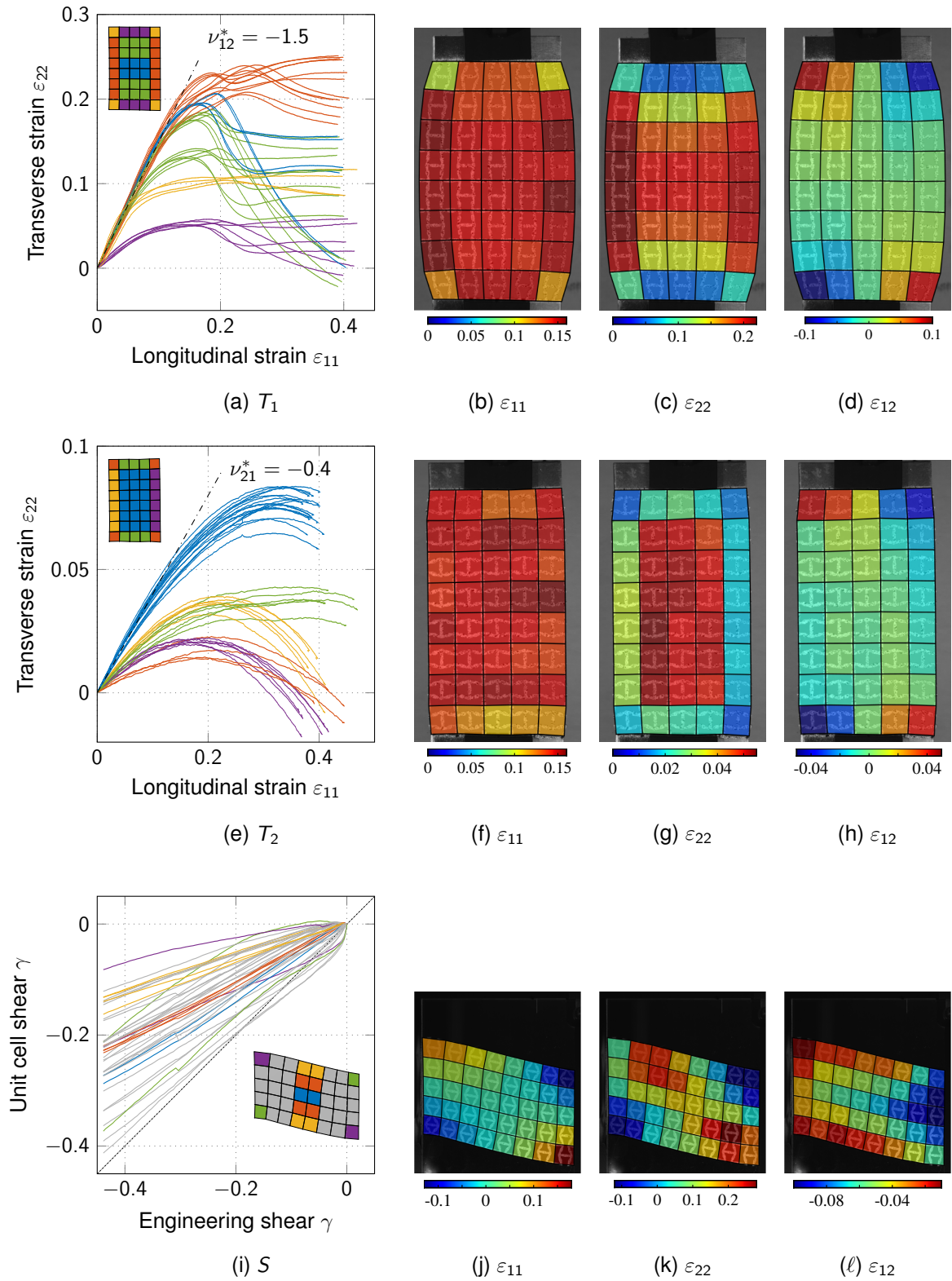


Fig. 5.7: Evolution of the macroscopic transverse strain ε_{22} with respect to the longitudinal strain ε_{11} for specimen T_1 (a) and specimen T_2 (e). Evolution of the macroscopic shear strain ε_{12} with respect to the effective engineering shear strain γ for specimen S (i). The behaviour of the unit cells can be regrouped in bundles represented by different colours. Macroscopic strains maps obtained via *local* DIC at a loading stage of 0.15 engineering strain, (b-d) for specimen T_1 ; (f-h) for specimen T_2 ; (j-l) for specimen S .

the *macroscopic* behaviour of the structure, hence considered as a continuum material with *homogenised* properties. The computation of this macroscopic apparent behaviour from the microscopic unit cell configuration (geometry and material properties) uses the assumption of an homogeneous state of strain in the structure [211], equivalent to considering a specimen of infinite size. However, the specimen size is in practice limited by the experimental setup. As a consequence, boundary conditions applied to the specimen (free surfaces, clamping, etc.) are the source of strain heterogeneities.

In all the tests, the macroscopic behaviour of the cells can be regrouped in *bundles*, identified by curves with different colours in Fig. 5.7(a,e,i). The scatter of the bundles is a evidence of heterogeneity in the specimen.

For specimen T_2 (see Fig. 5.7(e)), there is merely a single line of cells which is affected by the boundary conditions, generally showing a lower transverse strain than center cells: cells associated to the clamped boundaries (in green and yellow) are constrained kinematically, while cells located on free edges (orange and purple) are less strained transversely because of the vanishing transverse stresses. Apart from this boundary layer, the cells in the center of the specimen belong to the same bundle (coloured in blue), thus denoting a uniform state of strain in this region. Hence, the observed cell behaviour can be expected to be close to the homogenised behaviour; this is verified with the macroscopic Poisson's ratio identified close to the theoretical value of $\nu_{21}^H = -0.4$ (dash-dot black line).

By opposition, the specimen T_1 (see Fig. 5.7(a)) shows an highly heterogeneous state of strain, with cell bundles that are more difficult to separate. This is mainly due to the higher absolute value of the Poisson's ratio ($\nu_{12}^H \approx -1.5$, dash-dot black line). At small strain i.e., between 0 and 0.05 effective engineering strain, the specimen is rather homogeneous (besides the purple bundles, the unit cells all follow the same trend). Between 0.05 and 0.15, each bundle sequentially start to behave independently (yellow bundle, then green bundle, orange bundle, etc.). To better appreciate the average strain distribution in the specimen, A video of the test with the superimposed averaged strain field is provided (see Movie 3). We remark that at 0.15 effective engineering strain, we need three lines of cells from the constrained zones to neglect the influence of the boundary conditions. Hence, only the two central lines of the specimen are not affected by the boundary conditions (see Fig. 5.7(c)).

Regarding the shear specimen S (see Fig. 5.6(i-ℓ)), we notice that the unit cells shear strain γ is in general lower than the engineering shear γ_S imposed on the specimen. This is mostly due to the rotation of cells in the center region. In addition, a shear strain gradient is observed in the specimen, with a higher value in the center cells (in blue) that decreases with approaching boundaries (orange and yellow); this is in agreement with the free edge condition at which the shear stresses vanish. Moreover, the corner cells can be separated in two cases. First, bottom-left and top-right cells, in green, are first compressed in the early stages up to a point where contact occurs between members ($\gamma_S \approx 15\%$); then these cells are submitted to more shear in the latter stages. Second, top-left and bottom-right cells, in purple, are mostly stretched because of the specimen curvature. Despite the observed strain heterogeneity, it can be seen that the two center cells in blue are loaded proportionally to the imposed shear (with $\gamma \approx 0.65\gamma_S$).

5.3.3 Truss-hinge equivalent kinematic model

Since the strain distribution of specimen T_2 is localised at the hinges of the structure, we examine whether a simple kinematic model with rigid trusses and rotating hinges (nodes) is sufficient to predict the Poisson's ratio of the structure. To this end, we derive a generic parametrisation of the unit cell of Fig. 5.1 based upon its morphological *skeleton*, which is a "wire" version of the shape that is equidistant to its boundaries. In shape analysis, the *skeleton* is frequently used as shape descriptors as it usually emphasises geometrical and topological properties of the shape, such as its connectivity, topology, length, direction, and width. Interested readers may refer to [171, 132] for a mathematical definition of skeletons and algorithms to compute them. In our

work, the morphological skeleton of our architecture is computed from a rasterised binary version of Fig. 5.1 via the `SkeletonTransform` command from Wolfram Mathematica¹. The obtained result is depicted in Fig. 5.8(a,b) (geometry in black, that was duplicated for a better distinction with the models). We remark that in spite of the relative complexity of the cell geometry, the corresponding skeleton can be approximated by a couple of straight features (beams) and nodes connecting them (hinges), arranged like in a simple re-entrant honeycomb. In particular, two configurations are easily derivable from the skeleton:

- configuration \mathcal{K}_{beams} (depicted in blue in Fig. 5.8(a)) is meant to emphasise the arrangement of the principal beams at the expense of the nodes position. The identification of the beams is easily achieved through a linear fit. The `ImageLines` command from Wolfram Mathematica finds line segments of a rasterised binary image and returns the coordinates of their endpoints. This configuration presumably yields the *smallest* angle between trusses θ .
- configuration \mathcal{K}_{nodes} (depicted in orange in Fig. 5.8(a)) is meant to emphasise the position of the nodes. The identification of the nodes is done manually on the skeleton. This configuration presumably yields the *largest* angle between trusses θ .

Naturally, the real configuration may stand between \mathcal{K}_{beams} and \mathcal{K}_{nodes} . This configuration should accurately predict the evolution of the effective transverse strain ϵ_{22} with respect to the effective longitudinal strain ϵ_{11} observed experimentally. We define it to reproduce as accurately as possible the experimental behaviour:

- configuration \mathcal{K}_{ls} is obtained by finding the angle θ which best fits the experimental experimental curve $\epsilon_{22} = f(\epsilon_{11})$. We use the least square method to find the best angle θ that fits the experimental curve.

Given the equivalent truss-hinge model, we understand the whole unit cell kinematics are merely driven by the only variable angle θ , therefore strain components can be expressed as:

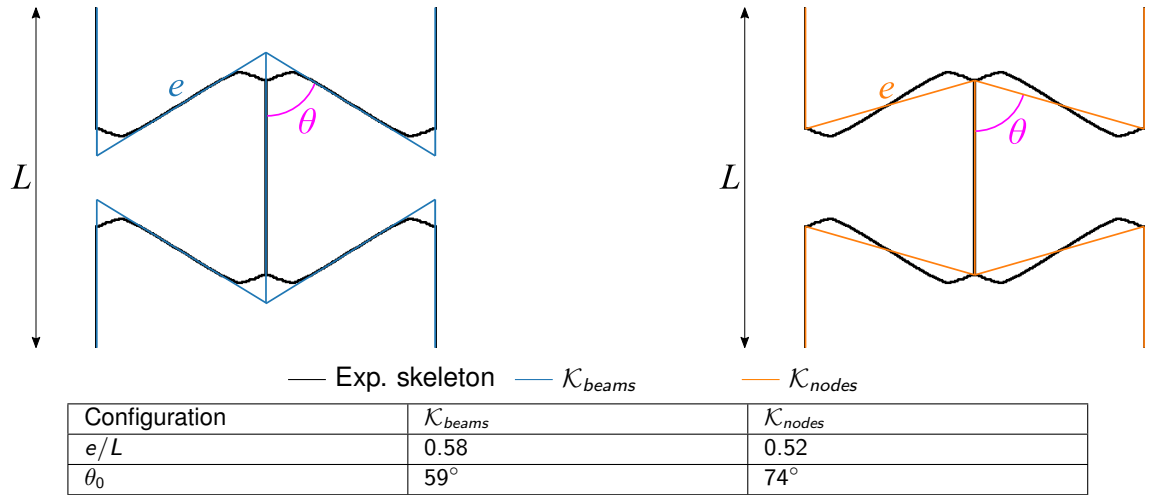
$$\begin{aligned} \text{Longitudinal: } \epsilon_{22}(\theta) &= \frac{2e}{L} (\cos(\theta_0) - \cos(\theta)) \\ \text{Transverse: } \epsilon_{11}(\theta) &= \frac{\sin(\theta)}{\sin(\theta_0)} - 1 \end{aligned} \tag{5.3.1}$$

where L is the characteristic length of the unit cell and θ_0 denotes the initial value of θ (when the structure has not been stretched yet).

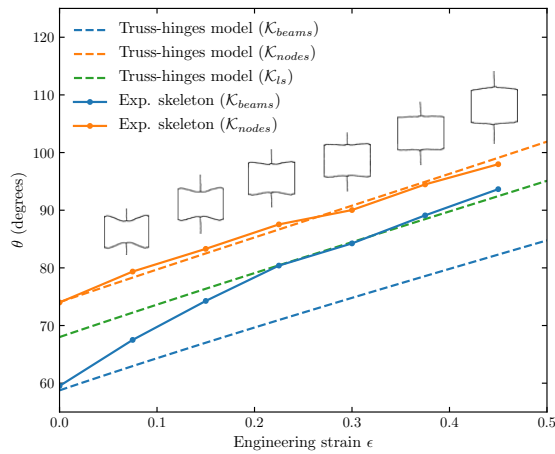
Starting from the images of specimen T_2 recorded during the tensile test, we compute the morphological skeleton of the central unit cell and inferred a measure of the angle θ considering both \mathcal{K}_{beams} and \mathcal{K}_{nodes} . The evolution of θ measured during the experiments is compared to the rigid trusses rotating hinges model (see eq. (5.3.1)) in Fig. 5.8(b) for both \mathcal{K}_{beams} and \mathcal{K}_{nodes} . We remark that configuration \mathcal{K}_{nodes} yield excellent agreement between model and experiments. Conversely, the model using configuration \mathcal{K}_{beams} tends to underestimate the experiments.

Next, we plot the evolution of the transverse strain with respect to the longitudinal strain (Fig. 5.8(c)) at the scale of the unit cell. We remark that the experimental evolution, obtained previously in Fig. 5.7(e), is bounded between the predictions of the two analytical models assuming \mathcal{K}_{beams} and \mathcal{K}_{nodes} . Using the least square method, we obtain that theoretical kinematic evolution (eq. (5.3.1)) best approximates the experiments (curve in black) assuming an initial angle $\theta_0 = 68^\circ$. This configuration corresponds to \mathcal{K}_{ls} . Remarkably, the results for \mathcal{K}_{ls} (dashed green curve) are in excellent agreement with the experiments, despite the simplicity of the model. It is also worth noting that the $\theta_0 = 68^\circ$ case fits particularly well the end of the experimental \mathcal{K}_{beams} (continuous blue curve) in Fig. 5.8(a). The obtained results support the idea that a rigid trusses rotating hinges kinematic model is suitable to predict the deformation pattern of specimen T_2 in spite of the soft elastomer used in the fabrication of the specimens.

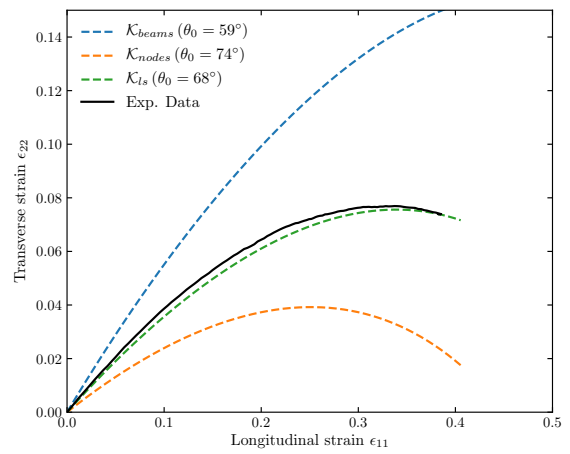
¹version 11.2, 2018



(a)



(c)



(d)

Fig. 5.8: truss-hinge model. (a) Parametrisation assuming configuration \mathcal{K}_{beams} (blue) and \mathcal{K}_{nodes} (orange) superimposed to the skeleton of the unit cell (black). (c) and (d): corresponding kinematic data with both experimental values (continuous curves) and predictions from equation (5.3.1) (dashed curves). (c) Hinge aperture angle θ as a function of the effective engineering strain. Experimental data is identified from the pictures of the tensile tests at different strain levels. The skeletal representation of the central cell for various strain level are included. (d) Interdependence of the macroscopic strain components. The experimental curve is a mean of the blue bundle in Fig. 5.7(e).

5.4 Concluding remarks

In this work, we have introduced a multi-scale experimental analysis designed to completely characterise the behaviour of architected sheets undergoing extreme deformation. Our techniques have been applied to the analysis of a soft, auxetic sheet subjected to large tensile and shear loads (up to 0.5 effective strain). Based on this analysis, we are able to:

- gain insight on the strain distribution of the specimen and identify the zones that have uniform strain field. This identification is particularly simple in our study, owing to our reconstruction of the macroscopic strain (the averaged kinematic values over each unit cell);
- determine that strain heterogeneities dominate the response of finite-size specimens and that, to accurately capture the tensile response of an infinite sheet, the number of unit cells should be greater than four in both horizontal and transverse directions;
- use the wealth of information obtained from the experiments to create a reduced order model (featuring rigid trusses and flexible hinges) that accurately describes the kinematic behaviour under tensile loads;
- determine that, despite the strong heterogeneity displayed by the shear test results, it is possible to identify zones in the center of the specimen where the shear state is proportional to the applied engineering shear strain.

As an outlook, the proposed procedures could benefit from a proper quantification of the errors associated to the identified data. This uncertainty analysis could be inspired from works already available in the literature [41, 252, 214]. The tools presented in this study can be readily adapted to any two-dimensional architected solid undergoing small or large deformations [235, 170, 152]. In turn, the results that can be obtained by using these methods can potentially be leveraged to create tunable and stretchable mechanical devices [127, 148].

Part III

Design of 3D printable thin composite panels

Chapter 6

Shape-shifting panel from 3D printed undulated ribbon lattice

Contents

6.1	Introduction	113
6.2	Design of the unit cell	115
6.3	Extension–bending coupling (EBC) mechanism	116
6.3.1	Deformation mechanisms of undulated ribbons	117
6.3.2	From undulated ribbons to architected unit cells	117
6.3.3	Influence of h^* and t^*	120
6.3.4	Extension–bending effect for smaller Poisson’s ratio interval	121
6.3.5	Influence of a varying stiffness along the height	122
6.4	Analysis of fabricated polymer panels	123
6.4.1	Additive manufacturing	123
6.4.2	Mechanical testing	124
6.5	Conclusion and perspectives	126
6.5.1	Projects associated	127

A novel microstructure with extension–bending coupling effect is designed and fabricated. It is obtained with a single material as a network of undulated ribbons. Ribbon lattice are easy to design and fabricate, and offer a wide range of tunable properties. The deformation modes and deformation mechanisms of the unit cells are investigated both under small strain assumption combining asymptotic homogenisation with Kirchhoff–Love plate theory (section 1.4), and at finite strains relying on numerical analysis. Patterned specimens are manufactured and are mechanically loaded in tension at finite strain. The displacement measured by point tracking match the predictions from the finite element simulations and indicate that the structure maintain its properties at finite strain. The design concept provides a framework to be harnessed in morphing and deployable structures for a wide range of scales.

6.1 Introduction

The morphing of shell-based structures into programmable three-dimensional geometries is a ubiquitous mechanism found in nature, which is attracting increasing interest for technological applications [185]. In engineering, flat panels are traditionally enticing due to their high strength-to-weight ratio which makes them structurally efficient. Including programmability into such structures expands the potential of available manufacturing techniques and increases the fabrication throughput for three-dimensional objects of complex geometries [107, 131, 159]. In addition, it unleashes new functionalities suitable for exploring harsh or inaccessible environments [137, 202]

and delivering increasingly large and complex payloads [28, 58]. Several concepts have already been reported for a broad range of length scales, from minimally invasive surgery [66, 203], to automotive [72], aeronautics [6] and up to space sector [22, 59, 123].

Systems with shape-shifting capacities are obtained through “transformation mechanisms”, tailored by the micro-architecture of the material. Recent advances in digital manufacturing technologies such as 3D printing [139, 158, 241] and laser cutting [170, 220, 235] have opened the way to a wide range of novel micro-architectures that couple locally prescribed in-plane kinematics to changes in curvature. These micro-architectures can be regrouped into model classes: origami structures, which feature axially-rigid but potentially-flexible panels connected by foldable creases, may be turned into nearly arbitrary shapes [86, 189, 256]. Yet, due to the independent folding motions of individual folds, they are challenging to fold [48, 77] or actuate. Kirigami tessellations, i.e., cut-patterned panel, allow compact flat shapes to conform approximately to any prescribed target shape in two or three dimensions [60, 134, 200]. Folding and cut patterns may be combined to design shape-shifting concepts as demonstrated in [179]. Compliant mechanism-like structures, featuring bendable trusses or hinges are suitable to shape three-dimensional objects with desired geometrical sizes and aspect ratios [52, 135], but due to the thin connections at the hinges, they are mechanically weak. Ribbon- and membrane-like flat structures can buckle out of plane and produce three-dimensional geometries when subject to mechanical actuation [53, 62, 258]. Lastly, bilayers sheets can morph into three-dimensional surfaces with non-zero Gaussian curvature [105, 242], but their fabrication is complex.

Most systems are paired with mechanical actuations through manual forming, boundary loading, or through the release of a pre-stretched layers. By releasing pre-stretched shape memory layers, it is possible to control the deformation in time, which is an essential feature to prevent collisions while undertaking complex morphing [84, 108, 160]. Other studies make use of pneumatic power to mechanically load the shapes [202, 221]. Alternatively, combining shape-morphing structures with multiphysics phenomena further opens up the space for various actuation mechanism. Self-actuation enables autonomous structural adaptation to changing environmental stimuli. For example, self-shaping concepts have been demonstrated in shells through hydrogel swelling [101, 154, 177], nematic-to-isotropic phase changes in liquid-crystal elastomers [136, 197], and using piezo-electric actuation [39, 105]. Multiple materials in heterogeneous lattice designs enabled unprecedented morphing capacities with complex and doubly curved shapes (e.g., a human face) [40]. Nevertheless, complex shapes remain difficult to achieve experimentally, as they often require advanced multi-material 3D printers with long and costly fabrication.

In this chapter, we propose a novel class of microstructures consisting in a combination of undulated ribbons, parametrised using B-spline surfaces. The undulations feature an asymmetry along the height that is leveraged to obtain an extension–bending coupling (EBC) mechanism. The unit cell is tessellated periodically to generate panels with programmable morphing capabilities when subject to mechanical actuation. While single undulated ribbons do not exhibit specific coupling mechanics, we demonstrate that their interconnection starts the mechanism. We then discuss the mechanical properties of a particular unit cell, computing the complete elastic stiffness tensor via two-scale homogenisation with thin plate theory. The range of achievable EBC ratio is then assessed with respect to the geometric parameters of the unit cell. We demonstrate that the EBC ratio is not degraded under finite strain up to 20%. Ribbon-based specimen are manufactured using a desktop fused filament fabrication 3D printer and are mechanically tested for validations. Both experiments and numerical simulations are conducted to measure the out of plane local mechanical fields. The present work distinguishes itself for the simplicity of fabrication and actuation, and for its potential applicability in material and structural systems at vastly different scales; it therefore illustrates a potential base to be harnessed in combination with responsive materials for the actuation of soft robots, compliant systems and reconfigurable structures, as alternatives to external mechanical motors, control systems and power devices.

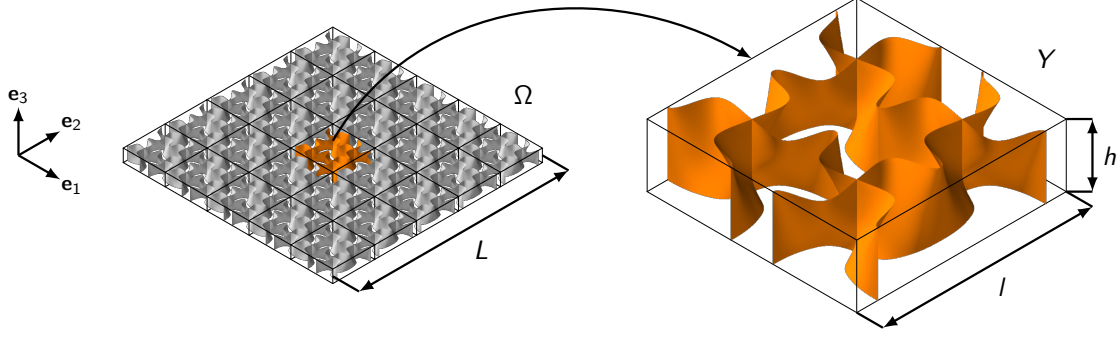


Fig. 6.1: architected panel Ω with a periodic arrangement of 5×5 unit cells. The unit cells are composed of structural shells parametrised by B-spline surfaces. The thickness of the shell t is not depicted (only the mid-surface is shown). The displayed unit cell is obtained following the procedure described in section 6.2. It has an aspect ratio $h^* = h/l = 0.3$.

6.2 Design of the unit cell

Let us consider an architected panel occupying a plane domain Ω , of characteristic in-plane dimension L , and of height h , as sketched in Fig. 6.1. It is a periodic or graded compound of quadrangular building blocks, referred to as *unit cells* and denoted as Y , of characteristic in-plane dimension l . The unit cells consist in a network of undulated ribbons of constant thickness t creating a composite similar to open cell foams described in [98, 23]. As unit cells may be scaled to various sizes, we define a rescaled unit cell Y^* characterised by two dimensionless parameters: the unit cell aspect ratio, $h^* = h/l$ and the normalised thickness, $t^* = t/l$. The material distribution inside the cell is parametrised using multiple B-spline surfaces, i.e., a bivariate vector-valued piecewise rational function of degree p in the u direction and degree q in the v direction respectively:

$$\mathbf{S}(u, v) = \sum_{i=0}^n \sum_{j=0}^m N_{i,p}(u) N_{j,q}(v) \mathbf{P}_{i,j}, \quad (6.2.1)$$

where $\mathbf{P}_{i,j}$ is a bidirectional net of control points (CP), while $N_{i,p}(u)$ and $N_{j,q}(v)$ are the B-spline basis functions [195]. The choice of the control points $\mathbf{P}_{i,j}$ is made with the aim to engender the extension bending (EBC) effect in the panel. It is achieved manually, according to the following design procedure:

1. Select five filament based two-dimensional unit cells with a negative effective Poisson's ratio equally dispersed within $[-0.8, 0.]$ (see Fig. 6.2(a)).
2. Thanks to the multiple symmetries, the parametrisation is restricted to a bundle of elementary corrugated branches, modelled as B-spline curves with five CP [195]. The global number of control points is reduced as all unit cells are sharing the end points and therefore only three independent CP per curve suffice to control the effective Poisson's ratio of each unit cell (see Fig. 6.2(b,d)).
3. CP for each B-spline curve (from Fig. 6.2(b)) are uniformly distributed along the thickness according to the desired height. Using a B-spline surface parametrization, ribbons are constructed as *lofted* surface, depicted in Fig. 6.2(c) and feature a two-fold undulation: (1) an in-plane corrugation stemming from the 2D microstructures and (2) a continuously varying profile along the height. Fixing the outermost CP for all curves ensures a resulting vertical border and permits the construction of the unit cell and of the periodic pattern by symmetry.

This ribbon-based unit cell encompasses a continuous stacking of two-dimensional shapes with varying effective Poisson's ratio. Hence, we can recover any two-dimensional unit cells that attain any effective Poisson's ratio between -0.8 and 0 by taking a slice of the micro-architected

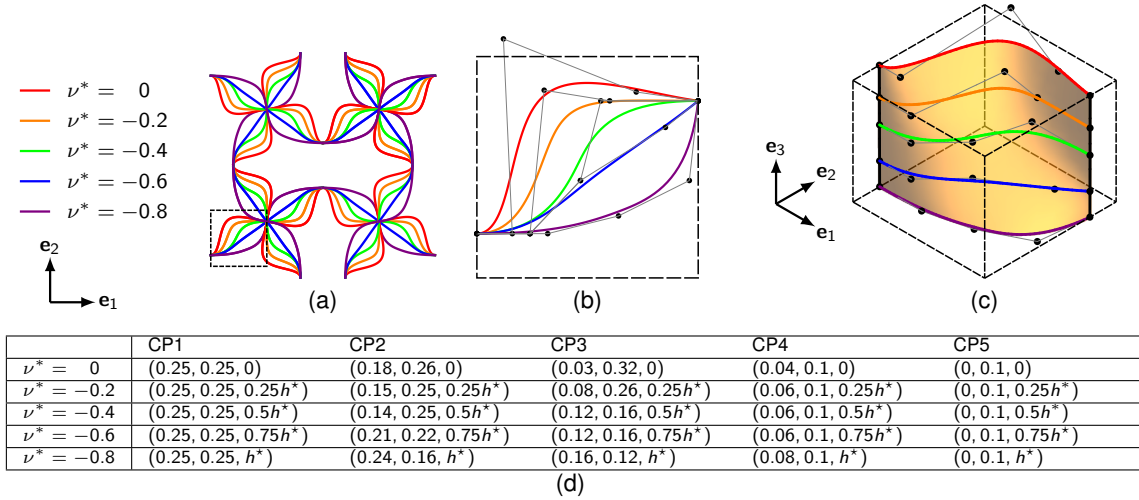


Fig. 6.2: B-spline parametrisation. (a) Class of architected materials, inspired by Clausen et al. [68]. The boxed branches on the bottom left are the most basic pattern required to reconstruct the whole unit cell. (b) elementary pattern parametrised using B-spline and their control points (CP). (c) B-spline surface built upon the uniform distribution of the CP in (b) along the thickness. (d) Coordinates of the CP defining each of the five B-spline curves needed to build the surface. The reported value are for a cell of characteristic length $l = 1$.

panel at the corresponding height. We recall that materials with a negative Poisson's ratio, also called auxetics, expand transversally under a uniaxial stretching. They often derive this property from microstructural deformation mechanisms that typically involve rotations [83, 142], which can confer enhanced mechanical properties. To date, several types of auxetic materials have been reported [102, 103, 261]. This class of auxetic unit cells considered here was first reported in [68] and stems from a topology optimisation with the objective to exhibit a prescribed effective Poisson's ratio over finite deformations of up to 20%. The choice to use these shapes was motivated by the following reasons: (1) In comparison with other shapes in the literature designed using topology optimisation [3, 95, 263], they are featuring high geometrical simplicity (arrangement of curved beams with constant thickness t), which is suitable for design flexibility, and manufacturability. In particular, they are adapted for specific additive manufacturing technologies based for example on wire deposition, such as Fused Filament Fabrication for polymers, or Wire Arc Additive Manufacturing for metals. (2) They share a common generic configuration, which simplifies their tessellation and enables a global parametrization using design points and B-spline curves (as shown in Figure 4 in [68]). (3) They were designed to maintain their auxetic effect at finite strains. This feature confers to the panel constant EBC effect at finite strain, as it will be shown in the sequel.

Finally, let us remark that the proposed design procedure based on stacking of filament unit cells using B-splines and lofted surfaces is not restricted to the present choice, neither as in-plane geometries nor in terms of symmetries, and opens up a new direction to create shell like panels.

6.3 Extension–bending coupling (EBC) mechanism

The extension-bending coupling (EBC) mechanism is investigated first by analysing the behaviour of a single undulated ribbon under tension in order to exhibit the particular features at the origin of the EBC effect. Then, the effective behaviour of the panel is numerically identified at small and finite strain. A parameter analysis permits to evaluate the variation of mechanical properties characterising the EBC effect against the geometrical parameters of the unit cell. Finally, the influence of a graded stiffness in the ribbon on the EBC effect is briefly discussed.

The analysis is based on finite element computations and is conducted using the solver Cast3M [51]. The parametric B-spline surfaces are triangulated by discrete Kirchhoff triangular (DKT)

shell elements [27, 233] to generate a discrete shell model. The ribbon material is considered to be elastic, isotropic and quasi-incompressible, with parameters $E^0 = 0.7599$ MPa and $\nu^0 = 0.49$. They yield a *normalised* in-plane elastic stiffness in tension, i.e., $A_{1111}^0 = A_{2222}^0 = 1.0$ MPa (under plane stress assumption) which simplifies the analysis for applications under an assumption of a linear elastic behaviour.

Displacement and rotation are vector valued functions in the Cartesian system of coordinates $(\mathbf{e}_1, \mathbf{e}_2, \mathbf{e}_3)$. For convenience, in-plane displacements will denote the components along \mathbf{e}_1 or \mathbf{e}_2 , while displacements along \mathbf{e}_3 are referred to as out of plane displacement. Meanwhile, rotations of cross sections around \mathbf{e}_3 are denoted as in-plane rotations, while rotations around \mathbf{e}_1 or \mathbf{e}_2 are referred to as out of plane rotations and characterise the bending deformation of the panel.

6.3.1 Deformation mechanisms of undulated ribbons

In order to understand the EBC effect, we propose to compare the kinematic deformations patterns of single undulated ribbon oriented along \mathbf{e}_1 under a uniaxial tensile load, with the deformation of the same ribbon connected with a transverse ribbon respecting the architecture of the panel. For all cases the effective strain reaches 10% and is applied assuming periodic boundary conditions and planes of symmetry as depicted for different cases in Fig. 6.3.

For the single ribbon, computed components of rotations and displacement fields along \mathbf{e}_3 are displayed in Fig. 6.3(a,d). As the ribbon elongates, the initial in-plane corrugations *unfold* through a bending mechanism about the \mathbf{e}_3 axes and align with the loading direction \mathbf{e}_1 . The bending is localised in the regions with a vertical cross-section oriented along \mathbf{e}_3 which exhibit an in plane rotation. These regions are denoted as “faces” that bend about \mathbf{e}_3 in Fig. 6.3(a)). In the zone of ribbon crossing, the displacement of the ribbon stays in-plane, with $u_3 \approx 0$, as illustrated in Fig. 6.3(d)). Furthermore the out of plane rotations are vanishing and the in plane rotation is constant, characterising the in-plane deformation of the ribbon and the absence of bending. Next, Fig. 6.3(b,e) exhibits the results of the tension of the same ribbon connected with a free transverse ribbon and show that the system will equally remain in-plane and will not bend out of plane. As expected, the transverse ribbon will simply rotate in plane as imposed by the crossing line of the longitudinal ribbon, as discussed before. See Fig. 6.3(b) for details.

For connected ribbons, with an imposed symmetry boundary conditions at the extremities of the transverse ribbon, an out-of-plane bending is revealed, as shown in Fig. 6.3(c,f). Now, upon pulling on the longitudinal ribbon, the transverse ribbons is also submitted to a bending load along \mathbf{e}_3 . As the longitudinal ribbon elongates, both in plane and out of plane bending of the transverse ribbon is observed about the \mathbf{e}_3 and \mathbf{e}_1 axes respectively. In other words, the longitudinal ribbon is tilted at the connection line, yielding out of plane deflection in the transverse ribbon (Fig. 6.3(f)). We conclude that the shifting mechanism is driven by the coupled in-plane and out of plane bending occurring inside the ribbons.

6.3.2 From undulated ribbons to architected unit cells

The quantitative estimation of the EBC effect can be obtained analysing the effective material behaviour, i.e., obtained as the ratio of the averaged stiffness and strain over the unit cells. The precise technique is defined by the two-scale homogenisation method applied to periodic plates. Due to the great number of unit cells in Ω , the dimension of the periodic cells l is assumed to be much smaller than L (i.e., $l/\epsilon = \mathcal{O}(L)$, where ϵ tends to 0), but is assumed to be comparable to h (i.e., $l = \mathcal{O}(h)$). Furthermore, the thickness t is assumed to be much smaller than l and h (so that we verify the shell assumption). In practice, we assume:

$$0.1 \leq h^* \leq 10, \quad t^* \leq 5h^*. \quad (6.3.1)$$

To interpret the observed bending in terms of effective material parameters, we need to map the behaviour within the classical Kirchhoff–Love plate theory (see Appendix A.1 for a short recall).

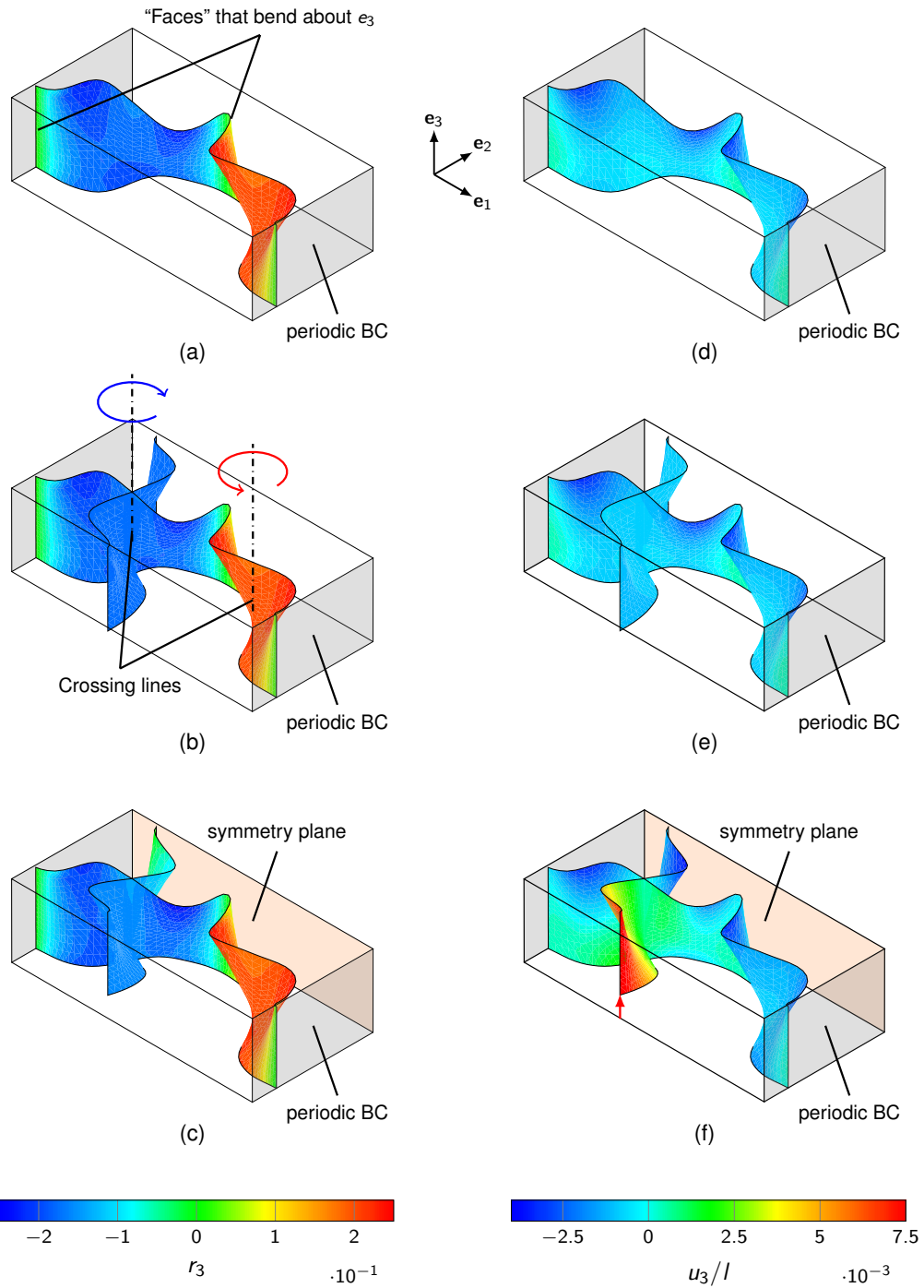


Fig. 6.3: Numerical results on ribbon blocks subjected to periodic boundary conditions, loaded in tension up to 10% effective strain. The aspect ratio is $h^* = h/l = 0.3$ and the normalised thickness is $t^* = t/l = 0.05$. In all figures, the deformed along the direction e_3 is amplified ten times. (a-c) In-plane rotation field r_3 (about e_3) plotted as a colour map on the deformed ribbon. The colour bar on the left applies to the three cases. (d-f) Out of plane displacement field u_3 (normalised by l) plotted as a colour map on the deformed ribbon. The colour bar on the left applies to the three cases. (a,d) Uniaxial response of a single undulated ribbon. (b,e) Are the same as (a,d), but we attach a transverse undulated ribbon. The free transverse ribbon undergoes an in-plane rotation about the e_3 axis, but no significant out of the plane displacement is reported. (c,f) The transverse ribbon is submitted to a symmetry condition ($u_2 = 0$, $r_3 = 0$), which reveals an out of plane displacement u_3 .

The constitutive behaviour of a general thin plate reads:

$$\begin{bmatrix} \mathbf{N} \\ \mathbf{M} \end{bmatrix} = \begin{bmatrix} \mathbf{A} & \mathbf{B} \\ \mathbf{B} & \mathbf{D} \end{bmatrix} : \begin{bmatrix} \boldsymbol{\varepsilon} \\ \boldsymbol{\chi} \end{bmatrix}$$

where \mathbf{N} and \mathbf{M} are the membrane stress and bending moments per unit width. Units are: $[\mathbf{N}] = \text{N.m}^{-1}$ and $[\mathbf{M}] = \text{N}$. The plate kinematic is described by the in-plane (membrane) strains $\boldsymbol{\varepsilon}$ and the out-of-plane curvatures $\boldsymbol{\chi}$. Units are: $[\boldsymbol{\varepsilon}] = \text{m.m}^{-1}$ and $[\boldsymbol{\chi}] = \text{m}^{-1}$. The tensor \mathbf{A} describes the in-plane behaviour, the tensor \mathbf{D} describes the bending behaviour, and their coupling is expressed through the tensor \mathbf{B} . Units are: $[\mathbf{A}] = \text{N.m}^{-1}$, $[\mathbf{B}] = \text{N}$ and $[\mathbf{D}] = \text{N.m}$. Note that in most engineering applications, where panels feature symmetric geometry and material distribution along the thickness, normal and shear behaviour get uncoupled for the membrane part, yielding $\mathbf{B} = 0$.

Homogenisation of plates with periodic microstructure was first studied by Caillerie [46], as well as Kohn and Vogelius [133]. A recall on the derivation of the linearised effective equations for infinitesimal deformation of panel with periodic microstructure is provided in 1.4, while interested readers may refer to [210, 163] for more extended explanations. Assuming a composite panel made of two isotropic phases (material and void in this case), the constitutive behaviour for Kirchhoff–Love thin plate exhibits an orthotropic behaviour in the most general case [210], hence it reads in its component form:

$$\begin{bmatrix} \mathbf{A}^* & \mathbf{B}^* \\ \mathbf{B}^* & \mathbf{D}^* \end{bmatrix}_{(h^*, t^*)} = \begin{bmatrix} A_{1111}^* & A_{1122}^* & 0 & B_{1111}^* & B_{1122}^* & 0 \\ A_{1122}^* & A_{2222}^* & 0 & B_{2211}^* & B_{2222}^* & 0 \\ 0 & 0 & A_{1212}^* & 0 & 0 & B_{1212}^* \\ \hline B_{1111}^* & B_{2211}^* & 0 & D_{1111}^* & D_{1122}^* & 0 \\ B_{1122}^* & B_{2222}^* & 0 & D_{1122}^* & D_{2222}^* & 0 \\ 0 & 0 & B_{1212}^* & 0 & 0 & D_{1212}^* \end{bmatrix} \quad (6.3.2)$$

Superscripts * denote an effective or homogenised quantity, defined at the macroscopic scale of the panel. For instance, the effective Young's modulus, Poisson's ratio and shear modulus are denoted as E^* , ν^* , and G^* respectively, hereinafter. In equation (6.3.2), the in-plane elastic moduli depend on h mainly according to $1/h$, whereas the flexural moduli depend on h mainly according to $1/h^3$.

Example of effective plate elastic stiffness tensor. In a rescaled unit cell with $h^* = 0.3$ and $t^* = 0.05$, the material volume fraction is of 26.7% and its constitutive tensor reads:

$$\begin{bmatrix} \mathbf{A}^* & \mathbf{B}^* \\ \mathbf{B}^* & \mathbf{D}^* \end{bmatrix}_{(0.3, 0.05)} = 10^{-3} \begin{bmatrix} 4.18 & -1.89 & 0 & 0.01 & 0.45 & 0 \\ -1.89 & 4.18 & 0 & 0.45 & 0.01 & 0 \\ 0 & 0 & 0.74 & 0 & 0 & 0.44 \\ \hline 0.01 & 0.45 & 0 & 1.05 & -0.14 & 0 \\ 0.45 & 0.01 & 0 & -0.14 & 1.05 & 0 \\ 0 & 0 & 0.44 & 0 & 0 & 1.02 \end{bmatrix} \quad (6.3.3)$$

Units are: $[\mathbf{A}] = \text{N.mm}^{-1}$, $[\mathbf{B}] = \text{N}$ and $[\mathbf{D}] = \text{N.mm}$.

The matrices \mathbf{A}^* , \mathbf{B}^* and \mathbf{D}^* are symmetric and exhibits an *quadratic* symmetry, i.e., the plate has the same tensile (respectively bending) stiffness along e_1 and e_2 . $A_{1122}^* < 0$ indicates an effective auxetic behaviour of the unit cell. An underlying effect accounted by $D_{1122}^* < 0$ is to undergo synclastic curvatures [141], i.e., shifting from flat to a dome shape under bending. The main non-vanishing coupling stiffness is B_{1122}^* . It links the in-plane stress along e_1 (respectively e_2) to the transverse curvature about e_1 (respectively e_2). This suggests that the EBC effect exists primarily between the longitudinal in plane displacements and the out of plane bending curvature, which is

in agreement with the concept of overlaying profiles with varying Poisson's ratios. We also note the presence of a coupling between the shears B_{1212}^* .

The elastic moduli, $A_{\alpha\beta\gamma\delta}^*$, $B_{\alpha\beta\gamma\delta}^*$ and $D_{\alpha\beta\gamma\delta}^*$ can be expressed in terms of materials parameters E^* and ν^* . We further introduce the effective longitudinal extension – transverse bending coupling ratio, referred in the sequel as to EBC ratio and denoted by β^* .

$$E^* = \frac{1}{h^*} A_{1111}^* \left(1 - \left(\frac{A_{1122}^*}{A_{1111}^*} \right)^2 \right) \quad \nu^* = \frac{A_{1122}^*}{A_{1111}^*} \quad \beta^* = \frac{1}{h} \frac{B_{1122}^*}{A_{1111}^*} \quad (6.3.4)$$

The division by h is here to obtain a dimensionless quantify.

Complementary investigations using the elastic compliance tensor. Complementary information on the plate deformation kinematics can be retrieved from the compliance tensor $S = (C)^{-1}$. The values in each row permit to assess the deformation modes for a given elementary load and indicate directly the final deformed shape. The compliance tensor for the rescaled unit cell discussed in eq. (6.3.3) reads:

$$\begin{bmatrix} (S^A)^* & (S^B)^* \\ (S^{\top B})^* & (S^D)^* \end{bmatrix}_{(0.3,0.05)} = \begin{bmatrix} 327.7 & 158.3 & 0 & -91.5 & -154.1 & 0 \\ 158.3 & 327.7 & 0. & -154.1 & -91.5 & 0 \\ 0 & 0 & 1818 & 0 & 0 & -784.0 \\ -91.5 & -154.1 & 0. & 1043 & 179.8 & 0. \\ -154.1 & -91.5 & 0. & 179.8 & 1043 & 0. \\ 0. & 0. & -784.0 & 0. & 0. & 1319. \end{bmatrix} \quad (6.3.5)$$

Units are: $[S^A] = \text{mm} \cdot \text{N}^{-1}$, $[S^B] = \text{N}^{-1}$ and $[S^D] = \text{mm}^{-1} \cdot \text{N}^{-1}$.

Again the compliance moduli, $(S_{\alpha\beta\gamma\delta}^A)^*$, $(S_{\alpha\beta\gamma\delta}^B)^*$ and $(D_{\alpha\beta\gamma\delta}^D)^*$ can be expressed in terms of materials parameters E^* and ν^* . Besides, a second effective longitudinal extension – transverse bending coupling ratio, referred in the sequel as to EBC ratio and denoted by γ^* .

$$E^* = \frac{1}{(S_{1111}^A)^*}, \quad \nu^* = -\frac{(S_{1122}^A)^*}{(S_{1111}^A)^*}, \quad \gamma^* = -\frac{(S_{1122}^B)^*}{(S_{1111}^A)^*}. \quad (6.3.6)$$

6.3.3 Influence of h^* and t^*

Next, we investigate the variations of the effective stiffness of the unit cell, as a function of the aspect ratio of the panel h^* , or the normalised thickness of the ribbons t^* . The analysis is numerically performed by varying: (i) h^* from 0.1 to 1 with a step of 0.02 and; (ii) t^* from 0.002 to 0.05 with a step of 0.002, provided both h^* and t^* satisfy the inequalities (6.3.1). The results are reported against the material volume fraction ρ/ρ^0 of the cell, which facilitates comparisons with standard materials property charts [87]. Estimations from the three-dimensional numerical models indicate that f is depending linearly to t^* , while it is almost unaltered by h^* .

Investigation under small strain assumption. The distribution of effective Young's modulus E^* , normalised by the base material modulus E^0 , is mapped against the volume fraction ρ/ρ^0 for different values of h^* in Fig. 6.4(a). It is proportional to the cube of the volume fraction. Conversely, its dependence on the aspect ratio h^* is much less pronounced, i.e., a unit cell of aspect ratio h^* is about as stiff as a pile of n unit cells of aspect ratio h^*/n . Macroscopically, this ribbon based unit cell is highly compliant, the Young's modulus E^* being from two to six orders of magnitude lower than its bulk equivalent (see base elastic coefficients in section 6.3 above). Next, the distribution of the EBC ratio γ^* (Fig. 6.4(b)) indicates the effect is stronger for smaller aspect ratios h^* . Moreover, we report that for $h^* > 0.25$, the EBC ratio γ^* is almost independent from the normalised thickness t^* , while for $h^* < 0.2$, the EBC ratio is affected by t^* . All things considered, E^* and γ^* can be tailored relatively independently. On a side note, the effective Poisson's ratio ν^* does not depend

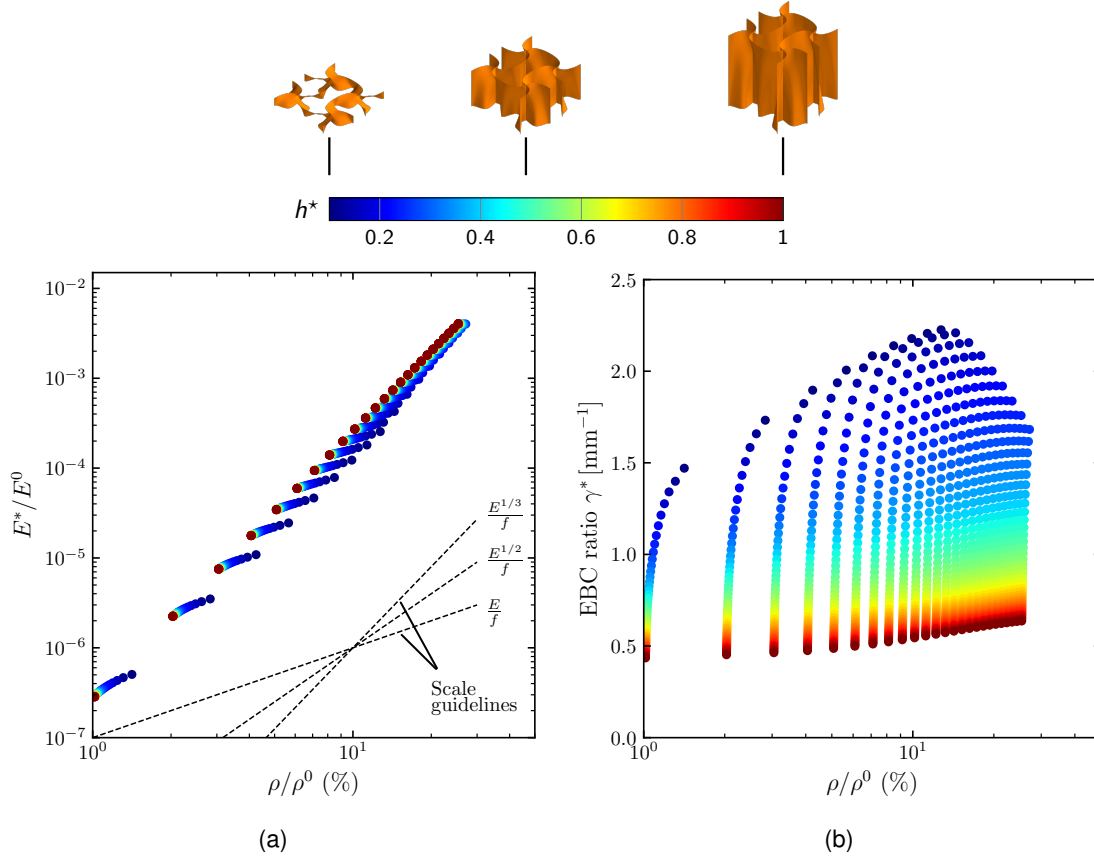


Fig. 6.4: Parameter analysis with respect to h^* and t^* . Material property charts (a) Normalised effective Young's modulus E^*/E^0 versus material volume fraction ρ/ρ^0 . Performances of these architected materials can be mapped in already existing material property charts, like in [87], for further comparisons with other materials. (b) EBC ratio γ^* from equation (6.3.6) versus material volume fraction ρ/ρ^0 . The colour bar on the top applies for both plots. The unit cells associated to specific heights are also depicted. These plots must be compared with results obtained in our original paper [5].

particularly depend on h^* and t^* . Its average value ≈ -0.4 matches the expectations considering the overlaying of initial two-dimensional profiles with an effective Poisson's ratio in range between -0.8 and 0 .

Uniaxial extension at finite strain. To characterize the out of plane capacities of the unit cell at finite strain up to 20% under uniaxial tension, a strip of 5 unit cells was loaded using periodic boundary conditions along the transverse direction of the strip, while longitudinal direction was traction free. Several characteristics of the transverse deflection angle per unit cell θ^* are displayed in Fig. 6.5. In particular, Fig. 6.5(a), represents the deformed strip of unit cells and the definition of the transverse deflection angle θ^* . The EBC effect as function of h^* , illustrated through the evolution of the transverse deflection angle as a function of engineering strain is exhibited in Fig. 6.5(b,c). However, for a fixed value of $h^* = 0.5 > 0.25$, θ^* is almost unaffected by t^* as shown in Fig. 6.5(c). Similar to [68], one can equally remark that the evolution of the deflection angle with respect to the engineering strain follows a linear trend, which indicates that the EBC ratio remains constant for deformations up to 20%.

6.3.4 Extension–bending effect for smaller Poisson's ratio interval

We have seen the effect of the aspect ratio h^* and of the normalised thickness t^* on the EBC effect. Let us now demonstrate how the EBC effect can be further tailored when h^* and t^* are a

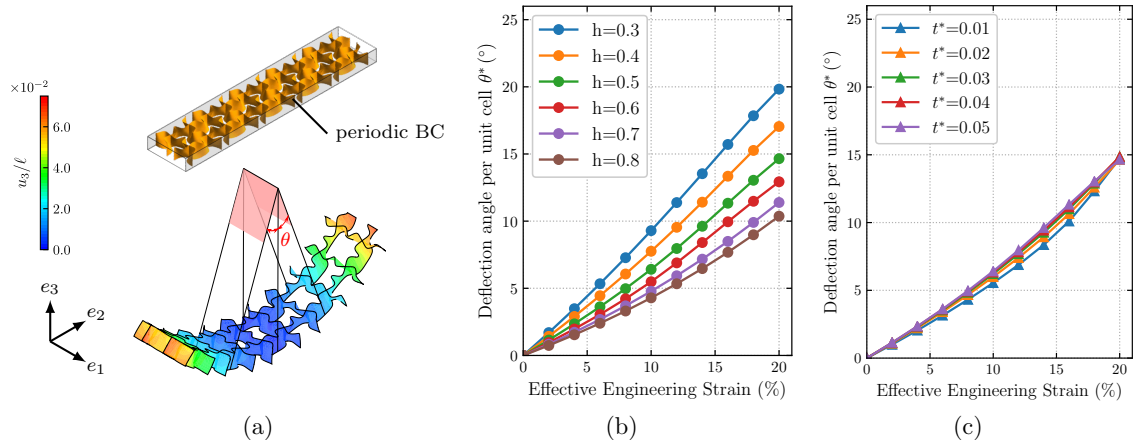


Fig. 6.5: (a) Deformed configuration under tension along e_1 up to 20% effective strain, with imposed periodic BC at front and rear faces. The deflection angle θ^* per unit cell induced in the direction perpendicular to the loading is illustrated. For different loading values, nodes at the two lateral boundary of the central cell (normal vectors to the faces are $-e_1$ and e_1) form two planes (depicted in pink). A least square fit permits to calculate the cartesian equation of these two planes, which in turn yields the deflection angle θ^* . (b) Evolution of θ^* against the longitudinal effective engineering strain. t^* is set at 0.05, h^* is varying. (c) Same as (b), but now h^* is set at 0.5, t^* is varying.

priori constrained (e.g., by manufacturing requirements). To address this point, a rather simple but efficient method consists in restricting the interval of initial curves - in the other words, consider a small interval of spanning Poisson's ratio. The domain of Poisson's ratio, denoted by d^* , is defined to express the interval of selected Poisson's ratio. A value of $d^* = 1$ indicates that the considered interval of Poisson's ratio spans from -0.8 to 0. At the opposite a value of $d^* = 0$ suggest that the three-dimensional unit cell is obtained by extruding the two-dimensional curve corresponding to $\nu^* = -0.4$.

We investigate the variations of the effective stiffness of the unit cell, as a function of the aspect ratio of the panel h^* , or the normalised thickness of the ribbons t^* . The analysis is numerically performed by varying d^* from 0.1 to 1 with a step of 0.1 and. The results are reported against the material volume fraction ρ/ρ^0 of the cell, which facilitates comparisons with standard materials property charts [87]. Estimations from the three-dimensional numerical models indicate that f is depending linearly to t^* , while it is almost unaltered by h^* .

The distribution of effective Young's modulus E^* , normalised by the base material modulus E^0 , is mapped against the volume fraction ρ/ρ^0 for different values of d^* in Fig. 6.6(a).

6.3.5 Influence of a varying stiffness along the height

A literature survey, see [130] and the references within, show that EBC effects in panels can be triggered in porous panels, provided the porosity density varies through thickness. Varying the materials properties along the thickness implies varying the elasticity properties or equivalently the thickness of the ribbons. As expected, a variation of the normalised Young's modulus E^*/E^0 along the panel's height h^* by a factor ranging from 1 to 10 engenders visible EBC effects. Fig. 6.7 presents a comparison of the deflection pattern of three panel comprising 5×5 unit cell of subject to an uniaxial tensile loading of 10% with (a) homogeneous, (b) increasing, (c) decreasing Young's modulus with height, respectively. The expected dome-shape out of plane deflection of the panel with a uniform E^* over the ribbons, is amplified for a decreasing Young's modulus with height. However, an increasing Young's modulus with height will trigger a a novel saddle-shape deformation of the panel. This example reveals that a variation of the material properties of the ribbons add a novel shape shifting dimension to the family of ribbon based unit cells.

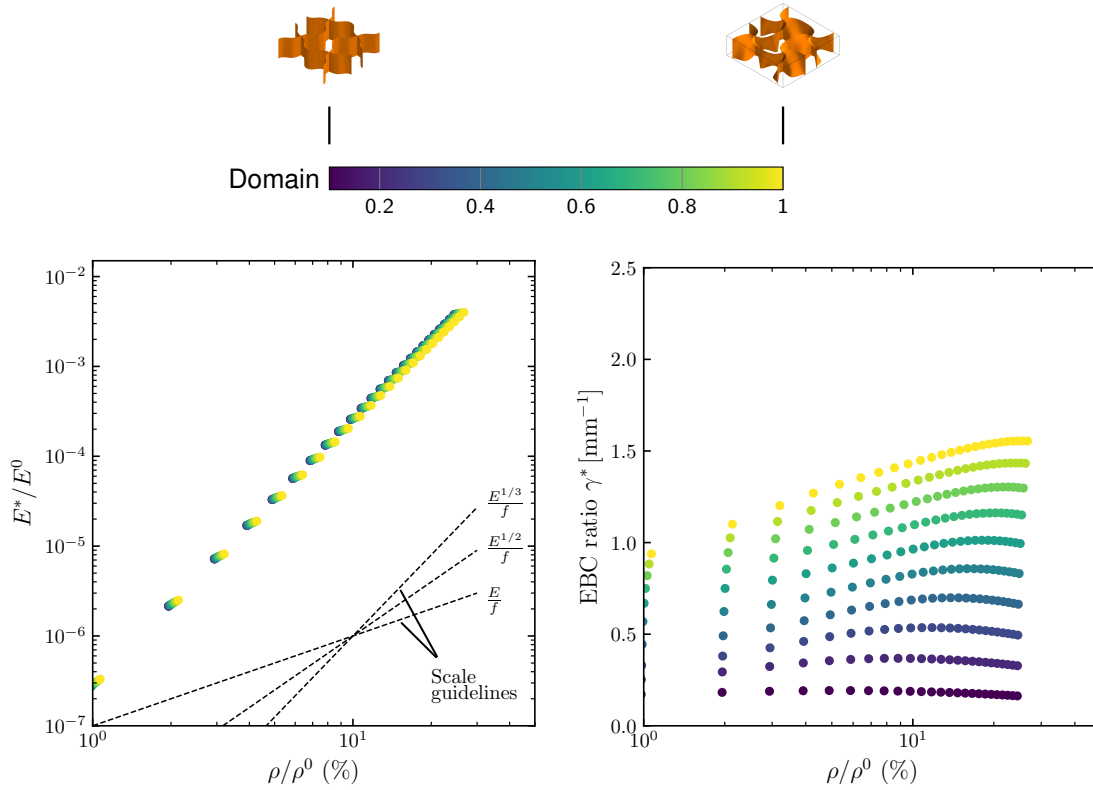


Fig. 6.6: Parameter analysis with respect to h^* and t^* . Material property charts (a) Normalised effective Young's modulus E^*/E^0 versus material volume fraction ρ/ρ^0 . Performances of these architected materials can be mapped in already existing material property charts, like in [87], for further comparisons with other materials. (b) EBC ratio β^* from equation (6.3.4) versus material volume fraction. The colour bar on the right applies for both plots. The unit cells associated to specific heights are also depicted.

6.4 Analysis of fabricated polymer panels

6.4.1 Additive manufacturing

Specimens of architected panels with ribbon-based unit cells have been additively manufactured with fused filament fabrication technology (FFF) using a commercial Ultimaker 3D printer and a thermoplastic polyurethane filament TPU 95A with a diameter 0.4mm ¹. The choice of TPU 95A was motivated by its compliant nature and capacity to undergo large deformations, i.e., $> 20\%$ strain without breaking.

The three-dimensional volume model of the unit cell was obtained by computing the normal vector field of the B-spline surface and by shifting it along the normal to create the upper and lower surfaces. The upper and lower surfaces are then completed with the bottom and top boundary a closed envelope. The complete envelope is triangulated exported as a watertight STL mesh. The specimen is a periodic array of 5×5 unit cells with $h^* = 0.3$ and $t^* = 0.05$. The dimension of the unit cell is $l = 16\text{mm}$ and conducts thus to a panel with $L = 80\text{mm}$ of dimensions $80\text{mm} \times 80\text{mm} \times 4.8\text{mm}$. The generated pattern was completed by a series of rings to ensure the fixing within the testing machine. The non-conventional ring fixture and the underlying boundary conditions is discussed in the next section.

¹Characteristics of TPU 95A filaments are provided here: <https://support.ultimaker.com/hc/en-us/sections/360003556679>

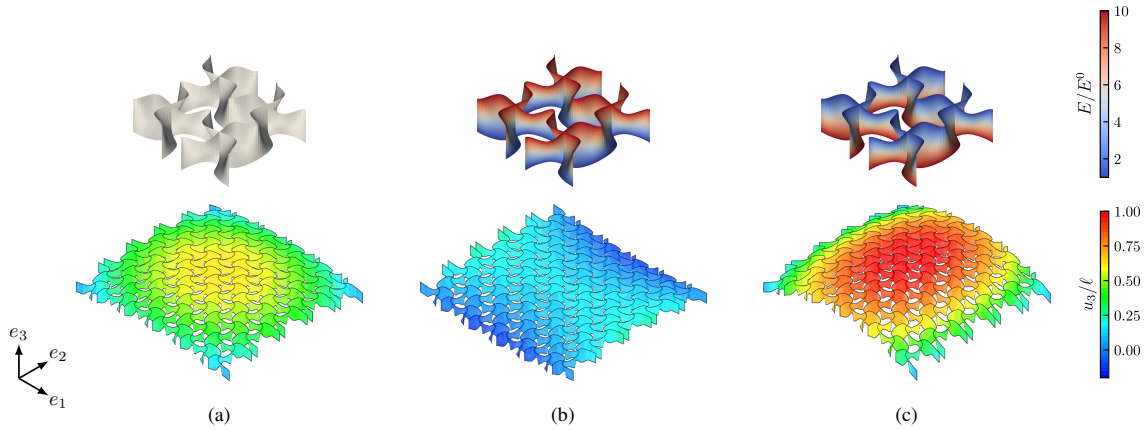


Fig. 6.7: deformed panel loaded in uniaxial tension up to 10% effective strain. The aspect ratio here is $h^* = h/l = 0.3$ and the normalised thickness is $t^* = t/l = 0.05$. (a) Uniform Young's modulus. (b) Increasing Young's modulus along the panel height. (c) Decreasing Young's modulus along the panel's height.

6.4.2 Mechanical testing

The experiments are performed on an Instron 10 kN universal testing machine, under displacement control at a quasi-static strain rate $\dot{\epsilon} = 0.125 \text{ min}^{-1}$ up to 20% effective engineering strain. Each mechanical test is recorded using a high-resolution digital camera (JAI Spark SP-20000-USB camera with a resolution of 5120×3840 pixels equipped with a Tokina AT-X Pro 100 mm F2.8 macro lens), mounted on a perpendicular axis with respect to the plane of the specimen. Using an inclined mirror, we capture the front and lateral view of the specimen in each picture, as shown in Fig. 6.8. Using an in-built computer program, 8-bit gray scale sub-images were stored every second during the loading. The out of plane displacement u_3 at the tip of the ribbon identified in the lateral mirror view is measured 2-d point tracking method² from the image sequence. A white grid is added to the sample to facilitate the optical measurements.

Early stage tests performed on specimens fixed by standard hard clamp montages (not shown here) gave unsatisfactory results. More precisely, the resulting out of plane displacement field was below the expected results of the computations with periodic boundary conditions displayed in Fig. 6.5, indicating that the 5×5 array specimen, with clamped boundaries does not approximate the results of an infinite periodic domain. Standard hard clamp montage are a dead load and induce over-constrained boundary conditions, preventing the out of the plane deformation of the specimen. A way to relax the the encastred boundary conditions of the clamps was to add an intermediate fixing comprising a rod and a series of rings which add additional degrees of freedom at the boundary of the specimen. Similar specimen fixing were attempted in previous works in the literature [52, 179, 255].

Extension with customised fixture. The specimen is hung between the clamps at both extremities by metallic rings to steel rods in a curtain-like fashion, as shown in Fig. 6.8. Prior to the montage, the steel rods were covered in oil to reduce the frictions with the rings. Although this fixture accommodates lateral expansions and rotations of the specimens undergoing tensile loads, it is worth noting that it introduces uncertainties, due to the unknown friction between the rings and the rods. This limitation is addressed by analysing two distinct types of boundary conditions in the numerical simulations associated to this tensile test: (i) free traction in the corresponding directions, neglecting friction and are compatible with periodic boundary conditions or (ii) adding stiff pinned rods at the extremity of the specimen, which permit an out-of-plane tilt without a transversal slide and are appropriate for the extension test discussed next.

The results of the extension experiment are depicted in Fig. 6.8. The different sub-figures represent: (a) the experimental setup, (b) the observed specimen during the experiment at maximal

²This operation was performed using the software Tracker: <https://physlets.org/tracker/>

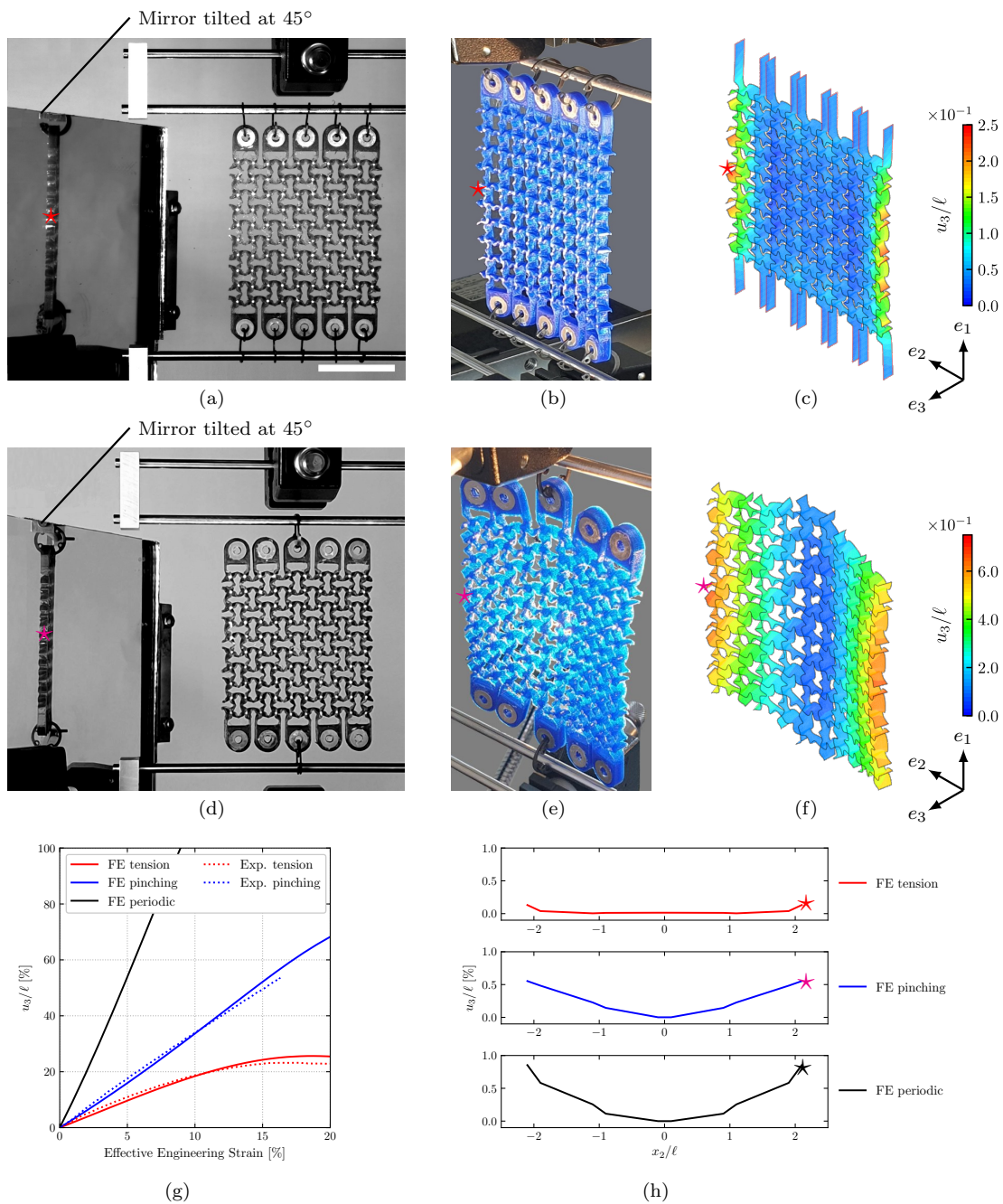


Fig. 6.8: comparison of experimental and computed results. Extension test: (a) experimental setup, (b) observed specimen at maximal extension $\varepsilon^* = 20\%$ (c) computed relative out of plane displacement u_3/l . Extension by concentrated load, *i.e.*; pinching test: (d) experimental setup, (e) observed specimen at maximal extension $\varepsilon^* = 16\%$ (f) computed relative out of plane displacement u_3/l . (g) Comparison of the evolution of the out of plane displacement at the measurement point (indicated by \star in the images). (h) Comparison between the numerical deformed cross-sections at mid specimen.

extension, i.e., 20% effective strain and (c) the computed relative out of plane displacement field u_3/l plotted on the deformed mesh assuming the boundary conditions (ii). The results present an excellent match between computations under experimental boundary conditions and experimental measurements as a deformation pattern and quantitatively when the displacements are compared at a given point, see red curves in subfigure (g). Moreover, a saturation of the out-of-plane displacement at about 15% engineering strain is observed on both experiments and computations. If the comparison between experiments and computation is satisfactory, they both exhibit an important discrepancy with the behaviour of the structure under perfect periodic boundary condition, both in the deformation pattern and quantitatively as the out-of-plane displacement is increased by a factor of six when compared with the tensile experiment.

Extension by concentrated force, referred to as pinching test. The results of the pinching experiment, where the extension is applied only on the central ring are represented in Fig. 6.8. The different sub-figures represent as before: (d) the experimental setup, (e) the observed specimen during the experiment at maximal extension, i.e., 16% effective strain and (c) the computed relative out of plane displacement field u_3/l plotted on the deformed mesh. As before one can remark an excellent match between experiments and computations, both in terms of deformation pattern and quantitatively when the displacements are compared at a given point, see blue curves in subfigure (g). The results exhibit on the one hand side a three-fold increase of the out-of-plane displacement when compared with the previous extension experiment and on the other hand side present a linear increase of the out of plane displacement with applied strain without the saturation plateau of the previous extension experiment.

Finally, Fig. 6.8(h) presents the computed out-plane displacements of a nodal line at the center of the specimen, transverse to the extension direction. The comparison of the shapes shows that the extension experiment does not reach an important curvature at the center and that the out-of-displacement is concentrated at the boundaries, which is in contrast with the extension by a concentrated force where a significative curvature at the center is obtained. Moreover the pinching experiment and the periodic boundary condition reach similar curvatures at the center of the specimen and that the quantitative difference of the measured out of plane experiment is due only in the deformation patterns of the last cell at the boundary of the specimens where the boundary conditions differ.

6.5 Conclusion and perspectives

In this chapter, we designed a new class of microstructures composed of undulated ribbon lattice. These microstructures can be arranged periodically to obtain panels exhibiting a bending deflection when submitted to in-plane tension, hence producing the EBC effect. For a prescribed shape of the unit cell, i.e., shape of the ribbons and intersections, the aspect ratio of the ribbons and their thickness, tailor the various elastic coefficients, like stiffness or EBC ratio.

Our work expands the spectrum of shape-morphing structures manufactured with a single material, and it indicates an approach that could be used to produce morphing and deployable structures for a wide range of scales. While the shapes we have obtained are relatively simple, similar principles could be extended to different families of materials, and could be coupled to parametric optimisation (using B-splines) and inverse-design strategies to obtain more extreme shapes. This type of analysis would also permit to shed light on the set of realizable moduli using undulated ribbon-based structures (refer for analogy to the study of [168] regarding laminates).

The geometric parameters of proposed ribbon based architectures can be tuned to create panels with controlled EBC effect and combined with active materials like swelling gels, piezo-electrics, nematic elastomers, LCE's, in the different layers of the unit cell to trigger the shape shifting effect by external stimuli.

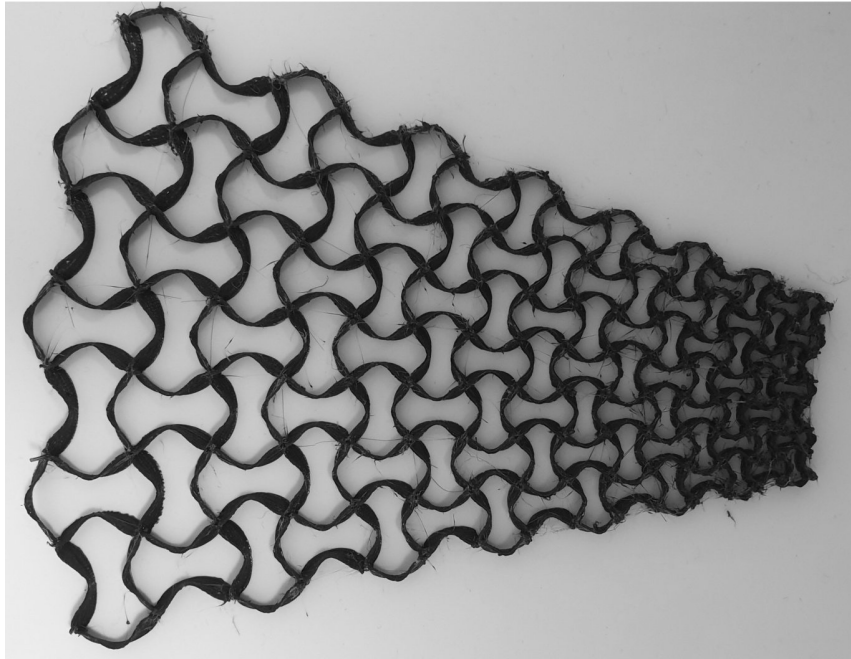


Fig. 6.9: a slice of the antenna in the undeformed configuration, fabricated using an FFF 3D printer of the Drahi-X, Ecole polytechnique (unpublished results).

6.5.1 Projects associated

Based upon this work, a 10-weeks master's internship was launched between the middle of May until the end of July, with the aim to build a self deployable space cellular antenna. The self-shaping behaviour is expected to emerge from a pre stretched shape memory polymer material actuated by a drastic change of temperature. Preliminary design and additive manufacturing have permitted to obtain a concept for a slice of the antenna. Future aspects regard the glueing of the micro-architecture to the SMP pre-stretched sheet.

Chapter 7

Design of thin architected panels with extension–bending coupling effects using topology optimisation

Contents

7.1	Introduction	129
7.2	Setting of the problem	131
7.3	Optimisation problem	133
7.3.1	Coupling shape sensitivity with a level set description	134
7.3.2	Shape derivative in the smooth inter-phase context	135
7.3.3	Approximate formula for the shape derivative	137
7.3.4	Volume constraint	139
7.3.5	Extension and regularisation of the velocity field and descent direction	139
7.4	Optimisation algorithm	140
7.5	Numerical results	142
7.5.1	Example 1	143
7.5.2	Example 2	146
7.5.3	Example 3	147
7.5.4	Example 4	151
7.6	Conclusion and perspectives	152

Topology optimisation via a level set method (Section 2.4) and asymptotic homogenisation in the context of thin panels (Section 1.4) permit to design periodic micro-architected materials with programmable macroscopic behaviour. The simultaneous control of the in-plane, out-of-plane and their coupled behaviour enables to shift a flat panel into a dome or saddle shaped structure under the action of an in-plane loading.

7.1 Introduction

Contemporary advancements of manufacturing technologies have led to the widespread adoption of materials with complex microstructures over the last decades [20, 29, 38, 91, 92, 138]. These materials, constructed through sophisticated, hierarchical microstructures, overcome inherently conflicting mechanical properties in engineering practice [99, 167]. Hence, it is no surprise that they are highly desirable by engineers and physical scientists.

An example of a material with periodic microstructure manufactured by classical processes is the honeycomb elastic panel [100, 122]. It has witnessed many applications in industry due to its high

strength-to-weight ratio [259] and its exceptional properties outside the elastic domain [155, 240, 266]. In the context of panels, the manufacturing of tailored micro-architected material through various 3D printing technologies opens the way to customise the material distribution through the thickness. The wide range of novel micro-architectures will locally couple various material properties, such as extension and bending response, in what are called generally “transformation mechanisms”. The underlying interest is the morphing of flat panels into three-dimensional shells, an ubiquitous mechanism found in nature with increasing technological applications [185].

In engineering, flat panels permitted the development of three-dimensional objects of complex geometries [107, 108, 131, 159] and unleashed new functionalities for exploring harsh or inaccessible environments [137, 201] and delivering increasingly large and complex payloads [28, 58]. However, due to their micro-structural intricacy, panel equations and associated boundary conditions are utilised and applied on a macroscopic scale where often extension–bending effects are present. Designing three-dimensional microstructures with desired extension–bending effects is one of the aims of this work.

One of the methods designed for the analysis of micro-architected materials is the theory of homogenisation [8, 25, 33, 163, 210]. In this theory, the effective material properties of periodic structures are defined by the analysis on a periodic cell and, in turn, these properties depend on the mechanics of constituents and the topology of the periodic structure but are independent of the external boundary conditions and applied forces. Naturally, there exists a large body of work deriving the homogenised equations of panels/plates [46, 133, 149, 163, 208]. For panels with thickness comparable to the length of the period, the derived effective model consists of a coupled system of equations, one equation models the in-plane behaviour of the panel while the second equation models the flexural curvature. Consequently, three sets of effective coefficients are obtained that can be computed numerically once a geometry and volume fraction are determined [46, 149, 163]. The first set of effective coefficients captures the in-plane panel stiffness, the second set captures the bending stiffness, and the third set captures the extension–bending effect of the panel. The extension to the next order of the asymptotic would lead to a bending-gradient model for thick plates as illustrated in [147, 208]. Equivalent homogenisation and dimension reduction that leads to the theory of Reissner–Mindlin for plates does not yet exist, to our knowledge.

When it comes to designing materials with microstructure, modern numerical methods such as shape and topology optimisation [9, 32, 80] have become prevalent in this realm, leading to the design of novel complex morphologies. Nowadays, the most common techniques adopted for structural design optimisation are density-based methods, e.g., the homogenisation method [8, 31] and the SIMP¹ [30, 32], or implicit method, such as phase-field [24, 49] and the level set methods [14, 248]. For periodic materials, the overall properties can be studied using homogenisation where the effective coefficients computed take into account the bulk material composition as well as the geometry layout [31]. Topology optimisation using inverse homogenisation exploits this fact in order to systematically identify optimal topologies and volume fractions for two-dimensional [181, 244, 249, 250, 247] (see also chapter 3) and more recently three-dimensional periodic cell [1, 21, 216, 246]. The works cited above designed optimal microstructures using inverse homogenisation in 2D or 3D for elastic or thermoelastic material. However, the optimal design of panels seems not to have progressed as rapidly. One of the pioneering papers in the design of composite plates is that of [97], where the authors consider the design of extremely rigid clamped square plates. In their analysis, they consider the out-of-plane displacement of the plate without taking into account any extension–bending effects. More recently two–scale topology optimisation of composite plates was undertaken in [182]. The authors assumed that, macroscopically, the plate follows the Reissner–Mindlin theory and considered two optimisation problems: in-plane optimisation of the periodic cell that maximises the macroscopic stiffness of the composite plate and in-plane optimisation of the periodic cell that maximises the macroscopic displacements at prescribed nodes.

¹Solid Isotropic Material with Penalisation

The novelty of the present work is to design thin elastic panels that simultaneously control in-plane stiffness, out-of-plane bending, and extension–bending coupling. The macroscopic behaviour of the panels is governed by the Kirchhoff–Love model as that is derived from the theory of homogenisation in [46, 133, 163, 208]. Building upon our previous work in [3, 5, 181], we use inverse homogenisation and a level set method coupled with the Hadamard shape derivative [14] to construct plate elastic moduli within the periodic cell. The approach is undertaken in the context of the diffuse (or smooth) interphase approach [15]. The diffuse interphase approach entails approximating the sharp interphase between material and “void” with a smooth, thin transitional layer of size $2e$, where $e > 0$ is a small number. This is primarily done for mathematical and physical reasons alike. The approach presented here allows for direct control of the extension–bending coefficient in addition to direct control of the in-plane stiffness and the out-of-plane bending stiffness. The diffuse inter-phase approach entails approximating the sharp interface between material and “void” with a smooth, thin transitional layer of size $2e$, where $e > 0$ is a small number. This is primarily done for mathematical and physical reasons alike. The approach presented here allows for direct control of the extension–bending coefficient in addition to direct control of the in-plane stiffness and the out-of-plane bending stiffness.

The chapter is organised as follows. In section 7.2 we specify the problem setting and we present the panel’s effective equations and the associate effective moduli. Section 7.3 is devoted to formulating the cost functional, introducing the level set method in the diffuse interface context and the discussion of the volume constraints. Section 7.4 presents the optimisation algorithm and addresses certain algorithmic issues that arise. Section 7.5 deals with the implementation and discussion of several numerical examples as well as the physical meaning of the extension-bending coupling. Finally, section 7.6 contains some conclusions and remarks.

7.2 Setting of the problem

Domain definition. The notation used in chapter 1 is maintained in this chapter. The composite panel under consideration is occupying a bounded domain $\Omega_h = \omega \times]-h/2, h/2[\subset \mathbb{R}^3$, characterised by its middle surface $\omega \subset \mathbb{R}^2$ of characteristic length L , and by its thickness h along the (O, x_3) axis, as sketched in Fig. 7.1. The domain Ω_h is delimited by a regular boundary Γ_h , which is decomposed into a lateral boundary $\Gamma_h^{lat} = \partial\omega \times]-h/2, h/2[$, and a top/bottom boundary $\Gamma_h^\pm = \omega \times \{\pm h/2\}$.

The panel’s microstructure is characterised by an in-plane periodic arrangement, composed of a large number of identical unit cells. The period, i.e., the characteristic length of a unit cell l , is assumed to be small in comparison to the characteristic size of the panel L . The small parameter $\epsilon = \mathcal{O}(l/L) \ll \mathcal{O}(1)$ referred to as the scale factor, expresses this difference of scales. In addition, h and l are assumed to be comparable in scale, for the purposes of this work. Their ratio, denoted by $r = h/l = \mathcal{O}(1)$, describes the cell’s aspect ratio.

Equations at the local scale. Let $Y = [0, 1]^2 \times [-r/2, r/2]$ be the rescaled periodic cell, described by the set of coordinates $\mathbf{y} = \mathbf{x}/\epsilon$. Note that the scaling is made with respect to ϵ for both in-plane and out of the plane components. Through this choice, the rescaled unit cell’s Y thus preserves its aspect ratio, unlike in the monograph of Caillerie [46].

The panel is assumed to behave as a linearly elastic anisotropic body. We recall from section 1.4 the spatial distribution of the elastic stiffness $C^{h\epsilon}$ is expressed by:

$$C^{h\epsilon}(\mathbf{x}) = \frac{1}{h^3} C\left(\frac{\mathbf{x}}{\epsilon}\right),$$

where $C(\mathbf{y})$ is an in-plane periodic, piecewise constant, isotropic fourth order tensor. Moreover, the solid is submitted to surface forces \mathbf{t} at the boundary Γ_h^\pm and a homogeneous Dirichlet boundary condition for the displacement at the boundary Γ_h^{lat} . In the framework of linear elasticity, the

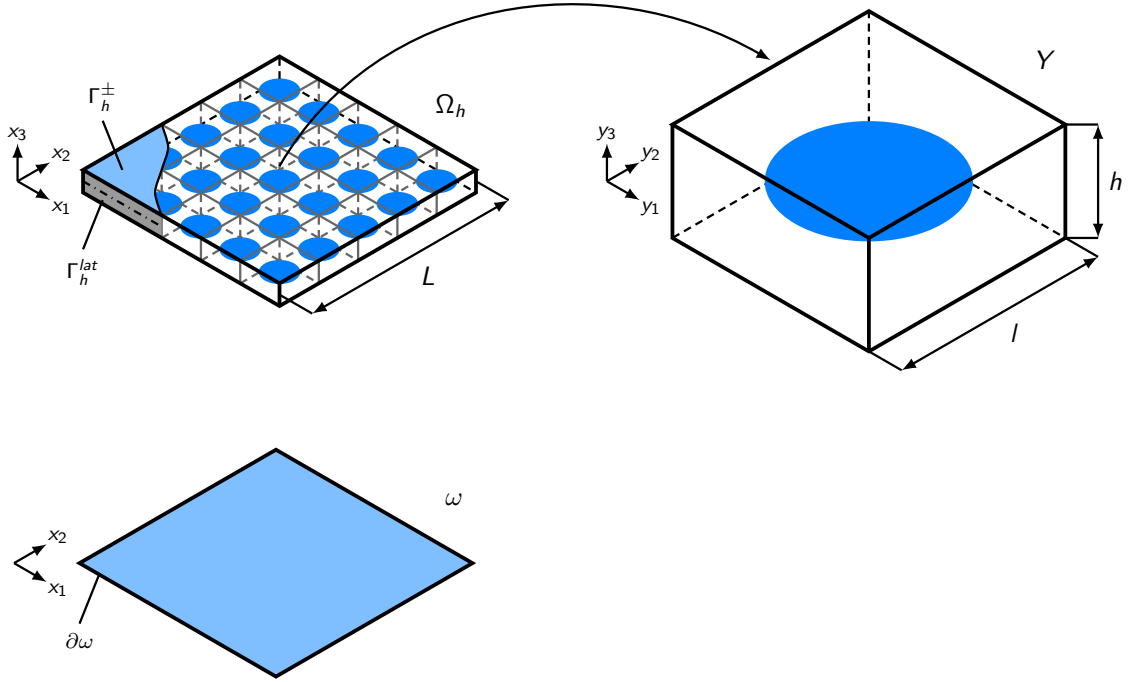


Fig. 7.1: architected panel Ω_h with a in-plane periodic arrangement of unit cells Y . The cell's aspect ratio r is defined as $r = h/l$. Concept of homogenisation yields an equivalent anisotropic homogeneous plate.

composite panel is governed by the following set of equations:

$$\begin{cases} \frac{\partial \sigma_{ij}^{h\epsilon}}{\partial x_j} + f_i = 0 & \text{in } \Omega_h, \\ \sigma_{ij}^{h\epsilon} = C_{ijkl}^{h\epsilon} \varepsilon_{kl}(\mathbf{u}^{h\epsilon}) & \text{in } \Omega_h, \\ u_i^{h\epsilon} = 0 & \text{on } \Gamma_h^{lat}, \\ \sigma_{ij}^{h\epsilon} n_j = t_i & \text{on } \Gamma_h^{\pm}. \end{cases} \quad (7.2.1)$$

where $\mathbf{u}^{h\epsilon}$ is the displacement field, $\varepsilon(\mathbf{u}^{h\epsilon})$ is the strain field, defined by:

$$\varepsilon(\mathbf{u}^{h\epsilon}) = \frac{1}{2} (\nabla \mathbf{u}^{h\epsilon} + \nabla^T \mathbf{u}^{h\epsilon}),$$

and \mathbf{n} is the external unit normal of Γ^{\pm} .

Equations at the macroscopic scale. A classical result from homogenisation theory [163, 208] indicate that the 3D heterogeneous problem (7.2.1) can be approximated at the macroscopic scale by an equivalent homogenised linearly elastic anisotropic thin plate model when the plate thickness h and the characteristic cell's length l are very small in comparison with the in-plane typical length of the plate L (i.e., $l \approx h \ll L$). We recall that the plate problem consists in finding a plate displacement field $\mathbf{U}(x_1, x_2)$ and the corresponding generalised strain field $(\varepsilon(\mathbf{U}), \chi(U_3))$ expressed by:

$$\varepsilon_{\alpha\beta}(\mathbf{U}) = \frac{1}{2} (U_{\alpha,\beta} + U_{\beta,\alpha}), \quad \chi_{\alpha\beta}(U_3) = -U_{3,\alpha\beta}, \quad (7.2.2)$$

and a generalised stress field (\mathbf{N}, \mathbf{M}) on ω satisfying the following set of equations (refer to section

8.2. in [208] for further details):

$$\begin{cases} \nabla \cdot \mathbf{N} + \mathbf{T} = \mathbf{0} & \text{in } \omega, \\ \nabla \cdot (\nabla \cdot \mathbf{M}) + \nabla \cdot \mathbf{Q} - T_3 = 0 & \text{in } \omega, \\ \mathbf{N} = \mathbf{A} : \varepsilon(\mathbf{U}) + \mathbf{B} : \chi(U_3) & \text{in } \omega, \\ \mathbf{M} = \mathbf{B}^\top : \varepsilon(\mathbf{U}) + \mathbf{D} : \chi(U_3) & \text{in } \omega, \\ \mathbf{U} = \mathbf{0} & \text{on } \partial\omega, \end{cases} \quad (7.2.3)$$

where \mathbf{T} and \mathbf{Q} represent the generalised loads:

$$\mathbf{T} = \int_{\pm h/2} \mathbf{t} \, dx_3, \quad \mathbf{Q} = \int_{\pm h/2} x_3 \mathbf{t} \, dx_3. \quad (7.2.4)$$

In eq. (7.2.3), the material behaviour is expressed through the tensors \mathbf{A} , \mathbf{B} and \mathbf{D} , which carry the following symmetries:

$$A_{\alpha\beta\gamma\delta} = A_{\beta\alpha\gamma\delta} = A_{\alpha\beta\delta\gamma} = A_{\gamma\delta\alpha\beta}, \quad (7.2.5)$$

$$B_{\alpha\beta\gamma\delta} = B_{\beta\alpha\gamma\delta} = B_{\alpha\beta\delta\gamma}, \quad (7.2.6)$$

$$D_{\alpha\beta\gamma\delta} = D_{\beta\alpha\gamma\delta} = D_{\alpha\beta\delta\gamma} = D_{\gamma\delta\alpha\beta}. \quad (7.2.7)$$

In more precise terms, \mathbf{A} describes the in-plane behaviour, \mathbf{D} describes the bending behaviour, and their coupling is expressed through \mathbf{B} . Note that in most engineering applications, where panels feature symmetric geometry and material distribution along the thickness, normal and shear behaviour get uncoupled for the membrane part, yielding $\mathbf{B} = \mathbf{0}$. The converse behaviour is investigated here, i.e., we aim at designing panels with exceptional extension–bending coupling effect.

7.3 Optimisation problem

Cost functional. The working domain (or design domain) of the optimisation is the periodic cell $Y \in [0, 1]^2 \times [-r/2, r/2]$ defined in the previous section. It may be decomposed into two phases: a strong phase S (typically the material phase), that will also be referred to as *shape*, and weak phase \bar{S} (which represents the void), separated by a interphase ∂S . Moreover, we assume that $(S, \bar{S}) \subset Y$ are smooth, open, bounded subsets and define the set of admissible shapes,

$$\mathcal{U}_{ad} := \{S \subset Y \text{ is open, bounded, and smooth} \mid f_m \leq |S| \leq f_M\}, \quad (7.3.1)$$

where f_m and f_M are two real numbers ranging between 0 and 1. Hence, we define an objective function \mathcal{J} , to be minimised over all possible admissible shapes, as a sum of weighted Euclidean norms:

$$\begin{aligned} \mathcal{J}(S) = & \frac{1}{2} \eta_{\alpha\beta\gamma\delta}^A \left(A_{\alpha\beta\gamma\delta}^* - A_{\alpha\beta\gamma\delta}^{\text{target}} \right)^2 \\ & + \frac{1}{2} \eta_{\alpha\beta\gamma\delta}^B \left(B_{\alpha\beta\gamma\delta}^* - B_{\alpha\beta\gamma\delta}^{\text{target}} \right)^2 \\ & + \frac{1}{2} \eta_{\alpha\beta\gamma\delta}^D \left(D_{\alpha\beta\gamma\delta}^* - D_{\alpha\beta\gamma\delta}^{\text{target}} \right)^2, \end{aligned} \quad (7.3.2)$$

where A^* , B^* and D^* are the effective elastic plate coefficients given in eq. (1.4.56) from chapter 1, while A^{target} , B^{target} and D^{target} denote given target thin plate tensor values. Finally, η^A , η^B and η^D denote the weight coefficients carrying the same type of symmetry as their respective tensor. Consequently, the topology optimisation problem under consideration reads:

$$\begin{aligned}
& \inf_{S \subset \mathcal{U}_{ad}} \mathcal{J}(S), \\
& \mathbf{w}^{\gamma\delta} \in \tilde{\mathcal{V}}(Y) \text{ satisfy: } \int_Y C_{ijpq} (\delta_{p\gamma} \delta_{q\delta} + \varepsilon_{ypq}(\mathbf{w}^{\gamma\delta})) \varepsilon_{yij}(\mathbf{v}) d\mathbf{y} = 0 \quad \forall \mathbf{v} \in \tilde{\mathcal{V}}(Y), \quad (7.3.3) \\
& \mathbf{p}^{\gamma\delta} \in \tilde{\mathcal{V}}(Y) \text{ satisfy: } \int_Y C_{ijpq} (y_3 \delta_{p\gamma} \delta_{q\delta} + \varepsilon_{ypq}(\mathbf{p}^{\gamma\delta})) \varepsilon_{yij}(\mathbf{v}) d\mathbf{y} = 0 \quad \forall \mathbf{v} \in \tilde{\mathcal{V}}(Y).
\end{aligned}$$

Recall that the functional $\tilde{\mathcal{V}}(Y)$ is defined as: $\tilde{\mathcal{V}}(Y) := \{\mathbf{v} \in H_{loc}^1(Y) \mid (y_1, y_2)\text{-periodic, } \langle v_i \rangle_Y = 0\}$. We have chosen an interval for the volume fraction in \mathcal{U}_{ad} since it is not a priori possible to guess a compatible target volume fraction for a target stiffness tensor. If the prescribed material volume fraction is set too low, the target stiffness could fall outside the range of achievable tensors [168, 169], resulting in a final shape with undesired effects (see for example the gap between the target and the obtained results in the two first final shapes of chapter 3). This is an even bigger issue considering that to our knowledge, variational bounds for elastic thin plates have not yet been studied. Conversely, in the case where prescribed material volume fraction is relatively high, the algorithm may converge to shapes that are excessively bulky (e.g., large blocks connected with thin hinges) or in the worst case scenario, the algorithm would leave some unconnected material phases (islands) in the final microstructure.

Note that the interval volume constraint is enforced using an augmented Lagrangian method, which is detailed in appendix B.3

7.3.1 Coupling shape sensitivity with a level set description

Shape sensitivity analysis. Shape optimisation problems are often not compatible with discrete or zero-order methods [224], rather, they are addressed using gradient-based continuous optimisation algorithms. As discussed in section 2.3, the notion of gradient for shape optimisation problems, namely the method for describing variations of a shape, is based on Hadamard's boundary variation method, which has become standard in the literature [9, 75, 196]. Henceforth, the characterisation of different phases is described using a level set function and as a consequence, a descent direction can be obtained by computing the shape derivative of $\mathcal{J}(S)$ within the classical shape sensitivity framework of Hadamard.

Shape representation by the level set method. The definition of an auxiliary level set function ϕ associated to a shape S is recalled in eq. (7.3.4).

$$\begin{cases} \phi(\mathbf{y}) < 0 & \text{if } \mathbf{y} \in S, & \text{(material)} \\ \phi(\mathbf{y}) = 0 & \text{if } \mathbf{y} \in \partial S, & \text{(boundary)} \\ \phi(\mathbf{y}) > 0 & \text{if } \mathbf{y} \in \bar{S} = Y \setminus S. & \text{(void)} \end{cases} \quad (7.3.4)$$

A pseudo time $t \in \mathbb{R}^+$ is defined to characterise the evolution of the shape $S(t)$ via its corresponding level set $\phi(\mathbf{y}(t), t)$. Initially the interphase of the shape is described by $\phi(\mathbf{y}) = 0$ if $y \in \Gamma^S$. Consequently, for any pseudo time t , $\mathbf{y}(t) \in \Gamma^S(t)$ satisfies $\phi(\mathbf{y}(t), t) = 0$. Differentiating with respect to the pseudo time t yields:

$$\frac{d\phi}{dt}(\mathbf{y}(t), t) = 0 \quad \Rightarrow \quad \frac{\partial \phi}{\partial t}(\mathbf{y}, t) + \boldsymbol{\theta}(\mathbf{y}, t) \cdot \nabla \phi(\mathbf{y}, t) = 0, \quad (7.3.5)$$

where $\boldsymbol{\theta} = \frac{\partial \mathbf{y}}{\partial t}$ is the velocity field of the interphase $\Gamma^S(t)$. For a small variation of the shape, its evolution is completely described by the normal component of velocity field $\boldsymbol{\theta}$, as justified by the Hadamard structure theorem [9, 175]. Hence, after introducing the normal component of $\boldsymbol{\theta}$:

$V = \boldsymbol{\theta} \cdot \mathbf{n}$, eq. (7.3.5) can be written as:

$$\frac{\partial \phi}{\partial t}(\mathbf{y}, t) + V(\mathbf{y}, t) |\nabla \phi(\mathbf{y}, t)| = 0, \quad \forall t, \forall \mathbf{y} \in Y, \quad (7.3.6)$$

which takes form of the Hamilton–Jacobi equation.

Smooth interphase approach. In each phase, the material properties are characterised by an isotropic elastic tensor C^n ($n = S$ refers to the stronger phase, $n = \bar{S}$ refer to the weaker one). Assuming a sharp interface would induce a discontinuity of C^n . For physical and mathematical reasons it is often desirable to model the interphase as a smooth, transitional layer of thickness $2e$, where e is a small positive parameter. Following the ideas in [15], the level set function serves as a base to define the local smooth stiffness tensor C^e in Y as a regular interpolation between the strong phase and the weak phase. The transition from a sharp to a smooth interface is achieved first by redistancing the level set ϕ to become the signed distance function d_S to the interface boundary Γ^S . Hence, the properties of the material occupying the unit cell Y are then defined by:

$$C^e = \mathcal{H}_e(d_S) (C^{\bar{S}} - C^S) + C^S, \quad (7.3.7)$$

where $\mathcal{H}_e(\phi)$ is a smooth Heaviside type of function defined in eq. (2.4.15).

Lastly, the material volume fraction $|S|$ in the context of a smooth inter-phase approach is also defined with respect to the Heaviside function \mathcal{H}_e by:

$$|S| = \frac{1}{|Y|} \int_Y (1 - \mathcal{H}_e) d\mathbf{y}. \quad (7.3.8)$$

7.3.2 Shape derivative in the smooth inter-phase context

Using the method of C ea, discussed in [45], for the calculation of the shape derivative of the objective function, we formulate the Lagrangian function $\mathcal{L} : W^{1,\infty}(Y, \mathbb{R}^3) \times \tilde{\mathcal{V}} \times \tilde{\mathcal{V}} \times \tilde{\mathcal{V}} \times \tilde{\mathcal{V}} \rightarrow \mathbb{R}$ as follows:

$$\begin{aligned} \mathcal{L}(S, \boldsymbol{\xi}^{\gamma\delta}, \boldsymbol{\Xi}, \boldsymbol{\zeta}^{\gamma\delta}, \mathbf{Z}) &= \frac{1}{2} \eta_{\alpha\beta\gamma\delta}^A (A_{\alpha\beta\gamma\delta}^* - A_{\alpha\beta\gamma\delta}^{\text{target}})^2 \\ &\quad + \frac{1}{2} \eta_{\alpha\beta\gamma\delta}^B (B_{\alpha\beta\gamma\delta}^* - B_{\alpha\beta\gamma\delta}^{\text{target}})^2 \\ &\quad + \frac{1}{2} \eta_{\alpha\beta\gamma\delta}^D (D_{\alpha\beta\gamma\delta}^* - D_{\alpha\beta\gamma\delta}^{\text{target}})^2 \\ &\quad + \int_Y C^e(\mathbf{y}) : (\mathbf{E}^{\gamma\delta} + \boldsymbol{\varepsilon}_y(\boldsymbol{\xi}^{\gamma\delta})) : \boldsymbol{\varepsilon}_y(\boldsymbol{\Xi}) d\mathbf{y} \\ &\quad + \int_Y C^e(\mathbf{y}) : (\mathbf{X}^{\alpha\beta} + \boldsymbol{\varepsilon}_y(\boldsymbol{\zeta}^{\alpha\beta})) : \boldsymbol{\varepsilon}_y(\mathbf{Z}) d\mathbf{y}, \end{aligned} \quad (7.3.9)$$

where $\mathbf{E}^{\alpha\beta}$ (resp. $\mathbf{X}^{\alpha\beta}$) are the prescribed mean in-plane (resp. flexural) strain modes on the unit cell (refer to Fig. 1.7 for a graphical illustration). They are chosen to form a vector basis in the space of second order symmetric tensors and are expressed as:

$$\mathbf{E}^{\alpha\beta} = \frac{1}{2} (\delta_{i\alpha} \delta_{j\beta} + \delta_{i\beta} \delta_{j\alpha}) \mathbf{e}_i \otimes \mathbf{e}_j, \quad \mathbf{X}^{\alpha\beta} = \frac{y_3}{2} (\delta_{i\alpha} \delta_{j\beta} + \delta_{i\beta} \delta_{j\alpha}) \mathbf{e}_i \otimes \mathbf{e}_j.$$

Here, $\boldsymbol{\Xi}$, \mathbf{Z} are intended as the Lagrange multipliers associated to the enforcement of the state equations. $\boldsymbol{\xi}^{\gamma\delta}$, $\boldsymbol{\Xi}$, $\boldsymbol{\zeta}^{\gamma\delta}$ and \mathbf{Z} are vector-valued functions defined in Y , which do not depend on S . As usual, the stationarity of the Lagrangian provides the optimality conditions for the minimisation problem.

Direct problem. Differentiating \mathcal{L} in (7.3.9) with respect to Ξ in the direction of a test function $\varphi \in \tilde{\mathcal{V}}(Y)$ gives:

$$\left\langle \frac{\partial \mathcal{L}}{\partial \Xi} \mid \varphi \right\rangle = \int_Y C^e(\mathbf{y}) : \left(\mathbf{E}^{\gamma\delta} + \varepsilon_{\mathbf{y}}(\xi^{\gamma\delta}) \right) : \varepsilon_{\mathbf{y}}(\varphi) d\mathbf{y}.$$

Upon setting the above equation equal to zero, we recover the variational formulation of first state equation (1.4.52). Similarly, differentiating \mathcal{L} (7.3.9) with respect to \mathbf{Z} in the direction of a test function $\varphi \in \tilde{\mathcal{V}}(Y)$ gives:

$$\left\langle \frac{\partial \mathcal{L}}{\partial \mathbf{Z}} \mid \varphi \right\rangle = \int_Y C^e(\mathbf{y}) : \left(\mathbf{X}^{\alpha\beta} + \varepsilon_{\mathbf{y}}(\zeta^{\alpha\beta}) \right) : \varepsilon_{\mathbf{y}}(\varphi) d\mathbf{y}.$$

Upon setting the above equation equal to zero, we recover the variational formulation of second state equation (1.4.53).

Adjoint problem. The partial derivative of \mathcal{L} in (7.3.9) with respect to $\xi^{\gamma\delta}$ in the direction of a test function $\varphi \in \tilde{\mathcal{V}}(Y)$ results in:

$$\begin{aligned} \left\langle \frac{\partial \mathcal{L}}{\partial \xi^{\gamma\delta}} \mid \varphi \right\rangle &= \frac{r}{|Y|} \eta_{\alpha\beta\gamma\delta}^A \left(A_{\alpha\beta\gamma\delta}^* (ds) - A_{\alpha\beta\gamma\delta}^{\text{target}} \right) \int_Y C^e(\mathbf{y}) : \varepsilon_{\mathbf{y}}(\varphi) : \left(\mathbf{E}^{\gamma\delta} + \varepsilon_{\mathbf{y}}(\xi^{\gamma\delta}) \right) d\mathbf{y} \\ &+ \frac{r}{|Y|} \eta_{\alpha\beta\gamma\delta}^B \left(B_{\alpha\beta\gamma\delta}^* (ds) - B_{\alpha\beta\gamma\delta}^{\text{target}} \right) \int_Y C^e(\mathbf{y}) : \varepsilon_{\mathbf{y}}(\varphi) : \left(\mathbf{X}^{\gamma\delta} + \varepsilon_{\mathbf{y}}(\zeta^{\gamma\delta}) \right) d\mathbf{y} \\ &+ \int_Y C(\mathbf{y}) : \varepsilon_{\mathbf{y}}(\varphi) : \varepsilon_{\mathbf{y}}(\Xi) d\mathbf{y} \end{aligned}$$

The integral over Y on the first two lines is equal to $\mathbf{0}$ from the state equations (1.4.52) and (1.4.53). Moreover, if we choose $\varphi = \Xi$ and using the positive definiteness of C as well as the Y -periodicity of Ξ , we obtain that the solution of the adjoint state is identically zero, $\Xi = \mathbf{0}$. Similarly, the partial derivative of \mathcal{L} with respect to $\zeta^{\gamma\delta}$ in the direction of a test function $\varphi \in \tilde{\mathcal{V}}(Y)$ results in:

$$\begin{aligned} \left\langle \frac{\partial \mathcal{L}}{\partial \zeta^{\gamma\delta}} \mid \varphi \right\rangle &= \frac{r}{|Y|} \eta_{\alpha\beta\gamma\delta}^B \left(B_{\alpha\beta\gamma\delta}^* (ds) - B_{\alpha\beta\gamma\delta}^{\text{target}} \right) \int_Y C(\mathbf{y}) : \left(\mathbf{E}^{\gamma\delta} + \varepsilon_{\mathbf{y}}(\xi^{\gamma\delta}) \right) : \varepsilon_{\mathbf{y}}(\varphi) d\mathbf{y} \\ &+ \frac{r}{|Y|} \eta_{\alpha\beta\gamma\delta}^D \left(D_{\alpha\beta\gamma\delta}^* (ds) - D_{\alpha\beta\gamma\delta}^{\text{target}} \right) \int_Y C(\mathbf{y}) : \left(\mathbf{X}^{\gamma\delta} + \varepsilon_{\mathbf{y}}(\zeta^{\gamma\delta}) \right) : \varepsilon_{\mathbf{y}}(\psi) d\mathbf{y} \\ &+ \int_Y C(\mathbf{y}) : \varepsilon_{\mathbf{y}}(\varphi) : \varepsilon_{\mathbf{y}}(\mathbf{Z}) d\mathbf{y} \end{aligned}$$

The integral over Y on the first two lines is equal to $\mathbf{0}$ from the state equations (1.4.52) and (1.4.53). Moreover, if we choose $\psi = \mathbf{Z}$ and using the positive definiteness of C as well as the Y -periodicity of \mathbf{Z} , we obtain that the solution of the adjoint state is identically zero, $\mathbf{Z} = \mathbf{0}$.

Shape derivative. Deforming the interface Γ^S in the direction of a smooth vector field θ (see Section 2.3.2 for details), the shape derivative of the objective function is found to be the shape derivative of the Lagrangian at the optimal point:

$$\mathcal{J}'(S)(\theta) = \left\langle \frac{\partial \mathcal{L}}{\partial S} (S, \mathbf{w}^{\gamma\delta}, \mathbf{0}, \mathbf{p}^{\gamma\delta}, \mathbf{0}) \mid \theta \right\rangle \quad (7.3.10)$$

Thus:

$$\begin{aligned}
\mathcal{J}'(S)(\boldsymbol{\theta}) &= \frac{r}{|\mathbf{Y}|} \eta_{\alpha\beta\gamma\delta}^A \left(A_{\alpha\beta\gamma\delta}^* (d_S) - A_{\alpha\beta\gamma\delta}^{\text{target}} \right) \\
&\quad \int_{\mathbf{Y}} d_S'(\boldsymbol{\theta}) C'(d_S) : (\mathbf{E}^{\gamma\delta} + \varepsilon_{\mathbf{y}}(\mathbf{w}^{\gamma\delta})) : (\mathbf{E}^{\alpha\beta} + \varepsilon_{\mathbf{y}}(\mathbf{w}^{\alpha\beta})) \, d\mathbf{y} \\
&+ \frac{r}{|\mathbf{Y}|} \eta_{\alpha\beta\gamma\delta}^B \left(B_{\alpha\beta\gamma\delta}^* (d_S) - B_{\alpha\beta\gamma\delta}^{\text{target}} \right) \\
&\quad \int_{\mathbf{Y}} d_S'(\boldsymbol{\theta}) C'(d_S) : (\mathbf{E}^{\gamma\delta} + \varepsilon_{\mathbf{y}}(\mathbf{w}^{\gamma\delta})) : (\mathbf{X}^{\alpha\beta} + \varepsilon_{\mathbf{y}}(\mathbf{p}^{\alpha\beta})) \, d\mathbf{y} \\
&+ \frac{r}{|\mathbf{Y}|} \eta_{\alpha\beta\gamma\delta}^D \left(D_{\alpha\beta\gamma\delta}^* (d_S) - D_{\alpha\beta\gamma\delta}^{\text{target}} \right) \\
&\quad \int_{\mathbf{Y}} d_S'(\boldsymbol{\theta}) C'(d_S) : (\mathbf{X}^{\gamma\delta} + \varepsilon_{\mathbf{y}}(\mathbf{p}^{\gamma\delta})) : (\mathbf{X}^{\alpha\beta} + \varepsilon_{\mathbf{y}}(\mathbf{p}^{\alpha\beta})) \, d\mathbf{y}
\end{aligned}$$

Moreover, as presented in Proposition 2.5 and then Proposition 2.9 from [15], the shape derivative can be expressed as follows:

$$\begin{aligned}
\mathcal{J}'(S)(\boldsymbol{\theta}) &= \frac{r}{|\mathbf{Y}|} \eta_{\alpha\beta\gamma\delta}^A \left(A_{\alpha\beta\gamma\delta}^* (d_S) - A_{\alpha\beta\gamma\delta}^{\text{target}} \right) \int_{\Gamma_S} -\boldsymbol{\theta} \cdot \mathbf{n} f_A(\mathbf{s}) \, ds \\
&+ \frac{r}{|\mathbf{Y}|} \eta_{\alpha\beta\gamma\delta}^B \left(B_{\alpha\beta\gamma\delta}^* (d_S) - B_{\alpha\beta\gamma\delta}^{\text{target}} \right) \int_{\Gamma_S} -\boldsymbol{\theta} \cdot \mathbf{n} f_B(\mathbf{s}) \, ds \\
&+ \frac{r}{|\mathbf{Y}|} \eta_{\alpha\beta\gamma\delta}^D \left(D_{\alpha\beta\gamma\delta}^* (d_S) - D_{\alpha\beta\gamma\delta}^{\text{target}} \right) \int_{\Gamma_S} -\boldsymbol{\theta} \cdot \mathbf{n} f_D(\mathbf{s}) \, ds,
\end{aligned} \tag{7.3.11}$$

where:

$$\left\{ \begin{aligned}
f_A(\mathbf{s}) &= \int_{\text{ray}_{\mathbf{s}} \cap \mathbf{Y}} \left[\prod_{i=1}^2 1 + d_S(\mathbf{z}) \kappa_i(\mathbf{s}) \right] \mathcal{H}'_e(d_S) \\
&\quad (C^{\bar{S}} - C^S) : (\mathbf{E}^{\gamma\delta} + \varepsilon_{\mathbf{z}}(\mathbf{w}^{\gamma\delta})) : (\mathbf{E}^{\alpha\beta} + \varepsilon_{\mathbf{z}}(\mathbf{w}^{\alpha\beta})) \, d\mathbf{z} \\
f_B(\mathbf{s}) &= \int_{\text{ray}_{\mathbf{s}} \cap \mathbf{Y}} \left[\prod_{i=1}^2 1 + d_S(\mathbf{z}) \kappa_i(\mathbf{s}) \right] \mathcal{H}'_e(d_S) \\
&\quad (C^{\bar{S}} - C^S) : (\mathbf{E}^{\gamma\delta} + \varepsilon_{\mathbf{z}}(\mathbf{w}^{\gamma\delta})) : (\mathbf{X}^{\alpha\beta} + \varepsilon_{\mathbf{z}}(\mathbf{p}^{\alpha\beta})) \, d\mathbf{z} \\
f_D(\mathbf{s}) &= \int_{\text{ray}_{\mathbf{s}} \cap \mathbf{Y}} \left[\prod_{i=1}^2 1 + d_S(\mathbf{z}) \kappa_i(\mathbf{s}) \right] \mathcal{H}'_e(d_S) \\
&\quad (C^{\bar{S}} - C^S) : (\mathbf{X}^{\gamma\delta} + \varepsilon_{\mathbf{z}}(\mathbf{p}^{\gamma\delta})) : (\mathbf{X}^{\alpha\beta} + \varepsilon_{\mathbf{z}}(\mathbf{p}^{\alpha\beta})) \, d\mathbf{z}
\end{aligned} \right.$$

7.3.3 Approximate formula for the shape derivative

Although formula (7.3.11) is satisfying from a mathematical point of view, its numerical evaluation is not completely straightforward. There are two delicate issues. First, one has to compute the principal curvatures $\kappa_i(\mathbf{s})$ for any point $\mathbf{s} \in \Gamma$ on the interface. Second, one has to perform a 1-d integration along the rays of the energy-like quantity. This is a classical task in the level set framework but, still, it is of interest to devise a simpler approximate formula for the shape derivative.

Following the ideas developed in [15], a first approximate formula is to assume that the interface is roughly plane, namely to assume that the principal curvatures $\kappa_i(\mathbf{s})$ vanish. In such a case we obtain a ‘‘Jacobian-free’’ approximate shape derivative. This gives a new expression for f_A , f_B and

f_D :

$$\begin{cases} f_A(\mathbf{s}) = \int_{\text{ray}_{\Gamma^S} \cap Y} \mathcal{H}'_e(d_S) \left(C^{\bar{S}} - C^S \right) : \left(\mathbf{E}^{\gamma\delta} + \varepsilon_z(\mathbf{w}^{\gamma\delta}) \right) : \left(\mathbf{E}^{\alpha\beta} + \varepsilon_z(\mathbf{w}^{\alpha\beta}) \right) dz \\ f_B(\mathbf{s}) = \int_{\text{ray}_{\Gamma^S} \cap Y} \mathcal{H}'_e(d_S) \left(C^{\bar{S}} - C^S \right) : \left(\mathbf{E}^{\gamma\delta} + \varepsilon_z(\mathbf{w}^{\gamma\delta}) \right) : \left(\mathbf{X}^{\alpha\beta} + \varepsilon_z(\mathbf{p}^{\alpha\beta}) \right) dz \\ f_D(\mathbf{s}) = \int_{\text{ray}_{\Gamma^S} \cap Y} \mathcal{H}'_e(d_S) \left(C^{\bar{S}} - C^S \right) : \left(\mathbf{X}^{\gamma\delta} + \varepsilon_z(\mathbf{p}^{\gamma\delta}) \right) : \left(\mathbf{X}^{\alpha\beta} + \varepsilon_z(\mathbf{p}^{\alpha\beta}) \right) dz \end{cases}$$

A second approximate formula is obtained when the smoothing parameter e is small. Note that, since the support of the function h_e is of size $2e$, the integral in formula (7.3.11) is confined to a tubular neighbourhood of Γ of width $2e$. Therefore, if e is small, one may assume that the functions depending on \mathbf{z} are constant along each ray, equal to their value at $\mathbf{y} \in \Gamma$. In other words, for small e we assume:

$$\varepsilon_z \approx \varepsilon_s \quad d_S(\mathbf{z}) \approx d_S(\mathbf{s}) = 0 \quad (7.3.12)$$

which yields the approximate formulas, for $\mathbf{y} \in \Gamma^S$:

$$\begin{cases} f_A(\mathbf{s}) = \left(C^{\bar{S}} - C^S \right) : \left(\mathbf{E}^{\gamma\delta} + \varepsilon_s(\mathbf{w}^{\gamma\delta}) \right) : \left(\mathbf{E}^{\alpha\beta} + \varepsilon_s(\mathbf{w}^{\alpha\beta}) \right) \int_{\text{ray}_{\Gamma^S} \cap Y} \mathcal{H}'_e(d_S) dz \\ f_B(\mathbf{s}) = \left(C^{\bar{S}} - C^S \right) : \left(\mathbf{E}^{\gamma\delta} + \varepsilon_s(\mathbf{w}^{\gamma\delta}) \right) : \left(\mathbf{X}^{\alpha\beta} + \varepsilon_s(\mathbf{p}^{\alpha\beta}) \right) \int_{\text{ray}_{\Gamma^S} \cap Y} \mathcal{H}'_e(d_S) dz \\ f_D(\mathbf{s}) = \left(C^{\bar{S}} - C^S \right) : \left(\mathbf{X}^{\gamma\delta} + \varepsilon_s(\mathbf{p}^{\gamma\delta}) \right) : \left(\mathbf{X}^{\alpha\beta} + \varepsilon_s(\mathbf{p}^{\alpha\beta}) \right) \int_{\text{ray}_{\Gamma^S} \cap Y} \mathcal{H}'_e(d_S) dz \end{cases}$$

Furthermore, most rays have a length larger than $2e$ so that

$$\int_{\text{ray}_{\Gamma^S} \cap Y} \mathcal{H}'_e(d_\omega) dz + \int_{\text{ray}_{\Gamma^S} \cap Y} \mathcal{H}'_e(d_\omega) dz = \mathcal{H}_e(e) - \mathcal{H}_e(-e) = 1 \quad (7.3.13)$$

In turn, the shape derivative in (7.3.11) can be approximated by:

$$\begin{aligned} \mathcal{J}'(S)(\boldsymbol{\theta}) &= \frac{r}{|Y|} \eta_{\alpha\beta\gamma\delta}^A \left(A_{\alpha\beta\gamma\delta}^* (d_S) - A_{\alpha\beta\gamma\delta}^{\text{target}} \right) \int_{\Gamma^S} -\boldsymbol{\theta} \cdot \mathbf{n} \\ &\quad \left(C^{\bar{S}} - C^S \right) : \left(\mathbf{E}^{\gamma\delta} + \varepsilon_s(\mathbf{w}^{\gamma\delta}) \right) : \left(\mathbf{E}^{\alpha\beta} + \varepsilon_s(\mathbf{w}^{\alpha\beta}) \right) ds \\ &+ \frac{r}{|Y|} \eta_{\alpha\beta\gamma\delta}^B \left(B_{\alpha\beta\gamma\delta}^* (d_S) - B_{\alpha\beta\gamma\delta}^{\text{target}} \right) \int_{\Gamma^S} -\boldsymbol{\theta} \cdot \mathbf{n} \\ &\quad \left(C^{\bar{S}} - C^S \right) : \left(\mathbf{E}^{\gamma\delta} + \varepsilon_s(\mathbf{w}^{\gamma\delta}) \right) : \left(\mathbf{X}^{\alpha\beta} + \varepsilon_s(\mathbf{p}^{\alpha\beta}) \right) ds \\ &+ \frac{r}{|Y|} \eta_{\alpha\beta\gamma\delta}^D \left(D_{\alpha\beta\gamma\delta}^* (d_S) - D_{\alpha\beta\gamma\delta}^{\text{target}} \right) \int_{\Gamma^S} -\boldsymbol{\theta} \cdot \mathbf{n} \\ &\quad \left(C^{\bar{S}} - C^S \right) : \left(\mathbf{X}^{\gamma\delta} + \varepsilon_z(\mathbf{p}^{\gamma\delta}) \right) : \left(\mathbf{X}^{\alpha\beta} + \varepsilon_z(\mathbf{p}^{\alpha\beta}) \right) ds \end{aligned} \quad (7.3.14)$$

Numerical results performed in [15] reveal that the latter simplification (7.3.15), which we shall refer to as the approximate shape derivative, works very well in practice for problems of compliance minimisation.

As a result, the expressions for the shape derivative of $\mathcal{J}(S)$ in direction $\boldsymbol{\theta}$ under the approximation of thin smooth inter-phase reads:

$$\mathcal{J}'(S)(\boldsymbol{\theta}) = - \int_{\Gamma^S} \boldsymbol{\theta} \cdot \mathbf{n} (f_A(\mathbf{s}) + f_B(\mathbf{s}) + f_D(\mathbf{s})) ds \quad (7.3.15)$$

where:

$$\begin{aligned}
f_A(\mathbf{s}) &= \frac{r}{|Y|} \eta_{\alpha\beta\gamma\delta}^A \left(A_{\alpha\beta\gamma\delta}^* (d_S) - A_{\alpha\beta\gamma\delta}^{\text{target}} \right) (\mathbf{E}^{\gamma\delta} + \varepsilon_{\mathbf{y}}(\mathbf{w}^{\gamma\delta})) : (\mathbf{C}^{\bar{S}} - \mathbf{C}^S) : (\mathbf{E}^{\alpha\beta} + \varepsilon_{\mathbf{y}}(\mathbf{w}^{\alpha\beta})) \\
f_B(\mathbf{s}) &= \frac{r}{|Y|} \eta_{\alpha\beta\gamma\delta}^B \left(B_{\alpha\beta\gamma\delta}^* (d_S) - B_{\alpha\beta\gamma\delta}^{\text{target}} \right) (\mathbf{E}^{\gamma\delta} + \varepsilon_{\mathbf{y}}(\mathbf{w}^{\gamma\delta})) : (\mathbf{C}^{\bar{S}} - \mathbf{C}^S) : (\mathbf{P}^{\alpha\beta} + \varepsilon_{\mathbf{y}}(\mathbf{p}^{\alpha\beta})) \\
f_D(\mathbf{s}) &= \frac{r}{|Y|} \eta_{\alpha\beta\gamma\delta}^D \left(D_{\alpha\beta\gamma\delta}^* (d_S) - D_{\alpha\beta\gamma\delta}^{\text{target}} \right) (\mathbf{P}^{\gamma\delta} + \varepsilon_{\mathbf{y}}(\mathbf{p}^{\gamma\delta})) : (\mathbf{C}^{\bar{S}} - \mathbf{C}^S) : (\mathbf{P}^{\alpha\beta} + \varepsilon_{\mathbf{y}}(\mathbf{p}^{\alpha\beta}))
\end{aligned}$$

Hence, a descent direction can always be selected by choosing $\boldsymbol{\theta} = (f_A(\mathbf{s}) + f_B(\mathbf{s}) + f_D(\mathbf{s})) \mathbf{n}$.

7.3.4 Volume constraint

The result in eq. (7.3.15) corresponds to the unconstrained problem. To ensure that $S \subset \mathcal{U}_{\text{ad}}$, an augmented Lagrangian approach is considered to enforce a two-sided inequality constraints [36, 183]. Hence, the optimisation problem (7.3.3) is a constraint-free minimisation of a (Lagrangian-like) weighted sum of the cost functional $\mathcal{J}(S)$ and the constraint $\mathcal{P}(S, \lambda, \mu)$ that reads:

$$\inf (\mathcal{J}(S) + \mathcal{P}(S, \lambda, \mu)), \quad (7.3.16)$$

where the constraint is expressed as follows:

$$\mathcal{P}(S, \lambda, \mu) = \min_{f_m \leq |S| - v \leq f_M} \left(\lambda v + \frac{\mu}{2} |v|^2 \right) \quad (7.3.17)$$

In the above equation, v is a slack variable, λ is the Lagrange multiplier for the volume constraint and μ is a penalty parameter. A brief presentation on used schemes to update these parameters during the optimization process is provided in appendix B.3. As indicated in eq. (7.3.16), the constraint gives rise to an additional term in the shape derivative. Let us denote by $\mathcal{P}'(S, \lambda, \mu)$ the shape derivative of the volume constraint $\mathcal{P}(S, \lambda, \mu)$ in the direction $\boldsymbol{\theta}$. Under the approximation of thin smooth inter-phase, $\mathcal{P}'(S, \lambda, \mu)$ is expressed as follows (see appendix B.3):

$$\mathcal{P}'(S)(\boldsymbol{\theta}) = - \int_{\Gamma^S} \theta_r(\mathbf{s}) n_r(\mathbf{s}) f_P(\mathbf{s}) d\mathbf{s}, \quad (7.3.18)$$

where

$$f_P(\mathbf{s}) = \begin{cases} \lambda^k + (|S| - f_M) \mu^k & \text{if } \lambda^k + \mu^k (|S| - f_M) > 0, \\ \lambda^k + (|S| - f_m) \mu^k & \text{if } \lambda^k + \mu^k (|S| - f_m) < 0 \\ 0 & \text{otherwise.} \end{cases}$$

Note the above expression has the same “ $-\boldsymbol{\theta} \cdot \mathbf{n}$ ” form of eq. (7.3.15), which means that a descent direction can be found in similar manners.

7.3.5 Extension and regularisation of the velocity field and descent direction

Although eq. (7.3.6) for the advection of the level set function is solved in the whole domain Y , shape sensitivity analysis provides us with a shape gradient defined only on the boundary of the domain Γ^S (see eq. (7.3.15)). Since the boundary is not explicitly discretised in our case, we can assume that the normal velocity V is defined for the nodes of the elements that are crossed by the zero level set. Then, one possibility is to consider $V = 0, \forall \mathbf{y} \in Y \setminus \Gamma^S$. Unfortunately, this choice would limit the movement of the boundary to small distance, which would result in an increased number of iterations until convergence, and thus a slower algorithm. A remedy to this inconvenience is to extend the velocity field in all the domain. At the same time, it would

be numerically beneficial to smooth a bit the shape gradient, but in a way that guarantees the descent nature of the new advection velocity. The sequel describes one way to combine these two requirements. Initially, the shape derivative has the form:

$$\mathcal{J}'(S)(\theta) = - \int_{\Gamma^s} \theta_r(\mathbf{s}) n_r(\mathbf{s}) f(\mathbf{s}) ds \quad (7.3.19)$$

or, for an advection velocity of the type $\theta(\mathbf{s}) = V(\mathbf{s}) \mathbf{n}(\mathbf{s})$,

$$\mathcal{J}'(S)(V\mathbf{n}) = \int_{\Gamma^s} -V(\mathbf{s}) f(\mathbf{s}) ds \quad (7.3.20)$$

Like in Section 2.4.2, instead of choosing $V(\mathbf{s}) = -f(\mathbf{s})$, the extended velocity $V(\mathbf{y})$ is chosen as the unique solution to the following problem expressed in its variational formulation:

$$\int_Y (\alpha^2 \nabla V(\mathbf{y}) \cdot \nabla W(\mathbf{y}) + V(\mathbf{y}) W(\mathbf{y})) d\mathbf{y} = \int_{\Gamma^s} W(\mathbf{s}) f(\mathbf{s}) ds \quad \forall W \in H^1(Y) \quad (7.3.21)$$

where $\alpha \in \mathbb{R}^{+*}$ is a small positive scalar (of the order of the mesh size) to control the regularisation width and take $W = -V$. This operation reveals that:

$$\mathcal{J}'(S)(V\mathbf{n}) = - \int_Y (\alpha^2 |\nabla V|^2 + V^2) d\mathbf{y} \quad (7.3.22)$$

which guarantees again a descent direction for \mathcal{J} .

7.4 Optimisation algorithm

The numerical algorithm used is adapted from [14] accounting for the additional local problem that is needed in order to compute the composite panel's effective coefficients.

Data: Initialise a level set function ϕ_0 corresponding to an initial shape S^0 ;

for $k \geq 0$ *iterate until convergence* **do**

 Redistance ϕ_k into the signed distance function d_{S^k} for stability reasons;

 Compute the local solutions $\mathbf{w}^{m\ell}$, $\mathbf{p}^{m\ell}$ for $m, \ell = 1, 2$ by solving (1.4.52), (1.4.53) for the domain S^k ;

 Update the Lagrange multiplier λ^k and penalty parameters μ^k ;

 Compute the shape gradient $\mathcal{J}(S^k)(\theta^k)$ for the domain S^k using eq. (7.3.15);

 Deform the domain S^k by solving the Hamilton-Jacobi equation (7.3.6);

 // Shape S^{k+1} is characterised by the level set ϕ_{k+1} after a time step Δt_k

 // The time step Δt_k is chosen so that $\mathcal{J}(S^{k+1}) \leq \mathcal{J}(S^k)$

end

Algorithm 3: Major steps of the algorithm in [14] adapted to Kirchhoff–Love composite panels.

Stopping criterion. The optimisation is assumed to be terminated when 200 iterative steps are reached, or else, when the time step Δt_k in the Hamilton-Jacobi equations becomes too small: $\Delta t_k < t_{\text{im}} = 10^{-8}$. In this case, the code reached a local minimum and cannot find a descent direction.

Algorithmic issues. As we already mentioned in section 2.2, it is well known that problems of designing optimal microstructures do not possess a global minimum [9]. As a result initial starting shapes/guesses have a considerable effect on the final design of the microstructure. Furthermore, they may lead the algorithm towards non-physical shapes (e.g., disconnected materials island in

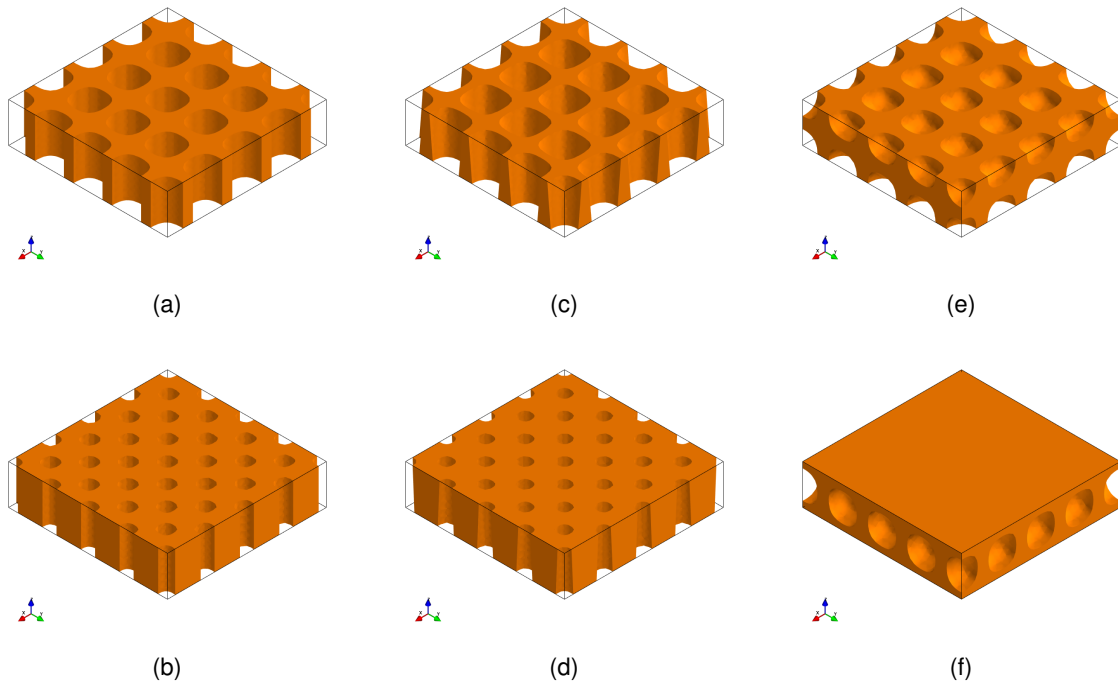


Fig. 7.2: initial shapes. (a) Square pattern of cylindrical micro-perforations. (b) Diagonal pattern of cylindrical micro-perforations. (c) Square pattern of conic micro-perforations. (d) Diagonal pattern of conic micro-perforations. (e) Straight bubble pattern. (f) Diagonal bubble pattern.

a void matrix), or to shapes representing local minima, yet very far from the target. In this case, we can always restart the algorithm, either using different initial guesses or using a different set of algorithmic parameters (like a different time step Δt_k , different penalization parameter μ_k). Additionally, we can start the algorithm with an initial shape that is a known local minimum from the literature, in which case the algorithm converges very fast.

Let us further note, that even though the notion of shape derivative does not permit nucleations, the level set method can naturally combine two adjacent “holes” into one by breaking the “barrier” between them, thus effectively changing the topology of the structure. This is why in practice, it is desirable to start with an initial guess that contains a large number of nucleations [14, 248]. However, as explained in [165], the topological change may induce an increase of the objective function \mathcal{J} , which we allow (up to a small tolerance) in the hope that afterwards the algorithm will locate a better shape. In practice, since most changes of topology occur in the first few iterations, the tolerance for accepting increases of the objective function \mathcal{J} is defined at the k^{th} iteration as:

$$\mathcal{J}(S^{k+1}) < \mathcal{J}(S^k) (1 + \eta_{\text{tol}} \exp(-0.1 k)),$$

where η_{tol} is a parameter set to a small value ($\eta_{\text{tol}} = 0.05$ in our scripts). The decreasing exponential reduces the tolerance over the iterations: until iteration 16, an increase by 1.e-2 is accepted, while after 40 iterations, an increase by 1.e-3 is no longer accepted.

Lastly, in order to discuss the influence of the initial design of the material cell on the optimised solution, six kinds of initial designs displayed in Fig. 7.2 were tested. Initial designs can be a straight or diagonal patterns with various micro-perforations. The initial design (a) and (b) feature cylinder inclusions, (c) and (d) feature cone inclusions, (e) and (f) feature circular inclusions. The number and the size of micro-perforations can be varied to tune the initial volume fraction.

7.5 Numerical results

In all the examples that follow, the unit cell Y is a cuboid of dimension $1 \times 1 \times 0.25$ (hence $r = 1/4$). It is meshed with a structured symmetric grid of $100 \times 100 \times 25$ quadrangular, each formed of four equal linear tetrahedron (P1) elements for the example 1; a structured symmetric grid of $50 \times 50 \times 12$ quadrangular, each formed of four equal linear tetrahedron (P1) elements for the examples 2 to 4. The choice to test different mesh size enables to appreciate the effects on the computational time required and its capacity to generate new morphological structures with prescribed behaviour. We recall that the distribution of elastic properties are defined by eq. (7.3.7). The material properties in each phases, S and \bar{S} are characterised by an isotropic fourth order tensor:

$$\mathbf{C}^\alpha = \frac{E^\alpha}{1 + \nu^\alpha} \mathbf{I}_4 + \frac{E^\alpha \nu^\alpha}{(1 + \nu^\alpha)(1 - 2\nu^\alpha)} \mathbf{I}_2 \otimes \mathbf{I}_2 \quad \alpha \in \{S, \bar{S}\} \quad (7.5.1)$$

where \mathbf{I}_2 is a second order identity matrix, and \mathbf{I}_4 is the identity fourth order tensor acting on symmetric matrices. The material properties are normalised as follows: the Young's modulus was set to $E^S = 0.91$ MPa for the strong phase (material) and $E^{\bar{S}} = 0.91 \times 10^{-4}$ MPa for the weak phase (ersatz). The Poisson's ratio was set to $\nu = 0.3$ for both phases. A homogeneous plate made of material C^S (resp. $C^{\bar{S}}$) features an effective in-plane behaviour $A_{1111}^* = A_{2222}^* = r$ (resp. $A_{1111}^* = A_{2222}^* = 10^{-4}r$).

All computations were carried out using an in house programming. The elasticity problems (1.4.52) and (1.4.53) are solved using the finite element solver `Cast3M` [51]. The Hamilton–Jacobi equation (7.3.6) is solved using the methods of characteristics using the `advect` package developed by Bui, Dapogny and Frey in [43]. The redistancing of the level set is undertaken using the `mshdist` package developed in [71].

Setting the target stiffness. The simultaneous in-plane, out-of-plane and their coupled behavior permits to program an out-of-plane response that results in either a dome shaped structure or a saddle shaped structure under the action of in-plane loading. As the primary interest in this work is the stretching-bending response of the panels, all shear coefficients, namely A_{1212}^* , B_{1212}^* and D_{1212}^* were left free and are denoted by a star, the controlled coefficients are therefore:

$$\mathbf{C}^{\text{target}} = \begin{bmatrix} A_{1111}^* & A_{1122}^* & \star & B_{1111}^* & B_{1122}^* & \star \\ A_{1122}^* & A_{2222}^* & \star & B_{2211}^* & B_{2222}^* & \star \\ \star & \star & \star & \star & \star & \star \\ \hline B_{1111}^* & B_{2211}^* & \star & D_{1111}^* & D_{1122}^* & \star \\ B_{1122}^* & B_{2222}^* & \star & D_{1122}^* & D_{2222}^* & \star \\ \star & \star & \star & \star & \star & \star \end{bmatrix} \quad (7.5.2)$$

Moreover, by methodically tuning the weights of the cost functional (7.3.2) permits to prioritize certain crucial components at the expense of others. Furthermore, all numerical examples reported in the sequel target an elastic tensor exhibiting “quadratic symmetry”, i.e., $A_{1111} = A_{2222}$ and $D_{1111} = D_{2222}$. This simplification, albeit fundamental, demonstrates the capability of the code to discriminate local solutions with general orthotropic behaviour.

Furthermore, we point out that the ranging values coefficients in A are usually much larger than in B and D . The difference in scale must be corrected through the weights η_A , η_B and η_D , else it can damage the good convergence of the code. Indeed, if we set $\mathcal{O}(\eta_A) = \mathcal{O}(\eta_B) = \mathcal{O}(\eta_D)$, the cost functional $\mathcal{J}(S)$ in (7.3.2) can be approximated during the first iterations:

$$\mathcal{J}(S) \approx \frac{1}{2} \|\mathbf{A}^* - \mathbf{A}^{\text{target}}\|_{\eta_A}^2$$

In this case, the algorithm will first satisfy the prescribed in plane behaviour $\mathbf{A}^{\text{target}}$. Unfortunately,

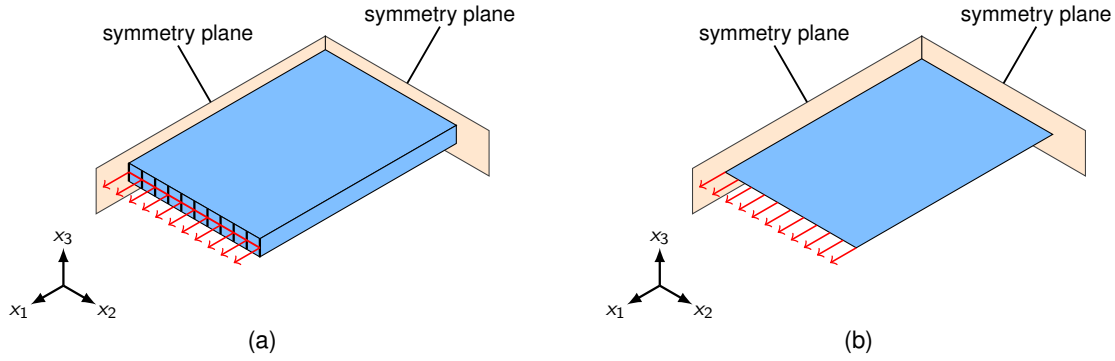


Fig. 7.3: Numerical problem with given boundary conditions for a tensile loading along the direction e_1 . The case for tensile loading along the direction e_2 is analogous. The simulations account for the plane symmetries in the specimen and are performed on a quarter of the geometry. (a) Analysis performed on the complete structure. The displacement component u_1 is imposed on the mid plane represented by the red line. The black lines indicate a rigid body kinematics applied along the thickness. (b) Analysis performed on the equivalent homogeneous thin plate, meshed with a structured pattern composed of 50×40 linear triangle elements. The amplitude of the imposed displacement is normalised at 0.1 macroscopic strain. The response to other loading can be easily recovered, since it is proportional to the loading at small strain.

the configuration that satisfy A^{target} may be not be compatible with B^{target} and D^{target} . In other words, the algorithm would most of the times fall in a local minima where the bending behaviour is not correctly controlled. In the numerical examples, we recommend to select the weight with the following scale factor: $10^2 \mathcal{O}(\eta_A) = \mathcal{O}(\eta_B) = \mathcal{O}(\eta_D)$. This choice can naturally be adjusted depending on the precision that is sought on a specific component.

Comparison between the full model and the homogeneous equivalent To demonstrate the effect of the extension–bending coupling, we simulate the deformation of an architected panel loaded in tension. Periodic assemblages consisting in 4×5 (resp. 5×4) unit cells were considered for the tensile specimen along direction e_1 (resp. along direction e_2). A sketch of the setting, provided in Fig. 7.3(a), describes the boundary conditions enforced on the lateral borders of the panel. The calculations are conducted with symmetry boundary conditions on the bottom and left side of the plate. The specimen is loaded by an imposed displacement on the mid-line of its right side (the red line Fig. 7.3(a)). Furthermore, all vertices belonging to the right face with the same in-plane coordinate are assumed to move as a rigid body (this is illustrated by the blue lines in Fig. 7.3(a)). As observed in our previous work [5], hard-clamp boundary conditions cancel out the bending response of the specimen in tension. It is thanks to this “exotic” boundary conditions that the right lateral face is allowed to tilt, so that the panel can undergo any out of plane deformation without restrictions.

In addition, an equivalent homogeneous plate is considered with an effective behaviour directly from the optimisation and is included in the calculation. The rectangular plate is meshed with 50×40 discrete Kirchhoff triangular (DKT) shell elements. A sketch of the setting is provided in Fig. 7.3(b). The right part is loaded in displacement along the direction e_1 (resp. along direction e_2), while all the other components and rotations are left free. Rigid body movements are eliminated by fixing the displacements and rotations on a node at the bottom left corner.

7.5.1 Example 1

The targets of the first microstructure to be optimised are given in the left side of Table 7.1. From a rapid analysis of these prescribed coefficients, it is clear that: the desired in-plane behaviour should be auxetic (i.e., exhibit an in-plane effective negative Poisson’s ratio of $\nu^{\text{target}} = -0.5$); the structure should exhibit a longitudinal extension–transverse bending coupled response, expressed by B_{1122}^{target} and B_{2211}^{target} ; a prescribed stiff longitudinal bending behaviour, expressed by D_{1111}^{target} and D_{2222}^{target} . To facilitate obtaining a desired quadratic symmetry, a symmetry of the shape

is enforced along both the Oxz and Oyz planes, by symmetrizing the level set function during the algorithmic iterations. Mathematically:

$$\phi_{\text{sym}}^k(\mathbf{y}) = \frac{1}{4} (\phi^k(y_1, y_2, y_3) + \phi^k(-y_1, y_2, y_3) + \phi^k(-y_1, -y_2, y_3) + \phi^k(y_1, -y_2, y_3)) \quad (7.5.3)$$

Additionally, the material volume fraction was constrained to be between $0.3 \leq |S| \leq 0.5$. The initial shape, depicted in Fig. 7.2(a), is consisting of a square pattern of “cylindrical” micro-perforations, with a initial material volume fraction of $|S| = 50\%$.

C^{target}						
0.12	-0.06	*	*	$2.3e^{-3}$	*	*
-0.06	0.12	*	$2.3e^{-3}$	*	*	*
*	*	*	*	*	*	*
*	$2.3e^{-3}$	*	$6.3e^{-4}$	*	*	*
$2.3e^{-3}$	*	*	*	$6.3e^{-4}$	*	*
*	*	*	*	*	*	*

C^*						
0.120	-0.059	0	$-1.5e^{-3}$	$1.8e^{-3}$	0	
-0.059	0.119	0	$1.7e^{-3}$	$1.0e^{-4}$	0	
0	0	0.03	0	0	$-2.7e^{-4}$	
$-1.5e^{-3}$	$1.7e^{-3}$	0	$6.1e^{-4}$	$-3.2e^{-5}$	0	
$1.8e^{-3}$	$1.0e^{-4}$	0	$-3.2e^{-5}$	$6.0e^{-4}$	0	
0	0	$-2.7e^{-4}$	0	0	$1.7e^{-4}$	

Table 7.1: Values of the target stiffness tensors and the effective tensors for the final form of the microstructure in Fig. 7.5. Only the entries in C^{target} that have numerical values are controlled. Conversely, the remaining entries are left free.

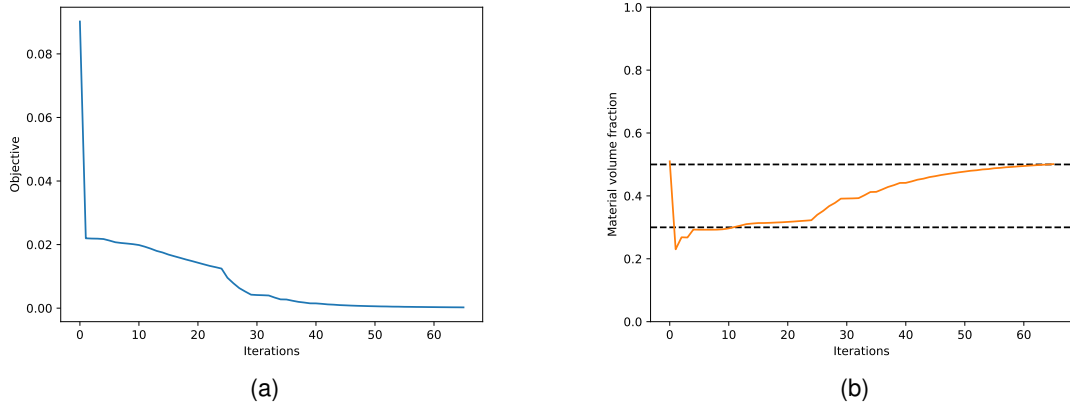


Fig. 7.4: Cost functional (a) and volume constraint (b) convergence plots for the microstructure depicted in Fig. 7.5. After 40 iterations we seem to have rather stable convergence both for the cost functional and volume constraint. The algorithm stops after 65 iterations, because the time step in the advection equation becomes too small.

The convergence history of the cost functional and of the volume constraint displayed in Fig. 7.4(a) shows that the target coefficient got stabilised in slightly more than 40 iterations and that the later iteration contributed only to small improvements without bringing the cost functional to less than 2×10^{-4} . We observe a significant drop in the cost functional (Fig. 7.4(a)) around iteration 25–30 that is associated with major changes in the microstructure’s topology. Beyond this point, most of the changes contribute as minor improvements. The evolution of material volume fraction displayed in Fig. 7.4(b) features an initial step decrease down to 0.25, attributed to the initial

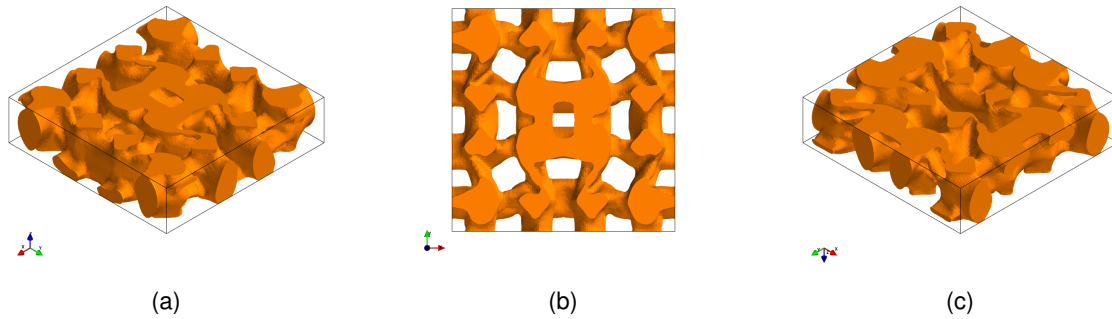


Fig. 7.5: Optimally designed periodic panels accounting for extension–bending coupling effects, with an attained volume fraction of 0.5. Images (a) and (c) show the front and rear isometric view of the periodic cell, while image (b) shows a bird's eye view of the cell.

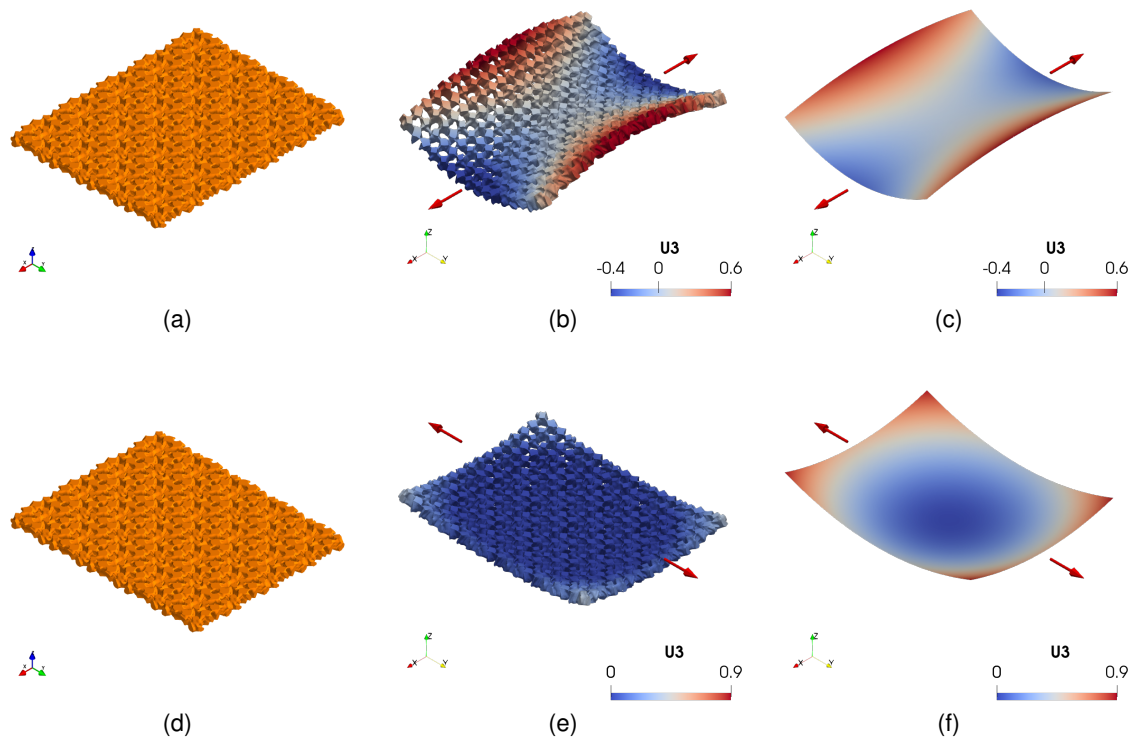


Fig. 7.6: 4×5 periodically assembled panel from the shape of Fig. 7.5. Image (a) corresponds to its reference flat configuration. The panel is submitted to an uniaxial tensile load along Ox up to 10% macroscopic strain. Image (b) depicts the deformed state computed on the complete panel while image (c) shows its macroscopic response assuming the homogeneous equivalent plate model with the coefficients of Table 7.1. The observed deformed shape is a saddle. The out-of-plane displacement is plotted as a color map on the deformed panel. It is recalled that the simulation was conducted in small strain, hence the out of plane response is proportional to the in-plane loading. The boundary conditions for the image (b) and (c) are reported in Fig. 7.3.

swelling of the holes, followed by a slower evolution to up to 0.5, which is the upper limit of the proposed range of the constraint.

The final shape, depicted in Fig. 7.5, is a lattice of complex shape. A view of a periodically assembled panel is also provided in Fig. 7.6(a,d). The collected values of all the coefficients of the aforementioned shape are included succinctly in the right side of Table 7.1. As prescribed, the final shape features an in-plane behaviour with an effective Poisson's ratio of -0.5 . It exhibits a significant value of B_{1122}^* and B_{2211}^* , which comes close to the target value. In addition, it is worth noticing that the diagonal coefficient B_{1111}^* is negative, while B_{2222}^* is positive. Yet, in terms of absolute values, B_{2222}^* is much smaller than B_{1111}^* . This implies that when the panel is loaded in the direction O_x , it will exhibit a significant negative Gaussian curvature, i.e., the panel will morph into a saddle shape. Conversely, when the panel is loaded in the direction O_y , the deformed shape will morph into a cylinder (hence the Gaussian curvature is close to 0 because B_{2222}^* is small). Let us finally note that the panel will also exhibit a significant coupled shear response, expressed through B_{1212}^* . Finally, the longitudinal out of the plane behaviour D_{1111}^* and D_{2222}^* also come close to the target value.

The computational time needed to design Example 1 using the $100 \times 100 \times 25$ elements structured mesh took more 10 hours to run 65 iterations on a machine with 128 CPU. In order to reduce this computational time, we explore the relevance of an optimization with a coarser mesh, i.e. $50 \times 50 \times 12$ elements, which results in computational time between 0.5 to 2 hours (when 200 iterations are required). The following examples are obtained on this coarser mesh.

7.5.2 Example 2

The second microstructure to be optimised was obtained using the same initial parameters as in Example 1, except for the mesh which is made of $50 \times 50 \times 12$ elements. The targets are recalled in the left side of Table 7.2. Like before, a symmetry of the shape is enforced along both the O_{xz} and O_{yz} planes, by symmetrizing the level set function during the algorithmic iterations (see eq. (7.5.3)). The material volume fraction remains constrained to be between $0.3 \leq |S| \leq 0.5$. The other main difference is the considered initial guess. Here, the initial shape, depicted in Fig. 7.2(e), is consisting of a regular "bubble" pattern, with an initial material volume fraction of $|S| = 75\%$.

C^{target}						
0.12	-0.06	*	*	$2.3e^{-3}$	*	*
-0.06	0.12	*	*	$2.3e^{-3}$	*	*
*	*	*	*	*	*	*
*	$2.3e^{-3}$	*	*	$6.3e^{-4}$	*	*
$2.3e^{-3}$	*	*	*	*	$6.3e^{-4}$	*
*	*	*	*	*	*	*

C^*						
0.097	-0.033	0	*	$2.9e^{-4}$	$2.2e^{-4}$	0
-0.033	0.098	0	*	$2.7e^{-4}$	$2.8e^{-4}$	0
0	0	0.023	*	0	0	$1.8e^{-4}$
$2.9e^{-4}$	$2.7e^{-4}$	0	*	$2.7e^{-4}$	$6.2e^{-5}$	0
$2.2e^{-4}$	$2.8e^{-4}$	0	*	$6.2e^{-5}$	$2.7e^{-4}$	0
0	0	$1.8e^{-4}$	*	0	0	$2.0e^{-4}$

Table 7.2: Values of the target stiffness tensors and the effective tensors for the final form of the microstructure in Fig. 7.8. Only the entries that have numerical values were controlled. The remaining entries were left free.

The convergence history of the cost functional and of the volume constraint displayed in Fig. 7.7(a) shows that the objective gets stabilised in the very first 5 iterations, while the later iteration contributed only to small improvements without bringing the cost functional to less than 5×10^{-3} . Major

changes in the microstructure’s topology are observable until iteration 25. Beyond this point, most of the changes contribute as minor improvements. Although the gain in the cost functional gets decreased by a factor of 10^3 , a remaining gap with respect to the target moduli can be read from Table 7.2, in particular in the sub-matrix B. We conclude that this shape corresponds to a local minima for the objective function, but not as effective as the one in Table 7.1. The evolution of material volume fraction displayed in Fig. 7.7(b) features an initial steep decrease down to 0.25, attributed to the initial swelling of the holes, followed by a slower evolution to up to 0.33.

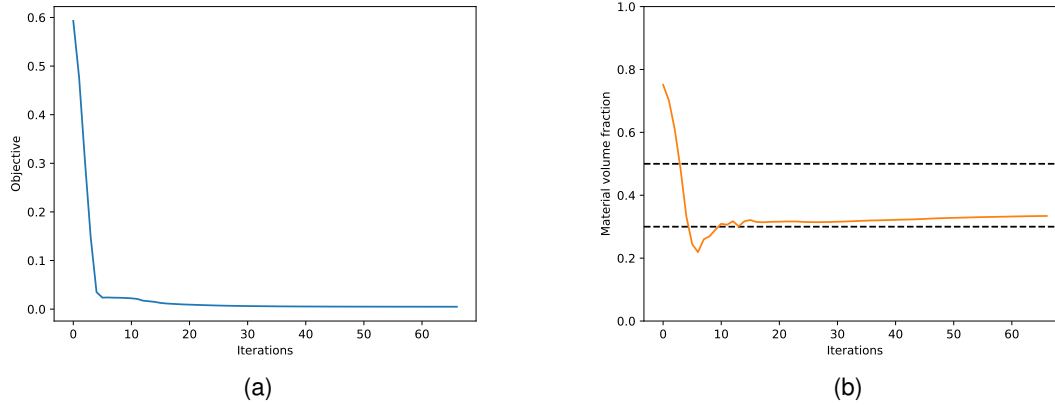


Fig. 7.7: Cost functional (a) and volume constraint (b) convergence plots for the microstructure depicted in Fig. 7.8. After 6 iterations, we seem to have rather stable convergence both for the cost functional and volume constraint. The algorithm stops after 65 iterations, because the time step in the advection equation becomes too small.

The final shape, depicted in Fig. 7.8, can be characterised as a “dimpled” sheet structure and looks similar to the designs imagined in [112]. A view of a periodically assembled panel is also provided in Fig. 7.9(a). Although one might suspect that the structure exhibits further symmetries from the illustration in Fig. 7.8(b), analyses of the volume fraction revealed that the structure is in fact slightly asymmetric along the direction O_z : the material volume fraction between $z \in [-h/2, 0]$ is equal to 0.35, while it is equal to 0.31 for $z \in [0, h/2]$. This asymmetry in the design is fundamental to obtain a significant coupling tensor B^* . The collected values of all the coefficients of the aforementioned shape are included succinctly in the right side of Table 7.2. As prescribed, the final shape features an in-plane auxetic behaviour, but the Poisson’s ratio is of $\nu^* = -0.33$ rather than -0.5 . It exhibits a rather mild longitudinal extension–transverse bending coupling, with values for B_{1122}^* and B_{2211}^* being one order below the target value. Yet, noticing that the diagonal coefficient B_{1111}^* and B_{2222}^* are not negligible, meaning that the shape will feature a longitudinal extension–bending coupling. Complementary information on the plate deformation kinematics can be retrieved from the compliance tensor $S^* = (C^*)^{-1}$, provided in eq. (D.2.2) of D.2.

Numerical simulations performed on a periodic panel reveal that the deformed shape in the linear regime will exhibit a mild positive Gaussian curvature, i.e., the panel will morph into a quasi-circular dome shape (see Fig. 7.9(b,e) for a loading in the O_x direction, and Fig. 7.9(c,f) for a loading in the O_y direction). This result was anticipated, since the longitudinal components and the transverse components of B have similar positive values.

7.5.3 Example 3

The third microstructure to be optimised was obtained using the same initial parameters as in Example 1 and 2. The targets are recalled in the left side of Table 7.3. Like before, a symmetry of the shape is enforced along both the O_{xz} and O_{yz} planes, by symmetrizing the level set function during the algorithmic iterations (see eq. (7.5.3)). The material volume fraction remains constrained to be between $0.3 \leq |S| \leq 0.5$. A third initial guess is tested in this example. Here, the

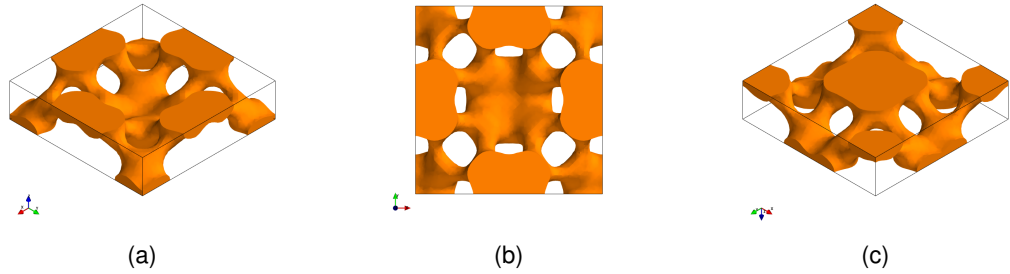


Fig. 7.8: Optimally designed periodic panel resulting in a “dimpled” sheet structure. The attained volume fraction is 33%. Images (a) and (c) show the top and bottom of the periodic cell, while image (b) shows a bird’s eye view of the cell.

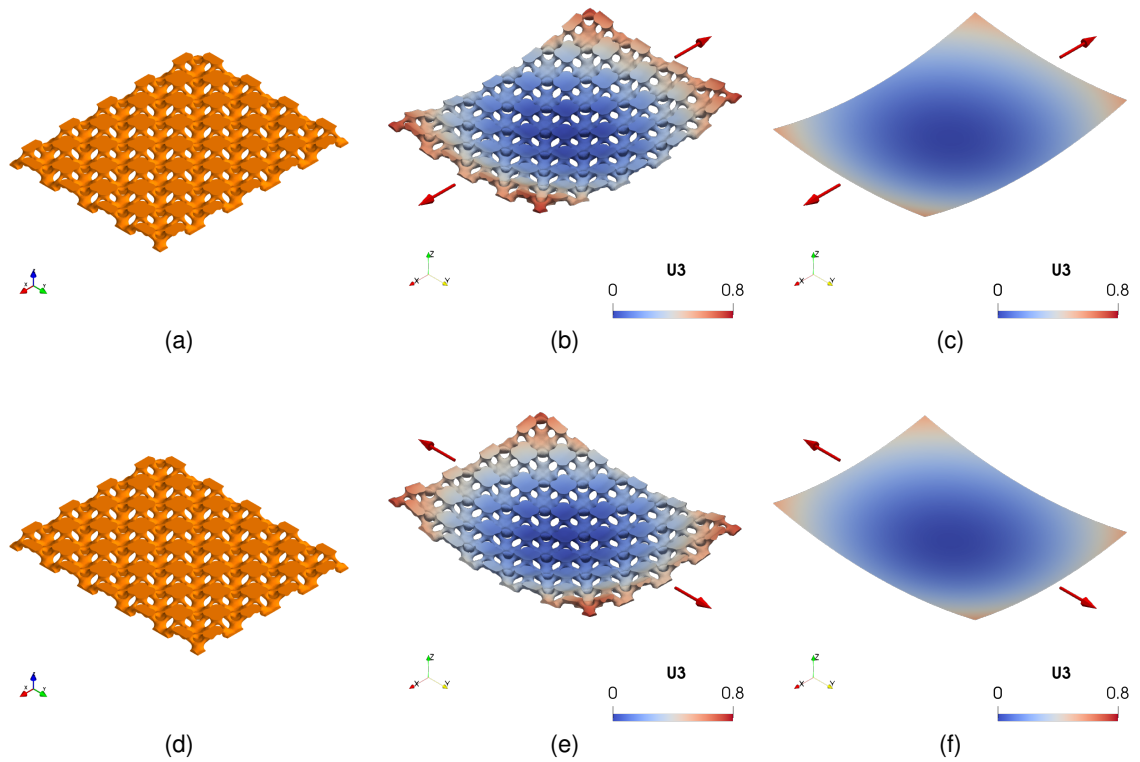


Fig. 7.9: 4×5 periodically assembled panel from the shape of Fig. 7.8. Image (a) corresponds to its reference flat configuration. The panel is submitted to an uniaxial tensile load along Ox up to 10% macroscopic strain. Image (b) depicts the deformed state computed on the complete panel while image (c) shows its macroscopic response assuming the homogeneous equivalent plate model with the coefficients of Table 7.2. The observed deformed shape is a saddle. The out-of-plane displacement is plotted as a color map on the deformed panel. It is recalled that the simulation was conducted in small strain, hence the out of plane response is proportional to the in-plane loading. The boundary conditions for the image (b) and (c) are reported in Fig. 7.3.

initial shape, depicted in Fig. 7.2(d), consists of a diagonal pattern of “cone” micro-perforations, with an initial material volume fraction of $|S| = 75\%$.

$$\begin{array}{c}
 \mathbf{C}^{\text{target}} \\
 \left[\begin{array}{ccc|ccc}
 0.12 & -0.06 & * & * & 2.3e^{-3} & * \\
 -0.06 & 0.12 & * & 2.3e^{-3} & * & * \\
 * & * & * & * & * & * \\
 \hline
 * & 2.3e^{-3} & * & 6.3e^{-4} & * & * \\
 2.3e^{-3} & * & * & * & 6.3e^{-4} & * \\
 * & * & * & * & * & *
 \end{array} \right] \\
 \\
 \mathbf{C}^* \\
 \left[\begin{array}{ccc|ccc}
 0.124 & -0.056 & 0 & 3.8e^{-3} & 1.2e^{-4} & 0 \\
 -0.056 & 0.125 & 0 & -2.1e^{-4} & 2.9e^{-3} & 0 \\
 0 & 0 & 0.028 & 0 & 0 & 8.5e^{-4} \\
 \hline
 3.8e^{-3} & -2.1e^{-4} & 0 & 8.8e^{-4} & 7.7e^{-5} & 0 \\
 1.2e^{-4} & 2.9e^{-3} & 0 & 7.7e^{-5} & 9.4e^{-4} & 0 \\
 0 & 0 & 8.5e^{-4} & 0 & 0 & 3.2e^{-4}
 \end{array} \right]
 \end{array}$$

Table 7.3: Values of the target stiffness tensors and the effective tensors for the final form of the microstructure in Fig. 7.11. Only the entries that have numerical values were controlled. The remaining entries were left free.

The convergence history of the cost functional and of the volume constraint displayed in Fig. 7.10(a) shows that the shape gets stabilised after the first 30 iterations, while the later iteration contributed only to small improvements without bringing the cost functional to less than 10^{-3} . This is corroborated by the evolution in the microstructure’s topology observable until iteration 30. Although the gain in the cost functional gets decreased by a factor of 10^4 , a remaining gap with respect to the target moduli can be read from Table 7.3, in particular in the sub-matrix **B**. We conclude that this shape corresponds to a local minima for the objective function, but the shape is not as effective as the one in Table 7.1. The evolution of material volume fraction displayed in Fig. 7.10(b) features an initial steep decrease down to 0.15, attributed to the initial swelling of the holes, followed by a and a slower evolution starting from iteration 40 to up to 0.48.

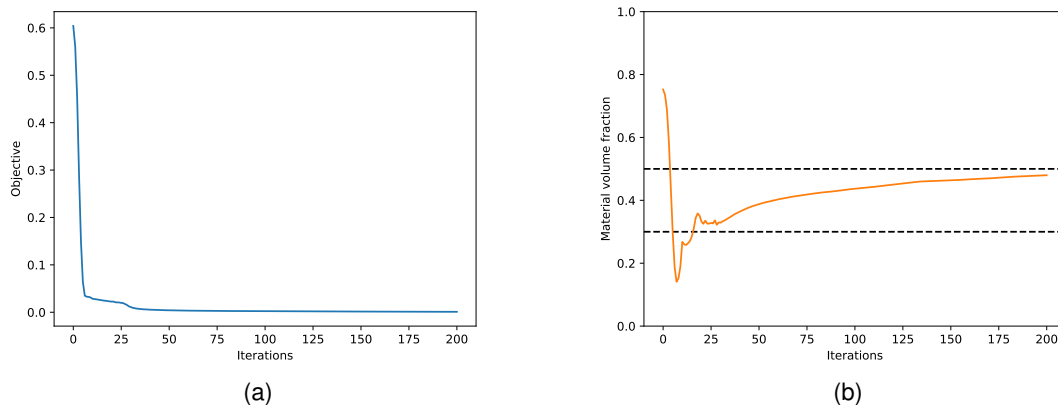


Fig. 7.10: Cost functional (a) and volume constraint (b) convergence plots for the microstructure depicted in Fig. 7.11. After 40 iterations, we seem to have rather stable convergence both for the cost functional and volume constraint. The algorithm stops after 200 iterations.

As mentioned in the last paragraph of section 7.4, this example illustrates how two initial guesses can lead to two completely different final shapes despite the identical target. Here, the final shape, depicted in Fig. 7.11, is of the rotating units type, discussed in [104] (see also the third example of a 2D design in [3]). A view of a periodically assembled panel is also provided in Fig. 7.12(a). Again, a clear asymmetry in the design is visible especially at the hinges connecting the rotating

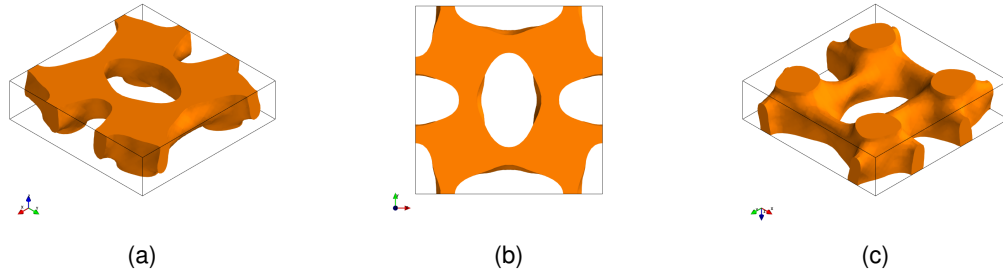


Fig. 7.11: Optimally designed periodic panels accounting for bending-stretch effects. The attained volume fraction is 0.48. Images (a) and (c) show the top and bottom of the periodic cell, while image (b) shows a bird's eye view of the cell.

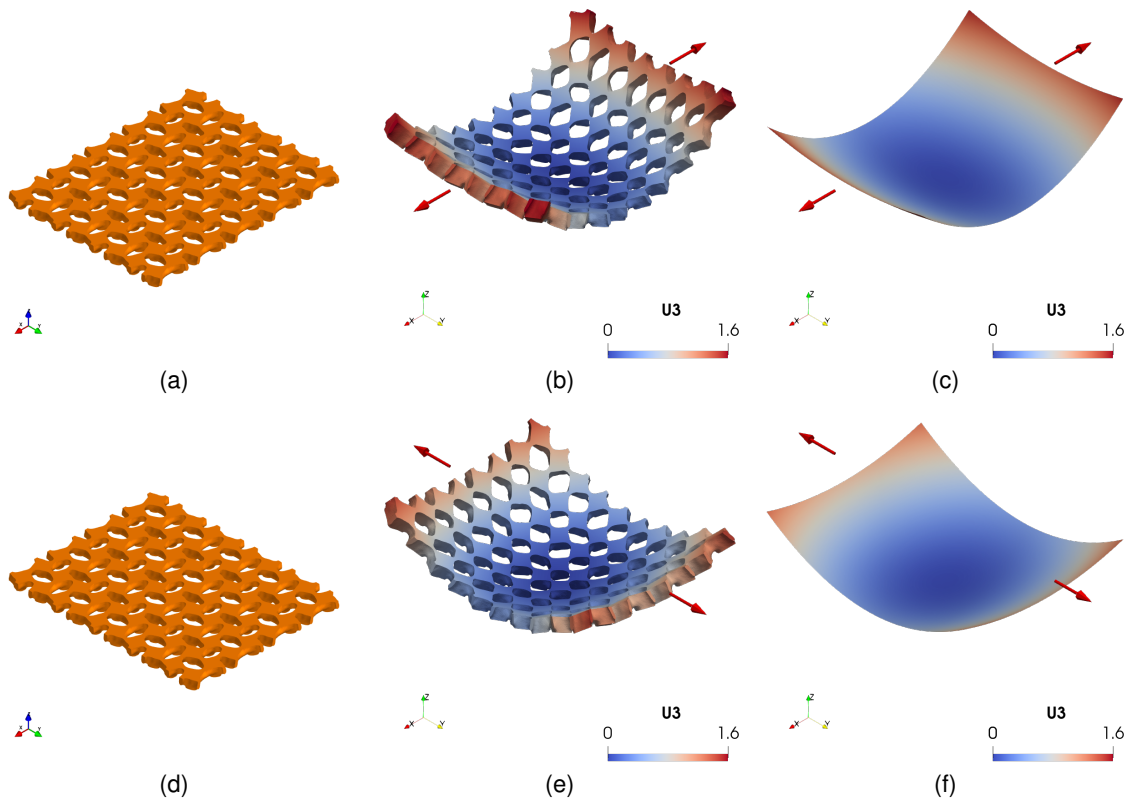


Fig. 7.12: 4×5 periodically assembled panel from the shape of Fig. 7.11. Image (a) corresponds to its reference flat configuration. The panel is submitted to an uniaxial tensile load along Ox up to 10% macroscopic strain. Image (b) depicts the deformed state computed on the complete panel while image (c) shows its macroscopic response assuming the homogeneous equivalent plate model with the coefficients of Table 7.3. The observed deformed shape is a saddle. The out-of-plane displacement is plotted as a color map on the deformed panel. It is recalled that the simulation was conducted in small strain, hence the out of plane response is proportional to the in-plane loading. The boundary conditions for the image (b) and (c) are reported in Fig. 7.3.

blocks. The collected values of all the coefficients of the aforementioned shape are included succinctly in Table 7.3. As prescribed, the resulting structure exhibits a “quadratic” symmetry. The final shape features an in-plane behaviour with an effective Poisson’s ratio of $\nu^* = -0.45$ which comes relatively close to the target. Like in Example 2, the obtained longitudinal extension–transverse bending coupling is quite small, with values for B_{1122}^* and B_{2211}^* being one order below the target value. By opposition with the last case, the longitudinal coupling coefficients B_{1111}^* and B_{2222}^* are one order of magnitude bigger than the transverse components B_{1122}^* and B_{2211}^* . As a consequence, the obtained curvature will be elliptical, i.e., the curvature in the longitudinal direction will be stronger than the transverse one.

Numerical simulations performed on a periodic panel reveal that the deformed shape in the linear regime will exhibit a positive Gaussian curvature, i.e., the panel will morph into an elliptical dome shape (see Fig. 7.12(b,e) for a loading in the Ox direction, and Fig. 7.12(c,f) for a loading in the Oy direction).

7.5.4 Example 4

The targets of the last microstructure to be optimised are given in the left side of Table 7.4. The material volume fraction, once again, was constrained to be between $0.3 \leq |S| \leq 0.5$. The initial shape, depicted in Fig. 7.2(d), consists of a diagonal pattern of “cone” micro-perforations. The collected values of all the coefficients of the aforementioned shape are succinctly included in Table 7.4.

C^{target}						
0.12	−0.03	*	*	$2.3e^{-3}$	*	*
−0.03	0.12	*	− $2.3e^{-3}$	*	*	*
*	*	*	*	*	*	*
*	− $2.3e^{-3}$	*	$6.3e^{-4}$	*	*	*
$2.3e^{-3}$	*	*	*	$6.3e^{-4}$	*	*
*	*	*	*	*	*	*

C^*						
0.106	− $2.8e^{-4}$	0	$9.5e^{-3}$	$1.8e^{-4}$	0	0
− $2.8e^{-4}$	0.114	0	− $8.3e^{-5}$	− $7.6e^{-3}$	0	0
0	0	$7.4e^{-3}$	0	0	$1.0e^{-4}$	0
$9.5e^{-3}$	− $8.3e^{-5}$	0	$9.4e^{-4}$	$2.4e^{-5}$	0	0
$1.8e^{-4}$	− $7.6e^{-3}$	0	$2.4e^{-5}$	$7.3e^{-4}$	0	0
0	0	$1.0e^{-4}$	0	0	$1.1e^{-4}$	0

Table 7.4: Values of the target stiffness tensors and the homogenised tensors for the final form of the microstructure in Fig. 7.14. Only the entries that have numerical values were controlled. The remaining entries were left free.

The convergence history of the cost functional and of the volume constraint displayed in Fig. 7.13(a) shows that the shape gets stabilised in the very first 10 iterations, while the later iteration contributed only to small improvements without bringing the cost functional to less than 6×10^{-3} . Although the gain in the cost functional gets decreased by a factor of 10^3 , a remaining gap with respect to the target moduli can be read from Table 7.4, in particular in the block matrix B. We conclude that this shape corresponds to a local minima for the objective function, but the shape is not as effective as the one in Table 7.1. The evolution of material volume fraction displayed in Fig. 7.13(b) features an initial steep decrease down to 0.17, attributed to the initial swelling of the holes, followed by a transient oscillatory evolution until iteration 20 and a slower evolution to up to 0.31. The oscillations are also visible in the evolution in the microstructure’s topology observable until iteration 20.

The final shape is similar to the pantograph structures discussed in [76], however, we notice that the vertical beams are on top of the horizontal beams. The collected values of all the coefficients

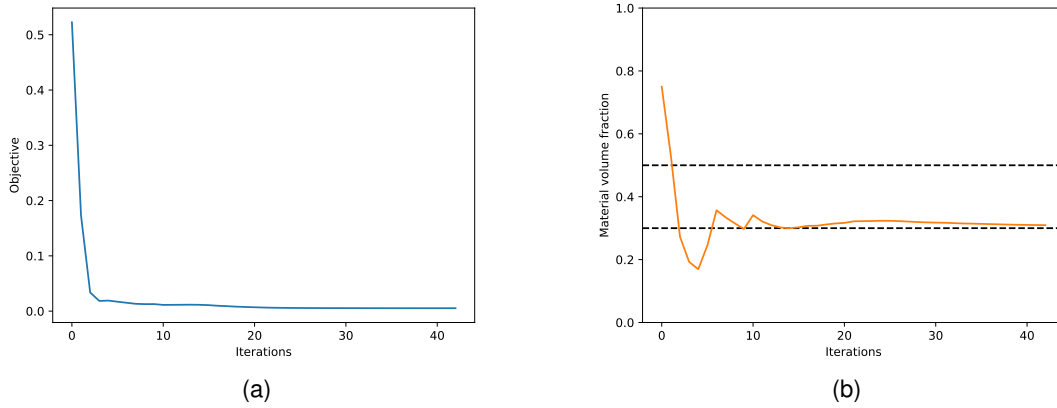


Fig. 7.13: Cost functional (a) and volume constraint (b) convergence plots for the microstructure depicted in Fig. 7.14. After 6 iterations, we seem to have rather stable convergence both for the cost functional and volume constraint. The algorithm stops after 43 iterations, because the time step in the advection equation becomes too small.

of the aforementioned shape are included succinctly in Table 7.4. The microstructure exhibits a mild auxetic response, but a remaining gap with respect to the target moduli can be read (significant difference in the A_{1122}^* coefficient). It exhibits a rather small longitudinal extension–transverse bending coupling, with values for B_{1122}^* and B_{2211}^* being quite far to the target value. These remaining gaps are no surprise, given the fact that the code stopped after a little more than 40 iterations, much less than in the other examples. However, it is worth noticing that the diagonal coefficient B_{1111}^* and B_{2222}^* are huge, meaning that the shape features a strong longitudinal extension–bending coupling. Let us further note that the panel is almost decoupled in the shear response, expressed through a small value of A_{1212}^* . Finally, the longitudinal out of the plane behaviour D_{1111}^* and especially D_{2222}^* come relatively close to the target value.

Numerical simulations performed on a periodic panel reveal that the deformed shape in the linear regime will morph into a cylinder (see Fig. 7.15(b,e) for a loading in the Ox direction. The panel loaded in the Oy direction will also morph into a cylinder, but with the longitudinal curvature of opposite sign (see Fig. 7.15(c,f)).

7.6 Conclusion and perspectives

We proposed a method for two-scale topology optimisation of microstructured thin panels with in-plane periodicity. We use inverse homogenisation and a level set method coupled with the Hadamard shape derivative to construct plate elastic moduli within the periodic cell in the context of the diffuse inter-phase approach that exhibit certain prescribed macroscopic behaviour for a single material and “void” while simultaneously accounting for bending–stretching effects. By controlling the microstructure of the panel, we simultaneously controlled the in-plane, out-of-plane and their coupled behaviour and in doing so we designed panels with an out-of-plane response that results in either a dome shaped structure or a saddle shaped structure under the action of in-plane loading. Interestingly, the direction of the loading can affect the type of obtained three-dimensional shape. By and large, these building blocks promote the systematic design of shape morphing structures. Moreover, the obtained shapes are directly realisable through additive manufacturing techniques as shown in Fig. 7.16.

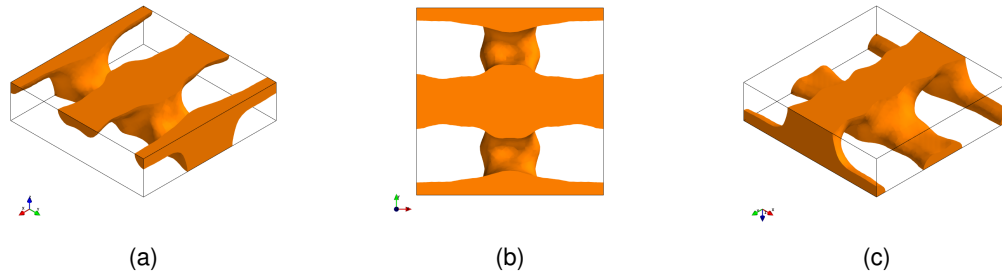


Fig. 7.14: Optimally designed periodic panels accounting for bending-stretch effects mimicking a pantograph structure. The attained volume fraction is 30%, which corresponds to lower bound of the volume interval set. Images (a) and (c) show the top and bottom of the periodic cell, while image (b) shows a bird's eye view of the cell.

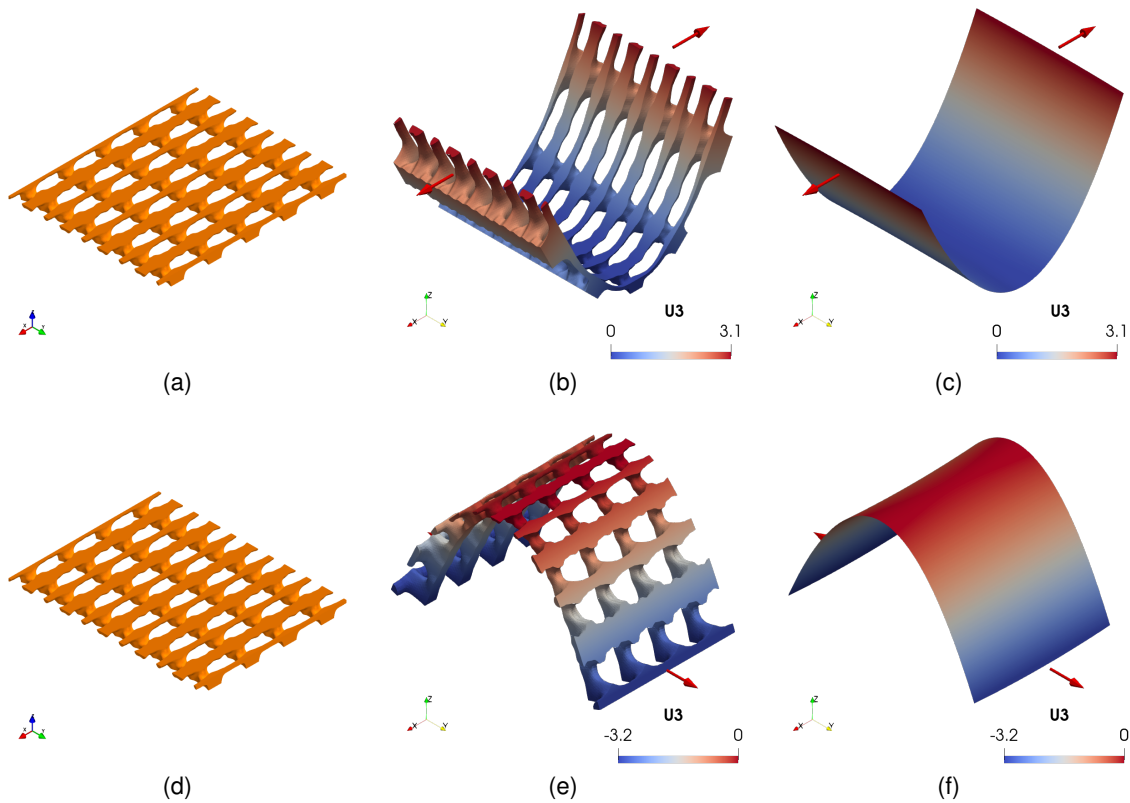


Fig. 7.15: 4×5 periodically assembled panel from the shape of Fig. 7.14. Image (a) corresponds to its reference flat configuration. The panel is submitted to an uniaxial tensile load along O_x up to 10% macroscopic strain. Image (b) depicts the deformed state computed on the complete panel while image (c) shows its macroscopic response assuming the homogeneous equivalent plate model with the coefficients of Table 7.4. The observed deformed shape is a saddle. The out-of-plane displacement is plotted as a color map on the deformed panel. It is recalled that the simulation was conducted in small strain, hence the out of plane response is proportional to the in-plane loading. The boundary conditions for the image (b) and (c) are reported in Fig. 7.3.

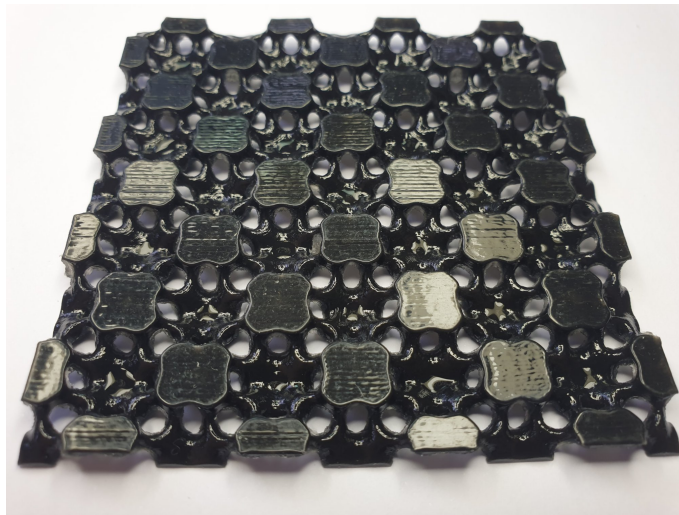


Fig. 7.16: Specimen designed from the microstructure of Example 2, manufactured on a stereo-lithography 3D printer by Stratasys using a TangoBlack resin. The specimen is composed of a 4×4 periodic arrangement and measures $80\text{mm} \times 80\text{mm} \times 5\text{mm}$, yielding a unit cell aspect's ratio $r = 0.25$.

Conclusion and perspectives for future work

This chapter summarizes and concludes the thesis with respect to the overall goal defined at the beginning to design and mechanically characterize architected sheets structures obtained by 3D printing.

The first part of this work presented a complete framework for designing elastic patterned sheets to meet a desired in-plane deformation behaviour. The approach efficiently generated a bunch of micro-structures that were fabricated and mechanically tested. Although the approach relies on simple elastic models, we note that the deformation mechanisms is mostly guided by structural rotations. The experimental results shown therefore a good agreement with the expected behaviour at small strain, both in terms of deformation mechanisms and in terms of stiffness target. At larger strains, non linear hyperelastic models convincingly simulated the experimental response of patterned rubber sheets.

In the context of elastic plates with periodic microstructures, which covered the second part of the thesis, we proposed a novel class of micro-structures to be harnessed in shape-shifting structures. They were obtained from a network of undulated ribbon, with constant thickness, with capabilities to maintain a prescribed property at finite strain. Furthermore, an adaptation of a topology optimisation algorithm to the case composite plates permitted to generate intricate micro-structures, yet compatible with 3D printing, and featuring a coupled deformation that allow them to turn from plate, to dome or saddles.

From the gathered knowledge on topology optimisation and on the characterization of these architected sheets at small and large strain, the perspective of this work could aim at generalizing these shape optimization techniques to include geometrical non-linearities, material non-linear behaviour (either elastoplasticity, or hyperelasticity) and perhaps formulate in a mathematical expression some geometric constraints associated the printing process in the design method. The most straightforward constraints regards the control on the thickness of the trusses inside the microstructures based upon the precision of the machines.

List of published articles or under review process

- [1] Filippo Agnelli, Andrei Constantinescu and Grigor Nika. Design and testing of 3D printed micro-architected polymer materials exhibiting a negative Poisson's ratio. Published in *Continuum Mechanics and Thermodynamics* (2020).
- [2] Filippo Agnelli, Pierre Margerit, Paolo Celli, Chiara Daraio and Andrei Constantinescu. Systematic two-scale image analysis of extreme deformations in soft architected sheets. Published in *International Journal of Mechanical Sciences* (2021).
- [3] Filippo Agnelli, Michele Tricarico and Andrei Constantinescu. Shape-shifting panel from 3D printed undulated ribbon lattice. Published in *Extreme Mechanics Letters* (2021).
- [4] Filippo Agnelli, Grigor Nika and Andrei Constantinescu. Design of thin micro-architected panels with extension-bending coupling effects using topology optimization. Preprint accepted in *Computer Methods in Applied Mechanics and Engineering* (2021).

Résumé en français

Les grandes avancées survenues sur les dernières décennies dans les techniques de fabrication additive (impression 3D) ont permis d'entreprendre la fabrication d'objets tridimensionnels aux géométries complexes, y compris les matériaux architecturés, c'est-à-dire des matériaux avec une micro-architecture interne de géométrie pouvant être ajustée. De nos jours, de telles techniques peuvent être réalisées avec plusieurs types de matériaux (y compris des alliages métalliques, des céramiques et des polymères) et à différentes échelles (depuis des objets microscopiques aux maisons imprimées en 3D). Étant donné que les propriétés effectives des matériaux architecturés découlent principalement de leur architecture interne, un contrôle de la microstructure assuré par les techniques de fabrication additive ouvre la voie vers de nouvelles gammes de matériaux avec des propriétés mécaniques prescrites efficaces. En partant d'arrangements élémentaires de matériau dans une cellule représentative conçue, on peut construire des structures complexes soit en répétant périodiquement ces arrangements, soit en répartissant les cellules pour obtenir une distribution macroscopique de propriétés désirée. La fabrication d'échantillons macroscopiques de ces matériaux hiérarchiques peut être utilisée pour diverses applications, y compris les échafaudages biocompatibles, les dispositifs médicaux, les applications aérospatiales à distance, les couches ultralégères absorbant les vibrations ou les couches absorbant les chocs, les structures à haute résistance avec des capacités de refroidissement exceptionnelles, non contrôlées -comportement linéaire, structures auto-pliantes. Les attentes élevées des technologies d'impression et de leurs applications structurelles ont soulevé une série de défis dans la conception de ces structures :

- conception de la forme des structures et réglage des propriétés des matériaux architecturés ;
- distribution spatiale des structures à petite échelle en fonction de la charge spécifiée ;
- paramètres, influence des paramètres du procédé sur la structure finale.

En ce qui concerne la conception de forme optimale, des algorithmes systématiques sont par exemple bien établis pour la distribution macroscopique prescrite des propriétés dans le cas d'élasticité linéaire de petite déformation. Pourtant, ces techniques restent assez limitées dans leur utilisation à l'échelle industrielle, en partie à cause du manque de compréhension, de l'absence de modèles constitutifs et d'outils de simulation qui abordent la possibilité de trouver une configuration optimale. Le paysage manque d'une approche de conception globale plus cohérente où l'optimisation structurelle répondrait aux contraintes de fabrication dont la précision géométrique, ou encore la transformation de la matière, dans le processus d'impression.

La première partie de ce manuscrit a un but bibliographique. Les deux domaines principaux du travail proposé - à savoir la méthode d'homogénéisation asymptotique et l'optimisation de forme - sont présentés dans deux chapitres séparés.

Chapitre 1. Caractérisation mécanique de matériaux composites élastiques

Ce chapitre traite de la détermination des propriétés globales, également appelées propriétés *efficace*, d'un matériau composite formé par des variations périodiques soit de propriétés matérielles, soit de construction géométrique. Après une introduction qui fait le point sur l'état de l'art de la caractérisation mécanique des structures élastiques, la discussion approfondit les détails de la théorie de l'homogénéisation asymptotique. La théorie consiste à troquer la représentation d'un matériau architecturé hétérogène qui demande une description géométrique fine et lourde, pour un milieu homogène équivalent qui présente typiquement un comportement plus complexe (par exemple, qui inclut des anisotropies, ou des degrés de liberté cinématiques plus). Premièrement, le cas général des matériaux architecturés avec un motif périodique dans toutes les directions est passé en revue. En supposant que le champ de déplacement à l'intérieur du milieu puisse être écrit en utilisant un développement asymptotique, des formules analytiques pour les coefficients élastiques effectifs qui dépendent de la distribution de matériau à l'intérieur d'une cellule élémentaire redimensionnée sont dérivées. Ensuite, après avoir identifié le comportement macroscopique général des nappes architecturées, l'espace des tenseurs admissibles à symétrie de matériau orthotrope est obtenu. Enfin, le cas particulier des structures en plaques avec une micro-architecture périodique dans le plan est discuté. En supposant que l'épaisseur du panneau est comparable à la longueur de la période, on obtient un comportement macroscopique généralisé de la plaque mince de Kirchhoff-Love. Encore une fois, les coefficients de plaque effectifs sont calculés analytiquement à partir de la répartition des matériaux à l'intérieur de la maille élémentaire.

Chapitre 2. Optimisation de forme et topologique

Les principaux ingrédients requis pour utiliser l'optimisation de la forme et de la topologie sont décrits dans ce chapitre. Après une introduction qui définit la philosophie du problème d'optimisation de forme, nous abordons brièvement le problème théorique de la non-existence d'un domaine optimal qui minimise une fonction de coût dépendante de la forme $\mathcal{J}(S)$ et discutons les techniques pour le contourner. La classification des principales catégories d'optimisation de forme, c'est-à-dire l'optimisation paramétrique, géométrique et topologique, est ensuite présentée succinctement. La discussion est alors centrée sur l'optimisation de la topologie, qui aborde le problème de l'optimisation de la forme en toute généralité. Nous passons rapidement en revue les principales méthodes d'optimisation de la topologie, y compris les méthodes de densité (par exemple, la méthode d'homogénéisation, le SIMP), la méthode de sensibilité topologique et les méthodes implicites (par exemple, la méthode du champ de phase, la méthode des ensembles de niveaux). Ensuite, nous rappelons le concept de dérivée de forme, en s'appuyant sur le cadre de la méthode d'Hadamard, où les variations d'une forme donnée S de la forme $(1 + \theta)(S)$ sont considérés, pour *petits champs de vitesse* θ . Des notions connexes de différenciation par rapport à la forme sont rappelées : notamment, nous introduisons la notion de dérivée de forme, et en extrayons une notion de gradient de forme pour la minimisation itérative de l'objectif. Pour les fonctions dépendantes de la forme, une méthode lagrangienne formelle pour obtenir des dérivées de forme est expliquée et les formules pour la dérivée de forme des intégrales de volume et de surface sont rappelées. Le matériel de base sur la méthode de sensibilité de forme est illustré par un exemple sur la façon de trouver l'expression dérivée de forme d'une fonctionnelle de type général :

$$\mathcal{J}(S, \mathbf{u}(S)) = \int_S j(\mathbf{x}, \mathbf{u}(S)) d\mathbf{x} + \int_{\partial S} k(\mathbf{s}, \mathbf{u}(S)) ds,$$

où \mathbf{u} est la solution d'un système d'élasticité linéaire. Le deuxième ingrédient de la méthode d'optimisation de la topologie sélectionnée, à savoir la méthode des niveaux définis pour la de-

scription de la forme, est ensuite décrit. Toutes les formes sont supposées être incluses dans un grand domaine de calcul \mathcal{D} et sont représentées implicitement via l'ensemble de niveau zéro d'une fonction scalaire ϕ . La propagation de la forme sous un champ de vitesse θ est ensuite décrite via la *advection* de la fonction level set à travers une équation de Hamilton-Jacobi. Enfin, le couplage de la sensibilité de forme avec une description d'ensemble de niveaux est expliqué. Le gradient de forme est interprété comme une vitesse d'advection pour la fonction level set et un algorithme itératif est construit pour la minimisation numérique de la fonction de coût. Deux étapes de base pour ce couplage sont expliquées, l'approche "matériau Ersatz" pour représenter la partie vide $\mathcal{D} \setminus S$ et l'extension et la régularisation du champ de vitesse afin d'accélérer la vitesse de convergence. Enfin, la dernière section du chapitre est consacrée à l'approche interphase diffuse, qui permet de dériver une formulation simplifiée, mais mathématiquement rigoureuse, pour la propagation de la forme.

Chapitre 3. Conception numérique de feuilles périodiques architecturées à coefficient de Poisson négatif

Le terme auxétique indique des matériaux avec un coefficient de Poisson négatif (ν), c'est-à-dire des matériaux qui ont tendance à se dilater transversalement à une charge d'étirement uniaxiale appliquée et vice versa. Dans ce premier chapitre, un algorithme d'optimisation de topologie mettant en jeu la méthode des level set et l'homogénéisation asymptotique permet d'obtenir des matériaux micro-architecturés périodiques avec un tenseur d'élasticité efficace et un coefficient de Poisson prescrits. La fonctionnelle a été définie par rapport aux composantes tensorielles élastiques cibles :

$$\mathcal{J}(S) = \nu_{ijkl} C_{ijkl}^* + \frac{1}{2} \eta_{ijkl} \left(C_{ijkl}^* - C_{ijkl}^{\text{target}} \right)^2,$$

où C_{ijkl}^* représentent les coefficients élastiques effectifs de la structure, tandis que C_{ijkl}^{target} sont les valeurs élastiques prescrites. L'efficacité de la méthode de résolution est illustrée à travers quatre exemples numériques où la forme conçue donne un coefficient de Poisson négatif important. Remarquablement, certaines des formes optimales obtenues sont en fait déjà bien connues dans la littérature. L'espace des formes micro-architecturales admissibles qui porte la symétrie matérielle orthotrope permet d'atteindre des formes avec un coefficient de Poisson effectif inférieur à -1 .

Chapitre 4. Impression 3D et caractérisation de feuilles polymères architecturées à coefficient de Poisson négatif

Ce chapitre conclut les compléments du cycle de conception de plusieurs matériaux auxétiques de chapitre 3 avec la fabrication du matériau et le test du matériau. Les spécimens sont fabriqués à l'aide d'une imprimante commerciale de stéréolithographie Ember et sont testés mécaniquement. Les champs de déplacement et de déformation observés lors des essais de traction obtenus par corrélation d'images numériques correspondent aux prédictions des simulations par éléments finis et démontrent l'efficacité du cycle de conception à faible déformation.

Chapitre 5. Analyse systématique d'images à deux échelles pour étudier les déformations extrêmes de feuilles souples architecturées

La nature multi-échelle des matériaux architecturés soulève le besoin de méthodes expérimentales avancées adaptées à l'identification de leurs propriétés effectives, en particulier lorsque leur

taille est finie et qu'ils subissent des déformations extrêmes. L'étude de ce chapitre démontre que des méthodes de traitement d'images de pointe combinées à des modèles numériques et analytiques fournissent une description quantitative complète de ces solides et de leur comportement global, y compris l'influence des conditions aux limites, du processus de fabrication et de non-linéarités géométriques et constitutives. À cette fin, une analyse de corrélation d'images numériques multi-échelles adaptée est utilisée pour suivre à la fois les allongements et les rotations de caractéristiques particulières de la maille élémentaire à l'échelle locale et globale (homogénéisée) du matériau. Cela permet d'observer avec une clarté sans précédent les champs de déformation pour diverses cellules unitaires de la structure et de détecter les modèles de déformation globaux et les hétérogénéités de la distribution de déformation homogénéisée. Cette méthode est ici démontrée sur des tôles élastiques subissant des déformations longitudinales et de cisaillement extrêmes. Ces résultats expérimentaux sont comparés à des simulations d'éléments finis non linéaires, qui sont également utilisées pour évaluer les effets des imperfections de fabrication sur la réponse. Une représentation squelettique du solide architecturé est ensuite extraite des expériences et utilisée pour créer un modèle de charnière en treillis purement cinématique qui peut capturer avec précision son comportement. L'analyse proposée dans ce travail peut être étendue pour guider la conception de solides architecturés bidimensionnels présentant d'autres motifs réguliers, quasi-réguliers ou gradués, et soumis à d'autres types de charges.

Chapitre 6. Panneau à changement de forme à partir de réseaux de rubans ondulés 3D imprimés

Les matériaux qui changent de forme en réponse à des stimuli externes ouvrent de nouvelles perspectives pour la conception et la mise en forme polyvalentes d'objets tridimensionnels. Dans ce chapitre, nous introduisons une nouvelle classe de microstructures présentant un effet de couplage extension-flexion, qui peut être exploité comme bloc de construction élémentaire pour fabriquer les panneaux à changement de forme. Ils sont construits avec un seul matériau sous la forme d'un réseau de rubans ondulés. Les mécanismes de déformations des rubans ondulés seuls et des rubans ondulés connectés sont analysés à l'aide de la méthode des éléments finis pour expliquer les principales caractéristiques du mécanisme de couplage. Pour une microstructure particulière de la classe proposée, le tenseur de rigidité élastique est calculé en combinant l'homogénéisation à deux échelles à la théorie des plaques minces généralisée de Kirchhoff–Love. La plage du coefficient de couplage extension–flexion réalisable est ensuite évaluée par rapport aux paramètres géométriques de la maille élémentaire. Des spécimens à motifs sont fabriqués à l'aide d'une imprimante 3D FFF Ultimaker et sont testés mécaniquement jusqu'à une déformation de 20%. Le déplacement hors plan mesuré par le suivi de points correspond aux prédictions des simulations par éléments finis et indique que la structure conserve ses propriétés à déformation finie. De plus, une charge d'essai de traction avec une frontière localisée est proposée pour mettre en évidence un déplacement hors plan exceptionnel. Ces structures peuvent être exploitées en combinaison avec des matériaux réactifs pour l'actionnement de soft robots, systèmes conformes et structures reconfigurables, comme alternatives à la mécanique externe moteurs, systèmes de contrôle et dispositifs de puissance.

Chapitre 7. Conception de panneaux périodiques 3D imprimables minces à couplage extension–flexion par optimisation de formes

Dans ce dernier chapitre, nous concevons la micro-architecture de panneaux élastiques minces pour contrôler leur comportement macroscopique, prenant en compte simultanément la rigidité dans le plan, la rigidité hors plan et les effets de couplage extension-flexion. La méthode

d'optimisation de la topologie utilisée combine l'homogénéisation inverse, la dérivée de forme d'Hadarnard et une méthode de level set dans le contexte de l'interface diffuse pour capturer systématiquement au sein de la maille élémentaire la micro-architecture optimale. L'efficacité de la méthode de résolution est illustrée à travers quatre exemples numériques où la forme conçue donne un important couplage extension–flexion. Les réponses de déformation sous charge de traction sont évaluées numériquement à la fois sur le panneau périodique complet et sur sa plaque jumelle homogénéisée. Les résultats démontrent que le contrôle simultané du dans le plan, du hors plan et de leur comportement couplé permet de transformer un panneau plat en une structure en forme de dôme ou de selle. De plus, les cellules unitaires obtenues sont des blocs élémentaires pour créer des objets directement imprimables en 3D avec des capacités de morphing de forme.

Conclusion

En conclusion, la première partie de ce travail a présenté un cadre complet pour la conception de feuilles à motifs élastiques pour répondre à un comportement de déformation dans le plan souhaité. L'approche a généré efficacement un tas de micro-structures qui ont été fabriquées et testées mécaniquement. Bien que l'approche repose sur des modèles élastiques simples, nous notons que les mécanismes de déformation sont principalement guidés par des rotations structurelles. Les résultats expérimentaux ont donc montré un bon accord avec le comportement attendu à faible déformation, à la fois en termes de mécanismes de déformation et en termes de rigidité cible.

Dans le contexte des plaques élastiques à microstructures périodiques, qui couvrait la deuxième partie de la thèse, nous avons proposé une nouvelle classe de microstructures à exploiter dans des structures à changement de forme. Ils ont été obtenus à partir d'un réseau de ruban ondulé, d'épaisseur constante, avec des capacités à maintenir une propriété prescrite à une déformation finie. De plus, une adaptation d'un algorithme d'optimisation de topologie au cas des plaques composites a permis de générer des micro-structures complexes, mais compatibles avec l'impression 3D, et présentant une déformation couplée qui leur permet de passer de la plaque, au dôme ou aux selles.

A partir des connaissances accumulées sur l'optimisation topologique et sur la caractérisation de ces plaques architecturées à petites et grandes déformations, la perspective de ce travail pourrait viser à généraliser ces techniques d'optimisation de forme pour inclure les non-linéarités géométriques, le comportement non-linéaire des matériaux (soit élastoplasticité, ou hyperélasticité) et peut-être formuler dans une expression mathématique certaines contraintes géométriques associées au processus d'impression dans la méthode de conception. Les contraintes les plus simples concernent le contrôle de l'épaisseur des fermes à l'intérieur des microstructures en fonction de la précision des machines.

Bibliography

- [1] N. Aage, E. Andreassen, and B. S. Lazarov. Topology optimization using PETSc: An easy-to-use, fully parallel, open source topology optimization framework. *Structural and Multidisciplinary Optimization*, 51(3):565–572, aug 2014. doi: 10.1007/s00158-014-1157-0.
- [2] B. E. Abali and E. Barchiesi. Additive manufacturing introduced substructure and computational determination of metamaterials parameters by means of the asymptotic homogenization. *Continuum Mechanics and Thermodynamics*, 10 2020. doi: 10.1007/s00161-020-00941-w.
- [3] F. Agnelli, A. Constantinescu, and G. Nika. Design and testing of 3d-printed micro-architected polymer materials exhibiting a negative poisson’s ratio. *Continuum Mechanics and Thermodynamics*, 32(2):433–449, 3 2020. doi: 10.1007/s00161-019-00851-6.
- [4] F. Agnelli, P. Margerit, P. Celli, C. Daraio, and A. Constantinescu. Systematic two-scale image analysis of extreme deformations in soft architected sheets. *International Journal of Mechanical Sciences*, 194:106205, 3 2021. ISSN 0020-7403. doi: 10.1016/j.ijmecsci.2020.106205.
- [5] F. Agnelli, M. Tricarico, and A. Constantinescu. Shape-shifting panel from 3D printed undulated ribbon lattice. *Extreme Mechanics Letters*, 42:101089, 1 2021. doi: 10.1016/j.eml.2020.101089.
- [6] R. M. Ajaj, C. S. Beaverstock, and M. I. Friswell. Morphing aircraft: The need for a new design philosophy. *Aerospace Science and Technology*, 49:154–166, 2 2016. doi: 10.1016/j.ast.2015.11.039.
- [7] M. N. Ali, J. J. C. Busfield, and I. U. Rehman. Auxetic oesophageal stents: structure and mechanical properties. *Journal of Materials Science: Materials in Medicine*, 25(2):527–553, 10 2013. doi: 10.1007/s10856-013-5067-2.
- [8] G. Allaire. *Shape Optimization by the Homogenization Method*. Springer New York, 2002. ISBN 1441929428. doi: 10.1007/978-1-4684-9286-6.
- [9] G. Allaire. *Conception optimale de structures*. Springer Berlin Heidelberg, 2007. ISBN 978-3-540-36856-4. doi: 10.1007/978-3-540-36856-4.
- [10] G. Allaire and F. Jouve. Minimum stress optimal design with the level set method. *Engineering Analysis with Boundary Elements*, 32(11):909–918, 11 2008. doi: 10.1016/j.enganabound.2007.05.007.
- [11] G. Allaire and O. Pantz. Structural optimization with `freefem++`. *Structural and Multidisciplinary Optimization*, 32(3):173–181, 7 2006. doi: 10.1007/s00158-006-0017-y.
- [12] G. Allaire, E. Bonnetier, G. Francfort, and F. Jouve. Shape optimization by the homogenization method. *Numerische Mathematik*, 76(1):27–68, 3 1997. doi: 10.1007/s002110050253.
- [13] G. Allaire, F. Jouve, and A.-M. Toader. A level-set method for shape optimization. *Comptes Rendus Mathematique*, 334(12):1125–1130, 1 2002. doi: 10.1016/s1631-073x(02)02412-3.
- [14] G. Allaire, F. Jouve, and A.-M. Toader. Structural optimization using sensitivity analysis and a level-set method. *Journal of Computational Physics*, 194(1):363–393, 2 2004. doi: 10.1016/j.jcp.2003.09.032.
- [15] G. Allaire, C. Dapogny, G. Delgado, and G. Michailidis. Multi-phase structural optimization via a level set method. *ESAIM: Control, Optimisation and Calculus of Variations*, 20(2):576–611, 3 2014. doi: 10.1051/cocv/2013076.

- [16] L. Allais, M. Bornert, T. Bretheau, and D. Caldemaison. Experimental characterization of the local strain field in a heterogeneous elastoplastic material. *Acta Metallurgica et Materialia*, 42(11):3865–3880, 11 1994. doi: 10.1016/0956-7151(94)90452-9.
- [17] R. F. Almgren. An isotropic three-dimensional structure with Poisson’s ratio $=-1$. *Journal of Elasticity*, 15(4):427–430, 12 1985. doi: 10.1007/bf00042531.
- [18] L. Ambrosio and G. Buttazzo. An optimal design problem with perimeter penalization. *Calculus of Variations and Partial Differential Equations*, 1(1):55–69, mar 1993. doi: 10.1007/bf02163264.
- [19] S. Amstutz, S. M. Giusti, A. A. Novotny, and E. A. de Souza Neto. Topological derivative for multi-scale linear elasticity models applied to the synthesis of microstructures. *International Journal for Numerical Methods in Engineering*, 84(6):733–756, 5 2010. doi: 10.1002/nme.2922.
- [20] M. N. Andersen, F. Wang, and O. Sigmund. On the competition for ultimately stiff and strong architected materials. *Materials and Design*, 198:109356, 1 2021. doi: 10.1016/j.matdes.2020.109356.
- [21] E. Andreassen, B. S. Lazarov, and O. Sigmund. Design of manufacturable 3d extremal elastic microstructure. *Mechanics of Materials*, 69(1):1–10, 2 2014. doi: 10.1016/j.mechmat.2013.09.018.
- [22] M. Arya, N. Lee, and S. Pellegrino. Ultralight structures for space solar power satellites. In *3rd AIAA Spacecraft Structures Conference*, page 1950. American Institute of Aeronautics and Astronautics, 1 2016. doi: 10.2514/6.2016-1950.
- [23] M. F. Ashby. The properties of foams and lattices. *Philosophical Transactions of the Royal Society A: Mathematical, Physical and Engineering Sciences*, 364(1838):15–30, 11 2005. doi: 10.1098/rsta.2005.1678.
- [24] F. Auricchio, E. Bonetti, M. Carraturo, D. Hömberg, A. Reali, and E. Rocca. A phase-field-based graded-material topology optimization with stress constraint. *Mathematical Models and Methods in Applied Sciences*, 30(08):1461–1483, jul 2020. doi: 10.1142/s0218202520500281.
- [25] N. S. Bakhvalov and G. Panasenko. *Homogenisation: Averaging Processes in Periodic Media*. Springer Netherlands, 2011. ISBN 9401075069. doi: 10.1007/978-94-009-2247-1.
- [26] Y. Balit, P. Margerit, E. Charkaluk, and A. Constantinescu. Crushing of additively manufactured thin-walled metallic lattices: Two-scale strain localization analysis. *Mechanics of Materials*, 160:103915, sep 2021. doi: 10.1016/j.mechmat.2021.103915.
- [27] K.-J. Bathe, E. Dvorkin, and L. W. Ho. Our discrete-kirchhoff and isoparametric shell elements for nonlinear analysis—an assessment. *Computers and Structures*, 16(1-4):89–98, 1 1983. doi: 10.1016/0045-7949(83)90150-5.
- [28] A. A. Bauhofer, S. Krödel, J. Rys, O. R. Bilal, A. Constantinescu, and C. Daraio. Harnessing photochemical shrinkage in direct laser writing for shape morphing of polymer sheets. *Advanced Materials*, 29(42):1703024, 9 2017. doi: 10.1002/adma.201703024.
- [29] T. Bückmann, N. Stenger, M. Kadic, J. Kaschke, A. Frölich, T. Kennerknecht, C. Eberl, M. Thiel, and M. Wegener. Tailored 3D mechanical metamaterials made by dip-in direct-laser-writing optical lithography. *Advanced Materials*, 24(20):2710–2714, 4 2012. doi: 10.1002/adma.201200584.
- [30] M. P. Bendsøe. Optimal shape design as a material distribution problem. *Structural Optimization*, 1(4):193–202, 12 1989. doi: 10.1007/bf01650949.
- [31] M. P. Bendsøe and N. Kikuchi. Generating optimal topologies in structural design using a homogenization method. *Computer Methods in Applied Mechanics and Engineering*, 71(2):197–224, 11 1988. doi: 10.1016/0045-7825(88)90086-2.
- [32] M. P. Bendsøe and O. Sigmund. *Topology Optimization*. Springer Berlin Heidelberg, 2004. ISBN 978-3-662-05086-6. doi: 10.1007/978-3-662-05086-6.
- [33] A. Bensoussan, J.-L. Lions, and G. Papanicolaou. *Asymptotic Analysis for Periodic Structures*. North-Holland Pub. Co. Sole distributors for the U.S.A. and Canada, Elsevier North-Holland, Amsterdam New York New York, 1978. ISBN 9780080875262. doi: 10.1090/chel/374.

- [34] M. J. Beran. Use of the vibrational approach to determine bounds for the effective permittivity in random media. *Il Nuovo Cimento*, 38(2):771–782, 7 1965. doi: 10.1007/bf02748596.
- [35] K. Bertoldi, P. M. Reis, S. Willshaw, and T. Mullin. Negative poisson's ratio behavior induced by an elastic instability. *Advanced Materials*, 22(3):361–366, 1 2010. doi: 10.1002/adma.200901956.
- [36] D. Bertsekas. *Constrained Optimization and Lagrange Multiplier Methods*. Athena Scientific, Belmont, Mass, 1982. ISBN 1886529043. doi: 10.1016/c2013-0-10366-2.
- [37] G. Besnard, F. Hild, and S. Roux. "finite-element" displacement fields analysis from digital images: Application to portevin–le châtelier bands. *Experimental Mechanics*, 46(6):789–803, 12 2006. doi: 10.1007/s11340-006-9824-8.
- [38] O. R. Bilal, R. Süssstrunk, C. Daraio, and S. D. Huber. Intrinsically polar elastic metamaterials. *Advanced Materials*, 29(26):1700540, 5 2017. doi: 10.1002/adma.201700540.
- [39] J. Boddapati, S. Mohanty, and R. K. Annabattula. An analytical model for shape morphing through combined bending and twisting in piezo composites. *Mechanics of Materials*, 144:103350, 5 2020. doi: 10.1016/j.mechmat.2020.103350.
- [40] J. W. Boley, W. M. van Rees, C. Lissandrello, M. N. Horenstein, R. L. Truby, A. Kotikian, J. A. Lewis, and L. Mahadevan. Shape-shifting structured lattices via multimaterial 4D printing. *Proceedings of the National Academy of Sciences*, 116(42):20856–20862, 10 2019. doi: 10.1073/pnas.1908806116.
- [41] M. Bornert, F. Brémand, P. Doumalin, J.-C. Dupré, M. Fazzini, M. Grédiac, F. Hild, S. Mistou, J. Molimard, J.-J. Orteu, L. Robert, Y. Surrel, P. Vacher, and B. Wattrisse. Assessment of digital image correlation measurement errors: Methodology and results. *Experimental Mechanics*, 49(3):353–370, 12 2008. doi: 10.1007/s11340-008-9204-7.
- [42] T. E. Bruns and D. A. Tortorelli. Topology optimization of non-linear elastic structures and compliant mechanisms. *Computer Methods in Applied Mechanics and Engineering*, 190(26-27):3443–3459, 3 2001. doi: 10.1016/s0045-7825(00)00278-4.
- [43] T. T. C. Bui, C. Dapogny, and P. Frey. An accurate anisotropic adaptation method for solving the level set advection equation. *International Journal for Numerical Methods in Fluids*, 70(7):899–922, 11 2011. doi: 10.1002/flid.2730.
- [44] M. Burger, B. Hackl, and W. Ring. Incorporating topological derivatives into level set methods. *Journal of Computational Physics*, 194(1):344–362, 2 2004. doi: 10.1016/j.jcp.2003.09.033.
- [45] J. Céa. Conception optimale ou identification de formes, calcul rapide de la dérivée directionnelle de la fonction coût. *ESAIM: Mathematical Modelling and Numerical Analysis*, 20(3):371–402, 1986. doi: 10.1051/m2an/1986200303711.
- [46] D. Caillerie and J.-C. Nedelec. Thin elastic and periodic plates. *Mathematical Methods in the Applied Sciences*, 6(1):159–191, 1 1984. doi: 10.1002/mma.1670060112.
- [47] V. Calisti, A. Lebéé, A. A. Novotny, and J. Sokolowski. Sensitivity of the second order homogenized elasticity tensor to topological microstructural changes. *Journal of Elasticity*, 144(2):141–167, may 2021. doi: 10.1007/s10659-021-09836-6.
- [48] S. J. P. Callens and A. A. Zadpoor. From flat sheets to curved geometries: Origami and kirigami approaches. *Materials Today*, 21(3):241–264, 4 2018. doi: 10.1016/j.mattod.2017.10.004.
- [49] M. Carraturo, E. Rocca, E. Bonetti, D. Hömberg, A. Reali, and F. Auricchio. Graded-material design based on phase-field and topology optimization. *Computational Mechanics*, 64(6):1589–1600, 6 2019. doi: 10.1007/s00466-019-01736-w.
- [50] E. Catmull and J. Clark. Recursively generated B-spline surfaces on arbitrary topological meshes. *Computer-Aided Design*, 10(6):350–355, nov 1978. doi: 10.1016/0010-4485(78)90110-0.
- [51] CEA. Cast3m, 2020. URL <http://www-cast3m.cea.fr>.

- [52] P. Celli, C. McMahan, B. Ramirez, A. Bauhofer, C. Naify, D. Hofmann, B. Audoly, and C. Daraio. Shape-morphing architected sheets with non-periodic cut patterns. *Soft Matter*, 14(48):9744–9749, 12 2018. doi: 10.1039/c8sm02082e.
- [53] P. Celli, A. Lamaro, C. McMahan, P. Bordeenithikasem, D. C. Hofmann, and C. Daraio. Compliant morphing structures from twisted bulk metallic glass ribbons. *Journal of the Mechanics and Physics of Solids*, 145:104129, 12 2020. doi: 10.1016/j.jmps.2020.104129.
- [54] A. Cemal Eringen. *Microcontinuum Field Theories*. Springer New York, 1999. ISBN 978-1-4612-6815-4. doi: 10.1007/978-1-4612-0555-5.
- [55] E. A. Cerda, K. Ravi-Chandar, and L. Mahadevan. Wrinkling of an elastic sheet under tension. *Nature*, 419(6907):579–580, 10 2002. doi: 10.1038/419579b.
- [56] A. Chambolle. A density result in two-dimensional linearized elasticity, and applications. *Archive for Rational Mechanics and Analysis*, 167(3):211–233, may 2003. doi: 10.1007/s00205-002-0240-7.
- [57] F. Chen, Y. Wang, M. Y. Wang, and Y. Zhang. Topology optimization of hyperelastic structures using a level set method. *Journal of Computational Physics*, 351:437–454, 12 2017. doi: 10.1016/j.jcp.2017.09.040.
- [58] T. Chen, O. R. Bilal, K. Shea, and C. Daraio. Harnessing bistability for directional propulsion of soft, untethered robots. *Proceedings of the National Academy of Sciences*, 115(22):5698–5702, 5 2018. doi: 10.1073/pnas.1800386115.
- [59] T. Chen, O. R. Bilal, R. J. Lang, C. Daraio, and K. Shea. Autonomous deployment of a solar panel using elastic origami and distributed shape-memory-polymer actuators. *Physical Review Applied*, 11(6), 6 2019. doi: 10.1103/physrevapplied.11.064069.
- [60] G. P. T. Choi, L. H. Dudte, and L. Mahadevan. Programming shape using kirigami tessellations. *Nature Materials*, 18(9):999–1004, 8 2019. doi: 10.1038/s41563-019-0452-y.
- [61] J. B. Choi and R. S. Lakes. Fracture toughness of re-entrant foam materials with a negative Poisson's ratio: experiment and analysis. *International Journal of Fracture*, 80(1):73–83, 3 1996. doi: 10.1007/bf00036481.
- [62] J. Chopin and A. Kudrolli. Helicoids, wrinkles, and loops in twisted ribbons. *Physical Review Letters*, 111(17), 10 2013. doi: 10.1103/physrevlett.111.174302.
- [63] D. L. Chopp. Computing minimal surfaces via level set curvature flow. *Journal of Computational Physics*, 106(1):77–91, 5 1993. doi: 10.1006/jcph.1993.1092.
- [64] P. W. Christensen and A. Klarbring. *An Introduction to Structural Optimization*. Springer Netherlands, 2009. doi: 10.1007/978-1-4020-8666-3.
- [65] R. M. Christensen. Mechanics of cellular and other low-density materials. *International Journal of Solids and Structures*, 37(1-2):93–104, 1 2009. doi: 10.1016/s0020-7683(99)00080-3.
- [66] M. Cianchetti, T. Ranzani, G. Gerboni, T. Nanayakkara, K. Althoefer, P. Dasgupta, and A. Menciassi. Soft robotics technologies to address shortcomings in today's minimally invasive surgery: The STIFF-FLOP approach. *Soft Robotics*, 1(2):122–131, 6 2014. doi: 10.1089/soro.2014.0001.
- [67] P. G. Ciarlet and P. Destuynder. A justification of a nonlinear model in plate theory. *Computer Methods in Applied Mechanics and Engineering*, 17-18:227–258, 1 1979. doi: 10.1016/0045-7825(79)90089-6.
- [68] A. Clausen, F. Wang, J. S. Jensen, O. Sigmund, and J. A. Lewis. Topology optimized architectures with programmable Poisson's ratio over large deformations. *Advanced Materials*, 27(37):5523–5527, 8 2015. doi: 10.1002/adma.201502485.
- [69] C. Coullais, A. Sabbadini, F. Vink, and M. van Hecke. Multi-step self-guided pathways for shape-changing metamaterials. *Nature*, 561(7724):512–515, 9 2018. doi: 10.1038/s41586-018-0541-0.
- [70] C. Dapogny. *Shape optimization, level set methods on unstructured meshes and mesh evolution*. phdthesis, Université Pierre et Marie Curie, 2013. URL <http://www.theses.fr/2013PA066498>.

- [71] C. Dapogny and P. Frey. Computation of the signed distance function to a discrete contour on adapted triangulation. *Calcolo*, 49(3):193–219, 1 2012. doi: 10.1007/s10092-011-0051-z.
- [72] S. Daynes and P. M. Weaver. Review of shape-morphing automobile structures: concepts and outlook. *Proceedings of the Institution of Mechanical Engineers, Part D: Journal of Automobile Engineering*, 227(11):1603–1622, 8 2013. doi: 10.1177/0954407013496557.
- [73] F. de Gournay. Velocity extension for the level-set method and multiple eigenvalues in shape optimization. *SIAM Journal on Control and Optimization*, 45(1):343–367, jan 2006. doi: 10.1137/050624108.
- [74] P. H. Dederichs and R. Zeller. Variational treatment of the elastic constants of disordered materials. *Zeitschrift für Physik A Hadrons and nuclei*, 259(2):103–116, 4 1973. doi: 10.1007/bf01392841.
- [75] M. C. Delfour and J.-P. Zolésio. *Shapes and geometries: metrics, analysis, differential calculus, and optimization*. Society for Industrial and Applied Mathematics, jan 2011. doi: 10.1137/1.9780898719826.
- [76] F. Dell’Isola, P. Seppecher, M. Spagnuolo, E. Barchiesi, F. Hild, T. Lekszycki, I. Giorgio, L. Placidi, U. Andreaus, M. Cuomo, S. R. Eugster, A. Pfaff, K. Hoschke, R. Langkemper, E. Turco, R. Sarikaya, A. Misra, M. D. Angelo, F. D’Annibale, A. Bouterf, X. Pinelli, A. Misra, B. Desmorat, M. Pawlikowski, C. Dupuy, D. Scerrato, P. Peyre, M. Laudato, L. Manzari, P. Göransson, C. Hesch, S. Hesch, P. Franciosi, J. Dirrenberger, F. Maurin, Z. Vangelatos, C. Grigoropoulos, V. Melissinaki, M. Farsari, W. Müller, B. E. Abali, C. Liebold, G. Ganzosch, P. Harrison, R. Drobnicki, L. Igumnov, F. Alzahrani, and T. Hayat. Advances in pantographic structures: design, manufacturing, models, experiments and image analyses. *Continuum Mechanics and Thermodynamics*, 31(4):1231–1282, 6 2019. doi: 10.1007/s00161-019-00806-x.
- [77] E. D. Demaine and T. Tachi. Origamizer: A practical algorithm for folding any polyhedron. In *33rd International Symposium on Computational Geometry (SoCG 2017)*, pages 34:1–34:16. Schloss Dagstuhl - Leibniz-Zentrum fuer Informatik GmbH, Wadern/Saarbruecken, Germany, 2017. doi: 10.4230/LIPICS.SOCG.2017.34.
- [78] O. Duncan, T. Shepherd, C. Moroney, L. Foster, P. Venkatraman, K. Winwood, T. Allen, and A. Alderson. Review of auxetic materials for sports applications: expanding options in comfort and protection. *Applied Sciences*, 8(6):941, 6 2018. doi: 10.3390/app8060941.
- [79] P. Duysinx and M. P. Bendsøe. Topology optimization of continuum structures with local stress constraints. *International Journal for Numerical Methods in Engineering*, 43(8):1453–1478, 12 1998. doi: 10.1002/(sici)1097-0207(19981230)43:8<1453::aid-nme480>3.0.co;2-2.
- [80] H. A. Eschenauer and N. Olhoff. Topology optimization of continuum structures: A review*. *Applied Mechanics Reviews*, 54(4):331–390, 7 2001. doi: 10.1115/1.1388075.
- [81] H. A. Eschenauer, V. V. Koblelev, and A. Schumacher. Bubble method for topology and shape optimization of structures. *Structural Optimization*, 8(1):42–51, aug 1994. doi: 10.1007/bf01742933.
- [82] K. E. Evans. Auxetic polymers: a new range of materials. *Endeavour*, 15(4):170–174, 1 1991. doi: 10.1016/0160-9327(91)90123-s.
- [83] K. E. Evans and A. Alderson. Auxetic materials: Functional materials and structures from lateral thinking! *Advanced Materials*, 12(9):617–628, 5 2000. doi: 10.1002/(sici)1521-4095(200005)12:9<617::aid-adma617>3.0.co;2-3.
- [84] S. M. Felton, M. T. Tolley, E. Demaine, D. Rus, and R. J. Wood. A method for building self-folding machines. *Science*, 345(6197):644–646, 8 2014. doi: 10.1126/science.1252610.
- [85] I. Fernandez-Corbaton, C. Rockstuhl, P. Ziemke, P. Gumbsch, A. Albiez, R. Schwaiger, T. Frenzel, M. Kadic, and M. Wegener. New twists of 3d chiral metamaterials. *Advanced Materials*, 31(26):1807742, 2 2019. doi: 10.1002/adma.201807742.
- [86] E. T. Filipov, T. Tachi, and G. H. Paulino. Origami tubes assembled into stiff, yet reconfigurable structures and metamaterials. *Proceedings of the National Academy of Sciences*, 112(40):12321–12326, 9 2015. doi: 10.1073/pnas.1509465112.

- [87] N. A. Fleck, V. S. Deshpande, and M. F. Ashby. Micro-architected materials: past, present and future. *Proceedings of the Royal Society A: Mathematical, Physical and Engineering Sciences*, 466 (2121):2495–2516, 6 2010. doi: 10.1098/rspa.2010.0215.
- [88] S. Forte and M. Vianello. Symmetry classes for elasticity tensors. *Journal of Elasticity*, 43(2):81–108, 5 1996. doi: 10.1007/bf00042505.
- [89] S. Forte and M. Vianello. A unified approach to invariants of plane elasticity tensors. *Meccanica*, 49 (9):2001–2012, 3 2014. doi: 10.1007/s11012-014-9916-y.
- [90] L. Foster, P. Peketi, T. Allen, T. Senior, O. Duncan, and A. Alderson. Application of auxetic foam in sports helmets. *Applied Sciences*, 8(3):354, 3 2018. doi: 10.3390/app8030354.
- [91] F. Fraternali and A. Amendola. Mechanical modeling of innovative metamaterials alternating pentamode lattices and confinement plates. *Journal of the Mechanics and Physics of Solids*, 99:259–271, 2 2017. doi: 10.1016/j.jmps.2016.11.010.
- [92] T. Frenzel, M. Kadic, and M. Wegener. Three-dimensional mechanical metamaterials with a twist. *Science*, 358(6366):1072–1074, 11 2017. doi: 10.1126/science.aao4640.
- [93] E. A. Friis, R. S. Lakes, and J. B. Park. Negative Poisson’s ratio polymeric and metallic foams. *Journal of Materials Science*, 23(12):4406–4414, 12 1988. doi: 10.1007/bf00551939.
- [94] M. Fu, O. Xu, L. Hu, and T. Yu. Nonlinear shear modulus of re-entrant hexagonal honeycombs under large deformation. *International Journal of Solids and Structures*, 80:284–296, 2 2016. doi: 10.1016/j.ijsolstr.2015.11.015.
- [95] J. Gao, H. Li, Z. Luo, L. Gao, and P. Li. Topology optimization of micro-structured materials featured with the specific mechanical properties. *International Journal of Computational Methods*, page 1850144, 9 2018. doi: 10.1142/s021987621850144x.
- [96] J. Gao, H. Xue, L. Gao, and Z. Luo. Topology optimization for auxetic metamaterials based on isogeometric analysis. *Computer Methods in Applied Mechanics and Engineering*, 352:211–236, 8 2019. doi: 10.1016/j.cma.2019.04.021.
- [97] L. V. Gibiansky and A. V. Cherkaev. Design of composite plates of extremal rigidity. In A. V. Cherkaev and R. V. Kohn, editors, *Topics in the Mathematical Modelling of Composite Materials*, pages 95–137. Springer International Publishing, 1997. doi: 10.1007/978-3-319-97184-1_5.
- [98] L. J. Gibson and M. F. Ashby. The mechanics of three-dimensional cellular materials. *Proceedings of the Royal Society A: Mathematical, Physical and Engineering Sciences*, 382(1782):43–59, 7 1982. doi: 10.1098/rspa.1982.0088.
- [99] L. J. Gibson and M. F. Ashby. *Cellular Solids*. Cambridge University Press, 5 1997. doi: 10.1017/cbo9781139878326.
- [100] L. J. Gibson, M. F. Ashby, G. S. Schajer, and C. I. Robertson. The mechanics of two-dimensional cellular materials. *Proceedings of the Royal Society A: Mathematical, Physical and Engineering Sciences*, 382(1782):25–42, 7 1982. doi: 10.1098/rspa.1982.0087.
- [101] A. S. Gladman, E. A. Matsumoto, R. G. Nuzzo, L. Mahadevan, and J. A. Lewis. Biomimetic 4d printing. *Nature Materials*, 15(4):413–418, 1 2016. doi: 10.1038/nmat4544.
- [102] G. N. Greaves, A. L. Greer, R. S. Lakes, and T. Rouxel. Poisson’s ratio and modern materials. *Nature Materials*, 10(11):823–837, 10 2011. doi: 10.1038/nmat3134.
- [103] J. N. Grima, A. Alderson, and K. E. Evans. Auxetic behaviour from rotating rigid units. *Physica Status Solidi B*, 242(3):561–575, 3 2005. doi: 10.1002/pssb.200460376.
- [104] J. N. Grima, V. Zammit, R. Gatt, A. Alderson, and K. E. Evans. Auxetic behaviour from rotating semi-rigid units. *Physica Status Solidi B*, 244(3):866–882, 3 2007. doi: 10.1002/pssb.200572706.
- [105] M. Gude and W. A. Hufenbach. Design of novel morphing structures based on bistable composites with piezoceramic actuators. *Mechanics of Composite Materials*, 42(4):339–346, 7 2006. doi: 10.1007/s11029-006-0043-2.

- [106] J. Guedes and N. Kikuchi. Preprocessing and postprocessing for materials based on the homogenization method with adaptive finite element methods. *Computer Methods in Applied Mechanics and Engineering*, 83(2):143–198, oct 1990. doi: 10.1016/0045-7825(90)90148-f.
- [107] R. Guseinov, E. Miguel, and B. Bickel. CurveUps : Shaping objects from flat plates with tension-actuated curvature. *ACM Transactions on Graphics*, 36(4):1–12, 7 2017. doi: 10.1145/3072959.3073709.
- [108] R. Guseinov, C. McMahan, J. Pérez, C. Daraio, and B. Bickel. Programming temporal morphing of self-actuated shells. *Nature Communications*, 11(1), 1 2020. doi: 10.1038/s41467-019-14015-2.
- [109] E.-H. Harkati, N. Daoudi, A. Bezazi, A. Haddad, and F. Scarpa. In-plane elasticity of a multi re-entrant auxetic honeycomb. *Composite Structures*, 180:130–139, 11 2017. doi: 10.1016/j.compstruct.2017.08.014.
- [110] Z. Hashin and S. Shtrikman. A variational approach to the theory of the elastic behaviour of multiphase materials. *Journal of the Mechanics and Physics of Solids*, 11(2):127–140, 3 1963. doi: 10.1016/0022-5096(63)90060-7.
- [111] B. Hassani and E. Hinton. A review of homogenization and topology optimization i—homogenization theory for media with periodic structure. *Computers and Structures*, 69(6):707–717, 12 1998. doi: 10.1016/s0045-7949(98)00131-x.
- [112] B. Hassani, S. M. Tavakkoli, and H. Ghasemnejad. Simultaneous shape and topology optimization of shell structures. *Structural and Multidisciplinary Optimization*, 48(1):221–233, feb 2013. doi: 10.1007/s00158-013-0894-9.
- [113] Y. He, Y. Zhou, Z. Liu, and K. M. Liew. Buckling and pattern transformation of modified periodic lattice structures. *Extreme Mechanics Letters*, 22:112–121, 7 2018. doi: 10.1016/j.eml.2018.05.011.
- [114] F. Hecht. New development in `freefem ++`. *Journal of Numerical Mathematics*, 20(3-4), 1 2012. doi: 10.1515/jnum-2012-0013.
- [115] F. Hild and S. Roux. Comparison of local and global approaches to digital image correlation. *Experimental Mechanics*, 52(9):1503–1519, 3 2012. doi: 10.1007/s11340-012-9603-7.
- [116] S. J. Hollister. Porous scaffold design for tissue engineering. *Nature Materials*, 4(7):518–524, 7 2005. doi: 10.1038/nmat1421.
- [117] S. J. Hollister and N. Kikuchi. A comparison of homogenization and standard mechanics analyses for periodic porous composites. *Computational Mechanics*, 10(2):73–95, 1992. doi: 10.1007/bf00369853.
- [118] S. J. Hollister and N. Kikuchi. Homogenization theory and digital imaging: A basis for studying the mechanics and design principles of bone tissue. *Biotechnology and Bioengineering*, 43(7):586–596, mar 1994. doi: 10.1002/bit.260430708.
- [119] S. Hou, T. Liu, Z. Zhang, X. Han, and Q. Li. How does negative Poisson’s ratio of foam filler affect crashworthiness? *Materials and Design*, 82:247–259, 10 2015. doi: 10.1016/j.matdes.2015.05.050.
- [120] T. J. R. Hughes, J. A. Cottrell, and Y. Bazilevs. Isogeometric analysis: CAD, finite elements, NURBS, exact geometry and mesh refinement. *Computer Methods in Applied Mechanics and Engineering*, 194(39-41):4135–4195, 10 2005. doi: 10.1016/j.cma.2004.10.008.
- [121] R. G. Hutchinson and N. A. Fleck. The structural performance of the periodic truss. *Journal of the Mechanics and Physics of Solids*, 54(4):756–782, 4 2006. doi: 10.1016/j.jmps.2005.10.008.
- [122] G. Imbalzano, P. Tran, T. D. Ngo, and P. V. S. Lee. A numerical study of auxetic composite panels under blast loadings. *Composite Structures*, 135:339–352, 1 2016. doi: 10.1016/j.compstruct.2015.09.038.
- [123] S. Jacobs, C. Coconnier, D. D. Maio, F. Scarpa, M. Toso, and J. Martinez Iglesias. Deployable auxetic shape memory alloy cellular antenna demonstrator: design, manufacturing and modal testing. *Smart Materials and Structures*, 21(7):075013, 6 2012. doi: 10.1088/0964-1726/21/7/075013.

- [124] L. Jakabčič and P. Seppecher. On periodic homogenization of highly contrasted elastic structures. *Journal of the Mechanics and Physics of Solids*, 144:104104, 11 2020. doi: 10.1016/j.jmps.2020.104104.
- [125] D. Jang, L. R. Meza, F. Greer, and J. R. Greer. Fabrication and deformation of three-dimensional hollow ceramic nanostructures. *Nature Materials*, 12(10):893–898, 9 2013. doi: 10.1038/nmat3738.
- [126] D. R. Jantos, C. Riedel, K. Hackl, and P. Junker. Comparison of thermodynamic topology optimization with SIMP. *Continuum Mechanics and Thermodynamics*, 31(2):521–548, 8 2018. doi: 10.1007/s00161-018-0706-y.
- [127] Y. Jiang, Z. Liu, N. Matsuhisa, D. Qi, W. R. Leow, H. Yang, J. Yu, G. Chen, Y. Liu, C. Wan, Z. Liu, and X. Chen. Auxetic mechanical metamaterials to enhance sensitivity of stretchable strain sensors. *Advanced Materials*, 30(12):1706589, 1 2018. doi: 10.1002/adma.201706589.
- [128] M. Kadic, T. Bückmann, R. Schittny, and M. Wegener. Metamaterials beyond electromagnetism. *Reports on Progress in Physics*, 76(12):126501, 11 2013. doi: 10.1088/0034-4885/76/12/126501.
- [129] M. Kapnisi, C. Mansfield, C. Marijon, A. G. Guex, F. Perbellini, I. Bardi, E. J. Humphrey, J. L. Puetzer, D. Mawad, D. C. Koutsogeorgis, D. J. Stuckey, C. M. Terracciano, S. E. Harding, and M. M. Stevens. Auxetic cardiac patches with tunable mechanical and conductive properties toward treating myocardial infarction. *Advanced Functional Materials*, 28(21):1800618, 4 2018. doi: 10.1002/adfm.201800618.
- [130] P. Khaneh Masjedi, A. Maheri, and P. M. Weaver. Large deflection of functionally graded porous beams based on a geometrically exact theory with a fully intrinsic formulation. *Applied Mathematical Modelling*, 76:938–957, 12 2019. doi: 10.1016/j.apm.2019.07.018.
- [131] Z. X. Khoo, J. E. M. Teoh, Y. Liu, C. K. Chua, S. Yang, J. An, K. F. Leong, and W. Y. Yeong. 3d printing of smart materials: A review on recent progresses in 4d printing. *Virtual and Physical Prototyping*, 10(3):103–122, 7 2015. doi: 10.1080/17452759.2015.1097054.
- [132] R. Kimmel, D. Shaked, N. Kiryati, and A. M. Bruckstein. Skeletonization via distance maps and level sets. *Computer Vision and Image Understanding*, 62(3):382–391, 11 1995. doi: 10.1006/cviu.1995.1062.
- [133] R. V. Kohn and M. Vogelius. A new model for thin plates with rapidly varying thickness. *International Journal of Solids and Structures*, 20(4):333–350, 1984. doi: 10.1016/0020-7683(84)90044-1.
- [134] M. Konaković, K. Crane, B. Deng, S. Bouaziz, D. Piker, and M. Pauly. Beyond developable: Computational design and fabrication with auxetic materials. *ACM Transactions on Graphics*, 35(4):1–11, 7 2016. doi: 10.1145/2897824.2925944.
- [135] M. Konaković-Luković, J. Panetta, K. Crane, and M. Pauly. Rapid deployment of curved surfaces via programmable auxetics. *ACM Transactions on Graphics*, 37(4):1–13, 8 2018. doi: 10.1145/3197517.3201373.
- [136] A. Kotikian, R. L. Truby, J. W. Boley, T. J. White, and J. A. Lewis. 3d printing of liquid crystal elastomeric actuators with spatially programmed nematic order. *Advanced Materials*, 30(10):1706164, 1 2018. doi: 10.1002/adma.201706164.
- [137] A. Kotikian, C. McMahan, E. C. Davidson, J. M. Muhammad, R. D. Weeks, C. Daraio, and J. A. Lewis. Untethered soft robotic matter with passive control of shape morphing and propulsion. *Science Robotics*, 4(33):eaax7044, 8 2019. doi: 10.1126/scirobotics.aax7044.
- [138] S. Krödel, L. Li, A. Constantinescu, and C. Daraio. Stress relaxation in polymeric microlattice materials. *Materials and Design*, 130:433–441, 9 2017. doi: 10.1016/j.matdes.2017.05.060.
- [139] X. Kuang, D. J. Roach, J. Wu, C. M. Hamel, Z. Ding, T. Wang, M. L. Dunn, and H. J. Qi. Advances in 4d printing: Materials and applications. *Advanced Functional Materials*, 29(2):1805290, 11 2018. doi: 10.1002/adfm.201805290.
- [140] R. S. Kumar and D. L. McDowell. Generalized continuum modeling of 2-d periodic cellular solids. *International Journal of Solids and Structures*, 41(26):7399–7422, dec 2004. doi: 10.1016/j.ijsolstr.2004.06.038.

- [141] R. S. Lakes. Foam structures with a negative Poisson's ratio. *Science*, 235(4792):1038–1040, 2 1987. doi: 10.1126/science.235.4792.1038.
- [142] R. S. Lakes. Deformation mechanisms in negative Poisson's ratio materials: structural aspects. *Journal of Materials Science*, 26(9):2287–2292, 1991. doi: 10.1007/bf01130170.
- [143] R. S. Lakes. Advances in negative Poisson's ratio materials. *Advanced Materials*, 5(4):293–296, 4 1993. doi: 10.1002/adma.19930050416.
- [144] R. S. Lakes and W. J. Drugan. Dramatically stiffer elastic composite materials due to a negative stiffness phase? *Journal of the Mechanics and Physics of Solids*, 50(5):979–1009, 5 2002. doi: 10.1016/s0022-5096(01)00116-8.
- [145] R. S. Lakes and K. J. Elms. Indentability of conventional and negative Poisson's ratio foams. *Journal of Composite Materials*, 27(12):1193–1202, 12 1993. doi: 10.1177/002199839302701203.
- [146] U. D. Larsen, O. Sigmund, and S. Bouwsta. Design and fabrication of compliant micromechanisms and structures with negative Poisson's ratio. *Journal of Microelectromechanical Systems*, 6(2):99–106, 6 1997. doi: 10.1109/84.585787.
- [147] A. Lebéé and K. Sab. A bending-gradient model for thick plates. part i: Theory. *International Journal of Solids and Structures*, 48(20):2878–2888, oct 2011. doi: 10.1016/j.ijsolstr.2011.06.006.
- [148] Y.-J. Lee, S.-M. Lim, S.-M. Yi, J.-H. Lee, S.-G. Kang, G.-M. Choi, H. N. Han, J.-Y. Sun, I.-S. Choi, and Y.-C. Joo. Auxetic elastomers: mechanically programmable meta-elastomers with an unusual Poisson's ratio overcome the gauge limit of a capacitive type strain sensor. *Extreme Mechanics Letters*, 31:100516, 9 2019. doi: 10.1016/j.eml.2019.100516.
- [149] T. Lewinski and J. J. Telega. *Plates, Laminates and Shells*. World Scientific, mar 2000. doi: 10.1142/3539.
- [150] H. Li, Z. Luo, L. Gao, and P. Walker. Topology optimization for functionally graded cellular composites with metamaterials by level sets. *Computer Methods in Applied Mechanics and Engineering*, 328:340–364, 1 2018. doi: 10.1016/j.cma.2017.09.008.
- [151] X. Liang and A. J. Crosby. Uniaxial stretching mechanics of cellular flexible metamaterials. *Extreme Mechanics Letters*, 35:100637, 2 2020. doi: 10.1016/j.eml.2020.100637.
- [152] B. Ling, K. Wei, Z. Wang, X. Yang, Z. Qu, and D. Fang. Experimentally program large magnitude of poisson's ratio in additively manufactured mechanical metamaterials. *International Journal of Mechanical Sciences*, 173:105466, 5 2020. doi: 10.1016/j.ijmecsci.2020.105466.
- [153] J. Liu and Y. Zhang. Soft network materials with isotropic negative poisson's ratios over large strains. *Soft Matter*, 14(5):693–703, 2018. doi: 10.1039/c7sm02052j.
- [154] J. Liu, T. Gu, S. Shan, S. H. Kang, J. C. Weaver, and K. Bertoldi. Harnessing buckling to design architected materials that exhibit effective negative swelling. *Advanced Materials*, 28(31):6619–6624, 5 2016. doi: 10.1002/adma.201600812.
- [155] F. López Jiménez and N. Triantafyllidis. Buckling of rectangular and hexagonal honeycomb under combined axial compression and transverse shear. *International Journal of Solids and Structures*, 50(24):3934–3946, nov 2013. doi: 10.1016/j.ijsolstr.2013.08.001.
- [156] A. E. H. Love. *A treatise on the mathematical theory of elasticity*, volume 1. Cambridge University Press, 1892. URL <https://hal.archives-ouvertes.fr/hal-01307751>.
- [157] L. Luu, Z. Wang, M. Vo, T. Hoang, and J. Ma. Accuracy enhancement of digital image correlation with b-spline interpolation. *Optics Letters*, 36(16):3070, 8 2011. doi: 10.1364/ol.36.003070.
- [158] E. MacDonald and R. Wicker. Multiprocess 3d printing for increasing component functionality. *Science*, 353(6307):aaf2093–aaf2093, 9 2016. doi: 10.1126/science.aaf2093.
- [159] L. Malomo, J. Pérez, E. Iarussi, N. Pietroni, E. Miguel, P. Cignoni, and B. Bickel. Flexmaps: Computational design of flat flexible shells for shaping 3d objects. *ACM Transactions on Graphics*, 37(6):1–14, 12 2018. doi: 10.1145/3272127.3275076.

- [160] Y. Mao, K. Yu, M. S. Isakov, J. Wu, M. L. Dunn, and H. J. Qi. Sequential self-folding structures by 3D printed digital shape memory polymers. *Scientific Reports*, 5(1), 9 2015. doi: 10.1038/srep13616.
- [161] J. Marty, J. Réthoré, A. Combescure, and P. Chaudet. Finite strain kinematics of multi-scale material by digital image correlation. *Experimental Mechanics*, 55(9):1641–1656, 7 2015. doi: 10.1007/s11340-015-0059-4.
- [162] A. Maury, G. Allaire, and F. Jouve. Elasto-plastic shape optimization using the level set method. *SIAM Journal on Control and Optimization*, 56(1):556–581, 1 2018. doi: 10.1137/17m1128940.
- [163] C. C. Mei and B. Vernescu. *Homogenization Methods for Multiscale Mechanics*. World Scientific, 9 2010. ISBN 978-981-4282-44-4. doi: 10.1142/7427.
- [164] D. Melancon, Z. S. Bagheri, R. B. Johnston, L. Liu, M. Tanzer, and D. Pasini. Mechanical characterization of structurally porous biomaterials built via additive manufacturing: experiments, predictive models, and design maps for load-bearing bone replacement implants. *Acta Biomaterialia*, 63:350–368, 11 2017. doi: 10.1016/j.actbio.2017.09.013.
- [165] G. Michailidis. *Manufacturing Constraints and Multi-Phase Shape and Topology Optimization via a Level-Set Method*. phdthesis, Ecole polytechnique X, 2014. URL <https://pastel.archives-ouvertes.fr/pastel-00937306>.
- [166] G. W. Milton. Composite materials with Poisson's ratios close to -1. *Journal of the Mechanics and Physics of Solids*, 40(5):1105–1137, 7 1992. doi: 10.1016/0022-5096(92)90063-8.
- [167] G. W. Milton. *The Theory of Composites*. Cambridge University Press, 2002. ISBN 0-521-78125-6. doi: 10.1017/cbo9780511613357.
- [168] G. W. Milton and A. V. Cherkaev. Which elasticity tensors are realizable? *Journal of Engineering Materials and Technology*, 117(4):483–493, 10 1995. doi: 10.1115/1.2804743.
- [169] G. W. Milton and R. V. Kohn. Variational bounds on the effective moduli of anisotropic composites. *Journal of the Mechanics and Physics of Solids*, 36(6):597–629, 1 1988. doi: 10.1016/0022-5096(88)90001-4.
- [170] L. Mizzi, E. Salvati, A. Spaggiari, J.-C. Tan, and A. M. Korsunsky. Highly stretchable two-dimensional auxetic metamaterial sheets fabricated via direct-laser cutting. *International Journal of Mechanical Sciences*, 167:105242, 2 2020. doi: 10.1016/j.ijmecsci.2019.105242.
- [171] U. Montanari. A method for obtaining skeletons using a quasi-euclidean distance. *Journal of the ACM (JACM)*, 15(4):600–624, 10 1968. doi: 10.1145/321479.321486.
- [172] L. C. Montemayor, L. R. Meza, and J. R. Greer. Design and fabrication of hollow rigid nanolattices via two-photon lithography. *Advanced Engineering Materials*, 16(2):184–189, 10 2013. doi: 10.1002/adem.201300254.
- [173] M. Mooney. A theory of large elastic deformation. *Journal of Applied Physics*, 11(9):582–592, 9 1940. doi: 10.1063/1.1712836.
- [174] N. Morris, A. Butscher, and F. Iorio. A subtractive manufacturing constraint for level set topology optimization. *Structural and Multidisciplinary Optimization*, 61(4):1573–1588, feb 2020. doi: 10.1007/s00158-019-02436-y.
- [175] F. Murat and J. Simon. Etude de problemes d'optimal design. In *Lecture Notes in Computer Science*, pages 54–62. Springer Berlin Heidelberg, 1976. doi: 10.1007/3-540-07623-9_279.
- [176] F. Murat and L. Tartar. Calcul des variations et homogénéisation. In *Les méthodes de l'homogénéisation : théorie et applications en physique*, volume 57, page 319–369. Eyrolles, 1985.
- [177] J.-H. Na, A. A. Evans, J. Bae, M. C. Chiappelli, C. D. Santangelo, R. J. Lang, T. C. Hull, and R. C. Hayward. Programming reversibly self-folding origami with micropatterned photo-crosslinkable polymer trilayers. *Advanced Materials*, 27(1):79–85, 10 2014. doi: 10.1002/adma.201403510.

- [178] P. B. Nakshatrala and D. A. Tortorelli. Nonlinear structural design using multiscale topology optimization. part II: Transient formulation. *Computer Methods in Applied Mechanics and Engineering*, 304: 605–618, 6 2016. doi: 10.1016/j.cma.2016.01.003.
- [179] R. M. Neville, F. Scarpa, and A. Pirrera. Shape morphing kirigami mechanical metamaterials. *Scientific Reports*, 6(1), 8 2016. doi: 10.1038/srep31067.
- [180] T. D. Ngo, A. Kashani, G. Imbalzano, K. T. Q. Nguyen, and D. Hui. Additive manufacturing (3d printing): A review of materials, methods, applications and challenges. *Composites Part B: Engineering*, 143: 172–196, 6 2018. doi: 10.1016/j.compositesb.2018.02.012.
- [181] G. Nika and A. Constantinescu. Design of multi-layer materials using inverse homogenization and a level set method. *Computer Methods in Applied Mechanics and Engineering*, 346:388–409, 4 2019. doi: 10.1016/j.cma.2018.11.029.
- [182] S. Nishi, K. Terada, J. Kato, S. Nishiwaki, and K. Izui. Two-scale topology optimization for composite plates with in-plane periodicity. *International Journal for Numerical Methods in Engineering*, 113(8): 1164–1188, mar 2017. doi: 10.1002/nme.5545.
- [183] J. Nocedal and S. J. Wright. *Numerical Optimization*. Springer New York, 2006. doi: 10.1007/978-0-387-40065-5.
- [184] H. Ohmori and K. Yamamoto. Shape optimization of shell and spatial structure for specified stress distribution. *Memoirs of the School of Engineering, Nagoya University*, 50:1–32, mar 1998. ISSN 0919-0805. doi: 10.18999/memsenu.50.1. URL <https://ci.nii.ac.jp/naid/120006890084/en/>.
- [185] K. Oliver, A. Seddon, and R. S. Trask. Morphing in nature and beyond: a review of natural and synthetic shape-changing materials and mechanisms. *Journal of Materials Science*, 51(24):10663–10689, 8 2016. doi: 10.1007/s10853-016-0295-8.
- [186] S. J. Osher and R. Fedkiw. *Level Set Methods and Dynamic Implicit Surfaces*. Springer New York, 2003. ISBN 978-0-387-95482-0. doi: 10.1007/b98879.
- [187] S. J. Osher and F. Santosa. Level set methods for optimization problems involving geometry and constraints. *Journal of Computational Physics*, 171(1):272–288, 7 2001. doi: 10.1006/jcph.2001.6789.
- [188] S. J. Osher and J. A. Sethian. Fronts propagating with curvature-dependent speed: algorithms based on hamilton-jacobi formulations. *Journal of Computational Physics*, 79(1):12–49, 11 1988. doi: 10.1016/0021-9991(88)90002-2.
- [189] J. T. B. Overvelde, T. A. de Jong, Y. Shevchenko, S. A. Becerra, G. M. Whitesides, J. C. Weaver, C. Hoberman, and K. Bertoldi. A three-dimensional actuated origami-inspired transformable metamaterial with multiple degrees of freedom. *Nature Communications*, 7(1), 3 2016. doi: 10.1038/ncomms10929.
- [190] S. D. Papka and S. C. Kyriakides. In-plane biaxial crushing of honeycombs—: Part ii: Analysis. *International Journal of Solids and Structures*, 36(29):4397–4423, 10 1999. doi: 10.1016/s0020-7683(98)00225-x.
- [191] J.-C. Passieux and R. Bouclier. Classic and inverse compositional gauss-newton in global DIC. *International Journal for Numerical Methods in Engineering*, 119(6):453–468, 3 2019. doi: 10.1002/nme.6057.
- [192] S. W. Pattinson, M. E. Huber, S. Kim, J. Lee, S. Grunsfeld, R. Roberts, G. Dreifus, C. Meier, L. Liu, N. Hogan, and J. Hart. Additive manufacturing of biomechanically tailored meshes for compliant wearable and implantable devices. *Advanced Functional Materials*, 29(32):1901815, 6 2019. doi: 10.1002/adfm.201901815.
- [193] N. L. Pedersen. Maximization of eigenvalues using topology optimization. *Structural and Multidisciplinary Optimization*, 20(1):2–11, 8 2000. doi: 10.1007/s001580050130.
- [194] P.-O. Persson and G. Strang. A simple mesh generator in MATLAB. *SIAM Review*, 46(2):329–345, 1 2004. doi: 10.1137/s0036144503429121.

- [195] L. Piegl and W. Tiller. *The NURBS Book*. Springer Berlin Heidelberg, 1997. doi: 10.1007/978-3-642-59223-2.
- [196] O. Pironneau. *Optimal Shape Design for Elliptic Systems*. Springer Berlin Heidelberg, 1984. doi: 10.1007/978-3-642-87722-3.
- [197] P. Plucinsky, B. A. Kowalski, T. J. White, and K. Bhattacharya. Patterning nonisometric origami in nematic elastomer sheets. *Soft Matter*, 14(16):3127–3134, 2018. doi: 10.1039/c8sm00103k.
- [198] F. Pradel and K. Sab. Cosserat modelling of elastic periodic lattice structures. *Comptes Rendus de l'Académie des Sciences - Series IIB - Mechanics-Physics-Astronomy*, 326(11):699–704, 11 1998. doi: 10.1016/s1251-8069(98)80002-x.
- [199] H. Qiu, Y. Li, T. F. Guo, X. Guo, and S. Tang. Deformation and pattern transformation of porous soft solids under biaxial loading: experiments and simulations. *Extreme Mechanics Letters*, 20:81–90, 4 2018. doi: 10.1016/j.eml.2018.01.008.
- [200] A. Rafsanjani and K. Bertoldi. Buckling-induced kirigami. *Physical Review Letters*, 118(8), 2 2017. doi: 10.1103/physrevlett.118.084301.
- [201] A. Rafsanjani and D. Pasini. Bistable auxetic mechanical metamaterials inspired by ancient geometric motifs. *Extreme Mechanics Letters*, 9:291–296, 12 2016. doi: 10.1016/j.eml.2016.09.001.
- [202] A. Rafsanjani, Y. Zhang, B. Liu, S. M. Rubinstein, and K. Bertoldi. Kirigami skins make a simple soft actuator crawl. *Science Robotics*, 3(15):eaar7555, 2 2018. doi: 10.1126/scirobotics.aar7555.
- [203] C. L. Randall, E. Gultepe, and D. H. Gracias. Self-folding devices and materials for biomedical applications. *Trends in Biotechnology*, 30(3):138–146, 3 2012. doi: 10.1016/j.tibtech.2011.06.013.
- [204] R. S. Rivlin. Large elastic deformations of isotropic materials. IV. further developments of the general theory. *Philosophical Transactions of the Royal Society A: Mathematical, Physical and Engineering Sciences*, 241(835):379–397, 10 1948. doi: 10.1098/rsta.1948.0024.
- [205] H. C. Rodrigues, J. M. Guedes, and M. P. Bendsøe. Hierarchical optimization of material and structure. *Structural and Multidisciplinary Optimization*, 24(1):1–10, 8 2002. doi: 10.1007/s00158-002-0209-z.
- [206] J. Réthoré, C. Kaltenbrunner, T. B. T. Dang, P. Chaudet, and M. Kuhn. Gradient-elasticity for honeycomb materials: validation and identification from full-field measurements. *International Journal of Solids and Structures*, 72:108–117, 10 2015. doi: 10.1016/j.ijsolstr.2015.07.015.
- [207] J. Réthoré, A. Leygue, M. Coret, L. Stainier, and E. Verron. Computational measurements of stress fields from digital images. *International Journal for Numerical Methods in Engineering*, 113(12):1810–1826, 12 2017. doi: 10.1002/nme.5721.
- [208] K. Sab and A. Lebé. *Homogenization of Heterogeneous Thin and Thick Plates*. John Wiley & Sons, Inc., 10 2015. doi: 10.1002/9781119005247.
- [209] J. Sanchez Hubert and E. Sanchez-Palencia. *Introduction aux méthodes asymptotiques et à l'homogénéisation : application à la mécanique des milieux continus*. Masson, Paris, 1992. ISBN 2225826439.
- [210] E. Sanchez-Palencia. *Non-Homogeneous Media and Vibration Theory*. Springer Berlin Heidelberg, 1980. ISBN 978-3-540-10000-3. doi: 10.1007/3-540-10000-8.
- [211] E. Sanchez-Palencia and A. Zaoui, editors. *Homogenization Techniques for Composite Media*. Springer Berlin Heidelberg, 1987. ISBN 978-3-540-47720-4. doi: 10.1007/3-540-17616-0.
- [212] K. K. Saxena, R. Das, and E. P. Calius. Three decades of auxetics research - Materials with negative Poisson's ratio: a review. *Advanced Engineering Materials*, 18(11):1847–1870, 6 2016. doi: 10.1002/adem.201600053.
- [213] T. A. Schaedler, A. J. Jacobsen, A. Torrents, A. E. Sorensen, J. Lian, J. R. Greer, L. Valdevit, and W. B. Carter. Ultralight metallic microlattices. *Science*, 334(6058):962–965, nov 2011. doi: 10.1126/science.1211649.

- [214] H. W. Schreier, J. R. Braasch, and M. A. Sutton. Systematic errors in digital image correlation caused by intensity interpolation. *Optical Engineering*, 39(11):2915, 11 2000. doi: 10.1117/1.1314593.
- [215] H. W. Schreier, J.-J. Orteu, and M. A. Sutton. *Image Correlation for Shape, Motion and Deformation Measurements*. Springer US, 2009. doi: 10.1007/978-0-387-78747-3.
- [216] J. Schwerdtfeger, F. Wein, G. Leugering, R. F. Singer, C. Körner, M. Stingl, and F. Schury. Design of auxetic structures via mathematical optimization. *Advanced Materials*, 23(22-23):2650–2654, apr 2011. doi: 10.1002/adma.201004090.
- [217] T. W. Sederberg, J. Zheng, A. Bakenov, and A. Nasri. T-splines and t-NURCCs. *ACM Transactions on Graphics*, 22(3):477–484, jul 2003. doi: 10.1145/882262.882295.
- [218] J. A. Sethian. Fast marching methods. *SIAM Review*, 41(2):199–235, jan 1999. doi: 10.1137/s0036144598347059.
- [219] J. A. Sethian and A. Wiegmann. Structural boundary design via level set and immersed interface methods. *Journal of Computational Physics*, 163(2):489–528, 9 2000. doi: 10.1006/jcph.2000.6581.
- [220] S. Shan, S. H. Kang, Z. Zhao, L. Fang, and K. Bertoldi. Design of planar isotropic negative poisson's ratio structures. *Extreme Mechanics Letters*, 4:96–102, 9 2015. doi: 10.1016/j.eml.2015.05.002.
- [221] E. Siéfert, E. Reyssat, J. Bico, and B. Roman. Bio-inspired pneumatic shape-morphing elastomers. *Nature Materials*, 18(1):24–28, 11 2018. doi: 10.1038/s41563-018-0219-x.
- [222] O. Sigmund. Materials with prescribed constitutive parameters: an inverse homogenization problem. *International Journal of Solids and Structures*, 31(17):2313–2329, 9 1994. doi: 10.1016/0020-7683(94)90154-6.
- [223] O. Sigmund. Tailoring materials with prescribed elastic properties. *Mechanics of Materials*, 20(4):351–368, 6 1995. doi: 10.1016/0167-6636(94)00069-7.
- [224] O. Sigmund. On the usefulness of non-gradient approaches in topology optimization. *Structural and Multidisciplinary Optimization*, 43(5):589–596, 3 2011. doi: 10.1007/s00158-011-0638-7.
- [225] J. Sokolowski and J.-P. Zolesio. *Introduction to Shape Optimization*. Springer Berlin Heidelberg, 1992. doi: 10.1007/978-3-642-58106-9.
- [226] A. Spadoni, M. Ruzzene, S. Gonella, and F. Scarpa. Phononic properties of hexagonal chiral lattices. *Wave Motion*, 46(7):435–450, 11 2009. doi: 10.1016/j.wavemoti.2009.04.002.
- [227] N. Sukumar, D. L. Chopp, N. Moës, and T. Belytschko. Modeling holes and inclusions by level sets in the extended finite-element method. *Computer Methods in Applied Mechanics and Engineering*, 190(46-47):6183–6200, sep 2001. doi: 10.1016/s0045-7825(01)00215-8.
- [228] Y. Sun, J. H. L. Pang, C. K. Wong, and F. Su. Finite element formulation for a digital image correlation method. *Applied Optics*, 44(34):7357, 12 2005. doi: 10.1364/ao.44.007357.
- [229] M. Sussman and E. Fatemi. An efficient, interface-preserving level set redistancing algorithm and its application to interfacial incompressible fluid flow. *SIAM Journal on Scientific Computing*, 20(4):1165–1191, jan 1999. doi: 10.1137/s1064827596298245.
- [230] M. A. Sutton, W. J. Wolters, W. H. Peters, W. F. Ranson, and S. R. McNeill. Determination of displacements using an improved digital correlation method. *Image and Vision Computing*, 1(3):133–139, 8 1983. doi: 10.1016/0262-8856(83)90064-1.
- [231] K. Svanberg. The method of moving asymptotes — a new method for structural optimization. *International Journal for Numerical Methods in Engineering*, 24(2):359–373, feb 1987. doi: 10.1002/nme.1620240207.
- [232] A. Takezawa, S. Nishiwaki, and M. Kitamura. Shape and topology optimization based on the phase field method and sensitivity analysis. *Journal of Computational Physics*, 229(7):2697–2718, apr 2010. doi: 10.1016/j.jcp.2009.12.017.

- [233] D. G. Talaslidis and I. I. Sous. A discrete kirchhoff triangular element for the analysis of thin stiffened shells. *Computers and Structures*, 43(4):663–674, 5 1992. doi: 10.1016/0045-7949(92)90507-v.
- [234] S. Tan, J. Gu, S. C. Han, D.-W. Lee, and K. Kang. Design and fabrication of a non-clogging scaffold composed of semi-permeable membrane. *Materials and Design*, 142:229–239, 3 2018. doi: 10.1016/j.matdes.2018.01.033.
- [235] Y. Tang and J. Yin. Design of cut unit geometry in hierarchical kirigami-based auxetic metamaterials for high stretchability and compressibility. *Extreme Mechanics Letters*, 12:77–85, 4 2017. doi: 10.1016/j.eml.2016.07.005.
- [236] L. Tartar. *The General Theory of Homogenization*. Springer Berlin Heidelberg, 2010. doi: 10.1007/978-3-642-05195-1.
- [237] T. C. T. Ting and T. Chen. Poisson’s ratio for anisotropic elastic materials can have no bounds. *Quarterly Journal of Mechanics and Applied Mathematics*, 58(1):73–82, 2 2005. doi: 10.1093/qjmamj/hbh021.
- [238] S. Torquato. Random heterogeneous media: Microstructure and improved bounds on effective properties. *Applied Mechanics Reviews*, 44(2):37–76, 2 1991. doi: 10.1115/1.3119494.
- [239] N. Triantafyllidis and S. Bardenhagen. The influence of scale size on the stability of periodic solids and the role of associated higher order gradient continuum models. *Journal of the Mechanics and Physics of Solids*, 44(11):1891–1928, 11 1996. doi: 10.1016/0022-5096(96)00047-6.
- [240] N. Triantafyllidis and M. W. Schraad. Onset of failure in aluminum honeycombs under general in-plane loading. *Journal of the Mechanics and Physics of Solids*, 46(6):1089–1124, jun 1998. doi: 10.1016/s0022-5096(97)00060-4.
- [241] R. L. Truby and J. A. Lewis. Printing soft matter in three dimensions. *Nature*, 540(7633):371–378, 12 2016. doi: 10.1038/nature21003.
- [242] W. M. van Rees, E. Vouga, and L. Mahadevan. Growth patterns for shape-shifting elastic bilayers. *Proceedings of the National Academy of Sciences*, 114(44):11597–11602, 10 2017. doi: 10.1073/pnas.1709025114.
- [243] S. L. Vatanabe, T. N. Lippi, C. R. de Lima, G. H. Paulino, and E. C. Silva. Topology optimization with manufacturing constraints: A unified projection-based approach. *Advances in Engineering Software*, 100:97–112, oct 2016. doi: 10.1016/j.advengsoft.2016.07.002.
- [244] P. Vogiatzis, S. Chen, X. Wang, T. Li, and L. Wang. Topology optimization of multi-material negative Poisson’s ratio metamaterials using a reconciled level set method. *Computer-Aided Design*, 83:15–32, 2 2017. doi: 10.1016/j.cad.2016.09.009.
- [245] H. Wan, H. Ohtaki, S. Kotosaka, and G. Hu. A study of negative poisson’s ratios in auxetic honeycombs based on a large deflection model. *European Journal of Mechanics - A/Solids*, 23(1):95–106, 1 2004. doi: 10.1016/j.euromechsol.2003.10.006.
- [246] F. Wang. Systematic design of 3D auxetic lattice materials with programmable poisson’s ratio for finite strains. *Journal of the Mechanics and Physics of Solids*, 114:303–318, 5 2018. doi: 10.1016/j.jmps.2018.01.013.
- [247] F. Wang, O. Sigmund, and J. S. Jensen. Design of materials with prescribed nonlinear properties. *Journal of the Mechanics and Physics of Solids*, 69:156–174, 9 2014. doi: 10.1016/j.jmps.2014.05.003.
- [248] M. Y. Wang, X. Wang, and D. Guo. A level set method for structural topology optimization. *Computer Methods in Applied Mechanics and Engineering*, 192(1-2):227–246, 1 2003. doi: 10.1016/s0045-7825(02)00559-5.
- [249] X. Wang, Y. Mei, and M. Y. Wang. Level-set method for design of multi-phase elastic and thermoelastic materials. *International Journal of Mechanics and Materials in Design*, 1(3):213–239, 9 2004. doi: 10.1007/s10999-005-0221-8.

- [250] Y. Wang, Z. Luo, N. Zhang, and Z. Kang. Topological shape optimization of microstructural metamaterials using a level set method. *Computational Materials Science*, 87:178–186, 5 2014. doi: 10.1016/j.commatsci.2014.02.006.
- [251] Y. Wang, Q. Liu, J. Zhang, T. Hong, W. Sun, L. Tang, E. Arnold, Z. Suo, W. Hong, Z. Ren, and C. F. Guo. Giant poisson's effect for wrinkle-free stretchable transparent electrodes. *Advanced Materials*, 31(35):1902955, 7 2019. doi: 10.1002/adma.201902955.
- [252] Y. Q. Wang, M. A. Sutton, H. A. Bruck, and H. W. Schreier. Quantitative error assessment in pattern matching: Effects of intensity pattern noise, interpolation, strain and image contrast on motion measurements. *Strain*, 45(2):160–178, 4 2009. doi: 10.1111/j.1475-1305.2008.00592.x.
- [253] Z. Wang and H. Hu. Auxetic materials and their potential applications in textiles. *Textile Research Journal*, 84(15):1600–1611, 3 2014. doi: 10.1177/0040517512449051.
- [254] Z.-P. Wang, L. H. Poh, J. Dirrenberger, Y. Zhu, and S. Forest. Isogeometric shape optimization of smoothed petal auxetic structures via computational periodic homogenization. *Computer Methods in Applied Mechanics and Engineering*, 323:250–271, 8 2017. doi: 10.1016/j.cma.2017.05.013.
- [255] Z.-P. Wang, L. H. Poh, Y. Zhu, J. Dirrenberger, and S. Forest. Systematic design of tetra-petals auxetic structures with stiffness constraint. *Materials and Design*, 170:107669, 5 2019. doi: 10.1016/j.matdes.2019.107669.
- [256] Z. Wei, Z. Guo, L. H. Dudte, H. Liang, and L. Mahadevan. Geometric mechanics of periodic pleated origami. *Physical Review Letters*, 110(21), 5 2013. doi: 10.1103/physrevlett.110.215501.
- [257] J. R. Willis. Bounds and self-consistent estimates for the overall properties of anisotropic composites. *Journal of the Mechanics and Physics of Solids*, 25(3):185–202, 6 1977. doi: 10.1016/0022-5096(77)90022-9.
- [258] S. Xu, Z. Yan, K.-I. Jang, W. Huang, H. Fu, J. Kim, Z. Wei, M. Flavin, J. McCracken, R. Wang, A. Badea, Y. Liu, D. Xiao, G. Zhou, J. Lee, H. U. Chung, H. Cheng, W. Ren, A. Banks, X. Li, U. Paik, R. G. Nuzzo, Y. Huang, Y. Zhang, and J. A. Rogers. Assembly of micro/nanomaterials into complex, three-dimensional architectures by compressive buckling. *Science*, 347(6218):154–159, 1 2015. doi: 10.1126/science.1260960.
- [259] X. F. Xu and P. Qiao. Homogenized elastic properties of honeycomb sandwich with skin effect. *International Journal of Solids and Structures*, 39(8):2153–2188, 4 2002. doi: 10.1016/s0020-7683(02)00111-7.
- [260] H. Yang and L. Ma. 1d and 2d snapping mechanical metamaterials with cylindrical topology. *International Journal of Solids and Structures*, 204-205:220–232, 11 2020. doi: 10.1016/j.ijsolstr.2020.08.023.
- [261] W. Yang, Z.-M. Li, W. Shi, B.-H. Xie, and M.-B. Yang. Review on auxetic materials. *Journal of Materials Science*, 39(10):3269–3279, 5 2004. doi: 10.1023/b:jmsc.0000026928.93231.e0.
- [262] L. Younes. *Shapes and Diffeomorphisms*. Springer Berlin Heidelberg, 2019. doi: 10.1007/978-3-662-58496-5.
- [263] G. Zhang and K. Khandelwal. Computational design of finite strain auxetic metamaterials via topology optimization and nonlinear homogenization. *Computer Methods in Applied Mechanics and Engineering*, 356:490–527, 11 2019. doi: 10.1016/j.cma.2019.07.027.
- [264] H. Zhang, Y. Luo, and Z. Kang. Bi-material microstructural design of chiral auxetic metamaterials using topology optimization. *Composite Structures*, 195:232–248, 7 2018. doi: 10.1016/j.compstruct.2018.04.058.
- [265] H. Zhao. A fast sweeping method for eikonal equations. *Mathematics of Computation*, 74(250):603–628, may 2004. doi: 10.1090/s0025-5718-04-01678-3.
- [266] H. X. Zhu and N. J. Mills. The in-plane non-linear compression of regular honeycombs. *International Journal of Solids and Structures*, 37(13):1931–1949, 3 2000. doi: 10.1016/s0020-7683(98)00324-2.

Part IV

Supplementary materials

Appendix A

Thin plates theories

A.1 Recall on Kirchhoff–Love thin plate theory

In a space endowed with an orthonormal reference $(O, \mathbf{e}_1, \mathbf{e}_2, \mathbf{e}_3)$, let us consider a plane plate of thickness h normal to the axis (O, \mathbf{e}_3) . Its mid-plane, referred to as ω , is a bounded domain of \mathbb{R}^2 , with regular boundary $\partial\omega$. For convenience, the mid-plane ω of the undeformed plate is assumed to lie in the $(O, \mathbf{e}_1, \mathbf{e}_2)$ plane. As a result, let Ω_h be the bounded domain of \mathbb{R}^3 occupied by the plate, defined as:

$$\Omega_h = \omega \times] - h/2, h/2[\quad (\omega \subset \mathbb{R}^2, h \in \mathbb{R}^{+*})$$

The plate is delimited by a regular boundary Γ_h , which may be decomposed as follows:

$$\Gamma_h = \Gamma_h^\pm \cup \Gamma_h^{\text{lat}} \quad \begin{cases} \Gamma_h^\pm = \omega \times \{\pm h/2\} & \text{(top and bottom)} \\ \Gamma_h^{\text{lat}} = \partial\omega \times] - h/2, h/2[& \text{(lateral)} \end{cases}$$

In this reference, a point M of Ω_h is represented by a set of Cartesian coordinates \mathbf{x} , which may be decomposed into in-plane coordinates $(x_\alpha) = (x_1, x_2)$ and transverse coordinate x_3 .

Thin plate kinematics. The following kinematic assumptions are made: (1) all straight lines normal to the mid-surface remain straight and normal after deformation; (2) the thickness of the plate does not change during a deformation. The following kinematics is the plate equivalent of the Euler–Bernoulli kinematics for beams. The displacement field $\mathbf{u}(x_1, x_2, x_3)$ of a thin planar plate is therefore defined as follows:

$$\begin{aligned} \mathbf{u}(x_1, x_2, x_3) &= \mathbf{U}(x_1, x_2) - x_3 \nabla U_3(x_1, x_2) \\ \Leftrightarrow \begin{cases} u_1(x_1, x_2, x_3) = U_1(x_1, x_2) - x_3 U_{3,1}(x_1, x_2) = v_1(x_1, x_2) - x_3 r_1(x_1, x_2) \\ u_2(x_1, x_2, x_3) = U_2(x_1, x_2) - x_3 U_{3,2}(x_1, x_2) = v_2(x_1, x_2) - x_3 r_2(x_1, x_2) \\ u_3(x_1, x_2, x_3) = U_3(x_1, x_2) \end{cases} \end{aligned} \quad (\text{A.1.1})$$

where $\mathbf{U}(x_1, x_2)$ is the displacement field of the mid-plane of the plate, and $\mathbf{r}(x_1, x_2) = \nabla v_3(x_1, x_2)$ are the rotations. Assuming the previous displacement field, the strain field ε reads:

$$\begin{aligned} \varepsilon(\mathbf{u}) &= \begin{bmatrix} \frac{\partial U_1}{\partial x_1} & \frac{1}{2} \left(\frac{\partial U_1}{\partial x_2} + \frac{\partial U_2}{\partial x_1} \right) \\ \frac{1}{2} \left(\frac{\partial U_1}{\partial x_2} + \frac{\partial U_2}{\partial x_1} \right) & \frac{\partial U_2}{\partial x_2} \end{bmatrix} - x_3 \begin{bmatrix} \frac{\partial^2 U_3}{\partial x_1^2} & \frac{\partial^2 U_3}{\partial x_1 \partial x_2} \\ \frac{\partial^2 U_3}{\partial x_1 \partial x_2} & \frac{\partial^2 U_3}{\partial x_2^2} \end{bmatrix} \\ &= \varepsilon(U_1, U_2) + x_3 \chi(U_3) \end{aligned} \quad (\text{A.1.2})$$

where ε represents the in-plane strains and χ the out-of-plane curvatures. Units are: $[\varepsilon] = \text{m.m}^{-1}$

and $[\chi] = m^{-1}$. Note that the out-of-plane strains ε_{i3} are all zero due to the chosen kinematic hypothesis. In particular, the normal out-of-plane strain ε_{33} is zero, which is generally not the case for thin structures, for which the plane stress behaviour is assumed.

Generalised stress components. The generalised stresses are defined as the dual of the generalised strains with respect to work. In order to define this duality, we consider the strain energy \mathcal{E}_d and impose the same energy for the complete three-dimensional and two-dimensional equivalent descriptions:

$$\begin{aligned}\mathcal{E}_d &= \frac{1}{2} \int_{\Omega} \sigma_{ij} \varepsilon_{ij}(\mathbf{u}) d\mathbf{x} = \frac{1}{2} \int_{\omega} \left(\int_{-h/2}^{h/2} \sigma_{ij} \varepsilon_{ij}(\mathbf{u}) dx_3 \right) d\mathbf{x}_{\alpha} \\ &= \frac{1}{2} \int_{\omega} \left(\int_{-h/2}^{h/2} \sigma_{ij} \delta_{i\alpha} \delta_{j\beta} \varepsilon_{\alpha\beta}(\mathbf{u}) + x_3 \sigma_{ij} \delta_{i\alpha} \delta_{j\beta} \chi_{\alpha\beta}(U_3) dx_3 \right) d\mathbf{x}_{\alpha} \\ &= \frac{1}{2} \int_{\omega} \left(\int_{-h/2}^{h/2} \sigma_{\alpha\beta} dx_3 \right) \varepsilon_{\alpha\beta}(\mathbf{u}) + \left(\int_{-h/2}^{h/2} x_3 \sigma_{\alpha\beta} dx_3 \right) \chi_{\alpha\beta}(U_3) d\mathbf{x}_{\alpha} \\ &= \frac{1}{2} \int_{\omega} N_{\alpha\beta} \varepsilon_{\alpha\beta}(\mathbf{u}) + M_{\alpha\beta} \chi_{\alpha\beta}(U_3) d\mathbf{x}_{\alpha}.\end{aligned}$$

The generalised stresses split into the membrane stress \mathbf{N} and bending moments \mathbf{M} , which are defined as follows:

$$\begin{cases} \mathbf{N} = \int_{-h^*/2}^{h^*/2} \boldsymbol{\sigma} dx_3, \\ \mathbf{M} = \int_{-h^*/2}^{h^*/2} x_3 \boldsymbol{\sigma} dx_3, \end{cases} \quad (\text{A.1.3})$$

where $\boldsymbol{\sigma}$ denotes the stress field.

Constitutive behaviour. The material under consideration in the plate features a linear elastic behaviour. In three-dimension, the constitutive behaviour is therefore governed by the Hooke's law. From a dimension reduction, we obtain the constitutive law of a thin Kirchhoff–Love plate, expressed under the following form:

$$\begin{bmatrix} \mathbf{N} \\ \mathbf{M} \end{bmatrix} = \begin{bmatrix} \mathbf{A} & \mathbf{0} \\ \mathbf{0} & \mathbf{D} \end{bmatrix} \begin{bmatrix} \boldsymbol{\varepsilon} \\ \boldsymbol{\chi} \end{bmatrix} \quad (\text{A.1.4})$$

where the tensor \mathbf{A} describes the in-plane behaviour, while the tensor \mathbf{D} describes the bending behaviour. The expression of \mathbf{A} and \mathbf{D} with respect to the three-dimensional elastic tensor \mathbf{C} is straightforward by plugging the Hooke's law into the strain energy. When the material carries a known symmetry (i.e., isotropic), an expression of in terms of the Young's moduli and Poisson's ratios can further be recovered.

A.2 Constitutive behaviour of laminate plate as a route for prescribing targets

The choice of a target plate tensor may seem a difficult task a priori. The prescribed stiffness coefficients should not compromise the positive definiteness, and should remain bounded imposed by the rule of mixture (e.g., the Voigt–Reuss bounds). Yet, to the best of our knowledge, the clear definition of elastic bounds in the context of thin plates has not been explored, and is beyond the scope of the present work. We rather address this aspect by studying the laminate plate, a sub-

category of elastic plate with periodic pattern. This simpler framework permits to rapidly construct achievable target tensors analytically.

In the sequel, we recall the expressions of A , B , D in the context of the classical laminate plate theory (CPLT) [208], and illustrate the construction of a target through an simple case which is used in the numerical examples (section 7.5).

Note that a limiting case for a homogeneous thin plate theory should be the Kirchhoff–Love plate equations. Let us consider the definition of \mathbf{N} as a sum of integrals in each layer:

$$\mathbf{N} = \sum_{k=1}^n \int_{h_k}^{h_{k+1}} \boldsymbol{\sigma} dx_3.$$

Introducing the constitutive behaviour layer by layer and using the generalised strain components gives:

$$\mathbf{N} = \sum_{k=1}^n \int_{h_k}^{h_{k+1}} \mathbf{C} : (\boldsymbol{\varepsilon}(\mathbf{U}) + x_3 \boldsymbol{\chi}(U_3)) dx_3.$$

Since the generalised strains do not depend upon x_3 , one can write:

$$\begin{aligned} \mathbf{N} &= \left[\sum_{k=1}^n \int_{h_k}^{h_{k+1}} \mathbf{C} dx_3 \right] : \boldsymbol{\varepsilon}(\mathbf{U}) + \left[\sum_{k=1}^n \int_{h_k}^{h_{k+1}} x_3 \mathbf{C} dx_3 \right] : \boldsymbol{\chi}(U_3) \\ &= \mathbf{A} : \boldsymbol{\varepsilon}(\mathbf{U}) + \mathbf{B} : \boldsymbol{\chi}(U_3). \end{aligned} \quad (\text{A.2.1})$$

Following the same reasoning for \mathbf{M} we can write:

$$\begin{aligned} \mathbf{M} &= \left[\sum_{k=1}^n \int_{h_k}^{h_{k+1}} x_3 \mathbf{C} dx_3 \right] : \boldsymbol{\varepsilon}(\mathbf{U}) + \left[\sum_{k=1}^n \int_{h_k}^{h_{k+1}} x_3^2 \mathbf{C} dx_3 \right] : \boldsymbol{\chi}(U_3) \\ &= \mathbf{B} : \boldsymbol{\varepsilon}(\mathbf{U}) + \mathbf{D} : \boldsymbol{\chi}(U_3). \end{aligned} \quad (\text{A.2.2})$$

Thus, the plate constitutive law is:

$$\begin{bmatrix} \mathbf{N} \\ \mathbf{M} \end{bmatrix} = \begin{bmatrix} \mathbf{A} & \mathbf{B} \\ \mathbf{B} & \mathbf{D} \end{bmatrix} : \begin{bmatrix} \boldsymbol{\varepsilon} \\ \boldsymbol{\chi} \end{bmatrix}$$

Comments. Like in the thin plates with periodic microstructure (section 1.4), the general laminate plate model induces an extension–bending coupling in the most general case. It is a consequence of the heterogeneous or anisotropic properties of the panel (variations between each ply). To illustrate this effect, let us consider a simple bi-phase composite panels, i.e. composed by two superposed plates that are perfectly glued at their interface. It is assumed in this example that the upper plate is stiffer than the lower one in the direction (O, \mathbf{e}_1) . Under a tensile loading in the direction (O, \mathbf{e}_1) , not only the plate is stretched in the direction (O, \mathbf{e}_1) , it also undergoes an out of plane curvature (hence a coupled response).

The main difference between the classical plate laminate theory (CPLT) and the panel with periodic micro-structure lies in the fact that \mathbf{B} is symmetric in the case of laminates, but not necessarily in the case of periodic plates.

Example. Let us consider a bi-phase laminate plate of thickness $2h$, composed of isotropic plies of equal thickness. The material in the upper ply S_p is described by Young’s modulus $E_p = 0.4608$ MPa and Poisson’s ratio is $\nu_p = -0.2$, whereas the material in lower ply S_m features a Young’s modulus $E_m = 0.1728$ MPa and Poisson’s ratio is $\nu_m = -0.8$. The resulting laminate plate

stiffness tensor, computed analytically from eqs. (A.2.1) and (A.2.2), reads:

$$\left[\begin{array}{ccc|ccc} 0.12 & -0.06 & 0 & 0. & 2.3e^{-3} & 0 \\ -0.06 & 0.12 & 0 & 2.3e^{-3} & 0. & 0 \\ 0 & 0. & * & 0 & 0. & * \\ \hline * & 2.3e^{-3} & 0 & 6.3e^{-4} & * & 0 \\ 2.3e^{-3} & * & 0 & * & 6.3e^{-4} & 0 \\ 0 & 0 & * & 0 & 0 & * \end{array} \right] \quad (\text{A.2.3})$$

The process can be extended to laminate with n ply, where each ply is orthotropic.

A.3 Two-scale analysis and effective coefficients

In our study, the unit cell is described with shell elements. The numerical computation of the coefficients in (1.4.56) is solved numerically as follows:

$$\begin{aligned} A_{\alpha\beta\gamma\delta}^* &= \frac{1}{|\mathcal{Y}|} \int_{\omega} \mathbf{C}(\mathbf{y}) (\mathbf{E}^{\alpha\beta} + (\mu(\mathbf{w}^{\alpha\beta}) + y_3\chi(\mathbf{w}^{\alpha\beta}))) : (\mathbf{E}^{\gamma\delta} + (\mu(\mathbf{w}^{\gamma\delta}) + y_3\chi(\mathbf{w}^{\alpha\beta}))) \, d\mathbf{y} \\ B_{\alpha\beta\gamma\delta}^* &= \frac{1}{|\mathcal{Y}|} \int_{\omega} \mathbf{C}(\mathbf{y}) (\mathbf{E}^{\alpha\beta} + (\mu(\mathbf{w}^{\alpha\beta}) + y_3\chi(\mathbf{w}^{\alpha\beta}))) : (y_3\mathbf{X}^{\gamma\delta} + (\mu(\tau^{\gamma\delta}) + y_3\chi(\tau^{\alpha\beta}))) \, d\mathbf{y} \\ D_{\alpha\beta\gamma\delta}^* &= \frac{1}{|\mathcal{Y}|} \int_{\omega} \mathbf{C}(\mathbf{y}) (y_3\mathbf{X}^{\gamma\delta} + (\mu(\tau^{\gamma\delta}) + y_3\chi(\tau^{\alpha\beta}))) : (y_3\mathbf{X}^{\gamma\delta} + (\mu(\tau^{\gamma\delta}) + y_3\chi(\tau^{\alpha\beta}))) \, d\mathbf{y} \end{aligned}$$

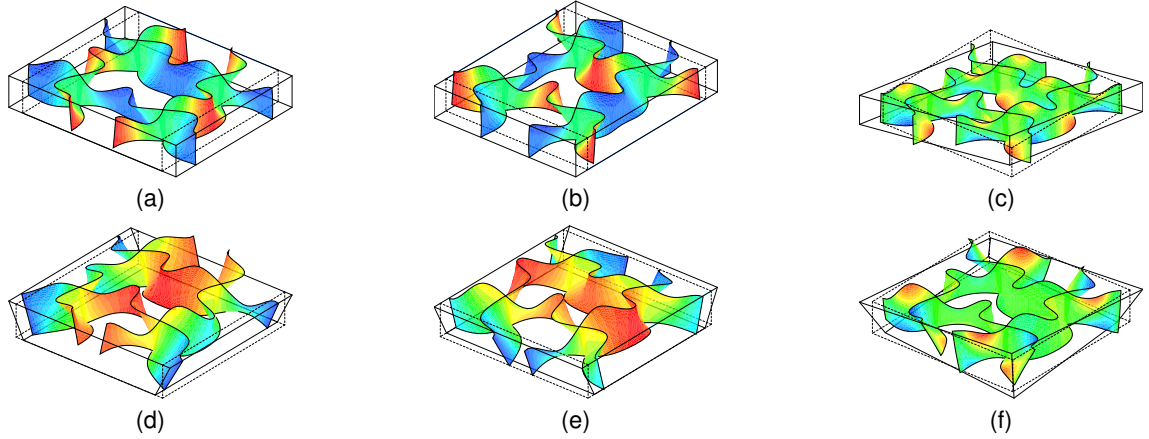


Fig. A.1: Deformation modes of the six solutions of the cells problem (1.4.52) and (1.4.53), namely (a-b) two tractions, (c) in-plane shear, (d-e) two flexures, (f) shear flexure. The colours indicate the “normalized” value of the vertical displacement u_3 plotted on the deformed mesh. The deformed correspond to a tension up to 20% effective strain

Appendix B

Penalty and augmented Lagrangian methods for constrained optimisation problem

This appendix describes two standard methods to include a constrain in optimization problems. The idea behind these methods is to replace the original problem by a sequence of sub-problems in which the constraints are represented by terms added to the objective. The results presented here are borrowed with some modifications from the monograph by Bertsekas, section 3.2, pages 164–167 [36], as well as the book by Nocedal & Wright, Chapter 17, pages 497–527 [183].

The constraints under consideration are limited to the volume of the shapes exclusively, although they could also be rapidly adapted to constrain the perimeter [18].

The notation of the previous chapters are maintained. Let $\mathcal{D} \subset \mathbb{R}^d$ denote the working (or design domain). The shape, i.e., the strong phase S is a sub-domain of \mathcal{D} , with a given volume fraction $f(S) = |S|/|\mathcal{D}|$. The next sections are devoted to present a few possibilities to control $f(S)$.

B.1 Problem setting

A general formulation for an optimisation problem under volume constraint is:

$$\inf_{S \subset \mathcal{D}} \mathcal{J}(S) \quad \text{subject to} \quad \begin{cases} |S| = \rho^{\text{target}}, & \text{or} \\ \rho_m \leq |S| \leq \rho_M, \end{cases} \quad (\text{B.1.1})$$

where \mathcal{J} denotes the objective function to be minimised, while ρ^{target} , ρ_m and ρ_M are some given coefficients. \mathcal{J} is a smooth, real-valued function on a subset of \mathcal{D} . We define the feasible set \mathcal{U}_{ad} to be the set of admissible shape S that satisfy the constraints as:

$$\mathcal{U}_{ad} = \{S \subset \mathcal{D} \text{ is open, bounded, and smooth} \mid |S| = \rho^{\text{target}} \oplus \rho_m \leq f(S) \leq \rho_M\}, \quad (\text{B.1.2})$$

so that eq. (B.1.1) can be rewritten more compactly as

$$\inf_{S \in \mathcal{U}_{ad}} \mathcal{J}(S). \quad (\text{B.1.3})$$

B.2 Equality volume constraint: Lagrange multipliers method

The simplest approach the constrained optimisation problem eq. (B.1.3) is brought back to that of the constraint-free minimization of a (Lagrangian-like) weighted sum $\mathcal{L}(S)$ of $\mathcal{J}(S)$, and $\mathcal{P}(S)$, the

latter being penalised with a fixed Lagrange multiplier λ :

$$\min_{S \subset \mathcal{D}} \mathcal{L}(S), \quad \mathcal{L}(S) = \mathcal{J}(S) + \lambda \mathcal{P}(S) \quad (\text{B.2.1})$$

where \mathcal{U}_{ad} stays defined as:

$$\mathcal{U}_{ad} := \{S \subset \mathcal{D} \text{ is open, bounded, and smooth} \mid |S| = \rho^{\text{target}}\},$$

while the penalisation function $\mathcal{P}(S)$ reads:

$$\mathcal{P}(S) = |S| - \rho^{\text{target}}.$$

This simple formulation may seem very crude, but has demonstrated its efficiency in treat example 3, section 3.4 of chapter 3. More sophisticated algorithms for handling constraints rely on such a formulation, in combination with an update strategy for the value of the Lagrange multiplier, so that the constraint is fulfilled in the end (e.g., the quadratic penalty method, the augmented Lagrangian method, or the log-barrier method, see [183], chap. 17). Other sophisticated (and efficient) algorithms exist, such as the Method of Moving Asymptotes (MMA), described in [231], or the Method of Feasible Directions (MFD), but we shall not deal with them in this manuscript.

B.3 Two-sided inequality constraints

Many problems in practice involve two-sided constraints of the form:

$$\rho_m \leq |S| \leq \rho_M \quad (\text{B.3.1})$$

where f_m and f_M are some given coefficients. Each two-sided constraint could of course be separated into two one-sided constraints which could be treated as discussed in the previous section. This would require, however, the assignment of two multipliers per two-sided constraint. We describe a more efficient approach which requires only one multiplier per two-sided constraint.

We consider for simplicity the following problem involving exclusively two-sided constraints.

$$\begin{aligned} & \inf_{S \subset \mathcal{U}_{ad}} \mathcal{J}(S) \\ & \text{subject to } \rho_m \leq |S| \leq \rho_M \end{aligned} \quad (\text{B.3.2})$$

where $\mathcal{J} : \mathcal{D} \rightarrow \mathbb{R}$, $f : \mathcal{D} \rightarrow \mathbb{R}$, and ρ_m and ρ_M are given scalars with $\rho_m < \rho_M$. The above problem is equivalent to the problem:

$$\begin{aligned} & \inf_{S \subset \mathcal{U}_{ad}} \mathcal{J}(S) \\ & \text{subject to } \rho_m \leq |S| - u \leq \rho_M \quad u = 0 \end{aligned} \quad (\text{B.3.3})$$

Now consider a multiplier method for problem (B.3.3), where only the constraints $u = 0$ are eliminated by means of quadratic penalty function. This corresponds to the partial elimination of constraints discussed in Section 2.4. This method consists of sequential minimisations over \mathbf{x} and u of the form:

$$\begin{aligned} & \inf_{S \subset \mathcal{U}_{ad}} \mathcal{J}(S) + \left(\lambda_k u + \frac{\mu_k}{2} |u|^2 \right) \\ & \text{subject to } \rho_m \leq f(S) - u \leq \rho_M \quad u = 0 \end{aligned} \quad (\text{B.3.4})$$

The Lagrange multiplier λ_k is updated by means of the iteration:

$$\lambda_{k+1} = \lambda_k + \mu_k u_k \quad (\text{B.3.5})$$

where u_k together with a vector x_k solve problem (B.3.4). Now similarly as in the previous section, minimization in problem can be carried out first with respect to u yielding the equivalent problem:

$$\begin{aligned} & \inf_{S \subset \mathcal{U}_{ad}} \mathcal{J}(S) + \mathcal{P}(f(S)) [\lambda_k, \mu_k] \\ & \text{subject to } \mathbf{x} \in \mathbb{R}^d \end{aligned} \quad (\text{B.3.6})$$

where:

$$\mathcal{P}[S, \lambda_k, \mu_k] = \min_{\rho_m \leq |S| - u \leq \rho_M} \left(\lambda_k u + \frac{\mu_k}{2} |u|^2 \right)$$

A straightforward calculation shows that the minimum above is attained at the point u_k given by:

$$u_k = \begin{cases} |S| - \rho_M & \text{if } \lambda_k + \mu_k (f(S) - \rho_M) > 0 \\ |S| - \rho_m & \text{if } \lambda_k + \mu_k (f(S) - \rho_m) < 0 \\ -\lambda_k / \mu_k & \text{otherwise} \end{cases} \quad (\text{B.3.7})$$

and \mathcal{P} is given by:

$$\mathcal{P}[S, \lambda_k, \mu_k] = \begin{cases} \lambda_k (|S| - \rho_M) + \frac{\mu_k}{2} (|S| - \rho_M)^2 & \text{if } \lambda_k + \mu_k (|S| - \rho_M) > 0 \\ \lambda_k (|S| - \rho_m) + \frac{\mu_k}{2} (|S| - \rho_m)^2 & \text{if } \lambda_k + \mu_k (|S| - \rho_m) < 0 \\ -(\lambda_k)^2 / 2\mu_k & \text{otherwise} \end{cases} \quad (\text{B.3.8})$$

The conclusion from the preceding analysis is that a method of multipliers for problem consists of sequential minimizations of the form, which do not involve the variables u . The (first-order) multiplier iteration is given by:

$$\lambda_{k+1} = \begin{cases} \lambda_k + \mu_k (|S| - \rho_M) & \text{if } \lambda_k + \mu_k (|S| - \rho_M) > 0 \\ \lambda_k + \mu_k (|S| - \rho_m) & \text{if } \lambda_k + \mu_k (|S| - \rho_m) < 0 \\ 0 & \text{otherwise} \end{cases} \quad (\text{B.3.9})$$

The last aspect consists in updating the penalty parameters μ every 10 iterations as follows:

$$\mu^{k+10} = 2\mu^k \quad (\text{B.3.10})$$

Appendix C

Experimental techniques

C.1 Digital Image Correlation

In the following paragraphs, a theoretical background and implementation details associated to the Digital Image Correlation methods implemented for the present work are presented.

Problem formulation. Given a *reference* image G and the *current* image g , DIC procedures aim at minimizing the following distance function:

$$\epsilon(\mathbf{x}) = \int_{\mathcal{D}} [g(\mathbf{x}) - G(\mathbf{X})]^2 d\mathcal{D} \quad (\text{C.1.1})$$

where \mathbf{X} is the reference configuration, $\mathbf{x} = \mathbf{X} + \mathbf{u}$ is the current configuration, \mathbf{u} is the displacement field and \mathcal{D} is the *Region Of Interest* (ROI, see Fig. C.1(a)).

Pixel interpolation. The images $G : \mathcal{D} \rightarrow \mathbb{R}$ and $g : \mathcal{D} \rightarrow \mathbb{R}$ are discrete-valued: their value is only known at integer pixel coordinates. However, both configurations \mathbf{X} and \mathbf{x} take *real values*, thus requiring the images to be probed at non-integer coordinates in order to evaluate the cost function (C.1.1). Various interpolation schemes can be implemented [214, 157], ranging from simple bilinear to bi-quintic B-spline approximations.

Discretisation. In order to solve the minimisation problem associated to the cost function (C.1.1), the displacement field \mathbf{u} is discretised as follows:

$$\mathbf{u}(\mathbf{X}) = \mathbf{N}(\mathbf{X}) \cdot \{\mathbf{u}\} \quad (\text{C.1.2})$$

where $\mathbf{N} : \mathcal{D} \rightarrow \mathbb{R}^2$ denotes a set of *shape functions* and $\{\mathbf{u}\}$ is the finite set of parameters to be determined.

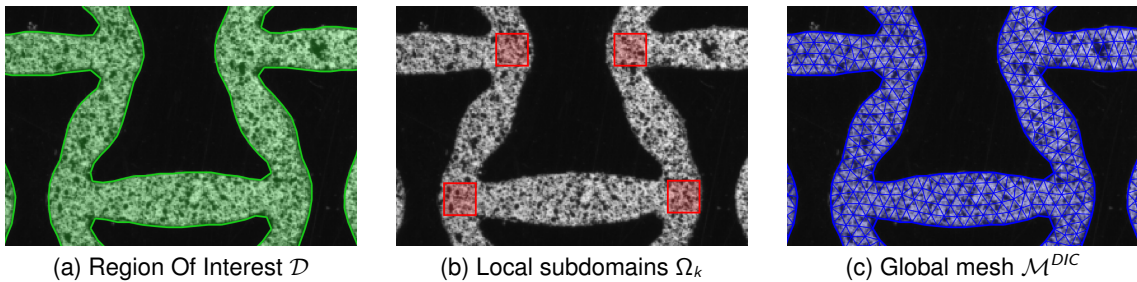


Fig. C.1: Geometries associated to digital image correlation.

Local DIC. In the *local* approach, the image is divided in a number of K *small subdomains* $\Omega_k \subset \mathcal{D}$, $k = 1 \dots, K$ (see Fig. C.1(b)). In each sub-domain, elementary displacement fields are taken, associated to simple shape functions. In the present work, a *uniform* displacement \mathbf{U}_k is assumed in each sub-domain Ω_k , corresponding to $\mathbf{N}(\mathbf{X}) = \mathbf{I}$, thus leading to the K following cost functions, for $k = 1, \dots, K$:

$$\epsilon_\ell(\mathbf{U}_k) = \int_{\Omega_k} \left[g(\mathbf{X} + \mathbf{U}_k) - G(\mathbf{X}) \right]^2 d\Omega \quad (\text{C.1.3})$$

that are to be minimised *independently*. In this formulation, the $2K$ parameters $\{\mathbf{u}\}_k = \mathbf{U}_k$ to be determined correspond to the *mean displacement* in each sub-domain Ω_k .

Global DIC. The *global* formulation is based on shape functions defined on the *entire* region of interest \mathcal{D} . In this work, piecewise-linear functions $\mathbf{N}(\mathbf{X})$ are taken as the shape functions of a finite element mesh \mathcal{M}^{DIC} (see Fig. C.1.c) composed of N nodes connected by linear triangles, thus leading to the following cost function:

$$\epsilon_g(\{\mathbf{u}\}) = \int_{\mathcal{D}} \left[g(\mathbf{X} + \mathbf{N}(\mathbf{X}) \cdot \{\mathbf{u}\}) - G(\mathbf{X}) \right]^2 d\mathcal{D} \quad (\text{C.1.4})$$

where the $2N$ parameters $\{\mathbf{u}\}$ to be determined correspond to the *nodal displacements*.

Regularisation. In contrast to the local formulation where the parameters \mathbf{U}_k are determined independently, the parameters $\{\mathbf{u}\}$ are determined *simultaneously* in the global formulation. This enables to introduce an additional term in the global cost function ϵ_g (C.1.4) associated to a Tikhonov regularisation of the strain field $\varepsilon(\mathbf{X})$. Introducing the matrix $\mathbf{B}(\mathbf{X}) = \text{sym}(\nabla_{\mathbf{X}}\mathbf{N}(\mathbf{X}))$ so that $\varepsilon(\mathbf{X}) = \mathbf{B}(\mathbf{X}) \cdot \{\mathbf{u}\}$, the regularised cost functions is expressed as:

$$\epsilon_r(\{\mathbf{u}\}) = \epsilon_g(\{\mathbf{u}\}) + \beta \int_{\mathcal{D}} \left\| \nabla_{\mathbf{X}}\mathbf{B}(\mathbf{X}) \cdot \{\mathbf{u}\} \right\|^2 d\mathcal{D} \quad (\text{C.1.5})$$

where the parameter β is fixed *a priori* and is a compromise between the regularised strain smoothness (higher values of β) and the image difference minimisation (lower values of β). However, as linear elements are used in this work, the strains are *uniform* in each triangle, thus the strain gradient *vanishes*. To get around the problem, the strain *gap* between two attached triangles is used instead. Hence the regularisation is formulated using the mesh *interior edges* (edges e with two connected triangles $t_{e,1}$ and $t_{e,2}$), leading to the following cost function:

$$\begin{aligned} \epsilon_r(\{\mathbf{u}\}) &= \epsilon_g(\{\mathbf{u}\}) + \beta \sum_e \left\| \Delta\mathbf{B}_e \cdot \{\mathbf{u}\} \right\|^2 \\ \text{with } \Delta\mathbf{B}_e &= \frac{\mathbf{B}(\mathbf{C}_{e,1}) - \mathbf{B}(\mathbf{C}_{e,2})}{\left\| \mathbf{C}_{e,1} - \mathbf{C}_{e,2} \right\|} \end{aligned} \quad (\text{C.1.6})$$

where $\mathbf{C}_{e,n}$ denotes the centroid of the triangle $t_{e,n}$.

Gauss–Newton minimisation algorithm. A Gauss-Newton algorithm is implemented to determine the parameters that minimize the cost functions (C.1.3), (C.1.4) or (C.1.5). Starting from an *initial guess* $\{\mathbf{u}^0\} = \mathbf{0}$, the parameter update is given by:

$$\{\mathbf{u}^{i+1}\} = \{\mathbf{u}^i\} - \mathbf{H}_i^{-1} \cdot \mathbf{j}_i \quad (\text{C.1.7})$$

where \mathbf{j} and \mathbf{H} are, respectively, the *Jacobian* and the *pseudo-Hessian* associated to the cost

functions ϵ . Noting that $\partial g(\mathbf{x})/\partial\{\mathbf{u}\} = \nabla_{\mathbf{x}}g(\mathbf{x}) \cdot \mathbf{N}(\mathbf{X})$, they are expressed as:

$$\mathbf{j}_i = \int_{\mathcal{D}} \nabla_{\mathbf{x}^i} g(\mathbf{x}^i) \cdot \mathbf{N}(\mathbf{X}) \cdot [g(\mathbf{x}^i) - G(\mathbf{X})] d\mathcal{D} \quad (\text{C.1.8})$$

$$\mathbf{H}_i = \int_{\mathcal{D}} \nabla_{\mathbf{x}^i} g(\mathbf{x}^i) \cdot \mathbf{N}(\mathbf{X}) \cdot (\nabla_{\mathbf{x}^i} g(\mathbf{x}^i) \cdot \mathbf{N}(\mathbf{X})) d\mathcal{D} \quad (\text{C.1.9})$$

with $\mathbf{x}^i = \mathbf{X} + \mathbf{N}(\mathbf{X}) \cdot \{\mathbf{u}^i\}$ and where the domain \mathcal{D} and the shape functions $\mathbf{N}(\mathbf{X})$ depend on the chosen formulation. The global regularisation terms introduced in (C.1.6) requires the modification of the preceding expressions as follows:

$$\mathbf{j}_i^r = \mathbf{j}_i + \beta \sum_e \nabla \Delta \mathbf{B}_e \cdot \Delta \mathbf{B}_e \cdot \{\mathbf{u}^i\} \quad (\text{C.1.10})$$

$$\mathbf{H}_i^r = \mathbf{H}_i + \beta \sum_e \nabla \Delta \mathbf{B}_e \cdot \Delta \mathbf{B}_e \quad (\text{C.1.11})$$

This updating procedure is repeated until convergence. The norm of the parameter update has been chosen here as the convergence criterion, as follows:

$$\|\{\mathbf{u}^{i+1}\} - \{\mathbf{u}^i\}\| < \delta \quad (\text{C.1.12})$$

where δ is taken as a small fraction of a pixel, depending on the quality of the images and the desired accuracy.

Image gradient estimation. The image gradient $\nabla_{\mathbf{x}}g(\mathbf{x})$ is required in the Jacobian (C.1.8) and the Hessian (C.1.9). This is performed here using a second order finite-differences scheme. However, the drawback of the update (C.1.7) is that it uses the gradient of the *current* image g with respect to the *current* configuration \mathbf{x}^i . As a consequence, it has to be evaluated at each iteration, thus leading to a high computational burden (differentiation followed by interpolation). In order to get around the problem, a *modified* Gauss-Newton formulation can be formulated using the fact that, *sufficiently close* to the solution, $g(\mathbf{x}^i) \approx G(\mathbf{X})$ so that:

$$\nabla_{\mathbf{x}^i} g(\mathbf{x}^i) \approx \nabla_{\mathbf{X}} G(\mathbf{X}) \quad (\text{C.1.13})$$

can be used to approximate the gradient of g with those of G in (C.1.8) and (C.1.9). The latter only needs to be computed once, at the beginning of the DIC procedure, thus drastically reducing the computational cost of the algorithm. However, the approximation in (C.1.13) only holds for *small* rotational motions: when large rotations occur, this *modified* formulation does not converge [191] and the gradient of g has to be used instead.

C.2 Macroscopic strain computation

When the measurement the full strain field cannot be achieved using DIC, it is still possible to compute the mean strain over a domain, provided that its boundaries can be tracked. This is used in the present work to compute the mean macroscopic strain from the unit cell corner nodes only, as the strains in the unit cell voids cannot be estimated (refer to Fig. 5.7). Following the procedure proposed by Bornert [16], we start by expressing the mean transformation gradient $\bar{\mathbf{F}}$ over a domain Ω as follows:

$$\bar{\mathbf{F}} = \langle \mathbf{F}(\mathbf{x}) \rangle_{\Omega} = \frac{1}{|\Omega|} \int_{\Omega} \left(\mathbf{I} + \frac{\partial \mathbf{u}}{\partial \mathbf{x}} \right) d\Omega \quad (\text{C.2.1})$$

which can be transformed to a *boundary* integral using Green's theorem:

$$\bar{\mathbf{F}} = \mathbf{I} + \frac{1}{|\Omega|} \int_{\partial\Omega} \mathbf{u} \otimes \mathbf{n} d\ell \quad (\text{C.2.2})$$

where \otimes denotes the outer product and \mathbf{n} is the outgoing normal to the contour $\partial\Omega$. Considering a domain Ω corresponding to a quadrilateral unit cell defined by its four corner points, this integral can be evaluated to retrieve the macroscopic transformation gradient. Finally, one can deduce the corresponding macroscopic Green-Lagrange strains $\bar{\mathbf{E}}$ as follows:

$$\bar{\mathbf{E}} = \frac{1}{2} [\mathbf{F}^T \bar{\mathbf{F}} - \mathbf{I}] \quad (\text{C.2.3})$$

Appendix D

Complementary documents

D.1 Homogenisation: numerical implementation with FreeFem++

A numerical algorithm presents a way to effectively compute these homogenised coefficients in case of a 2D plane stress problem. Here is the code written in FreeFem++ [114].

```
// Lamé coefficients in 2D (0: material - 1: void)
real lda0 = nu0 * E0 / ((1. + nu0)*(1. - nu0)),
    lda1 = nu1 * E1 / ((1. + nu1)*(1. - nu1));
real mu0 = E0 / (2.*(1. + nu0)),
    mu1 = E1 / (2.*(1. + nu1));

// Stiffness tensor in 2D of material (isotropic material)
macro C0 [[2.*mu0+lda0,lda0,0], [lda0,2.*mu0+lda0,0], [0,0,mu0]] //
macro C1 [[2.*mu1+lda1,lda1,0], [lda1,2.*mu1+lda1,0], [0,0,mu1]] //

// Stiffness distribution: properties of the material occupying the
// unit cell Y are defined as a smooth interpolation between the
// tensor C0 and C1, using the equation (2.2) in [Allaire2014].
macro Cy [heps*(C1 - C0) + C0] //
macro Cp [X3 * (C1 - C0)] //

problem elas11(u,s) = int2d(Th)((Cy * e(u))' * e(s) + p * (u' * s))
    + int2d(Th)((Cy * E11)' * e(s));

problem elas22(v,s) = int2d(Th)((Cy * e(v))' * e(s) + p * (v' * s))
    + int2d(Th)((Cy * E22)' * e(s));

problem elas12(w,s) = int2d(Th)((Cy * e(w))' * e(s) + p * (w' * s))
    + int2d(Th)((Cy * E12)' * e(s));

elas11; elas22; elas12;

real CH1111, CH1122, CH2222, CH1212;

CH1111 = int2d(Th)((Cy * (e(u) + E11))' * (e(u) + E11));
CH1122 = int2d(Th)((Cy * (e(u) + E11))' * (e(v) + E22));
CH2222 = int2d(Th)((Cy * (e(v) + E22))' * (e(v) + E22));
CH1212 = int2d(Th)((Cy * (e(w) + E12))' * (e(w) + E12));
```

D.2 Compliance plate tensors for shape of chapter 7

Example 1

$$S^* = \left[\begin{array}{ccc|ccc} 11.83 & 5.74 & 0 & 11.23 & -35.85 & 0 \\ 5.74 & 11.54 & 0 & -19.10 & -20.15 & 0 \\ 0 & 0 & 33.82 & 0 & 0 & 53.71 \\ \hline 11.23 & -19.10 & 0 & 1723 & 61.42 & 0 \\ -35.85 & -20.15 & 0 & 61.42 & 1723 & 0 \\ 0 & 0 & 53.71 & 0 & 0 & 5968 \end{array} \right] \quad (\text{D.2.1})$$

Example 2

$$S^* = \left[\begin{array}{ccc|ccc} 11.74 & 4.02 & 0 & -14.23 & -10.47 & 0 \\ 4.02 & 11.63 & 0 & -13.12 & -12.33 & 0 \\ 0 & 0 & 43.79 & 0 & 0 & -39.41 \\ \hline -14.23 & -13.12 & 0 & 3934 & -878.1 & 0 \\ -10.47 & -12.33 & 0 & -878.1 & 3927 & 0 \\ 0 & 0 & -39.41 & 0 & 0 & 5035 \end{array} \right] \quad (\text{D.2.2})$$

Example 3

$$S^* = \left[\begin{array}{ccc|ccc} 12.20 & 5.73 & 0 & -49.99 & -15.15 & 0 \\ 5.73 & 11.33 & 0 & -19.07 & -34.12 & 0 \\ 0 & 0 & 38.85 & 0 & 0 & -103.2 \\ \hline -49.99 & -19.07 & 0 & 1352 & -45.51 & 0 \\ -15.15 & -34.12 & 0 & -45.51 & 1175 & 0 \\ 0 & 0 & -103.2 & 0 & 0 & 3399 \end{array} \right] \quad (\text{D.2.3})$$

Example 4

$$S^* = \left[\begin{array}{ccc|ccc} 100.2 & 0.27 & 0 & -1013 & -11.37 & 0 \\ 0.27 & 28.70 & 0 & -7.794 & 299.0 & 0 \\ 0 & 0 & 136.8 & 0 & 0 & -124.4 \\ \hline -1013 & -7.794 & 0 & 11302 & -203.0 & 0 \\ -15.15 & -34.12 & 0 & -203.0 & 4486 & 0 \\ 0 & 0 & -124.4 & 0 & 0 & 9204 \end{array} \right] \quad (\text{D.2.4})$$

Titre : Sur la conception de feuilles architecturées 3D imprimables

Mots clés : optimisation topologique, micro-architecture, panneaux, impression 3D, corrélation d'image numérique

Résumé : Cette thèse s'intéresse à la conception et la caractérisation mécanique de matériaux architecturés périodiques, avec un accent porté sur les feuilles minces. Ces solides se caractérisent par leur micro-architecture obtenue en répétant périodiquement des mailles élémentaires, qui confèrent des propriétés macroscopiques exceptionnelles. L'avènement des techniques d'impression 3D offre la possibilité de fabriquer des micro-architectures de formes toujours plus complexes, ouvrant de nouvelles problématiques liées à leur conception. L'étude se place dans le cadre de matériaux à comportements linéaires élastiques et s'appuie sur des méthodes d'homogénéisation asymptotique, et d'optimisation topologique avec des surfaces de niveaux. La première partie porte sur le cycle de conception systématique de feuilles minces architecturées à coefficient de Poisson négatif. Après avoir fixé les propriétés élastiques cibles, la configuration optimale de la micro-architecture s'obtient en résolvant le problème inverse par le biais d'un algorithme d'optimisation topologique. Des spécimens de feuilles architecturées sont fabriqués et sollicités mécaniquement en tractions ou cisaillements. Une méthode d'analyse multi-échelles par

corrélation d'images numériques permet d'identifier les mécanismes de déformations dans le plan. Ces analyses expérimentales agrémentées par des simulations par éléments finis permettent d'évaluer les effets des non-linéarités géométriques et des imperfections de fabrication sur la réponse structurelle. La deuxième partie concerne l'étude de plaques architecturées, présentant un mécanisme de couplage extension-flexion, qui peut être exploité pour fabriquer des panneaux qui changent de forme. Ces panneaux ont été obtenus dans un premier temps à partir d'un réseau de rubans ondulés paramétrés par des B-splines, et plus récemment en utilisant une méthode d'optimisation topologique adaptée aux plaques. Dans les deux cas, les propriétés élastiques sont estimées en utilisant les modèles de plaque de Kirchhoff-Love généralisé. Le contrôle simultané du comportement dans le plan, hors plan et du couplage permet de transformer des structures planes en formes de dôme ou de selle sous l'action de chargement dans le plan. Des essais expérimentaux avec un chargement ponctuel a mis en évidence des déplacements hors plan conséquents.

Title : On the design of 3D printable architected sheets

Keywords : topology optimisation, micro-architecture, panels, 3D printing, digital image correlation

Abstract : The aim of this thesis is to design and mechanically characterise periodic architectural materials, with a focus on the case of thin sheets. These solids are characterised by their micro-architecture, obtained by periodically repeating elementary meshes, which confer exceptional macroscopic properties. The advances in 3D printing techniques offer the possibility to manufacture micro architectures of ever more complex shapes, opening the way to new possibilities related to their design. The study is placed within the framework of materials with elastic linear behaviours and is based upon asymptotic homogenisation, and topology optimisation with the level set method. The first part deals with the systematic design cycle of thin architected sheets exhibiting a negative Poisson's ratio. After fixing the target elastic properties, the final configuration of the micro-architecture is obtained by solving the inverse problem with topology optimisation algorithms. Architected sheets specimens are fabricated and mechanically loaded in ten-

sion and shear. A multi-scale analysis method using digital image correlation makes it possible to identify the in-plane mechanisms of deformation. These experimental analyses, supplemented by finite element simulations, make it possible to evaluate the effects of geometric non-linearities and manufacturing imperfections on the structural response. The second part is devoted to the study of composite panels, featuring an extension-bending coupling mechanism, which can be harnessed to manufacture panels that change shape. These panels were first build as a network of undulated ribbons, parametrised by B-splines, and more recently using topology optimisation method adapted to plates. In both cases, the elastic properties are estimated using the generalised Kirchhoff-Love thin plate models. Simultaneous control of in-plane, out-of-plane and coupling behaviour enable to morph flat structures into dome- or saddle shapes under the action of in-plane loading. Experimental tests with point-like boundary highlights exceptional out of plane displacement.